Dissertation

Andrew S. Crampton

Systematic UHV Study of Ethylene Hydrogenation on Supported, Size-Selected Clusters

TECHNISCHE UNIVERSITÄT MÜNCHEN

Lehrstuhl für Physikalische Chemie

Systematic UHV Study of Ethylene Hydrogenation on Supported, Size-Selected Clusters

Andrew Scott Crampton

Vollständiger Abdruck der von der Fakultät für Chemie der Technischen Universität München zur Erlangung des akademischen Grades eines

Doktors der Naturwissenschaften

genehmigten Dissertation.

Vorsitzender: Univ.-Prof. Dr. Sebastian Günther

Prüfer der Dissertation:
1. Univ.-Prof. Dr. Ulrich K. Heiz
2. Univ.-Prof. Dr. Johannes A. Lercher
3. Prof. Dr. Uzi Landman, Georgia Institute of Technology/USA (nur Gutachter)

Die Dissertation wurde am 27.10.2015 bei der Technischen Universität München eingereicht und durch die Fakultät für Chemie am 26.11.2015 angenommen.

Dissertation

Systematic UHV Study of Ethylene Hydrogenation on Supported, Size-Selected Clusters

Andrew S. Crampton

Technische Universität München
October 2015

This dissertation was written with the text formatting system TEX.

How, in such an alien and inhuman world, can so powerless a creature as man preserve his aspirations untarnished? A strange mystery it is that nature, omnipotent but blind, in the revolutions of her secular hurrying through the abysses of space, has brought forth at last a child, subject still to her power, but gifted with sight, with knowledge of good and evil, with the capacity of judging all the works of his unthinking mother. In spite of death, the mark and seal of the parental control, man is yet free, during his brief years, to examine, to criticize, to know, and in imagination to create. To him alone, in the world with which he is acquainted, this freedom belongs;

Bertrand Russell (1903)

Abstract

Ethylene hydrogenation on metal clusters was applied as a model system for alkene catalysis under UHV conditions and the reactivity systematically investigated as a function of the metal catalyst component (Ni, Pd and Pt), the atomically precise size of the clusters (Pt) and the support material (MgO and SiO_2). Contrary to preceding studies, the combined experimental and theoretical results demonstrated that the individual parameters have a significant influence on various catalytic properties.

In particular, it was shown that ethylene hydrogenation, contrary to popular opinion, is a structure sensitive reaction on sub-nanometer platinum particles, and that this is induced by the dehydrogenation of ethylene to form co-adsorbed carbon species during the reaction. Furthermore, changing the support material and support stoichiometry were shown to enable the tuning of catalytic properties of individual cluster sizes. Aside from uncovering these effects, the dissertation provides a foundation for future studies of more complex hydrocarbon based catalytic reactions on supported metal particles.

Zusammenfassung

Anhand der Hydrierung von Ethylen als Modellreaktion für heterogene Olefinkatalyse wurde die Reaktivität von Clustern als Funktion der Metallkomponente (Ni, Pd und Pt), ihrer präzisen atomaren Größe (Pt) sowie des Trägermaterials (MgO und SiO_2) unter UHV Bedingungen untersucht. Die experimentellen Ergebnisse zeigen, zusammen mit theoretischen Berechnungen, dass die Variation jedes einzelnen Parameters drastischen Einfluss auf die katalytische Aktivität hat.

Diese Ergebnisse belegen, dass die Hydrierung von Ethylen auf Platinpartikeln (< 1 nm), im Gegensatz zu vorangegangenen Studien, eine struktursensitive Reaktion ist. Diese Struktursensitivität wird bedingt durch die Dehydrierung von Ethylen, welche zur Bildung von Kohlenstoffspezies auf den Partikeln führt. Des Weiteren können die katalytischen Eigenschaften einer individuellen Partikelgröße durch das Trägermaterial und dessen stöchiometrischen Zusammensetzung gezielt verändert werden. Durch die Identifizierung dieser entscheidenden Faktoren wurde eine Basis geschaffen, welche die Untersuchung der Chemie von komplexeren Kohlenwasserstoffen auf geträgerten Metallpartikeln erlaubt.

Contents

Foreword

The following dissertation is the culmination of a total of five years working in the group of Prof. Ueli Heiz as a student 'Hilfskraft', a master student, and finally a doctoral student. The decision to write the dissertation in the cumulative format was multi-faceted. The results in the lab over the past three years have been very productive and this allowed for the publication of a number of research papers used in this dissertation. Additionally, my Master Thesis, written in 2011, contains technical and theoretical descriptions of many of the experimental techniques used within this work and as no major revision to the instrument was made, a traditional dissertation would contain a large amount of repetition compared to my Master Thesis. For these reasons the experimental section provides a basic introduction to the techniques used, rather than a rigorous theoretical exposition.

The dissertation is composed of four chapters; the first is a review of literature on the platinum catalyzed ethylene hydrogenation; the second is an overview of the experimental techniques; the third is the results and discussion section; and the fourth provides a conclusion and outlook. It is incumbent upon the reader to place focus on reading the papers presented in chapter 2 and chapter 3, as they provide many experimental details and descriptions that may be lacking elsewhere.

1 Introduction

The study of model heterogeneous catalysts has its origin with the advent of surface science in the 1970's, where it was identified that by studying single crystal surfaces in ultra high vacuum (UHV) environments, one can extrapolate trends to realistic systems comprised of disperse metal particles on a support. The underlying focus was the improved understanding, and hence fabrication, of heterogeneous catalysts for a wide range of applications. The UHV model systems became more complex with the fabrication of thin metal-oxide films grown on metal single crystals to model real catalyst supports, and the use of evaporation techniques to synthesize metal particles on these thin films.

The further development of advanced experimental techniques brought about a new field of research within the vacuum community: size-selected clusters. It had been observed that clusters in the gas phase exhibited chemical and physical properties which could be drastically changed by adding or removing an atom from the cluster. Before long, the prospect of investigating the catalytic properties of these clusters supported on surfaces, and using them to model heterogeneous catalysts, became a reality. For heterogeneous catalysis this opened up a completely new realm of research, where reactions could be studied as a function of the precise number of atoms per cluster in a mono-disperse system. Such a well defined system, which can be synthesized and studied in a highly reproducible environment, UHV, represents the ultimate model catalyst system.

Ethylene hydrogenation is one of the classical reactions studied on single crystal surfaces under UHV conditions, as well as standard heterogenous catalysts. It is a model system and the most elementary olefin hydrogenation, but represents an important increase in complexity compared to the better understood CO oxidation due to competing reactions of unsaturated hydrocarbons on surfaces as well as the wide array of intermediates that can be formed at elevated temperatures. It is also considered a 'structure insensitive' reaction, as the reaction rate is not observed to be dependent on particle size or single crystal plane.

The goal of this dissertation was to investigate this reaction on size-selected clusters in UHV for the first time, as a foundation for later studies on more advanced and industrially relevant hydrocarbon based reactions. Hereby, focus was placed on isolating and investigating targeted characteristics of the catalyst system including: *cluster size*, *metal-oxide support*, *support stoichiometry* and lastly *catalyst metal*. The review given in the following pages focuses exclusively on literature pertaining to platinum, as this is by far the most well studied catalyst for the reaction and provides the necessary information for the reading of this dissertation.

1.1 Ethylene Hydrogenation on Platinum

1.1.1 Early Studies

The catalytic hydrogenation of ethylene to ethane was first reported by Paul Sabatier in 1897 on a nickel catalyst [1]. It was not until the 1930's that a major advancement was made in describing hydrogenation catalysis, with the postulation of what is now known as the Horiuti-Polanyi reaction mechanism [2]. In their paper, the authors described the discrimination between two proposed reaction mechanisms for hydrogen exchange with benzene and ethylene, which can be seen in figure 1.1 for benzene.

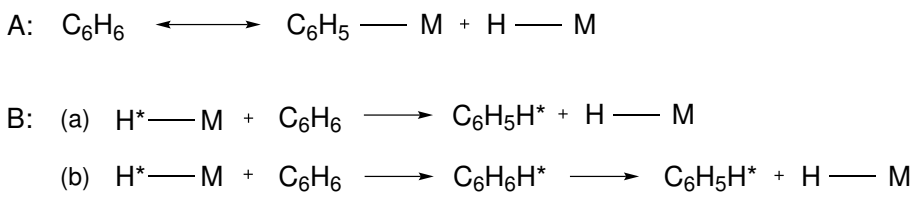

Figure 1.1: Proposed reaction mechanisms for hydrogen exchange of benzene over a metallic catalyst (M). (A) represents the dissociation of a C−H bond, (B): (a) is a simultaneous exchange of hydrogen, and (B): (b) involves a 'half hydrogenated' transition state. Mechanism B (b) was determined to be the correct path for hydrogen exchange of benzene and ethylene on a nickel catalyst and is known as the Horiuti-Polanyi Mechanism [2].

The first proposed mechanism, (A), involved the dissociation of the carbon-hydrogen bond, followed by a subsequent re-hydrogenation. The authors proposed a simple experiment whereby they claimed that if the bond dissociation is occurring, then changing the source of hydrogen from gaseous hydrogen to water should not impact the reaction rate. This was under the assumption that co-reactants would not affect adsorption characteristics of the hydrocarbon. Their results showed that the reaction rate decreased upon changing from gaseous hydrogen to water which led them to reject mechanism A. Mechanism B represents two possibilities for hydrogen addition; (a) corresponds to a transition state where there is simultaneous abstraction and addition of a hydrogen atom to a carbon atom and (b) is the case where the double bond opens upon adsorption to the surface in order to reach a transition state that is 'half hydrogenated' to use the language of the authors. Choosing between (a) and (b), was achieved by considering the quantum mechanical nature of the respective transition states. As (a) requires a five atom transition state, mechanism (b), with only a four atom transition state, was predicted to have a lower activation barrier. Experimental evidence was then cited which accrued even more evidence for the selection of mechanism (b). In particular, it was noted that saturated alkanes do not undergo hydrogen exchange, a fact which would not be expected from (a), where the carbon-carbon bond plays no role in the reaction. The observation of isomerism on hydrogenation catalysts was also a very important observation, as this presupposed an activation of carbon bonds by the catalyst. The combined evidence led the authors to conclude that mechanism B(b) was correct. They also added that the extension to a complete hydrogenation is in concordance with their mechanism. The only difference is that in the 'half hydrogenated'

state another adsorbed hydrogen atom can approach the second carbon of the double bond and hydrogenation will occur. The mechanism of a step-wise hydrogen atom addition across a double bond was therefore given the name: Horiuti-Polanyi.

After the proposal of this reaction mechanism, copious amounts of experiments were performed on a variety of metal catalysts. It would be unrealistic to provide a complete overview, but the reader is directed towards a very comprehensive review [3].

The following details are important to note:

- The ethylene hydrogenation exhibits a decrease in activity over time due to the build-up of carbonaceous deposits.
- Self-hydrogenation can occur, whereby hydrogen atoms are abstracted from ethylene and then subsequently used to hydrogenate another ethylene molecule.
- The reaction is most efficient with hydrogen being introduced first to the catalyst.
- Activity varies greatly with catalyst preparation method.
- The reaction is first order with respect to hydrogen and the activation barrier on Pt was seen to vary from 0.2 - 0.7 electron volts (eV).

1.1.2 Surface Science - Adsorption of Ethylene on Pt(111)

The studies of the catalytic ethylene hydrogenation on metallic catalysts up until the 1970's had a major difficulty of reproducibility. This entailed many important experimental details, including the preparation of the catalyst, product detection, particle size/dispersion, surface morphology determination, etc. The study of surfaces along with their physical and chemical properties required technology that ensured a high degree of purity and homogeneity of the catalyst surface. The advent of surface science in the late 60's and 70's enabled just this, as the concurrent advances in vacuum systems and characterization tools for single crystal surfaces yielded these aforementioned, experimental necessities. The study of ethylene hydrogenation under ideal, UHV conditions began with first studying the adsorption of ethylene on single crystal surfaces using low energy electron diffraction (LEED). LEED can provide details on the structure(s) of an adsorbed overlayer on an ordered surface (single crystal) and can reveal bonding geometries and molecular structure of adsorbates on single crystals.

Starting with a LEED analysis of a clean Pt(111) single crystal [4], studies determined that after room temperature adsorption followed by either a short annealing step at 100° C [5], or exposure to an electron beam [6], ethylene formed a (2x2) ordered structure on Pt(100) and Pt(111). The molecular nature of the adsorbate was proposed to be an acetylenic species, due to the same LEED pattern resulting from adsorption of pure acetylene. Ethylene was also proposed to be π-bonded to the surface, due to a decrease in the work function [5–7]. These experimental conclusions were shown to be incorrect from electron energy loss spectroscopy (EELS), where the dehydrogenated species ethylidene ($CH - CH_3$) was proposed as the stable form of ethylene on Pt(111) at T $>$ 300 Kelvin (K), and sp^3 hybridization of the carbon atoms at low temperature ($<$ 260 K) better explained the vibrational data [8].

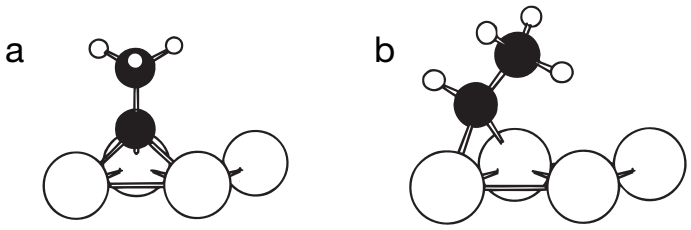

*Figure 1.2: Adsorption of ethylidyne (a) and ethylidene (b) on a Pt(111) surface. Both fragments were in contention as the adsorbed state of ethylene at room temperature until ethylidyne was finally proven. Adapted with permission from (Watwe et al. J. Phys. Chem. B **2000**, 104, 2299.). Copyright (2015) American Chemical Society.*

The authors also concluded that ethylidene was the likely intermediate or 'half-hydrogenated' state on the way to ethane. Although the question of this stable species seemed to be clarified, another structure was proposed shortly thereafter which better matched available data and is now the accepted species: ethylidyne ($C-CH_3$) [9]. Ethylidyne was proposed to be bonded to a three-fold symmetric site with a $C-C$ bond length of 1.5 Å. Figure 1.2 shows these two adsorption configurations on a Pt(111) surface. The identification of the species as ethylidyne was at first not accepted by all, notably Demuth and Ibach continued to propose a vinyl and ethylidene species, respectively [10, 11]. These two C_2 moieties both displayed one convincing property: vinyl has the correct stoichiometry of C_2H_3, and ethylidene has an aliphatic $C-C$ bond perpendicular to the surface. The correct stoichiometry was supported by temperature programmed desorption (TPD) measurements [12] where it was also seen that no hydrogen desorption from acetylene accompanied the formation of this species, which is expected given the stoichiometry.

The decisive evidence for the identification of ethylidyne was achieved by using organometallic chemistry and IR spectroscopy, where a cobalt complex with ethylidyne, ($CH_3CCo_3(CO)_9$), provided the necessary organometallic analog of ethylidyne on Pt(111) and allowed for a correct interpretation of the vibrational bands observed [13]. This was further confirmed using angle resolved photoemission with synchrotron radiation [14]. As synchrotron radiation is plane polarized, simple symmetry arguments can be used to assign molecular orbitals to emission peaks and this provided more conclusive evidence that ethylidyne is indeed the surface species which forms a (2x2) structure at 300-350 K. These results seemed to have convinced Ibach that ethylidyne is the correct assignment and in the same publication he further identified that on an oxygen pre-covered surface at high coverages, both π and di-σ-bonded ethylene were present, and that di-σ-bonded ethylene was the precursor of ethylidyne [15].

A further TPD study by Somorjai on Pt(111) showed that after adsorption at 110 K, ethylene desorbs at ≈ 285 K, with an activation energy (E_a) of 0.5 eV and there are three subsequent dehydrogenation steps. At ≈ 290 K ethylene first loses a hydrogen atom to form ethylidyne followed by a second, large dehydrogenation step at $\approx$ 490 K leaving CH groups on the surface ($E_a = 0.95$ eV). The dehydrogenation of these carbon species then occurs at 550, 641 and 704 K, all with $E_a > 1.4$ eV [16]. Finally, using an as yet to be mentioned

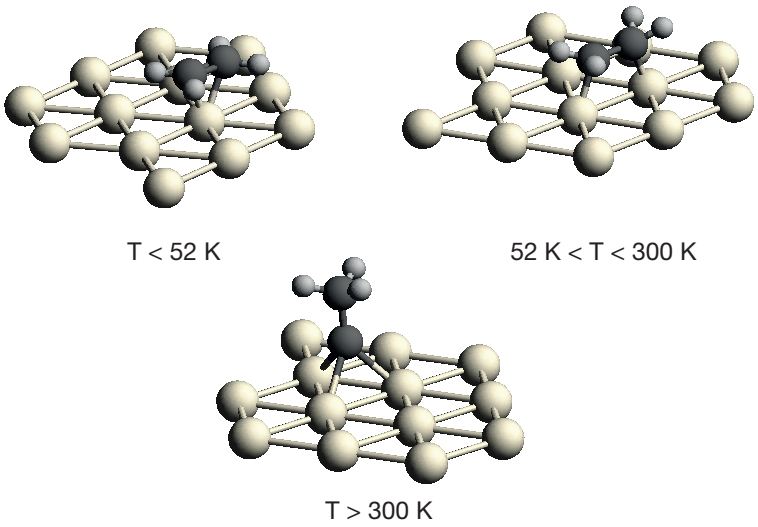

Figure 1.3: Preferred ethylene adsorption on Pt(111) as a function of temperature. Under 52 K, ethylene prefers to adsorb in a π-configuration, from 52 to $\approx$ 300 K, ethylene prefers di-σ and above 300 K ethylidyne is the preferred mode. Note that ethylidyne formation already requires a dehydrogenation step.

experimental technique, (secondary ion mass spectrometry (SIMS)), all previous conclusions were confirmed [17].

Ethylene was shown to adsorb in a di-σ configuration at 150 K based on EELS data but less is written in the literature about what types of sites it occupies and the specific molecular structure, e.g. bond lengths [18]. These early studies seemed to be less concerned with the nature of pure ethylene adsorption and more concerned about the structure formed upon slight heating above 300 K and the resulting (2x2) LEED pattern. Indeed, the absence of an ordered structure of ethylene adsorbed at lower temperatures on Pt(111) could have been the reason for the lack of experimental data [19].

Using ultraviolet photoelectron spectroscopy (UPS) it was later shown that at temperatures below 52 K ethylene adsorbs in a π-bonded state [20, 21]. This was deduced from the similarity between UPS spectra from the gas phase, an ethylene multilayer on Pt(111) and from monolayer coverage of the surface, which all indicated that the $C-C$ double bond was preserved at these temperatures. The orientation of the double bond was also later shown to be parallel to the surface [22]. From these data a complete picture of ethylene adsorption can be constructed showing the preferred form of adsorption as a function of temperature, and can be seen in figure 1.3.

The previous section is meant to be not only an introduction to ethylene adsorption properties on Pt(111) in order to facilitate the following section, but also conveys the difficulty in dealing with the simplest alkene on model surfaces. The referenced literature here is by no means all-inclusive, but the most important concepts have been covered to give the reader the essential background information.

1.1.3 Surface Science - Catalytic Hydrogenation

The last section has shown that surface science techniques enable copious amounts of data to be gathered from a relatively simple hydrocarbon system and that these data can often lead to controversy due to their complexity. In this section the studied system was made more intricate by applying surface science techniques to a catalytic reaction: ethylene hydrogenation.

Pt(111)

The seminal paper regarding the hydrogenation of ethylene on Pt(111) is the work of Zaera and Somorjai [23]. This paper reported, for the first time, a catalytic study of ethylene hydrogenation using surface science techniques. The authors warned at the beginning though[1]:

> One of the problems is that most of these studies are carried out over clean surfaces and under ultra-high vacuum conditions. The catalytic reactions, on the other hand, generally take place on surfaces covered with adsorbed species, and at several atmospheres of reactant gases. Then, the intermediates in the reactions need not necessarily be related to the chemisorbed states of the reactants under vacuum conditions.

This aspect plays a very decisive role in the ethylene hydrogenation, as ethylidyne has been shown in chapter 1.1.2 to be omnipresent on Pt(111) at ambient temperatures. The authors performed the ethylene hydrogenation at 300 - 373 K and measured an activation barrier of $E_a = 0.47$ eV, and a reaction order for ethylene and hydrogen of -0.6 and 1.3, respectively. They also observed the same (2x2) LEED pattern after adsorbing ethylene onto the clean surface at room temperature and after the ethylene hydrogenation, albeit less ordered in the latter case. This led to the conclusion that ethylidyne was present during the hydrogenation but its exact role was difficult to ascertain. As no self-poisoning was observed under their reaction conditions, and a pre-covered ethylidyne surface showed the same activity as an initially clean surface, ethylidyne could not be an inhibitor of the hydrogenation. Through a series of isotope labeled experiments the authors concluded that it is also unlikely that ethylidyne is a reaction intermediate, but rather that the reaction occurs on the overlayer itself.

The question still remained as to why different metals exhibited different activities. This was rationalized by assuming that hydrogen could still access metallic sites on the surface and that ethylidyne acted as the transport agent for ethylene to access hydrogen,

[1] This exemplifies one of the inherent difficulties regarding surface science and catalysis: UHV studies represent ideal circumstances, many of which are not found under normal catalytic conditions. Nevertheless, it has been shown that ideal studies can yield very insightful information regarding catalytic reactions run under normal conditions. Two famous examples of this (as well as leading to a Chemistry Nobel Prize) were the identification of the Langmuir-Hinshelwood Mechanism for the CO oxidation on palladium [24, 25], and work done on elucidating the ammonia synthesis mechanism on iron [26–29], both by Gerhard Ertl. These studies show that surface science can play a critical role in unraveling the mechanisms and chemistry of heterogeneous catalytic reactions under ambient conditions.

possibly through an ethylidene intermediate. This was also supported by the reaction order of 1.3 with respect to hydrogen. Lastly, after comparing their data to other results on dispersed catalysts, the structure insensitivity[2] they observed was attributed to the fact that the reaction was occurring on this alkylidyne overlayer.

Shortly thereafter, a TPD study showed that the ethylene hydrogenation had two pathways on the Pt(111) surface [30]. It was shown that pre-adsorbed hydrogen led to a low temperature ethane desorption peak at $\approx$ 200 K and in the absence of hydrogen the ethane desorption shifted[3] to 235 K. The authors concluded that there are two types of reactive sites on Pt(111); the low temperature ethane production occurred on a 'Pt atom' site where hydrogen was readily accessible to ethylene; the high temperature peak took place on a site where ethylene was more strongly adsorbed without the presence of hydrogen, and required hydrogen atom migration from a neighboring site in order to hydrogenate. Th authors also claimed that when no hydrogen is co-adsorbed, then the source of hydrogen, leading to exclusively the site 2 mechanism, is from the background UHV environment.

This interpretation of TPD data was supported by results from Godbey *et al.*, who also showed that the ethane desorption temperature decreased to 250 K when hydrogen was pre-adsorbed [33]. The self-hydrogenation mechanism (site 2 in the previous study) was seen to not be due to background hydrogen adsorption but rather from a hydrogen atom abstracted during ethylidyne formation. The authors concluded that on a clean platinum surface, the hydrogenation proceeds more efficiently, but under steady state conditions at elevated temperatures the formation of carbonaceous deposits (ethylidyne or even ethylidene as a reaction intermediate) directly participate in the reaction, making it less efficient. They also mentioned the possibility that ethylidyne could be acting as a hinderance to the accessibility of metal sites for ethylene, but said that this is unlikely as neither ethylene or ethane was observed to desorb from a ethylidyne covered Pt(111) surface when dosed at atmospheric pressure. The hydrogen source for the self-hydrogenation mechanism being from ethylene and not from the background was later proven using isotope experiments [34].

The proposed reaction mechanism involving ethylidyne as a hydrogen transport intermediate from the surface to ethylidyne was shown to be incorrect by Beebe and Yates on alumina supported palladium [35]. In this paper they demonstrated that the presence of ethylidyne had no effect on the hydrogenation rate and therefore must be an inactive spectator species.

The rate determining step of the reaction was revealed using ethyl iodide as a reactant. TPD studies showed that the reaction temperature of ethane decreased when using ethyl iodide, which is a strong indication that the formation of an ethyl intermediate is the rate determining step [36].

It is important to note that up to this point, relatively little was hypothesized about the precise nature of the reactive species. The Horiuti-Polanyi mechanism properly described the kinetics but there was still no indication as to the state of ethylene on the surface before

[2] Structure sensitivity-insensitivity will be discussed in chapter 1.2.

[3] A similar result on the less densely packed surfaces (210), 1x1(110) and 2x1(110) also showed a temperature decrease to 220, and 200 K (for both 1x1 and 2x1), respectively [31, 32].

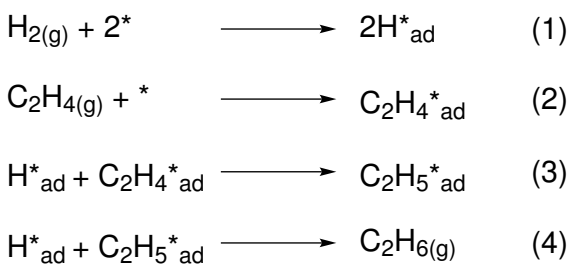

Figure 1.4: General Horiuti-Polanyi ethylene hydrogenation reaction mechanism on platinum.

it is hydrogenated. The adsorbed species, described in chapter 1.1.2, were known, but there was no experimental evidence pointing unequivocally to the active adsorbed state. Figure 1.4 shows the general mechanism that was accepted at this point.

In a transmission Fourier Transform Infrared Spectroscopy (FTIR) study on alumina supported Pt particles, Mohsin *et al.* showed that π-bonded ethylene was also present on the catalyst at 180 K and that di-σ ethylene was the ethylidyne precursor [37]. They also showed that both di-σ and π-bonded ethylene can both be hydrogenated in the presence of hydrogen, and supported the claim of Beebe and Yates that ethylidyne is purely a spectator species.

The quintessential study that produced the complete molecular nature of the ethylene hydrogenation was published in 1996 [38]. Cremer *et al.*, using the exclusively surface sensitive sum frequency generation (SFG) spectroscopic technique, showed that the rate of ethylene hydrogenation on Pt(111) was independent of the concentration of di-σ-bonded ethylene and also observed that π-bonded ethylene was present during hydrogenation at 295 K. The concentration of π-bonded ethylene, and the hydrogenation rate, were seen to be unchanged on a clean and ethylidyne pre-covered Pt(111) surface indicating that this was the reactive species. In contrast, the di-σ-bonded ethylene surface concentration decreased on the ethylidyne pre-covered surface. The formation of an ethyl intermediate observed in the SFG spectra further confirmed the Horiuti-Polanyi mechanism. While π-bonded ethylene was determined to be the active precursor, the authors did note that ethylidyne and di-σ-bonded ethylene were also hydrogenated, but orders of magnitude slower. These results showed for the first time that π-bonded ethylene is the active ethylene species in the catalyzed hydrogenation reaction.

The idea that a weakly bound form of ethylene was responsible for the formation of ethane was also proposed by Zaera concurrently with the paper by Cremer *et al.* [39]. This review provided a comprehensive look at the ethylene hydrogenation, as well as hydrogen-deuterium exchange reactions and the surface chemistry of ethylene, on Pt(111) up to that point. Shortly thereafter Öfner *et al.* applied isothermal molecular beam experiments under vacuum and atmospheric conditions, and showed that a weakly bound species was the kinetically relevant one for ethylene hydrogenation [40].

Using SFG in a similar experiment, McCrea *et al.* demonstrated that the ethylene hydrogenation proceeds at the same rate under atmospheric conditions on both the Pt(111)

and Pt(100) surfaces [41]. This provided more direct evidence that the reaction is structure insensitive on platinum. The authors also observed that the adsorption properties of ethylene were, however, structure dependent, in that the concentration of ethylidyne was higher on Pt(111) than on Pt(100), while the converse was true for di-σ bonded ethylene.
As the reactivity remains the same, this was further proof that these two surface species cannot be reaction intermediates.

At this point, the surface chemistry of ethylene during hydrogenation on Pt(111) was finally understood at the molecular level. π-bonded ethylene is the active form of ethylene on both Pt(111) and Pt(100) and the formation of an ethyl intermediate confirmed the Horiuti-Polanyi mechanistic pathway. Both di-σ bonded ethylene and ethylidyne act as spectator species and play no role in the catalytic reaction, other than perhaps occupying surface sites. Ethylidyne can also be hydrogenated at a much slower rate than π-bonded ethylene, but it was unknown if this alkylidyne layer was passivating the surface, leading to the observed structure insensitivity. The competing reaction of ethyliydne formation and hydrogenation to form ethane represent two important pathways which will be used in this dissertation. It can be hypothesized that if the activation barriers of the two reaction paths can be tuned, e.g. by cluster size, then hydrogenation or dehydrogenation activity can be controlled.

1.1.4 Nanoparticles

Before reviewing the most recent literature on nanoparticle systems, it is important to mention one paper which is rarely mentioned in papers dealing with the ethylene hydrogenation on platinum [42]. The paper appeared in 1986 under the title "Intrinsic size effect of platinum particles supported on plasma-grown amorphous alumina in the hydrogenation of ethylene". The title itself shows the major discrepancy the authors had discovered with other results at that time, namely that by changing the particle size the ethylene hydrogenation rate also changes. This is at odds with the conclusion by a variety of researchers that the reaction is structure insensitive. As of 2015, this paper has been cited 21 and 24 times according to SciFinder and Science Direct, respectively. Not one of those citations has been from the well known researchers in this field. The paper shows a variety of platinum catalysts, generated by atomic vapor deposition, which had been characterized using nucleation theory and where the particle size formed is dependent on the substrate temperature, impinging atom flux and evaporation time. This method of controlling particle size was a standard tool before mass spectrometry techniques, allowing for atomic size control, became available. From the nucleation equations, the authors were able to calculate a particle size from 2.6-37 Å, i.e. in the range of tens of atoms per particle to hundreds. The catalyst was supported on alumina and the ethylene hydrogenation was performed at 373 K. The results showed that the rate varied with particle size and that the maximum is found between 10 and 20 atoms per particle. The authors also had previously shown the same trend with the same catalyst supported on SiO_2. The data apparently show a direct contradiction to the published literature which has consistently presented the reaction as being structure insensitive. An explanation for neglecting this result is difficult to imagine, but the most reasonable criticism of the work is the method of determining the particle size, which in

turn can change the turnover frequency (TOF). The method of particle size determination is based on equation 1.1,

$$\mathrm{d} = 2\left(\mathrm{R}\exp\left(\frac{\mathrm{E_{ad}} - \mathrm{E_d}}{2k\mathrm{T}}\right)\right)^{\frac{1}{2}}\sqrt{\mathrm{t}} \tag{1.1}$$

where d is the resulting particle diameter, $\mathrm{E_{ad}}$ is the adsorption energy, $\mathrm{E_d}$ is the diffusion barrier for an atom on the surface, t is the evaporation time, R is the atom flux, k is the Boltzmann constant, and T is the temperature. This equation is purely theoretical and does not take into consideration things like surface roughness, variations in the atom flux, variations in the adsorption energy for different surface sites, etc. Using transmission electron microscopy (TEM) analysis for samples with larger particle sizes (e.g. 24 Å)[4] the authors did see a size-distribution, but claimed that as particle size decreases this distribution should also decrease. The particle size was also determined using x-ray photoelectron spectroscopy (XPS), where Pt(4d) core level shifts were correlated to particle diameters using Wood's equation [43]. These methods, while accurate to some degree, fail to ensure true monodispersity of the catalyst. The compounded effect of possible agglomeration, small size-distributions and impurities can lead to incorrect normalization for the calculation of TOFs. It cannot be said for sure if these effects were present to a significant degree in the experiments, but the number of unknowns and uncertainties concerning the particle size-distribution make the results less convincing.

Aside from this single paper hinting at structure sensitivity, other steady state measurements on Pt particles supported by SiO_2 performed around the same time supported the previous conclusions that the reaction is structure insensitive and similar activation energies to those of other studies were measured [44]. It was also shown that the reaction order, with respect to hydrogen, changed from unity at 336 K to 0.5 at 243 K, while that for ethylene was zero at higher relative pressures and became negative as the relative pressure decreased. The authors noted that the reaction exhibited an initial period of deactivation before attaining a steady state, which was attributed to formation of carbonaceous species, although ethylidyne was considered to be improbable. This supported the idea that the reaction took place on a carbon covered surface where the intrinsic metal properties have been essentially erased, hence the reaction being structure insensitive [45]. An identical study using deuterium was then used to develop a micro-kinetic model based on the Horiuti-Polanyi Mechanism [46]. The deuterium distribution within the product showed that ethane containing 0-4 deuterium atoms constituted $\approx 90\%$ of the reaction product and this distribution was seen to vary based on temperature and relative amounts of the reactants. They also observed that competitive adsorption of hydrogen was seen to increase as the partial pressure of ethylene was lowered, i.e. less carbonaceous species blocking surface adsorption sites.

The most recent work published on the ethylene hydrogenation on platinum has been mainly concerned with the method of nanoparticle synthesis, in order to achieve a monodisperse size-distribution, and the application of ethylene hydrogenation as a model structure insensitive reaction. Well defined nanoparticle systems offer a much better model for real dispersed catalysts used by industry and the application of 'model catalysis' as it pertains

[4] At this time a better TEM resolution could likely not have been achieved.

to this work will be discussed in chapter 1.3.1. Additionally, the method of using CO and ethylene to probe poisoning, and particle geometries of platinum nanoparticles have also been successful in furthering the understanding of surface chemistry involving these two molecules. This section will give a selected overview of important publications that pertain specifically to the work presented in this dissertation.

While the mechanism had been well studied on single crystals, whether or not supported particles exhibited the same behavior with regards to intermediates and rate determining steps was an open question. An important study from an alumina supported platinum catalyst showed using millisecond-resolved IR spectroscopy, that the formation of surface ethyl is the rate determining step of the reaction on supported platinum. After the formation of the ethyl species, the next hydrogenation step occurs quickly and ethane is readily desorbed [47, 48].

With the most pressing questions regarding mechanism now understood further studies could be performed. Electron beam lithography (EBL) was used to synthesize well defined arrays of particles with diameters of 28 ± 2 nm [49]. Comparing the ethylene hydrogenation rates on these nanoparticles with a Pt(111) surface, with and without CO co-adsorbed, the authors found that the activation energy was much less affected for the Pt nanoparticles, although the rate decrease was the same magnitude in both cases. The conclusion was that the metal-surface interface sites were the likely culprits for the discrepancy between the single crystal and the supported particles. This is understood as allowing CO higher surface mobility freeing up active sites, the alumina support making the interface sites immune to CO adsorption and therefore poisoning, or even providing sites where CO hydrogenation can take place, thereby freeing these sites again for ethylene hydrogenation. Scanning tunneling microscopy (STM) was then used to show that, on the Pt(111) surface, CO blocks the mobility of ethylidyne which effectively poisons the catalyst [50].

Using EBL and nanoimprint lithography (NIL), platinum particles ranging in size from 20-60 nm were synthesized on alumina and silica supports. The ethylene hydrogenation was seen to be structure insensitive and CO poisoning studies revealed the same behavior previously described [51].

At this time a series of papers were published using an identical nanoparticle synthesis procedure which will be explained here to support the following discussion. Different hexachloroplatinic acid solutions were used as a platinum precursor and added to either ethanol (2.6 and 2.9 nm particles), methanol (3.6 nm particles) or ethylene glycol (1.7 and 7.1 nm particles) along with polyvinylpyrrolidone. For 1.7 nm platinum particles, NaOH was also added and precipitation was performed with HCl. This generated a colloidal platinum solution which was added to SBA-15 silica to create a slurry. The precipitates were then separated by a centrifuge and calcined, with particle size determined by TEM, x-ray diffraction (XRD) and chemisorption. This general procedure is well known for nanoparticle synthesis and yields relatively mono-disperse particle size distributions [52]. Reaction studies carried out at ambient pressures on these catalyst samples showed the expected structure insensitivity at 298 K to ethylene hydrogenation and at 643 K structure sensitivity to ethane dehydrogenolysis, see chapter 1.2. Similar catalyst samples were also synthesized using a nanoparticle encapsulation method, where the encapsulation into SBA-15 silica

was performed under neutral conditions to mitigate agglomeration on the support and instability of the colloidal nanoparticle solution. The reactivity studies produced, however, different results in that there was a size-effect observed in the deactivation during ethylene hydrogenation. All particle sizes (1.7-7.1 nm) showed the same initial reactivity but the larger particle sizes showed a decrease in activity during the reaction. This was explained as a poisoning effect from the formation of ethylidyne or the presence of residual polymer from the synthesis process but the authors did not go into further details about the origin of this effect [53].

The effect of CO poisoning was then investigated on these Pt/SBA-15 silica catalysts with respect to the ethylene hydrogenation and a decrease of 4-5 orders of magnitude was observed. It was also observed that the reaction order of ethylene change from a negative value, without CO present, to unity in the presence of CO leading to the conclusion that CO and ethylene adsorb on the same surface site.

The most recent work on the ethylene hydrogenation on platinum has been the application of more advanced experimental techniques in order to elucidate the intricacies of the reaction. This includes operando studies using infrared reflection absorption spectroscopy (IRRAS) during the ethylene hydrogenation on platinum [54], highly effusive molecular beam experiments on Pt(111) yielding unity reaction probability [55], recovery of platinum active sites by treatment with O_2 [56] and operando x-ray absorption spectroscopy (XAS) studies on Pt(1 nm)/SiO_2 [57]. The first three papers cited offer some fresh information on the reaction but fall short of fundamentally increasing our knowledge of the reaction system. The XAS studies provide the most interesting results and will be discussed further.

A Pt/SiO_2 catalyst with a narrow size distribution of 1.11 ± 0.34 nm were studied using XAS spectroscopy during the ethylene hydrogenation. This technique enables structural details to be measured under catalytic conditions including bond lengths, metal coordination numbers and density of states (DOS) at the Fermi level. The hydrogenation was performed by gradually changing a gas mixture at 1 atm from 100 % H_2 to 100 % C_2H_4, and then back again while measuring spectra. The x-ray absorption near-edge structure (XANES) results showed that in the hydrogen rich atmosphere the 'white line' intensity, which is a measure of the population of empty Pt(5d) states, decreases, which indicates partial filling of these states upon hydrogen adsorption. After changing over to the ethylene rich atmosphere the white line intensity increases, which signifies a transition to a carbonaceous surface. Extended x-ray absorption fine structure (EXAFS) data showed a very interesting progression within the platinum particles. After reaching the ethylene rich atmosphere two new Pt bonds are observed, one of which disappears again after transition into the hydrogen rich atmosphere. One of the bonds was rationalized to be that of ethylidyne, which first forms in a hydrocarbon rich atmosphere. This species is then seen to disappear when returning the hydrogen rich atmosphere, which is in agreement with the slow hydrogenation of ethylidyne observed on Pt(111). The second contribution was seen to remain upon return to the hydrogen rich atmosphere and it was assigned to a Pt-carbide species which forms irreversibly. In light of the Pt-Pt coordination number decreasing from 6.20 to 3.32 in the ethylene rich atmosphere and then returning to 4.74 in hydrogen, the authors proposed the formation of a carbide phase forming in-between layers of the nanoparticle. They are very

critical of this assessment as this type of behavior has not been previously observed, but their results clearly point in this direction especially in conjunction with their observation of no sintering using scanning-TEM (STEM). This presents a significant complication in studies of this reaction as structural changes of this magnitude can have an enormous impact on theoretical calculations and mechanistic proposals. A puzzling fact of this study is that even after the formation of this carbide phase, the reaction kinetics did not change.

The nanoparticle studies reviewed here again show that the classification of the reaction as structure insensitive has been promulgated further down to particle sizes as small as $\approx$ 1.5 nm. One of the issues recognized here was that ethylidyne is no longer clearly observed as the particle size decreases. In order to investigate the nature of carbon species, co-adsorption of CO and ethylene has proven to be a powerful technique to acquire insight into the nature of ethylene, or in general carbon, species formed on the nanoparticle surface.

CO Adsorption As A Surface Chemical Probe

In this section a brief overview will be given regarding studies where CO has been used in order to probe platinum surfaces and nanoparticles during ethylene co-adsorption. This technique will play an important role in the results of this dissertation.

SFG and IR spectroscopy on Pt(111) showed that a surface pre-covered in ethylidyne exhibited a linear bonded CO stretch (ν(CO)) redshifted 75 cm^{-1} [58] and 40 cm^{-1} [59] from the clean surface value of $\approx$ 2095 cm^{-1}. This redshift had been previously attributed to a Stark effect, where neighboring surface dipole interactions between CO molecules are attenuated in presence of co-adsorbed ethylene[5] [60]. This hypothesis was rejected, however in favor of a charge transfer occurring from ethylidyne to the Pt(111) surface and subsequently to the $2\pi^*$ orbital of adsorbed CO, thereby weakening the CO bond. This trend has also been observed on supported platinum nanoparticles using a variety of techniques including, diffuse reflectance infrared Fourier transform spectroscopy (DRIFTS), IRRAS and normal transmission IR spectroscopy [59, 61, 62]. Nanoparticles in general showed a redshift in the initial ν(CO) which is attributed to stronger bonding on step and kink adsorption sites [63, 64]. Adsorption on both terrace and step/kink sites was identified on nanoparticles using the ν(CO), with the terrace sites displaying a blueshift towards values closer to the (111) surface. Pre-adsorbed ethylene at approximately room temperature caused a further redshift in ν(CO) in all studies and these results are presented in table 1.1.

It was observed that on small platinum particles (d $<$ 2.6 nm), the amount of ethylidyne formed was very small compared to larger particles and this correlated with a smaller $\Delta\nu$(CO). It was inferred that ethylidyne requires terrace like facets in order to form, and the high concentration of steps/kinks increases the amount of π-bonded ethylene. Although it was originally rejected in [58], the possibility of the redshift being caused by the Stark effect or charge transfer has yet to be resolved. The presence of both step and terrace like desorption peaks from CO TPD measurements in ref. [62] on an ethylidyne pre-covered surface indicate

[5]The surface species is unlikely to be ethylene but rather ethylidyne or some dehydrogenated product. This paper was written around the time when the identification of ethylidyne on Pt(111) had just been accepted.

Table 1.1: Position of $\nu(CO)$ cm^{-1} for a variety of platinum catalysts with and without ethylene.

catalyst	clean ν(CO) cm^{-1}	with C_2H_4
Pt(111) (SFG) [58]	2095	2020
Pt(111) (IRRAS) [59]	2080	2040
Pt(d > 30Å)/Al_2O_3 [60]	2085	2050
Pt(d > 30Å)/SiO_2	2075	2045
Pt(5-15 nm)/SiO_2 [59]		2045
Pt/SBA-15 SiO_2 (DRIFTS) [61]		
1.9 nm	2075	
2.9	2079	2050
3.6	2082	
7.1	2090	
Pt/SiO_2 (IRRAS) [62]		
2.5 nm	2094/2077	2081
2.6	2094/2077	2069
3.3	2100/2080	2067
4.2	2100/2085	2062
>4	2100	2065

that both steps and terraces are still present. The single ν(CO) peak, however, demonstrates that they both have to some degree a similar local environment.

The main results can be summarized as:

- There is a redshift in the clean ν(CO) as one transitions from a single crystal to supported nanoparticles, and this shift grows with decreasing particle size.
- A CO pre-covered surface effectively quenches ethylene adsorption, whereas pre-covering with ethylene still allows for an appreciable amount of CO to be adsorbed.
- ν(CO) redshifts even further under the presence of co-adsorbed ethylene (ethylidyne), however, the mechanism (Stark effect or charge transfer) is still unresolved.

1.2 Structure Sensitivity

Michel Boudart coined the expression 'structure insensitive' in 1969 in order to describe the phenomenon of a catalytic reaction TOF being independent of the metal dispersion[6] and hence particle size [45, 65]. Reactions that were structure insensitive were also called 'facile', a term which implies a more general characteristic of a given reaction-catalyst system. Prominent examples of facile reactions were: hydrogenation of cyclopropane, 1-hexene, cyclohexane, benzene and ethylene, i.e. hydrogenation reactions seemed to all be facile. He then labeled as 'structure sensitive' or 'demanding' reactions, those where the rate, normalized to the number of active sites (dispersion), changed for different particle size, or catalyst preparation. This classification was the culmination of the original theories of active surface sites initiated by Hugh Taylor in the 1920's [66]. A major difficulty in determining whether or not a catalyzed reaction is facile or demanding is excluding all possible external causes such as mass transfer, procedure for active site determination and catalyst support interactions. Only with highly reproducible experimental conditions can the determination of structure sensitivity be ensured.

The terms facile and demanding fell out of style with the rise of single crystal studies, where a given Miller index plane more accurately described a specific structure. This was then extrapolated to the surface morphology of smaller particles, where particle size was said to influence the concentration of specific surface structures and these structures were simply a specific single crystal plane [67, 68]. It was observed that the terms 'structure sensitive' and 'structure insensitive' unnecessarily erected boundaries with respect to the nature of the observed phenomena. It seems premature to label a given reaction or metal as structure insensitive, if one only relies on data from specific size regimes, i.e. a given reaction/catalyst system cannot be labeled as unequivocally structure sensitive or insensitive unless all particle sizes have been studied, from an atom to an extended surface [67, 69]. This was summed up very well already in 1985 by Boudart [70]:

> In a way, changing particle size in the range from 1 to 5 nm is similar to looking at different crystallographic planes on a macroscopic single crystal. But below 1 nm, other effects, not observable on large crystals, may become important as the relative proportion of surface atoms with very low coordination numbers becomes appreciable, if not dominant.

This implies that although geometric argumentations can be insightful for many systems, they are not as universally applicable as, for example, those based on electronic structure.

The origin of structure sensitivity is also a subject which displays complications. As has already been discussed, ethylene hydrogenation appears to be catalyzed in the presence of a large amount of inactive spectator species (ethylidyne on Pt(111)). It has also been proposed that this carbonaceous layer could effectively mask the underlying properties of the metal and be responsible for the structure insensitivity [33, 44], but no study has been able to experimentally control this passivation of the metal surface, i.e. it is, at best, observed as a slow deactivation over time. Being able to control the formation of the carbonaceous

[6] This is the ratio of surface atoms to total number atoms composing the catalyst.

overlayer, while concurrently controlling hydrogenation activity, would provide the necessary evidence to prove this concept.

The general idea of a carbonaceous overlayer being an active component was postulated in the 1970's, where the formation of C_xH_y in essence defines the active site [71]. This exact point has been made twice in the literature, in 1985 by Boudart: "however, the nature of the catalytic entity is postulated to be not a site at the metallic surface, but an alkyl-metal" [70] and also in 2013 by Zaera: "This lack of appreciable changes in performance with the structure of the metal particles has historically been explained by assuming that the carbonaceous deposits that form on the surface, the alkylidyne fragments, cover the naked metal and mask any structural defect that may alter its performance. However, virtually no detailed studies have been carried out to specifically quantify this behavior," [72]. The same unanswered question being posed almost 30 years apart signifies the current understanding of structure sensitivity and the potential that studies on atomically precise metal clusters could have[7].

It is beneficial to describe here two cases of a structure sensitive reaction, with the goal of showing that structure sensitivity can be operative to varying degrees, depending on the studied system. The most prominent example of a very structure sensitive reaction is the ammonia synthesis on iron, where a difference in rate of over two orders of magnitude was observed between a (111) and (100) surface [73]. In this case the terminology structure sensitive fits best as it is clear that the local atomic arrangements are controlled by the extended surface structure, and must be the decisive factor. The (111) plane provides the highest concentration of iron atoms with a coordination number of 7, so called C_7 sites, which means that particles, where iron has a higher coordination number, should also be more active. This was also shown to be true as a pronounced particle size-effect is observed, where smaller particle have a much lower activity than larger particles. Using straightforward geometric argumentations, it is clear that larger particles will have a larger number of higher coordinated iron atoms and this directly correlates with the results from single crystals [45, 67].

A reaction also exhibiting structure sensitivity and a TOF dependent on particle size is the ethane hydrogenolysis. In this reaction the $C-C$ bond is dissociated in the presence of hydrogen and methane is formed. The reaction is known to be structure sensitive on nickel, with larger particles exhibiting a lower catalytic activity [74, 75]. A similar trend was also observed for supported platinum particles, with a maximum activity observed for particles with 1.7 nm diameter [76, 77]. Results from Ni(100) and Ni(111) showed the expected structure sensitivity, with the (100) plane being more active [78]. This correlated with theoretical calculations on a Pt_{10} 'cluster'[8], Pt(211) and Pt(111), where lower coordinated sites were observed to bond stronger with hydrocarbon fragments, thereby increasing the activity, and the predominant reaction pathways involved highly hydrogenated species, such as an ethyl intermediate [79]. These conclusions were supported by results on platinum particles synthesized by the previously described nanoparticle encapsulation method [53].

[7] See chapter 1.3.1 for examples.

[8] This is not a Pt_{10} cluster particle, but rather a cut-out of three atomic layers from a (111) surface with 6 surface atoms, 3 in the second layer and 1 in the third.

Titration of these catalysts after the reaction was run showed that carbon deposition from ethane decomposition also displayed a particle size dependency. 2.9 nm particles were observed to have the highest fractional carbon coverage and this was attributed to a higher concentration of under coordinated surface atoms [80]. This size-dependent carbon formation was used to rationalize the observed structure sensitivity, where larger particles are less active but more selective for methane formation, and smaller particles are more active but less selective. This dichotomy between hydrocarbon transformation and carbon deposition appears to play a critical role in understanding structure sensitivity for this class of reactions. The ethane hydrogenolysis shows that particle size sensitivity can also manifest itself as structure *selectivity*, where a size-effect is simply related to a preference for a specific reaction pathway. This concept has been more precisely defined as the 'parallel reaction selectivity criterion' [65], where a metal's changing proclivity for one of, e.g. two, possible reaction pathways, as a function of particle size, defines a structure sensitive reaction. This describes again a fundamental aspect of this dissertation, where it is expected that clusters consisting of only a few atoms, will exhibit divergent reactivities for these fundamental reaction pathways.

In conclusion, structure sensitivity/insensitivity is a powerful tool for the characterization and design of catalyst materials. The efficiency and cost of a catalyst can be greatly enhanced by choosing a protocol which generates the most active particles at the lowest cost. Use of the term itself, however, runs into self-imposed limitations with regards to the broader understanding of catalytic phenomena by confining the structure of catalysts to model structures. In practice, these model structures are unlikely to be present during the reaction itself and at very small particle sizes. In these cases, it seems that electronic effects, induced by non-reactive intermediates near active sites or simply by the intrinsic nature of the element at the relevant particle size, coupled with local geometric structure influenced by the particle support, enable a more complete, prescient understanding of the nature of hydrocarbon heterogeneous catalysis.

As a last note, the classification of a reaction as 'structure insensitive' is in general very problematic, as "a system cannot therefore be classified as 'size-insensitive' unless catalysts having dispersions of up to almost 100 % have been tested," [67], and with sub-nanometer, size-selected clusters, exactly this question is one which this dissertation will address in the case of ethylene hydrogenation on platinum.

1.3 Model Catalysis

The ability to investigate catalyst materials under UHV conditions enables superlative control of all reaction parameters from catalyst synthesis to post reaction analyses. This enables the isolation of specific parameters, such as particle size, support material, defect density etc., underlying reaction activity and selectivity and study them in a systematic way. These type of investigations have proven over the years to provide a level of insight into the molecular and atomic interactions governing catalytic reactions that were otherwise unattainable [81–84].

1.3.1 Model Catalysis With Size-Selected Clusters

Particle size has long been known to effect changes in the physical and chemical properties of a given element. At the extreme, one has a particle comprised of a very specific number of atoms, i.e. a cluster of atoms. The properties of these clusters has been shown to be very sensitive to the exact cluster size [85–87]. This means that by changing a cluster size by a single atom, impactful differences in stability, electronic and geometric structure, chemical, and physical properties can be observed.

Ultra High Vacuum

Model heterogeneous catalysis using atomically precise mass-selected metal clusters has grown into a well established technique over the past decade [87–89]. Much work has been published revealing interesting properties of reactions on clusters supported by metal-oxides under UHV conditions as well as under ambient conditions. The progress has always been intimately coupled with the ability to control specific catalytic properties, such as mechanism and reactivity, through effecting minute changes in electronic structure and morphology by changing the particle size by a single atom. In particular, the CO oxidation reaction mechanism was shown to be tunable on small Pt clusters supported on MgO [90], while the catalytic activity of similar sized clusters was also shown to be size dependent on TiO_2 [91]. The unique ability of small gold clusters to oxidize CO was further elucidated on MgO, where addition of a single atom separated inactive and active clusters [92, 93]. Similar results were also shown on iron oxide where 2-D and 3-D gold clusters were the inactive and active species, respectively [94]. Palladium clusters were also shown to have size-dependent activity on MgO [95–98] and TiO_2 [99, 100], while also revealing a temperature dependent reaction mechanism [101]. Not only the specific atomic size of a cluster has been shown to influence catalysis, but also the interaction between the support and the cluster has also been shown to play a decisive role [102–105].

Apart from the CO oxidation the variety of reactions performed on size-selected clusters under model UHV conditions is sparse. The acetylene trimerization [106, 107] and the NO reduction by CO [108] are two examples of work done outside of the CO oxidation on truly size-selected samples. The group of Stefan Vajda has performed the oxidative dehydrogenation of propane and cyclohexene on platinum and cobalt, respectively, but

atomic size-control was not achieved [109, 110]. They did observe a large increase in activity, but the lack of single atomic size control leaves the most interesting parameter untested.

From these studies a number of key concepts have been extracted that can be used to describe cluster's peculiarities. These include cluster charging [104], fluxionality and adsorbate induced electronic structure change [97, 111, 112], reverse spill over [113] and symmetry [98]. All of these concepts are reasoned by the fact that every cluster size has a unique electronic and geometric structure (although this in no way means that *every* cluster size will behave differently). The uniqueness of each cluster size means that all of its interactions with a surface or reactants has the ability to be fundamentally different from another size separated by a single atom. Apart from discovering new catalytic behavior, the finite size allows for a more straightforward theoretical foundation than larger sizes, i.e. the finite number of atoms provides a parameter which is definitively known, in contrast to larger nanoparticles where the catalytic reaction is modeled by a finite number of atoms defining a surface site. It will be shown in chapter 3.1 that theoretical studies on clusters end up being very complicated and at times ambiguous, due to the number of approximately energetically degenerate structural isomers. Nevertheless, because the exact number of atoms is known, the structures generated are those which *completely* describe the particle in contrast to using a few atoms to describe a particle consisting of hundreds.

Ambient Conditions

In order to overcome the obvious gaps between catalysis in UHV and under industrial conditions, efforts have increased to extract size-selected cluster samples from the setup used in this work for a wide variety of applications in electrocatalysis [114], photocatalysis [115, 116], liquid-solid phase catalysis, and thermal catalysis with micro reactors developed in the group of Ib Chorkendorff. Additionally, studies of cluster dynamics on surfaces have revealed sintering properties both under vacuum [112, 117, 118] and ambient conditions [119]. The group of Scott Anderson has also built a system directly onto a vacuum chamber where electrocatalysis can be performed on clusters without removing them from the vacuum environment [120, 121].

The promise for studies comparing identical cluster sizes in UHV and under ambient conditions has clearly become reality. Nevertheless, synthesizing clusters *in vacuo* is a time consuming, costly endeavor. Wet chemical synthesis of clusters represents the future in terms of the production of size-selected clusters and much progress has been made in synthesizing size-selected gold clusters with ligand stabilizers [122, 123]. This research area is still in its infancy but new synthesis methods and the possibility of using it on less expensive metals are very attractive for industrial use. The future of cluster catalysis will be ever more coupled to comparing results from UHV and those from ambient conditions. The profuse areas of catalysis that have yet to be investigated with size-selected clusters promise for a fruitful research field in the future. The work done thus far has provided a foundation, but there is still much to be discovered.

1.3.2 Support Effects

Under UHV conditions, metal-oxides grown on metal single crystals represent an indispensable tool for modeling heterogeneous catalytic reactions. The metal-oxides used to support disperse metal particles are generally inert, i.e. inactive, but in some cases they can play a role in the catalytic processes (e.g. the bifunctional catalyst Pt/Al_2O_3 in naphtha reforming) [124]. Surface science techniques allow for the unique opportunity to investigate the influence that changes in the support stoichiometry, atomic structure, thickness and metal component have on supported clusters. Additionally, the underlying metal support, upon which the thin metal-oxide film is grown, can also effect changes on adsorbed clusters. The most prominent experimental result showing this effect is from the Freund Group, which also confirmed previous theoretical predictions [125–128]. Using STM, it was shown that thin MgO films (3 monolayers) cause adsorbed gold clusters to wet the surface due to a charge transfer from the underlying metal support (Ag(001)). A similar effect was observed for the CO oxidation activity on Au_{20} clusters supported on different MgO thicknesses grown on Mo(100) [103].

Another interesting effect which has been observed is the selective penetration of palladium atoms into thin silica films grown on Mo(112). In particular, it was observed that palladium atoms exhibit a propensity to penetrate at hexagonal rings within the silicon film, while gold atoms did not show this ability. This indicates a distinct difference in the fundamental interaction between a metal catalyst and support, which could be exploited in a catalytic setting [129, 130].

While the thickness of a film has been shown to induce changes on particle morphology and reactivity, the chemical nature of the film is a factor which has yet to be investigated. In particular, changing the metal component of the metal-oxide support, while keeping the particle size exactly constant at an atomic level, is something that has yet to be reported in the literature. This is one of the goals that was set at the beginning of this dissertation, testing a reaction on the same cluster size on two different supports.

The stoichiometry of thin films have also been shown to be controllable, in particular on SiO_2 thin films grown on Mo(112), by varying the growth parameters and subsequent annealing temperature [131]. This produces thin films which can be labeled as silicon rich, stoichiometric and oxygen rich. The effect of these different films on the adsorption of silver nanoparticles was investigated, but no effect was observed [132]. Recently, a theoretical paper investigated the effect of these three silica films on Pt_{13} clusters and found that Pt-Si and Pt-O bonding leads to per atom charging of -1.0 e and 0.6 e, respectively [133]. This result shows that the film stoichiometry should be able to tune the electronic structure of adsorbed clusters and their catalytic activity.

The precise chemical and physical characteristics of the support material can play a pronounced role in not only a catalytic reaction on a metal particle, but also on the particle's fundamental properties. Only with the precise control of the support parameters and the particle size, can these possible support effects be disentangled. Again, UHV model catalysis on size-selected clusters represents an unparalleled methodology to investigate exactly these features.

1.4 Afterword to the Introduction

The goal of this introduction was to provide a review of the necessary concepts and scientific work performed on the platinum catalyzed ethylene hydrogenation and size-selected clusters, along with the peripheral concepts which have been used to describe this reaction in the past. The scientific aim of this dissertation, while mentioned throughout the previous pages can be summarized as follows: what are the catalytic properties of size-selected clusters (in particular platinum), towards ethylene hydrogenation and how can these results be understood, both experimentally and theoretically, within the context of how this reaction system has been described in the scientific literature? Additionally, what effects can be observed when specific reaction system parameters are varied, e.g. cluster size and support material. Figure 1.5 pictorially displays these fundamental cornerstones of this dissertation.

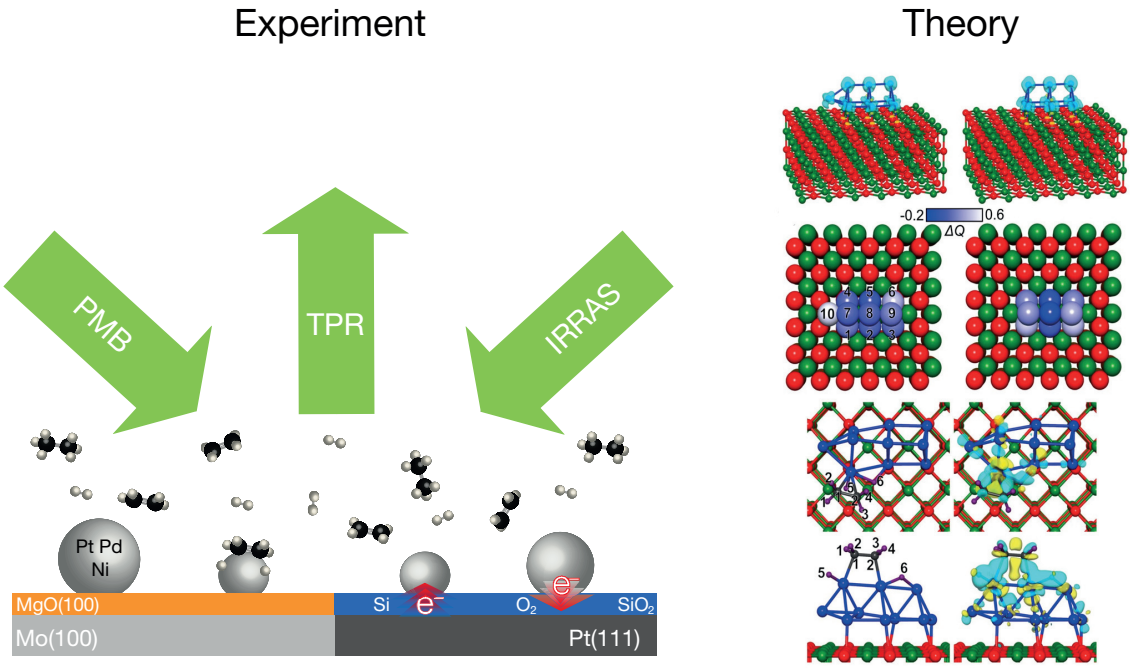

Figure 1.5: Graphical representation of the targeted catalysis parameters to be investigated in this dissertation along with select experimental and theoretical tools applied. The targeted parameters are cluster metal, cluster size, support material, stoichiometry of support material and the application of theoretical techniques to provide deeper insight in the studied systems.

In order to pursue this goal, an advanced UHV chamber with the necessary experimental techniques is required. This includes a cluster source, which can produce atomically resolved particle sizes and deposit them onto a thin, metal-oxide film as support material.

2 Experimental

In this chapter, the instrument used for the experiments presented in this dissertation will be introduced, along with some further experimental details which cannot be found from other sources (in particular chapter 2.2.6.). Emphasis is placed on the general functioning principle of the experimental techniques applied, along with the preparation of the single crystals and thin films. Figure 2.1 shows the schematic of the instrument used for this dissertation, showing the cluster source and the analysis chamber [134].

2.1 Cluster Source

The clusters used for the experiments in this dissertation were generated using a laser vaporization cluster source. The cluster source's functioning principle is the vaporization of a small amount of metal from a rotating target, which generates a plasma. This plasma is then cooled and extracted into the vacuum chamber with a delayed pulse of helium gas.[1] This expansion and cooling supersaturates the metal vapor and induces cluster formation. A fraction of the clusters formed are charged and this allows electrostatic lenses and a focusing octupole to guide the clusters to a quadrupole bender. The bender allows for the selection of only cationic clusters to be directed into the quadrupole mass spectrometer (QMS) chamber. The neutral and anionic species either continue straight through the bender chamber or are bent in the opposite direction. The cationic species can be mass-selected, with atomic precision, using the QMS, and ion lenses guide the clusters to the analysis chamber for deposition. The kinetic energy of the clusters, to ensure soft-landing, and the mass selection accuracy have been thoroughly characterized in a previous dissertation and will not be reviewed here [135].

2.2 Analysis Chamber

Included in figure 2.1 is the schematic of the analysis chamber used in this work [134]. The chamber has a base pressure of $1 \cdot 10^{-10}$ mbar and is equipped with IRRAS, TPD, pulsed molecular beams (PMB), a molecular beam doser (MBD), argon sputter gun, electron gun, Auger electron spectroscopy (AES), UPS and metastable impact electron spectroscopy (MIES). A brief introduction will be given to the functioning principles of these techniques, however, detailed technical descriptions and complimentary theoretical background information can be found elsewhere [124, 135–143].

[1] The delay time and pressure generated within the source chamber must be carefully optimized in order to find the parameters which lead to the highest cluster current for each cluster size.

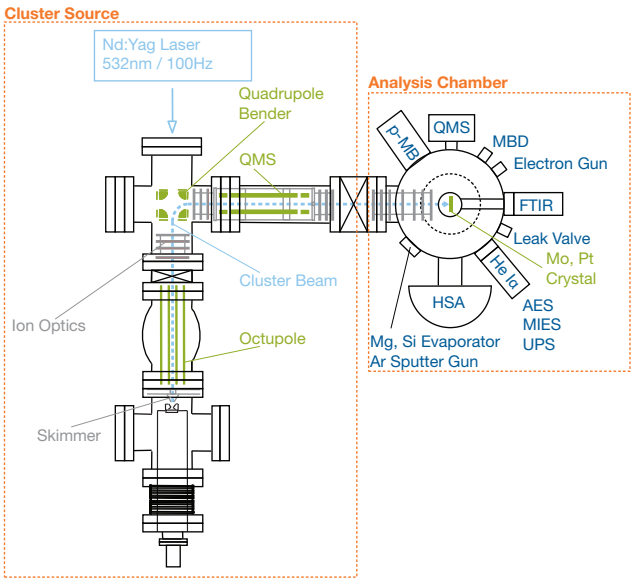

Figure 2.1: Schematic of the experimental apparatus used for this dissertation. Included are the cluster source (left) and analysis chamber (right). The experimental techniques have been abbreviated and further description can be found in the text [135, 158].

2.2.1 Auger Electron Spectroscopy

AES is a classical qualitative and quantitative vacuum technique based on the Auger effect. The Auger effect is induced when an energetic electron (used in this work), or photon (typically in the keV range) impinges on a surface causing the ejection of a core level electron. This destabilizes the atom and an electron from a higher shell then fills the electron hole. This process leads to energy being released and this energy can be transferred to yet another electron in a higher shell, causing it to be ejected from the material. As this process involves electrons from three specific energetic levels, each element has characteristic Auger peaks which allows this technique to be used for chemical analysis. For this work the main application of AES was to ensure the chemical purity of the single crystals and thin metal-oxide films.

2.2.2 Electron Emission Spectroscopy

Ultraviolet Photoelectron Spectroscopy

UPS is a technique based on the photoelectric effect, whereby the valence electronic structure of a molecule or surface is probed by ejecting an electron with a UV photon[2] and measuring the electron's kinetic energy [144]. In this work, the source used for UPS and MIES (next section) is based on the design of the Kempter Group from TU Clausthal [145], and electron

[2]In this work a He Iα source is used which yields an excitation energy of 21.22 eV.

detection was performed with a hemispherical analyzer (VSW HSA 150 with a HAC 5000 controller) [146].

Restricting the discussion to surfaces, UPS generates a spectrum which mirrors the density of states (DOS), i.e. the electron occupation at a given energy below the Fermi energy, which allows for investigating the valence band electronic structure of the solid. It should be noted that the DOS obtained is not the complete band structure of the solid, but rather the joint-DOS, as the electron emission intensity is also proportional to the unoccupied state into which the electron is excited. As the excitation energy is constant, the initial state and final state are both changing as one analyzes the electron kinetic energy and therefore the real DOS is not measured. Variable excitation energy is one method to overcome this deficiency. For a thorough discussion see refs. [138, 140].

In the presence of adsorbed molecules, UPS from a surface also leads to emission from adsorbate molecular orbitals, and their energetic position relative to the gas phase can reveal chemical bonding properties as well as general insight into adsorbate/adsorbent interactions [140, 147–149].

Metastable Impact Electron Spectroscopy

MIES utilizes helium atoms excited in their metastable triplet state to excite electrons from exclusively the uppermost surface layer of a surface [139, 150]. These excited helium atoms are a byproduct of the excitation used for the He Iα UV photons and therefore are generated in the same source as for the UPS system. This allows for a simultaneous measuring of both signals [146]. The advantage of MIES is that it provides information only from the uppermost surface layer, making it a very sensitive technique compared to UPS where 2-5 atomic layers are probed. Two drawbacks regarding the MIES technique are that only electrons emitted via Auger deexcitation processes can be readily compared to UPS spectra, and the excitation energy imparted by the metastable atom can vary depending upon surface adsorbates, i.e. the excitation energy is not constant as in UPS [151].

2.2.3 Infrared Reflection Absorption Spectroscopy

Infrared spectroscopy performed for this dissertation was applied using a single reflection absorption mode (Thermo Electron Corp. Nicolet FT-6700). A basic diagram for the IRRAS experiment can be seen in figure 2.2. The IR beam is directed, at a very high angle to the surface normal, at the single crystal surface using a focusing mirror. The reflected beam from the single crystal is then focused by a KBr lens into the mercury cadmium telluride (MCT) detector (Thermo Electron Corp., MCTA-TRS). The diagram displays the different chambers that are pumped in the setup. The important theoretical background regarding the surface dipole selection rule and the reflectivity properties which necessitate the grazing angle needed for efficient reflection can be found in the literature [152–154]. Briefly, the surface dipole selection rule states that only surface dipoles with a component perpendicular to the surface can be IR active. For example, when CO is bonded to a surface through the carbon atom, the linear stretch exhibits a very strong signal. However, if CO were bonded

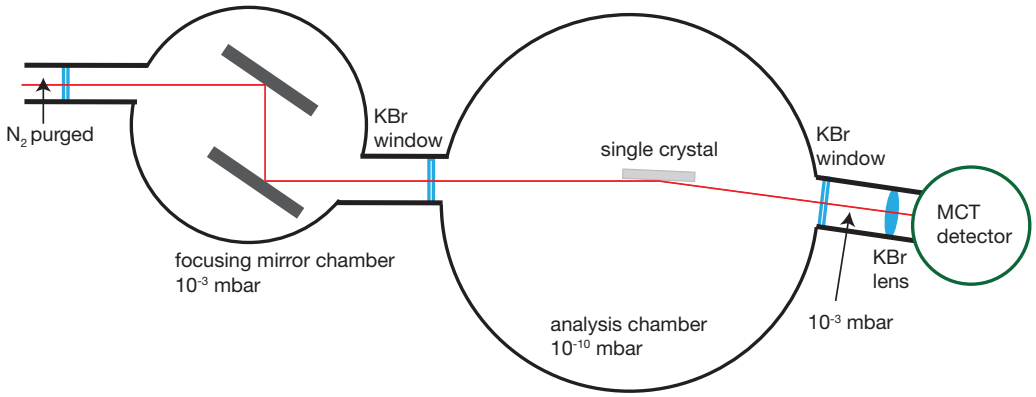

Figure 2.2: Infrared reflection absorption setup used in this work. In a rotary pumped chamber the IR beam is guided onto a focusing mirror, which focuses the beam onto the single crystal within the main chamber at a grazing angle. The beam is then reflected at the surface and then focused again with a lens into the detector.

with its carbon-oxygen bond parallel to the surface, then this vibration would be forbidden due to the surface selection rule. For a molecule like ethylene, this makes IR spectroscopy on surfaces somewhat difficult as if the molecule sits parallel, the $C-H$ stretch is very weak as only a small component is positioned parallel to the surface. However, ethylidyne has a $C-C$ bond axis perpendicular to the surface (see figure) 1.3 and has a well known absorption at 1339 cm^{-1} [155].

2.2.4 Molecular Beam Doser

The dosing of gases for TPD experiments is performed with a MBD, after the design of Yates [156, 157]. The functional principle is that a micro-capillary plate, with a known back pressure of gas, can be precisely calibrated to calculate the gas flow through the plate. This leads to a very precise and reproducible gas dosing. The following equation has been previously determined to describe the doser used in this dissertation [158]:

$$dN = 2.5 \cdot 10^{13} \cdot p_g \cdot \frac{1}{\sqrt{M}} \cdot \Delta t \tag{2.1}$$

where dN is the number of molecules released by the doser over the time Δt, p_g is the pressure measured behind the plate and M is the molar mass of the gas being dosed.

2.2.5 Temperature Programmed Desorption

TPD is a standard surface science tool where a linear temperature ramp (Eurotherm 2408 temperature controller) is applied to a substrate in order to induce surface reactions or simple desorption. A QMS (for this dissertation: Balzers QMA 430, Liechtenstein) is commonly used to detect at which temperature a particular species desorbs form the surface and this can be used to extract adsorption energetics. The presence of multiple peaks

indicates either different modes of adsorption or chemical processes occurring.
For example, molecular hydrogen desorption occurs from a Pt(111) single crystal at ≈ 250 K[3] If, however, ethylene is present on the surface, hydrogen also desorbs at higher temperatures due to dehydrogenation followed by recombination. This means that a TPD of hydrogen and ethylene adsorbed on Pt(111) will yield more than one peak and these originate from completely different chemical precursor states of hydrogen. This makes TPD a powerful surface analysis tool, but the presence of multiple peaks can sometimes lead to confusion. Judicious adsorption conditions, however, often allow one to discriminate between adsorbed species and the respective desorption signals they produce.

A last derivative of TPD is the TP reaction technique (TPR), whereby the product of a surface reaction is measured in the QMS. The desorption temperature of the product species can provide a good measure of the reaction activation barrier, and multiple peaks are indicative of different reaction mechanisms [141].

2.2.6 Pulsed Molecular Beam

General Principle

The PMB technique technique is based on pulsed molecular beam reactive scattering, whereby a gas is pulsed onto a surface under UHV conditions and its desorption (scattering) profile measured (usually with a QMS). For simple surface interactions, detailed kinetic data can be extracted by pulsing at high frequency [160–164]. For this dissertation, the goal was to retrieve a reaction product signal, wherein a quasi steady state can be defined which can be converted into a TOF. This was achieved by recording the raw signal of the QMS with an oscilloscope[4]. This quasi steady state is then merely a time interval where the rate of reaction product being formed remains constant (see figure 2.3a for an example pulse).

This technique, while providing a real TOF under UHV conditions, is however difficult to compare directly with ambient pressure experiments due to a pressure difference of over seven orders of magnitude (compare $2 \cdot 10^{-6}$ mbar for all PMB experiments in this dissertation vs. 146 mbar in [53]). Nevertheless, it will be shown in chapter 3.1.2 that results from this dissertation compare well to literature values.

Pulsed Molecular Beam Calibration for Ethane

The calibration of the PMB experiments was performed by first determining the sensitivity factor between CO and ethane, followed by calibrating the QMS response to a precise number of molecules from the TPD spectrum of a CO monolayer from Pt(111). The sensitivity factor is determined by generating a background pressure in the chamber where CO and ethane have the same collision rate over a given surface area, i.e. for our system this equates to the flux of molecules through the QMS skimmer being equal:

[3] In actuality the peak is broad and coverage dependent [159].
[4] For further experimental details regarding the PMB experiments see chapter 3.1 and 3.5

$$F_{C_2H_6} = F_{CO} \tag{2.2}$$

The following relation for gas collisions per unit surface area was used:

$$F = 2.64 \cdot 10^{22} \frac{p}{\sqrt{TM}} \tag{2.3}$$

where p is the pressure in mbar, M is the molar mass of the gas (g/mol), T is the temperature in K and F the flux in $\frac{\text{collisions}}{\text{cm}^2}$ [165].

Now a pressure of CO is defined and the resulting flux is used to calculate the pressure of ethane. From the user manual of the pressure gauge the gas sensitivity factor for CO and ethane is reported. It should be noted that gas sensitivities are prone to errors depending on the gases used and also how the ion gauge was originally calibrated. Using the values from the manual where p is the pressure read from the pressure gauge:

$$\text{CO:} \quad \frac{p}{1.05} = p_{real} \tag{2.4}$$

$$\text{Ethane:} \quad \frac{p}{2.6} = p_{real} \tag{2.5}$$

A CO pressure of $5.00 \cdot 10^{-8}$ mbar was set in the analysis chamber which means the real pressure is $4.76 \cdot 10^{-8}$ mbar at 300 K. The QMS signal (m/z = 28) was $9.1 \cdot 10^{-9}$ amperes (A) which is the *background corrected* QMS response. The baseline is simply read when no CO gas has been let in.

Using equation 2.3, and the real pressure, the ethane pressure required to achieve the same flux was calculated to be $4.92 \cdot 10^{-8}$ mbar. Using the ion gauge sensitivity, the pressure that must be set using the gauge is $1.27 \cdot 10^{-7}$ mbar. The QMS signal was determined to be $5.2 \cdot 10^{-9}$ A. Now the sensitivity factor was calculated:

$$\frac{I_{CO}}{I_{C_2H_6}} = \frac{9.1}{5.2} = 1.75 \tag{2.6}$$

In order to calculate the number of molecules for the QMS response, the CO TPD of a saturated Pt(111) single crystal was used. It is known that for saturated CO adsorption on Pt(111) and from the packing density of a Pt(111) single crystal that for a 0.785 cm^2 surface area, $8 \cdot 10^{14}$ molecules constitute a saturated monolayer [166]. Using the MBD, CO TPD's were performed until the peak area remained constant. This happened around the dosed amount of ≈ 0.7 CO/SA (SA = surface atoms). The integral for this TPD was calculated to be $2.35 \cdot 10^{-7}$ A $\cdot$ s. Using the sensitivity factor, this means that the same amount of ethane molecules would produce a peak with an area of $1.34 \cdot 10^{-7}$ A $\cdot$ s.

The strategy for converting the signal into a TOF is the following:

- Define a time range in the raw signal which designates the 'steady state' regime, from figure 2.3a this would be from 50 to 100 ms.
- Subtract the baseline.
- Do the same for the background signal and subtract this from the 'steady state'.

Figure 2.3a shows the average of 20 pulses from a Pt_{11} cluster sample taken at 300 K, and figure 2.3b shows the background corrected signal from each individual pulse. Using the average signal from a series of pulses, this value in millivolt (mV) was then converted to a TOF using the previously calculated sensitivity factor. For simplification, one should visualize the mV signal as being constant for a period of 1 s in order to avoid confusion. This means that a signal of 100 mV would have an integral of 100 mV· s, which makes it much easier to follow the next steps.

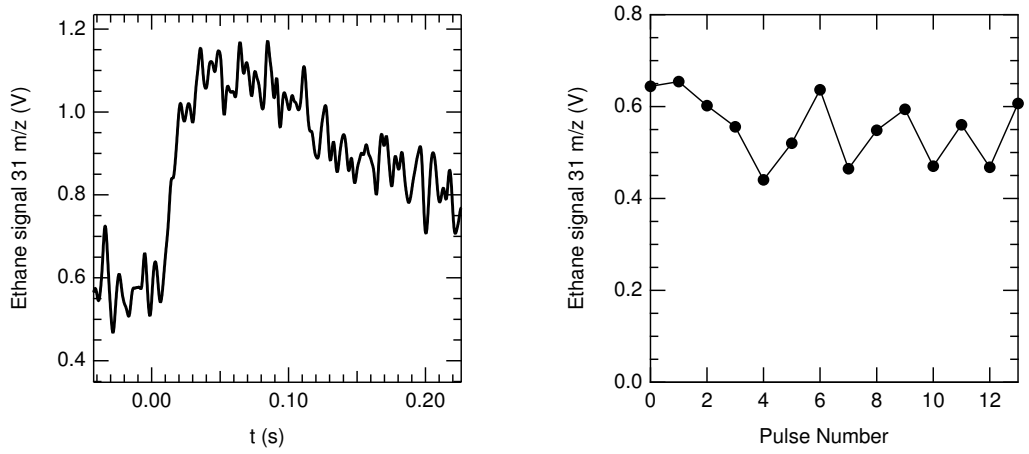

(a) *(b)*

Figure 2.3: Exemplary average of the ethane QMS response to ethylene pulses on Pt_{11} at 300 K (a), and the extracted values of each pulse (b).

The signal in mV was converted into amperes by comparing the readout on the mass spec computer and the oscilloscope. In general, the preamplifier out of which the cable goes to the oscilloscope has a set of resistors which defines the 'Amp Range' in the mass spectrometer settings. This means that the voltage readout is just the current seen on the computer converted into a voltage by measuring it over the resistor (i.e. E = IR). At an amp range of 10^{-9}, 100 mV = $1 \cdot 10^{-11}$ A, i.e. if the baseline on the oscilloscope was 100 mV, the current on the computer was $1 \cdot 10^{-11}$ A, which means that 100 mV·s = $1 \cdot 10^{-11}$ A·s. Using this simple relation the TOF of a signal of e.g. 492 mV (a representative signal observed for Pt_{13} at 300 K) can be readily converted into TOF.

Starting with the relation:

$$1.34 \cdot 10^{-7}\ \mathrm{A \cdot s} = 8 \cdot 10^{14}\ \text{molecules} \tag{2.7}$$

a formula was devised in order to find a constant, by which an arbitrary value in mV can be multiplied and the output is equal to the TOF of ethane:

$$\frac{\mathrm{TOF}}{(x(\mathrm{mV}) \cdot 10^{-2}) \cdot 10^{-11}\ \mathrm{A}} = \frac{8 \cdot 10^{14}}{1.34 \cdot 10^{-7}\ \mathrm{A \cdot s}} \tag{2.8}$$

In this instance it can be said that a current of $1.34 \cdot 10^{-7}$ A over time of 1 s would equal $8 \cdot 10^{14}$ molecules. Simplifying:

$$\frac{\mathrm{TOF}}{x(\mathrm{mV})} = 6 \cdot 10^{8} \tag{2.9}$$

Now this number was normalized to the number of clusters, and by dividing by the number of atoms per cluster the TOF (normalized to Pt atoms) is found. For most experiments $9 \cdot 10^{12}$ clusters were deposited:

$$\mathrm{TOF} = \frac{\frac{6 \cdot 10^{8} \cdot x(\mathrm{mV})}{9 \cdot 10^{12}}}{\mathrm{N}} \tag{2.10}$$

where N is the number of atoms per cluster. Simplifying:

$$\mathrm{TOF} = \frac{x(\mathrm{mV}) \cdot 0.66 \cdot 10^{-4}}{\mathrm{N}} \frac{\text{molecules}}{\text{Pt atom} \cdot \mathrm{s}} \tag{2.11}$$

which leads to a value of 0.002497 $\frac{\text{ethane}}{\text{Pt atom} \cdot \mathrm{s}}$ for 492 mV. This value has a very large systematic error due to the uncertainty in the ionization sensitivities of the ion gauge and the mass spectrometer. The values calculated are far from being an accurate quantitative measure, however, they are very precise. One should generally accept a range of $10^{\pm 1}$ as a systematic error. The error bars observed in the TOF results in chapter 3, are the standard deviations from multiple measurements on the same cluster size.

Pulsed Molecular Beam Calibration for Ethylene

In addition to quantifying the reaction product, the amount of ethylene per pulse is also important to determine what the local pressure is above the catalyst. To this end the same strategy was employed as for ethane: determine the sensitivity factor between CO and ethylene, and use the CO Pt(111) TPD as the calibration standard.

Using the same pressure as with ethane, the sensitivity factor was determined to be 2.275 which makes the left side of equation 2.7 be $1.03 \cdot 10^{-7}$. As the amplifier range is different for m/z = 28 the current voltage relation from above is not correct. For the amplifier range used (10^{-8}) 1 mV $= 1 \cdot 10^{-11}$ A. Using equation 2.8:

$$\frac{\text{ethylene molecules}}{x(\mathrm{mV}) \cdot 10^{-11}\ \mathrm{A}} = \frac{8 \cdot 10^{14}}{1.03 \cdot 10^{-7}\ \mathrm{A \cdot s}} \tag{2.12}$$

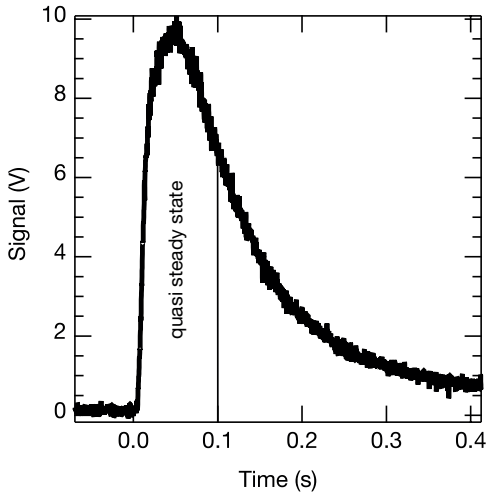

Figure 2.4: QMS signal from a pulse of ethylene with a backing pressure of 2 Torr, pulse width of 600 µs and a piezo voltage of -350 V. The area defined as quasi steady state is the same region where constant ethane production is observed in figure 2.3a.

the number of molecules in an ethylene pulse can be calculated.

Figure 2.4 shows a sample pulse of ethylene measured with the Mo(100) crystal placed before the QMS at 100 K. The quasi steady state region labeled yielded an integral of 763 mV, which corresponds to $5.93 \cdot 10^{13}$ molecules, and a local pressure (using the definition of $1 \cdot 10^{15}$ molecules = 1 Langmuir = $\frac{1 \cdot 10^{-6} \text{ mbar}}{\text{s}}$) of $5.93 \cdot 10^{-7}$ mbar. This is the region where the steady state activity has also been measured (see figure 2.3a). Integrating the ethylene pulse until 0.4 s, i.e. where the baseline is reached again, yields a value of 1.286 V, which equates to $1 \cdot 10^{14}$ molecules per pulse.

2.3 Sample Preparation

In this section the experimental procedures used for the cleaning of the single crystal surfaces and the growth of the thin metal-oxide films will be given.

Mo(100)

The Mo(100) single crystal (MaTeck, Germany) was cleaned by heating with an electron gun to 2000 K followed by oxidation at 900 K in a $5 \cdot 10^{-7}$ mbar oxygen (5.5 purity, Air Liquide, Germany) background. In order to increase the purity of the surface additional flashes to $\approx$ 1000 K is effective at removing excess oxygen. The purity of the single crystal is checked by AES and UPS/MIES. Figure 2.5 shows an exemplary AES spectrum excerpt from a clean Mo(100) surface.

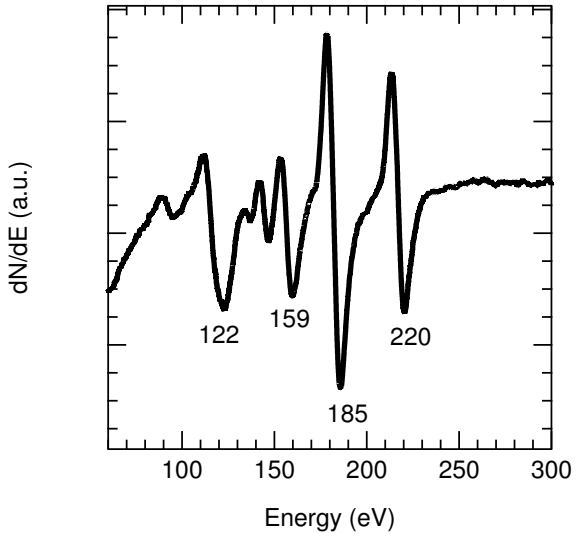

Figure 2.5: Auger electron spectrum of the relevant energy region from the Mo(100) single crystal used in this work. Characteristic peaks have been marked [167].

MgO(100)/Mo(100)

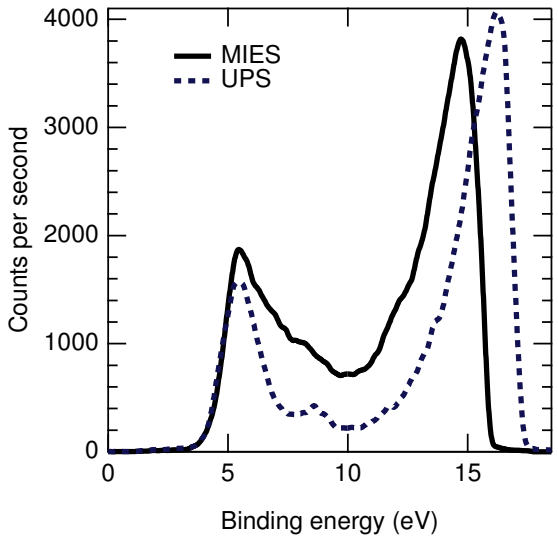

Figure 2.6: MIE and UP spectrum of an MgO(100)/Mo(100) thin film. The peak just above 5 eV corresponds to the O2p state.

The MgO thin film was grown on the Mo(100) single crystal surface by evaporation of a Mg ribbon ($\geq$ 99.95 %, Merck, Germany) in a $5 \cdot 10^{-7}$ mbar oxygen background atmosphere.

The Mg ribbon is wrapped in a tantalum wire and housed in a metal shield with a ≈ 1 cm diameter opening facing the manipulator axis. The Mo(100) single crystal is placed approximately 10 cm from the opening for film growth. After the film growth step the sample is annealed at 800 K for 10 minutes. The film is grown such that the subsequent Auger spectrum shows only a negligible contribution from the Mo(100) substrate. According to previous work in our lab, the film is on the order of 10-15 atomic layers thick [103]. Figure 2.6 shows the UP/MIE spectra from the synthesized film. The characteristic O2p peak is clearly visible at 5.5 eV, and the smaller O2p peak from parallel oriented orbitals is only visible in the UP spectrum at 8 eV due to the inability to MIES to probe beyond the surface perpendicular orbitals.

Pt(111)

The Pt(111) (MaTeck, Germany) surface was cleaned by cycles of sputtering, oxidizing and annealing. The sputtering was performed with an argon sputter gun operating with an ion kinetic energy of 0.8-1 keV and a current on the sample of 10 μA. Afterwards, remaining carbon is oxidized at 650 K for five minutes in a $5 \cdot 10^{-7}$ mbar oxygen atmosphere and then annealed at 1300 K for one minute. The purity of the sample is confirmed with AES and an exemplary spectrum is shown in figure 2.7.

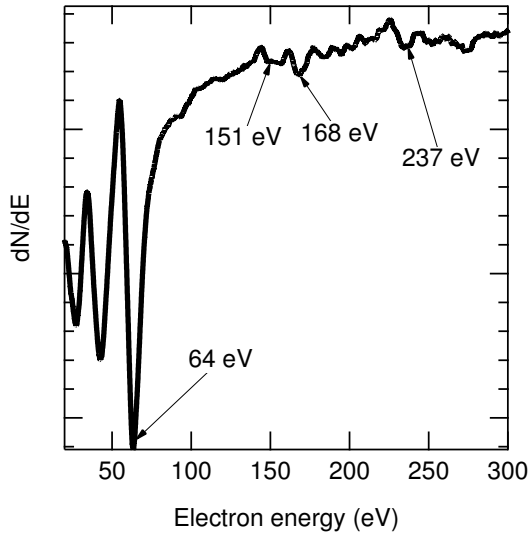

Figure 2.7: Auger spectrum from the Pt(111) single crystal. Characteristic peaks have been marked [167].

2.4 Growth of Three-Dimensional Silica Films on Pt(111)

It has already been shown (chapter 1.3.2) that the support material can have an effect on the physical and chemical properties of adsorbed metal particles, especially at small sizes. The ability to grow and test a diverse cross section of metal-oxide supports while maintaining control of film properties such as surface structure, stoichiometry, atomic structure etc., is indispensable to the research of model catalysts. Additionally, the effect of the metal on which a thin film is grown is a parameter that has yet to be thoroughly investigated with respect to catalytic properties. If the film is thin enough, then electron transfer between adsorbates and the thin film/metal system, should be a way to model the effect of different dopants (i.e. electron withdrawing or donating species).

Silicon dioxide is one of the most ubiquitous metal-oxide supports employed in catalysis but differs from MgO in that it is more acidic [168]. In this section, the successful growth of an amorphous, 3-dimensional film on Pt(111) is presented as a support for cluster catalysts.

THE JOURNAL OF PHYSICAL CHEMISTRY C

Article

pubs.acs.org/JPCC

Atomic Structure Control of Silica Thin Films on Pt(111)

A. S. Crampton,[†,‡] C. J. Ridge,[†,‡] M. D. Rötzer,[†] G. Zwaschka,[†] T. Braun,[†] V. D'Elia,[‡] J.-M. Basset,[‡] F. F. Schweinberger,*[,†] S. Günther,[§] and U. Heiz[†]

[†]Lehrstuhl für Physikalische Chemie, Zentralinstitut für Katalyseforschung und Fakultät für Chemie and [§]Fachgebiet Physikalische Chemie mit Schwerpunkt Katalyse, Zentralinstitut für Katalyseforschung und Fakultät für Chemie, Technische Universität München, Lichtenbergstrasse 4, 85748 Garching, Germany

[‡]KAUST Catalysis Center (KCC), King Abdullah University of Science and Technology, 23955 Thuwal, Kingdom of Saudi Arabia

ABSTRACT: Metal oxide thin films grown on metal single crystals are commonly used to model heterogeneous catalyst supports. The structure and properties of thin silicon dioxide films grown on metal single crystals have only recently been thoroughly characterized and their spectral properties well established. We report the successful growth of a three-dimensional, vitreous silicon dioxide thin film on the Pt(111) surface and reproduce the closed bilayer structure previously reported. The confirmation of the three-dimensional nature of the film is unequivocally shown by the infrared absorption band at 1252 cm^{-1}. Temperature-programmed desorption was used to show that this three-dimensional thin film covers the Pt(111) surface to such an extent that its application as a catalyst support for clusters/nanoparticles is possible. The growth of a three-dimensional film was seen to be directly correlated with the amount of oxygen present on the surface after the silicon evaporation process. This excess of oxygen is tentatively attributed to atomic oxygen being generated in the evaporator. The identification of atomic oxygen as a necessary building block for the formation of a three-dimensional thin film opens up new possibilities for thin film growth on metal supports, whereby simply changing the type of oxygen enables thin films with different atomic structures to be synthesized. This is a novel approach to tune the synthesis parameters of thin films to grow a specific structure and expands the options for modeling common amorphous silica supports under ultra-high-vacuum conditions.

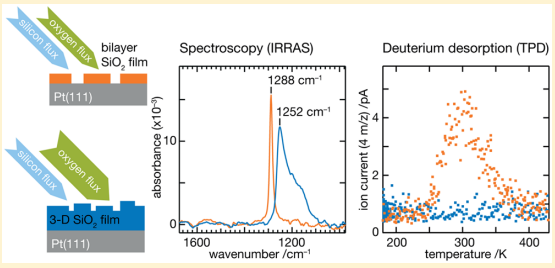

INTRODUCTION

Thin metal oxide films have become a standard tool to support model heterogeneous catalysts under ultra-high-vacuum (UHV) conditions,[1−3] as well as being studied for an assortment of applications in materials science. Silicon dioxide (SiO_2) is one of the most commonly used supports in heterogeneous catalysis,[4,5] and much progress has been made in growing thin SiO_2 films on metal single crystals, as well as revealing the underlying growth mechanisms and structures formed. Mo(110), Mo(112), and Ru(0001) have all been shown to be ideal candidates for the growth of these films, and their structural properties have been well documented.[6−17] From these studies it has been shown that the type of silica film can be solely determined by its infrared vibration band: ∼1300 cm^{-1} for a bilayer, ∼1250 cm^{-1} for a thick, vitreous film, and ∼1065 or ∼1135 cm^{-1} for a monolayer film on Mo(112) or Ru(0001), respectively.[16] SiO_2 films have also been successfully grown on Ni(111),[18] Pd(100),[19] and Pd(111)[20] but have not been characterized to the extent of the aforementioned surfaces. Pt(111) has only recently emerged as another candidate for growing thin SiO_2 films and has been shown to form a closed bilayer structure, similar to the one observed on Ru(0001), and scanning tunneling microscopy (STM) showed that it is vitreous and does not completely cover the surface.[9,16]

The trend observed for the structure of these thin films was shown to follow two parameters: lattice mismatch and oxygen affinity of the metal support. A greater lattice mismatch results in a noncrystalline thin film, as was shown for the bilayer on Pt(111) compared to Ru(0001). Oxygen affinity influences the ability to form Si−O−metal bonds, and this is believed to allow for the formation of a monolayer film seen on Mo(112) and Ru(0001).[9] Both the large lattice mismatch and the low oxygen affinity of Pt(111) mean that silica has only been grown as a closed bilayer with no Si−O−Pt bond (low oxygen affinity) and in a vitreous state (large lattice mismatch).[9,16] In this paper we reproduce on Pt(111) the bilayer previously reported and successfully synthesize a three-dimensional vitreous film. Using Auger electron spectroscopy (AES), metastable impact electron spectroscopy (MIES), ultraviolet photoelectron spectroscopy (UPS), and infrared reflection absorption spectroscopy (IRRAS), we show that the atomic structure of the film is determined by the amount of oxygen on the surface after silicon deposition and that the thicker films exhibit similar spectroscopic behavior observed for other thick SiO_2 films grown on Mo(112) and Ru(0001) while retaining the vitreous

Received: March 19, 2015
Revised: May 21, 2015
Published: May 27, 2015

DOI: 10.1021/acs.jpcc.5b02667
J. Phys. Chem. C 2015, 119, 13665−13669

nature observed for the bilayer. Lastly, the applicability of a bilayer or three-dimensional film as a support for model catalyst systems is also investigated using temperature-programmed desorption (TPD). The ability to grow a thin silica film on a Pt(111) surface that completely covers the metal enables the direct comparison between a catalytically active single crystal and supported metal particles using the same experimental instrumentation, i.e., random error arising from the use of two single crystals (e.g., Mo(112) for supported clusters and Pt(111) as a model single-crystal catalyst) can be ruled out. Furthermore, it has been shown that the metal upon which thin films are grown can influence nanoparticle morphology by a charge transfer mechanism from the thin film/metal interface.[21−23] The ability to grow thin, closed silica films on Pt(111) allows for the investigation of these structure−property relationships with regard to to the underlying metal support. The change in work function between Mo, Ru, and Pt represents a decisive parameter governing surface charging effects, whose influence on nanoparticle morphology and hence catalytic activity can now be investigated. This also represents a corollary to dopants in bulk metal oxides, and these effects can now be modeled by simply changing the metal support. This is an important step to expand the variety of parameters of model heterogeneous catalyst systems under UHV and their comparability to more applied systems.

EXPERIMENTAL SECTION

All experiments were performed in a UHV chamber at a base pressure of 2×10^{-10} mbar; details about the setup can be found elsewhere.[24]

Prior to the measurements the Pt(111) crystal (MaTeck, Germany) was cleaned by repeated cycles of Ar^+ sputtering (T = 900 K, $p(Ar^+) = 5 \times 10^{-6}$ mbar, Δt = 60 min, U = 1 keV, $I \approx 10$ μA) followed by oxidation (T = 650 K, $p(O_2) = 5 \times 10^{-7}$ mbar, $\triangle$ $t\Delta t$ = 5 min) and annealing (T = 1300 K, Δt = 1 min); subsequently, the single-crystal purity was checked by means of AES and MIES/UPS and is in good agreement with the literature.

The SiO_2 thin film was prepared by e-beam evaporation (Tectra, Germany) of a silicon rod (99.999% purity, Alfa-Aesar, Germany) in an oxygen (5.5 purity, AirLiquide, Germany) background pressure (T = 400 K, $p(O_2) = 2 \times 10^{-6}$ mbar) onto the Pt(111) single-crystal surface. The flux of the silicon beam was measured using an electrode on the end of the evaporator, with the normal flux being ∼10 nA and, where specified, half-flux being ∼5 nA. The film was then annealed at 1200 K in a 2×10^{-6} mbar oxygen atmosphere before experimental data was acquired, unless otherwise mentioned. A single-shot 4 and 10 min film growth step was performed to synthesize the bilayer and three-dimensional thin film, respectively. The electron emission spectra (EES) were all recorded at 100 K, and further details regarding the spectroscopic setup can be found in our previous publications.[25,26] The IRRAS experiments were performed at 100 K (Thermo-Nicolet FT-6700, Thermo-Nicolet MCT detector) and averaged 256 scans at 4 cm^{-1} resolution. The TPDs (Balzers QMG 430, Lichtenstein) were run with a temperature ramp of 2 K/s, and the gas dosage was performed with a calibrated molecular beam doser.[27]

RESULTS

IRRAS spectra taken after 4 and 10 min of film growth on Pt(111) followed by annealing at 1200 K are shown in Figure 1.

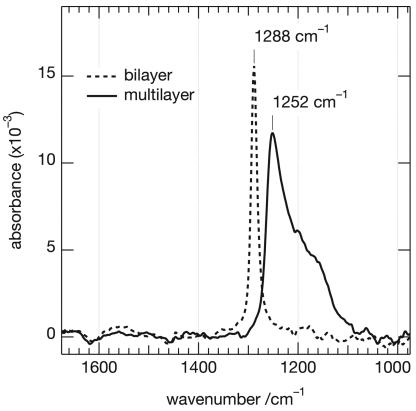

Figure 1. IRRAS spectra for the three-dimensional and bilayer silica film. Each film shows a characteristic peak: bilayer at 1288 cm^{-1} and the three-dimensional film at 1252 cm^{-1}.

The peak at 1288 cm^{-1} corresponds to Si−O−Si vibrations within a closed bilayer thin film after 4 min of film growth.[16] After 10 min of silicon evaporation a peak at 1252 cm^{-1} with a broad shoulder down to 1100 cm^{-1} appeared, and these are the asymmetric longitudinal phonon vibrations, characteristic for a thick vitreous film. Ru(0001) also exhibited this exact trend where a bilayer was first observed with a peak at 1300 cm^{-1}, and upon further film growth the bilayer peak disappeared and a peak centered at 1257 cm^{-1} with a broad shoulder down to 1100 cm^{-1} appeared.[15] The clear formation of the bilayer after 4 min indicates that the film deposition rate is on the order of 0.5 monolayer/min. The presence of the thick film after 10 min would mean a film thickness of 5 atomic layers, which is similar to the thickness of 3-dimensional films grown on Ru(0001).[15] Assuming similar values for the thin films on Ru, the approximate thickness of the 3-dimensional film grown on Pt(111) is 10 Å.

The EES spectra in Figure 2 show the SiO_2 valence bands after 4 and 10 min of film growth each followed by 1200 K annealing before spectral characterization. The UP spectra have been background corrected by means of a previously introduced method in order to remove secondary electron contributions.[25] This procedure was not applied to the MIE spectra as the secondary electron contribution was not as significant. After 4 min of film growth a broad peak appeared, centered at 6.4 and 6.7 eV for UPS and MIES, respectively, belonging to the O(2p) nonbonding state. Additionally, a MIES peak emerged at 10.7 eV belonging to the Si−O bonding state. After 10 min of film growth the O(2p) peak shifted to 6.8 and 7.4 eV for UPS and MIES, respectively, while the Si−O peak appeared at 11.0 eV for UPS and MIES.[12]

Deuterium TPD spectra collected from both the three-dimensional and the bilayer film can be seen in Figure 3. The spectra show that the thick film has no D_2 desorption peak, whereas the bilayer shows a small peak centered at 300 K corresponding to desorption from uncovered Pt(111).

DISCUSSION

The results of Figure 1 demonstrate that a three-dimensional, vitreous silica film can be grown on Pt(111). This overcomes the limitations which restricted silica films to exclusively a bilayer structure.[9,16] The reason for the formation of the three-

DOI: 10.1021/acs.jpcc.5b02667
J. Phys. Chem. C 2015, 119, 13665−13669

The Journal of Physical Chemistry C Article

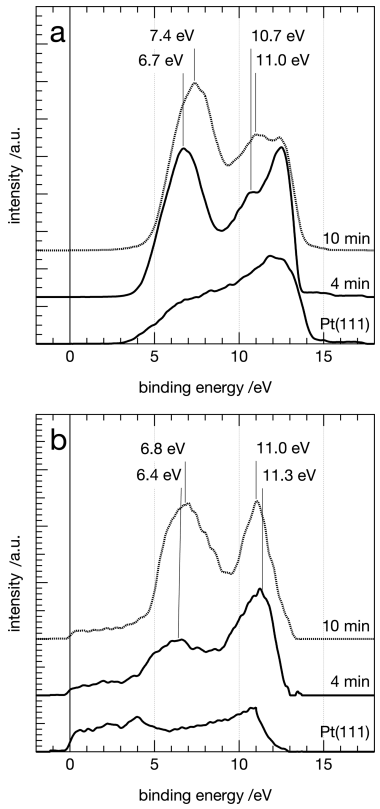

Figure 2. MIE (a) and background-corrected UP (b) spectra of the silica thin film at different preparation steps. The bottom spectrum shows the clean Pt(111) single-crystal surface, then after 4 min of film growth with subsequent annealing at 1200 K, and last after 10 min of growth and annealing at 1200 K. The uppermost spectrum can be assigned to the vitreous, three-dimensional SiO_2 and the middle spectrum to the bilayer thin film.

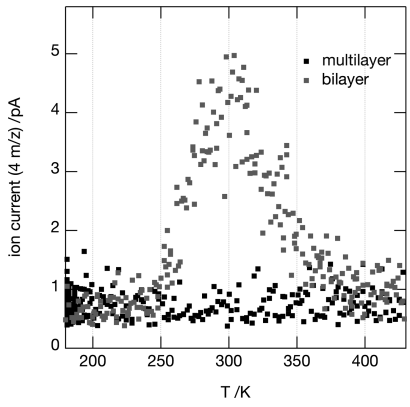

Figure 3. Deuterium TPD spectrum of 0.4 D_2/surface atom dosed at 100 K on the three-dimensional and bilayer silica film.

dimensional film in contrast to previous reports was identified by varying the film growth parameters. A SiO_2 film was grown for 20 min using one-half the silicon flux previously used, followed by acquisition of an IR spectrum seen in Figure 4a.

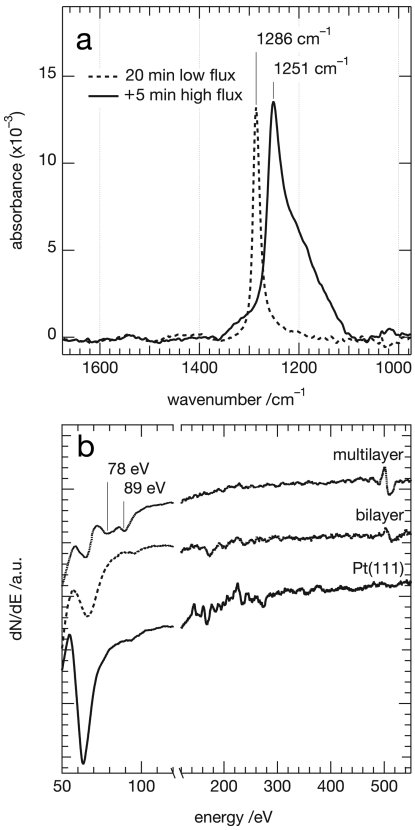

Figure 4. IRRAS spectra (a) after 20 min film growth using one-half the silicon flux as previously reported, followed by 5 min of normal flux film growth, both after annealing at 1200 K. AES spectra (b) for a clean Pt(111) surface, the bilayer SiO_2 film after 20 min of low-flux silicon deposition, and the multilayer film after 10 min of film growth at normal flux (both without annealing at 1200 K), keeping the total amount of silicon deposited constant. The region above 150 eV has been multiplied by a factor of 2.

Even after 20 min of film growth, only the bilayer formed. On top of this film, 5 min of the normal flux film growth protocol was performed and the three-dimensional film was observed. Auger spectra taken after an identical low-flux experiment were compared with those taken after the normal flux experiment (the 10 min standard growth protocol), both seen in Figure 4b. Both AES experiments were performed in a way that an equal amount of silicon was evaporated on the Pt(111) surface. As both spectra were taken before high-temperature annealing, both are showing the same surface concentration of silicon. No large elemental silicon peak at 92 eV is visible, in contrast to silicon deposited[28] on and segregated[29] from the Pt(111) surface. This is, however, to be expected in the presence of atomic oxygen, where no elemental silicon peak is observed after oxidizing at ~400 K. Instead, when using molecular oxygen as the oxidizing agent, a very large peak at 92 eV is visible.[29] The absence of a well-defined peak at 92 eV implies that atomic oxygen, likely being generated in the evaporator, is oxidizing the deposited silicon. We identify the oxygen species as atomic oxygen based on the similarity of our Auger spectra to those in ref 29. Direct identification of atomic oxygen is not

DOI: 10.1021/acs.jpcc.5b02667
J. Phys. Chem. C 2015, 119, 13665−13669

possible due to the geometry of the evaporator with respect to the mass spectrometer, and therefore, a definitive assignment is not possible. It is, however, unlikely that ionized oxygen species are responsible due to the potential of −18 V applied to the electrode at the end of the evaporator, but excited states of molecular and/or atomic oxygen cannot be ruled out.

The normal flux spectrum shows two peaks at 78 and 89 eV, which are known SiO_x(LVV) transitions from SiO_2 and $SiO_{x<2}$, respectively. The low-flux spectrum shows only a very small feature at ∼93 eV, indicating that the nature of silicon deposited under these conditions is more varied than with the higher flux, i.e., the degree of oxidation varies from completely unoxidized to fully oxidized which causes the Auger peak to smear out over a wide range of energies, rendering it unresolvable in AES.

The amount of oxygen can be readily quantified from the O(KLL) Auger peak at 508 eV. Comparing the size of the oxygen peak to the Pt transition at 237 eV, the amount of oxygen almost doubles when doubling the flux. As both low- and normal-flux experiments have deposited the same amount of silicon, the only difference between the two surfaces is the amount of oxygen present. As the same background oxygen pressure was used for both experiments, the increase in oxygen must be originating from the increased evaporation rate (more specifically the increased filament current in the evaporator) and the most probable oxygen source which could be affected is atomic oxygen generated in the evaporator.

As SiO_4 tetrahedra have been proposed as the structural units for three-dimensional films on Ru(0001),[9] the concentration of these types of units during deposition and annealing must be a decisive factor discriminating between formation of purely the bilayer and formation of three-dimensional SiO_2. The SiO_2(LVV) Auger peak at 78 eV clearly shows that the three-dimensional growth protocol produces more oxidized silicon, which indicates that increasing atomic oxygen has the effect of increasing the surface concentration of fully oxidized silicon species. These species ultimately lead to the formation of a three-dimensional structure that completely covers the metal surface. It is also known that the saturation coverage of atomic oxygen on Pt(111) is approximately double that from molecular oxygen adsorption and dissociation.[30,31] This evidences a compound effect, whereby increased atomic oxygen leads to a higher oxygen saturation coverage of open platinum surface domains, which facilitates the formation of fully oxidized silicon species and a complete covering of the metal. This shows that limitations on film growth imposed by a surface's oxygen affinity and adsorption properties can be circumvented by using atomic oxygen while concomitantly changing the atomic structure of the thin film grown.

A second factor governed by the degree of silicon oxidation during deposition is etching of the film during annealing at 1200 K, effectively "dissolving" the metal oxide.[32] This could also play a factor in the unsuccessful attempts to grow three-dimensional SiO_2 on Pt(111) where a combination of a lower concentration of oxidized silicon and a higher concentration of elemental silicon both act to suppress the formation of three-dimensional SiO_2. After annealing our film to 1200 K all $SiO_{x<2}$ features disappeared, which we attribute to the desorption of SiO, in agreement with the known desorption above 1200 K from silicon surfaces.[33−35]

The peak positions from the EES experiments compare well to experiments performed on Mo(112) but do show slight deviations, the most obvious being the O(2p) state, which does not split into two well-resolved peaks after annealing at high temperatures (∼1100−1200 K).[8,12] Instead, this peak remains broad and shifts to higher binding energy for the thicker film. The broad nature of the valence band peaks has been attributed to a higher concentration of defect sites[36] and a lack of crystallinity within the thin film.[8] The deviation of 0.6 eV between the two spectroscopic methods can be explained by the surface sensitivity of MIES compared to UPS. MIES probes only the uppermost surface layer due to impenetrability of helium atoms into the surface. Thus, the UPS spectra originate from a convolution of the pure surface states seen in MIES and the underlying emission from the bulk, leading to the broader UPS peak and its shoulders on the high binding energy side.

The presence of a single peak centered at 11.0 eV, in both the UP spectrum and the MIE spectrum, also corroborates the lack of Si−O−Pt linkages. This is in contrast to EES spectra from SiO_2 on Mo(112) where a shoulder at 10.5 eV on the larger Si−O peak at 11.5 eV was observed and attributed to a Si−O−Mo bond.[12] The presence of only one peak in this binding energy range is to be expected when Si−O−Pt bonds are absent. As previously mentioned, results on Pt(111) have shown a distinct lack of crystallinity when compared to Mo(112) and Ru(0001),[9] and our MIES/UPS results show that silica grown on Pt(111) produces no twin peak O(2p) feature corresponding to a crystalline film, and no feature belonging to a Si−O−Pt state is observed.

The D_2 TPD experiments showed a desorption peak at 300 K from the bilayer film. This peak originates from an incomplete covering of the Pt(111) single crystal, which has been observed using STM.[9,16] Covering the Pt(111) support entirely by the SiO_2 film is essential in order to be able to differentiate between signals originating from the underlying metal and, e.g., deposited, subnanometer catalyst particles. The three-dimensional SiO_2 film showed no such desorption peak, indicating a complete covering of the surface, which makes it an ideal candidate for the use as a catalyst support material which may model industrially relevant supports.

CONCLUSION

In summary, we reproduced the growth of a bilayer SiO_2 thin film on Pt(111) and observed the expected spectral behavior based on previous reports, including an incomplete covering of the surface which supports STM results.[9] In addition, the growth of a three-dimensional vitreous SiO_2 film was achieved on the Pt(111) surface and exhibits the same characteristics as thick SiO_2 films produced on Ru(0001), Mo(110), and Mo(112).[10,14,15] The confirmation that the film belongs to the three-dimensional category was confirmed with IRRAS where a peak at 1252 cm^{-1} with a shoulder down to 1100 cm^{-1} is indicative of a multilayer silica film, in contrast to the sharp bilayer absorption band observed at 1288 cm^{-1}.

The absence of O(2p) peak splitting and fine structure within the EES spectra further indicates the lack of crystallinity in both the bilayer and three-dimensional silica film. Additionally, no other emission peak was observed that could be attributed to a Si−O−Pt state.

TPD measurements show that the bilayer film is a poor choice as a nanoparticle support for catalytic measurements due to incomplete coverage of the active Pt(111) surface. The three-dimensional film, however, shows that it completely covers the Pt(111) surface and can therefore be applied as a catalyst support for UHV experiments which more closely models supports used for ambient pressure experiments.

DOI: 10.1021/acs.jpcc.5b02667
J. Phys. Chem. C 2015, 119, 13665−13669

The Journal of Physical Chemistry C Article

Catalytic measurements on an active metal single crystal as well as from particles supported on a thin film grown on the same single crystal eliminates random error and allows for the most accurate comparison of measurements from the pure single crystal and the supported metal particles. The ability to grow the same thin film on three different metals (Mo, Ru, and Pt) also allows for a systematic study of their influence on clusters/nanoparticles. The difference in work function between the metals is one interesting parameter which could lead to different particle morphologies by attenuating or enhancing the degree of charge transfer from the thin film/metal interface while also providing a technique to model dopant effects in bulk metal oxides.

The exclusive growth of a bilayer film was observed when one-half the silicon flux compared to the normal procedure was used. By increasing the flux it was observed that the amount of oxygen present after deposition doubles even though the deposited amount of silicon and oxygen background pressure remain the same. This excess oxygen is tentatively attributed to atomic oxygen being generated by the silicon evaporator. Atomic oxygen would overcome the limitation imposed by the low oxygen affinity of Pt(111) and allows for a higher oxygen coverage on the surface during silicon evaporation compared to molecular oxygen. This leads to the formation of more fully oxidized silicon species needed for three-dimensional film growth and a complete covering of the surface. Excess elemental silicon deposited on the bilayer, and multilayer film is oxidized to volatile SiO when annealing the sample to 1200 K, which etches the film. Since in this case the multilayer SiO_2 film is also etched, the ability to grow three-dimensional films is dependent on the more oxidized silicon suppressing the etching along with the concomitant increase in the concentration of the requisite building blocks for a three-dimensional film. The identification of atomic oxygen as the discriminating factor between two atomic structures of silica thin films grown on the same metal support has, to our knowledge, never been demonstrated before. This represents an important parameter that can in principle be investigated for the control of atomic structure of any metal oxide thin film on any metal support.

AUTHOR INFORMATION

Corresponding Author

*E-mail: florian.schweinberger@tum.de.

Notes

The authors declare no competing financial interest.

ACKNOWLEDGMENTS

C.J.R. and F.F.S. thank Prof. Hans-Joachim Freund and Dr. Shamil Shaikhutdinov for their hospitality during our stay at the FHI and their insights into the preparation and characterization of silica thin films. We acknowledge financial support from the DFG through the Nanosystems Initiative Munich (NIM) (F.F.S., C.J.R., M.D.R., A.S.C., and U.H.) and the Project He 3454/9-2 (F.F.S. and U.H.).

REFERENCES

(1) Heiz, U.; Sherwood, R.; Cox, D. M.; Kaldor, A.; Yates, J. T. *J. Phys. Chem.* **1995**, *99*, 8730−8735.
(2) Heiz, U.; Sanchez, A.; Abbet, S.; Schneider, W.-D. *J. Am. Chem. Soc.* **1999**, *121*, 3214−3217.
(3) Sanchez, A.; Abbet, S.; Heiz, U.; Schneider, W.-D.; Häkkinen, H.; Barnett, R. N.; Landman, U. *J. Phys. Chem. A* **1999**, *103*, 9573−9578.
(4) In *Modern Surface Organometallic Chemistry*; Basset, J.-M., Psaro, R., Roberto, D., Ugo, R., Eds.; Wiley-VCH Verlag GmbH & Co. KGaA, Weinheim, Germany, 2009.
(5) Ertl, G.; Knözinger, H.; Schüth, F.; Weitkamp, J. *Handbook of Heterogeneous Catalysis*, 2nd ed.; Wiley-VCH, Weinheim, Germany, 2008.
(6) Löffler, D.; Uhlrich, J. J.; Baron, M.; Yang, B.; Yu, X.; Lichtenstein, L.; Heinke, L.; Büchner, C.; Heyde, M.; Shaikhutdinov, S.; et al. *Phys. Rev. Lett.* **2010**, *105*, 146104.
(7) Schroeder, T.; Adelt, M.; Richter, B.; Naschitzki, M.; Bäumer, M.; Freund, H.-J. *Surf. Rev. Lett.* **2000**, *7*, 7−14.
(8) Schroeder, T.; Giorgi, J. B.; Bäumer, M.; Freund, H.-J. *Phys. Rev. B* **2002**, *66*, 165422.
(9) Shaikhutdinov, S.; Freund, H.-J. *Adv. Mater.* **2013**, *25*, 49−67.
(10) Stacchiola, D. J.; Baron, M.; Kaya, S.; Weissenrieder, J.; Shaikhutdinov, S.; Freund, H.-J. *Appl. Phys. Lett.* **2008**, *92*, 011911.
(11) Weissenrieder, J.; Kaya, S.; Lu, J.-L.; Gao, H.-J.; Shaikhutdinov, S.; Freund, H.-J.; Sierka, M.; Todorova, T. K.; Sauer, J. *Phys. Rev. Lett.* **2005**, *95*, 076103.
(12) Wendt, S.; Ozensoy, E.; Wei, T.; Frerichs, M.; Cai, Y.; Chen, M. S.; Goodman, D. W. *Phys. Rev. B* **2005**, *72*, 115409.
(13) Włodarczyk, R.; Sierka, M.; Sauer, J.; Löffler, D.; Uhlrich, J. J.; Yu, X.; Yang, B.; Groot, I. M. N.; Shaikhutdinov, S.; Freund, H.-J. *Phys. Rev. B* **2012**, *85*, 085403.
(14) Xu, X.; Goodman, D. W. *Surf. Sci.* **1993**, *282*, 323−332.
(15) Yang, B.; Kaden, W. E.; Yu, X.; Boscoboinik, J. A.; Martynova, Y.; Lichtenstein, L.; Heyde, M.; Sterrer, M.; Włodarczyk, R.; Sierka, M.; et al. *Phys. Chem. Chem. Phys.* **2012**, *14*, 11344−11351.
(16) Yu, X.; Yang, B.; Boscoboinik, J. A.; Shaikhutdinov, S.; Freund, H.-J. *Appl. Phys. Lett.* **2012**, *100*, 151608.
(17) He, J.-W.; Xu, X.; Corneille, J. S.; Goodman, D. W. *Surf. Sci.* **1992**, *279*, 119−126.
(18) Kundu, M.; Murata, Y. *Appl. Phys. Lett.* **2002**, *80*, 1921−1923.
(19) Zhang, Z.; Jiang, Z.; Yao, Y.; Tan, D.; Fu, Q.; Bao, X. *Thin Solid Films* **2008**, *516*, 3741−3746.
(20) Kershner, D. C.; Medlin, J. W. *Surf. Sci.* **2008**, *602*, 786−794.
(21) Sterrer, M.; Risse, T.; Heyde, M.; Rust, H.-P.; Freund, H.-J. *Phys. Rev. Lett.* **2007**, *98*, 206103.
(22) Risse, T.; Shaikhutdinov, S.; Nilius, N.; Sterrer, M.; Freund, H.-J. *Acc. Chem. Res.* **2008**, *41*, 949−956.
(23) Sauer, J.; Freund, H.-J. *Catal. Lett.* **2014**, *145*, 109−125.
(24) Heiz, U.; Vanolli, F.; Trento, L.; Schneider, W.-D. *Rev. Sci. Instrum.* **1997**, *68*, 1986−1994.
(25) Schweinberger, F. F.; Crampton, A. S.; Zimmermann, T.; Kwon, G.; Ridge, C. J.; Günther, S.; Heiz, U. *Surf. Sci.* **2013**, *609*, 18−29.
(26) Spirkl, F. M.; Kunz, S.; Schweinberger, F. F.; Farnbacher, A. N.; Schröter, R.; Heiz, U. *Rev. Sci. Instrum.* **2012**, *83*, 013114.
(27) Bozack, M. J.; Muehlhoff, L.; J.N. Russel, J.; Choyke, W. J.; Yates, J. *J. Vac. Sci. Technol. A* **1987**, *5*, 1−8.
(28) Niehus, H.; Comsa, G. *Surf. Sci.* **1981**, *102*, L14−L20.
(29) Bonzel, H. P.; Franken, A. M.; Pirug, G. *Surf. Sci.* **1981**, *104*, 625−642.
(30) Gland, J. L. *Surf. Sci.* **1980**, *93*, 487−514.
(31) Parker, D. H.; Bartram, M. E.; Koel, B. E. *Surf. Sci.* **1989**, *217*, 489−510.
(32) Leroy, F.; Saito, Y.; Cheynis, F.; Bussmann, E.; Pierre-Louis, O.; Müller, P. *Phys. Rev. B* **2014**, *89*, 235406.
(33) Engel, T. *Surf. Sci. Rep.* **1993**, *18*, 93−144.
(34) Lander, J. J.; Morrison, J. *J. Appl. Phys.* **1962**, *33*, 2089−2092.
(35) Walkup, R. E.; Raider, S. I. *Appl. Phys. Lett.* **1988**, *53*, 888−890.
(36) Kim, Y. D.; Wei, T.; Goodman, D. W. *Langmuir* **2003**, *19*, 354−357.

DOI: 10.1021/acs.jpcc.5b02667
J. Phys. Chem. C 2015, 119, 13665−13669

3 Results and Discussion

This chapter presents the research, in the form of both accepted papers and as of yet unpublished data, encompassing the scientific work performed for this dissertation. Four major cornerstones of the catalytic system are represented: the ethylene hydrogenation on Pt_n/MgO where the influence of cluster size was investigated, Pt_n/SiO_2 where not only cluster size but the difference compared to the MgO film was studied, the effect of the support stoichiometry on the Pt_{13}/SiO_2 catalyzed ethylene hydrogenation and a comparison of ethylene hydrogenation on small nanoparticles of group VIII metals.

The composition of results demonstrates both a fresh perspective on a well-known model reaction, while also investigating the intricacies introduced by particle sizes in the sub-nanometer range. The high reproducibility of experimental conditions, enabled by UHV techniques and surface sensitive electron spectroscopies, allows for a facile interpretation among the aforementioned cornerstones. The first section on Pt_n/MgO is the topic which embodies the bulk of the measurements and analysis in this dissertation. It also represents a collaboration with the Landman Group from Georgia Tech, where extensive first principles calculations were performed in order to supplement and improve the understanding of this system.

3.1 Ethylene Hydrogenation on MgO Supported Platinum Clusters

Chapter 1 introduced ethylene hydrogenation as a classical model system in heterogeneous catalysis, which touches on hydrocarbon surface chemistry as well as the general concept of structure sensitivity. The current state of thought regarding this reaction on platinum single crystals and nanoparticles has been described and in this section the results from platinum particles, in the size region where the established effects of fluxionality, charging, isomerism etc. are expected to be maximized, are presented. An unmatched theoretical investigation has also established a peerless database of MgO supported cluster structures and energies, while investigating the influence that changing particle size by a single atom can have on reaction pathways, energetics and kinetics.

nature COMMUNICATIONS

ARTICLE

Received 21 Aug 2015 | Accepted 7 Dec 2015 | Published xx xxx 2016

DOI: 10.1038/ncomms10389 OPEN

Structure sensitivity in the nonscalable regime explored via catalysed ethylene hydrogenation on supported platinum nanoclusters

Andrew S. Crampton[1], Marian D. Rötzer[1], Claron J. Ridge[1,2], Florian F. Schweinberger[1], Ueli Heiz[1], Bokwon Yoon[3] & Uzi Landman[3]

The sensitivity, or insensitivity, of catalysed reactions to catalyst structure is a commonly employed fundamental concept. Here we report on the nature of nano-catalysed ethylene hydrogenation, investigated through experiments on size-selected Pt_n ($n = 8$–15) clusters soft-landed on magnesia and first-principles simulations, yielding benchmark information about the validity of structure sensitivity/insensitivity at the bottom of the catalyst size range. Both ethylene-hydrogenation-to-ethane and the parallel hydrogenation–dehydrogenation ethylidyne-producing route are considered, uncovering that at the <1 nm size-scale the reaction exhibits characteristics consistent with structure sensitivity, in contrast to structure insensitivity found for larger particles. The onset of catalysed hydrogenation occurs for Pt_n ($n \geq 10$) clusters at $T > 150$ K, with maximum room temperature reactivity observed for Pt_{13}. Structure insensitivity, inherent for specific cluster sizes, is induced in the more active Pt_{13} by a temperature increase up to 400 K leading to ethylidyne formation. Control of sub-nanometre particle size may be used for tuning catalysed hydrogenation activity and selectivity.

[1] Chair of Physical Chemistry, Catalysis Research Center, Chemistry Department, Technische Universität München, Lichtenbergstraße 4, Garching 85748, Germany. [2] Air Force Research Laboratory, Energetic Materials Branch, 2306 Perimeter Road, Eglin AFB, Florida 32542, USA. [3] School of Physics, Georgia Institute of Technology, Atlanta, Georgia 30332-0430, USA. Correspondence and requests for materials should be addressed to U.L. (email: uzi@gatech.edu).

The classification and systematization[1–3] of heterogeneously catalysed reactions as 'demanding' or 'facile', with the former term describing dependence on catalyst particle size and the latter associated with reactions that are size invariant, has been a central guiding theme of research in heterogeneous catalysis for over half a century[4–7]. The early focus on particle size came from the realization that the fraction of atoms situated at a metal particle's surface to the total number of metal atoms, sometimes termed the 'fraction of exposed atoms'[6] or 'degree of dispersion'[1], varies with particle size, approaching unity for very small particles (diameter $\leq$1 nm) and taking small values for large particles. It was recognized early, based on simple geometric (polyhedral) models (tetrahedral, octahedral, cuboctahedral and so on), that the above-mentioned size-related classification may be related to the size-dependent abundance of atomic configurations characterized by surface atoms with low coordination numbers (for example, edges or corners). These under-coordinated atoms were expected to express varying proclivities for engaging in chemical reactions depending on the nature of the reactants and the ambient conditions[1,4–6].

The advent and proliferation of atomic and molecular scale surface science preparation and characterization techniques in the 1970s focused on reactions catalysed on well-defined single-crystal model systems. It then became customary (extending up to date) to classify heterogeneously catalysed reactions as structure sensitive or structure insensitive, corresponding to the aforementioned classifications of demanding and facile, in order to better describe the primary difference between these single-crystal model systems. An example of a structure-sensitive reaction is ammonia synthesis through the reaction of nitrogen and hydrogen on iron single-crystal surfaces where the Fe(111) surface exhibits a higher turnover frequency (TOF) than Fe(100) or Fe(110)[8]. Ethylene hydrogenation catalysed by platinum serves as an example of a structure-insensitive reaction, that is, no change in the TOF has been observed on different single-crystal planes[9]. The latter fundamental and technological important reaction stands out as the first reaction for which a catalytic mechanistic pathway has been formulated (the Horiuti-Polanyi mechanism, HP), and it forms the focus of our investigation in this paper[10].

The classification of the ethylene hydrogenation as structure insensitive is supported by decades of experimental work employing mostly surface science techniques for reactions taking place on well-characterized extended transition metal surface planes (see Supplementary Note 1 for details), or investigations on samples made of surface-supported distributions of relatively large metal particles with sizes ranging from 1.5 to 10 nm diameter. Although full understanding pertaining to the microscopic origins of the observed structure insensitivity is still lacking[5,7,11,12], a commonly cited view holds that formation of carbonaceous species (in particular ethylidyne) in the course of the hydrogenation reaction, leads to saturation coverage (poisoning) of the metal surface that results in masking of structural features that could have otherwise brought about different reactivities, and/or alternative reactive outcomes, for surfaces showing different crystallography; that is, if not for the formation of poisonous carbonaceous species, metal surfaces with different crystallography (that is, different Miller indices) would have exhibited structure sensitivity.

Metal particles with sizes reduced to the $<$1 nm in 'diameter' range (containing 10–20 atoms) may be viewed as quasi-zero-dimensional (0D) quantum dots, characterized by electronic quantum size effects[13,14] and specific atomic organization motifs, that lead to the emergence of unique size-dependent physical and chemical properties. In this regime, extrapolations from larger sizes using arguments relying on surface-to-volume ratios and scaling relations based on the enumeration of special sites (for example, corner and edge atoms) as a function of the size are not operative[15–17]. In this size scale—that is, in the limit of ultimate dispersion—where almost all of the atoms of the metal cluster are essentially surface atoms and where almost all the cluster atoms can be classified as under-coordinated (compared with the bulk), a new materials' size regime is entered[13,14,18,19]. Explorations of materials' properties in this limiting reduced-size scale requires experiments and first-principles theoretical treatments with atom-by-atom resolution. This is indeed the approach that we have taken in this study.

In quest of appraising the applicability of the fundamental concept of structure sensitivity/insensitivity to nanoscale catalysts, founded on the basis of observations made at larger size scales, we focus here on the hydrogenation of ethylene catalysed by size-selected platinum nanoclusters containing between 7 and 40 Pt atoms supported on an MgO(100)/Mo(100) surface, which is inactive for ethylene hydrogenation. As previously mentioned, ethylene hydrogenation serves often as a generic example of a structure insensitive reaction, obeying the parallel reactions selectivity criterion (PRSC)[1], with the full-hydrogenation-to-ethane channel and the alternative half-hydrogenation-to-ethyl/dehydrogenation-to-ethylidyne pathway serving as the operative two parallel reactions. The PRSC stipulates that: 'The best way to proceed is to choose a molecule reacting along two parallel paths and measure the selectivity defined as the rate of the two parallel reactions. If the two products come from different adsorbed states requiring different surface structures, a change of selectivity with dispersion or mode of preparation of the metal may be found. The most unequivocal case is when the specific activity for one of the parallel reactions changes from one catalyst to the next, whereas the specific activity for the other remains unchanged". Thus, our present experimental and theoretical studies of the ethylene hydrogenation reaction catalysed by nanoscale platinum clusters with atom-by-atom size-controlled resolution, joined with the first adaptation of the PRSC to nanoscale catalysts, provides, as elaborated below, benchmark results pertaining to the reaction's structure sensitivity/insensitivity at the bottom of the catalyst particle size range. As in the case of larger catalyst particles, both the ethylene-hydrogenation-to-ethane channel and the parallel ethylidyne-producing, poisoning, route must be considered, culminating in the fundamental uncovering that at the ultimate $<$1 nm size scale, the ethylene hydrogenation reaction catalysed by supported platinum particles exhibits characteristics consistent with being a structure-sensitive reaction, in contrast to the accepted structure insensitivity of the reaction found for particles with a lower dispersion.

Results

Research plan. We begin with temperature programmed reaction (TPR) experiments, starting from the low temperature adsorption of the two reactants (H_2 and C_2H_4) where all reaction pathways are quenched (except H_2 dissociation which may occur spontaneously even at low temperatures, see Methods for details). Subsequent measurement of the thermally desorbed species (reaction products and/or unreacted molecules), made at increased temperature, yields an effective hierarchical scan of the spectrum of activation energies operative in the catalysed reaction under study; for technical detail see Methods. It should be noted that the MgO(100) thin film used in this study has been determined to be defect poor[19–21] by a combined metastable impact electron spectroscopy (MIES) and temperature programmed desorption (TPD) study (see Methods and Supplementary Figs 2–4 for the spectroscopic and chemical characterization of the thin film). Analysis of the results of the above-mentioned

NATURE COMMUNICATIONS | DOI: 10.1038/ncomms10389 ARTICLE

characterizations lead us to conclude that the films prepared for the investigations described herein are essentially free of surface defects such as F-centres or other under-coordinated electron trapping sites, and that effects because of roughness, disorder effects, island formation and grain boundaries/corners/steps, are of no consequence (or below the detection limit) for the interpretation of the measurements and analysis presented in this paper.

The information obtained from these measurements is directly amenable to analysis and comparison with *ab initio*, first-principles, theoretical calculations (see Methods for details) that provide microscopic insights about the reaction mechanisms. To go beyond the above one-catalytic-cycle experiments, the reactivity of the size-selected Pt clusters is subsequently studied under isothermal, quasi-steady-state, conditions with the use of a pulsed molecular beam of ethylene. Under such circumstances, all the reaction channels that open at temperatures up to the selected temperature of the experiment are operative, including parallel reaction paths that are potentially detrimental to the full hydrogenation of ethylene to ethane, namely the aforementioned coking reactions such as the one resulting in the formation of ethylidyne.

One-catalytic-cycle experiments. Representative cluster-TPR spectra depicted in Fig. 1a and compared with one measured for a Pt(111) surface show negligible reactivity of the Pt_9 cluster and ethane production for Pt_{10} and Pt_{13} peaking at $\sim$150 K, that is $\sim$100 K below the temperature measured for the extended Pt(111) surface. This indicates similar activation energies for clusters in this size range that are considerably lower than the one found for the reaction catalysed on the Pt(111) surface. The integrated areas under the measured TPR curves, normalized to the number of atoms per cluster (Fig. 1b) illustrate that the supported platinum clusters catalyse the formation of more ethane per Pt atom than the corresponding amount generated from the Pt(111) surface, with a maximum found for Pt_{13}. Most importantly, the temperature-dependent variation of the ethylene hydrogenation reactivity of the Pt_n ($n=9$, 10 and 13) clusters as a function of their size and, in particular, the appearance of a threshold size ($n=10$) for onset of the catalytic activity, suggest that ethylene hydrogenation catalysed by Pt nanoclusters in the 1 nm size range falls under the classification of a size (structure)-sensitive reaction, in contrast to the commonly accepted structure insensitivity when catalysed by larger particles and extended surfaces. As demonstrated below, this conjectured new classification in the sub-nanometre size range is indeed supported by measurement of TOFs manifesting size (structure) sensitivity under steady-state conditions at room temperature (300 K).

Structures and reaction mechanisms from *ab-initio* calculations. In light of the above-observed size dependencies, it is evident that uncovering the atomic-arrangement motifs of the sub-nanometre-size supported Pt cluster catalysts is imperative to advancing our understanding of the physical principles underlying the above-noted apparent structural sensitivity of the catalysed reactions. The development and implementation of efficient and practical optimization strategies (global optimization in particular[22]) is a vexing problem of great importance in diverse fields, including the physical sciences, where we mention continuing efforts in the areas of protein folding, and the atomic arrangements in biomolecules, clusters and crystals[23]. A main difficulty in this area originates from the fact that the global extremum of a real multivariate function (for example, the total potential energy of an atomic cluster as a function of the locations of the atoms) is actually a local property, thus requiring an exhaustive search.

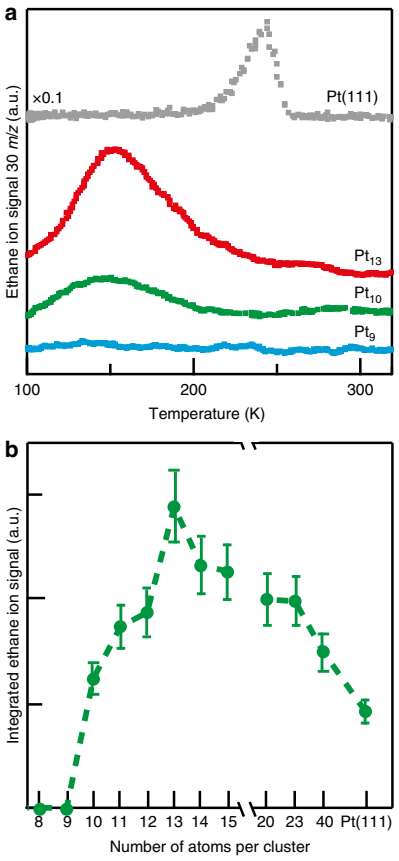

Figure 1 | TPR of ethylene hydrogenation on Pt_n clusters and Pt(111). (**a**) The measured ethane ion signals ($m/z=30$) for Pt_9, Pt_{10}, Pt_{13} and Pt(111) as a function of substrate temperature are shown. (**b**) The integrated signal from the curves in **a** as well as for cluster sizes up to Pt_{40} normalized to the number of Pt atoms, are displayed. The TPR experiments were performed by first dosing 0.4 H_2 molecules per MgO surface atom ($1\,cm^2 = 2.25\times10^{15}$ surface atoms) followed by 0.4 C_2H_4 ethylene molecules per MgO surface atom at 100 K followed by applying a temperature ramp of $2\,K\,s^{-1}$. The error bars represent a 16% error, which was determined from multiple measurements on a single cluster size.

Consequently, a large number of diverse methods for global structure optimizations have been proposed (see, for example, refs 22,24 and citations therein). Although significant progress has been achieved, proving that the global extremum has indeed been found seems to be a rather unattainable task for most systems of interest[22].

The optimal (lowest-energy) structures of the surface-supported Pt_9, Pt_{10} and Pt_{13} clusters determined through first-principles calculations (based on extensive searches, guided by cluster structural motifs gathered for other systems and by previously proposed search methodologies[24]) are displayed in Fig. 2 as well as in Supplementary Figs 7–15. It is evident that these clusters prefer a three-dimensional (3D) prismatic two-layer structure. In addition, we observe that these adsorbed clusters possess a large number of higher-energy isomeric structures (with the preferred ones having 3D geometries), reflecting the complex nature of their potential energy surface; see in particular the extensive rich spectra of structural isomers in Supplementary

Figs 7–13. Although we focus in the following on the lowest-energy clusters, it is possible that some higher-energy isomers are also present on the supporting surface.

It is pertinent to remark here that the optimal (minimum total energy) configurations, as well as those of the higher-energy isomers, were determined through unconstrained relaxation of the atomic positions in conjunction with density functional calculations of the total energy (see Methods for details). The bare clusters were positioned on the MgO(100) surface, and their configurations, together with the positions of the atoms of the underlying Mg(100) substrate, were optimized via unconstrained relaxations. Once the optimal cluster structures have been determined, the binding (adsorption) energies and atomic positions of the reactants (that is, the individual H_2 and C_2H_4 molecules, as well as multiply adsorbed, and co-adsorbed, systems) were determined through total energy minimization; similarly, in determination of the reaction path, the degrees of freedom of all atoms of the system (substrate, cluster and reactants) have been relaxed except for the very few describing the chosen reaction coordinate (for example, the distance, or combination of distances, between atoms of the reactants), which is varied in a stepwise manner (recording the total energy change along the change in the reaction coordinate yields the reaction energy profile and the activation barrier for the reaction (see Methods for details)).

The relaxation procedure described above allows for adsorbate/reactant-induced structural relaxations of the underlying metal cluster and metal-oxide (MgO(100)) substrate; this form of adsorbate-induced cluster-catalyst relaxation (Supplementary Fig. 16 where inter-isomer structural crossover is shown) is a manifestation of a more general class of cluster relaxation processes termed fluxionality[14,18], which includes also cluster relaxation in the course of a chemical reaction, named dynamical reaction-induced cluster fluxionality[18]. By considering systematically only relaxed configurations, the size-dependent fluxional propensity of clusters in the size regime studied here becomes one of the characteristics that determine the response of the clusters to the presence of reactants and intermediates (for example, ethylidyne) and the consequent size-dependent reactivities and the course of reactions catalysed by these clusters. Finally, in addition to being of physical significance in the description of the mechanisms of cluster-catalysed reactions, the inter-isomer structural conversion shown in Supplementary Fig. 16 illustrates the use of the dynamical reaction-induced cluster fluxionality as a method for uncovering structural isomers; in fact, it has been used by us to discover the ground-state structure of the metal cluster in Pt_{13}/MgO (see Fig. 2e,f and Supplementary Figs 11 and 16).

The spin state of the bare-adsorbed Pt clusters is $N_{\uparrow}$-$N_{\downarrow}=2$ (where N_s is the number of electrons with spin $s=\uparrow$ or $\downarrow$), and they are found, through total charge differences (calculated before and after adsorption and shown in Fig. 2a,c,e and Bader charge analysis (BCA, see Fig. 2b,d,f and Supplementary Figs 14 and 15)), to be negatively charged with the total excess Bader electronic charges on the adsorbed cluster being: $\delta\rho_B[Pt_n/MgO]=1.68$ e, 1.78 e and 1.92 e for $n=9$, 10 and 13, respectively. We find that whereas the total excess electronic charges on the $n=9$ and 10 clusters are quite similar, close to a

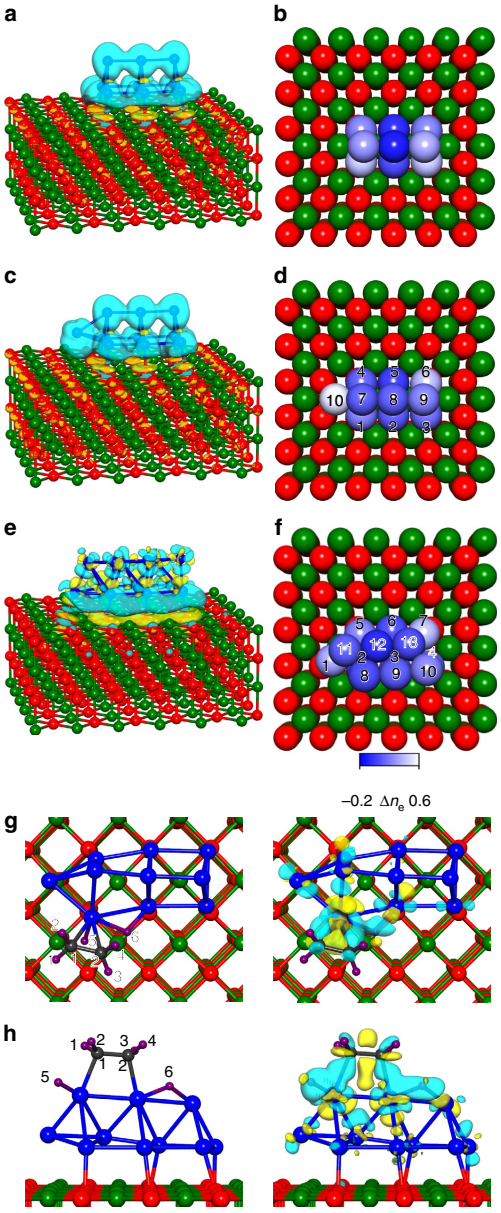

Figure 2 | Optimal configurations and charge distribution of bare Pt_n/MgO and co-adsorbed $C_2H_4+H_2$. **a**, **c** and **e**, corresponding to Pt_9, Pt_{10} and Pt_{13} clusters, the blue and yellow contour hyper-surfaces correspond to excess (light blue) and deficient (yellow) charge distributions obtained as the difference between the total charges before and after adsorption of the clusters; these hypersurfaces are drawn such that the excess electronic (negative) charge inside the light blue hypersurface is 50% of the total electronic charge and the same for the positive charge inside the yellow hypersurfaces. Bader charge analysis is given in **b**,**d** and **f**, with lighter colour corresponding to excess number of electrons (that is, excess negative charge on the corresponding atom); for the values of the Bader charges, see Supplementary Figs 14 and 15. Co-adsorption of C_2H_4 and H_2 on Pt_{10}/MgO is shown for the π (**g**) and di-σ (**h**) bonding modes. The adsorption geometries are shown on the left, and on the right, we depict the bonding frontier orbitals of the adsorption system (the light blue and yellow denote different signs of the wave function); the σ-type Pt-C bonds are clearly seen in **h** (note the directed wave function contours on the right). In both **g** and **h**, atoms 5 and 6 are the proximal dissociated co-adsorbed H atoms.

NATURE COMMUNICATIONS | DOI: 10.1038/ncomms10389 ARTICLE

third (0.51e) of $\delta\rho_B[Pt_{10}/MgO]$ is located for the Pt_{10} cluster on the capping atom (the 10th atom in Fig. 2d); similarly, a large contribution to $\delta\rho_B[Pt_{13}/MgO]$ is also found on the capping atom (the first atom (marked 1) of Pt_{13}, shown in Fig. 2f, which is found to have an excess local charge of 0.34 e out of a total of 1.92 e, with the atoms marked 7 having also a large excess charge of 0.36 (Supplementary Fig. 15). For the Pt_{10} cluster, this excess charge distribution leaves a smaller amount of excess charge (1.78 e − 0.51 e = 1.27 e) to be distributed over the remaining nine atoms of the Pt_{10} cluster in comparison with the total excess charge (1.68 e) available for distribution over the compact (no capping atom) Pt_9 triangular prism cluster. This smaller amount of negative excess charge on most of the atoms of the Pt_{10} cluster compared with the Pt_9 case, are found to influence binding sites, adsorption energies and consequent reaction pathways on the adsorbed clusters as well as demonstrating that, in this size-range, even the addition of a single atom, while not changing the basic geometric structure, can drastically alter the electronic properties of a cluster.

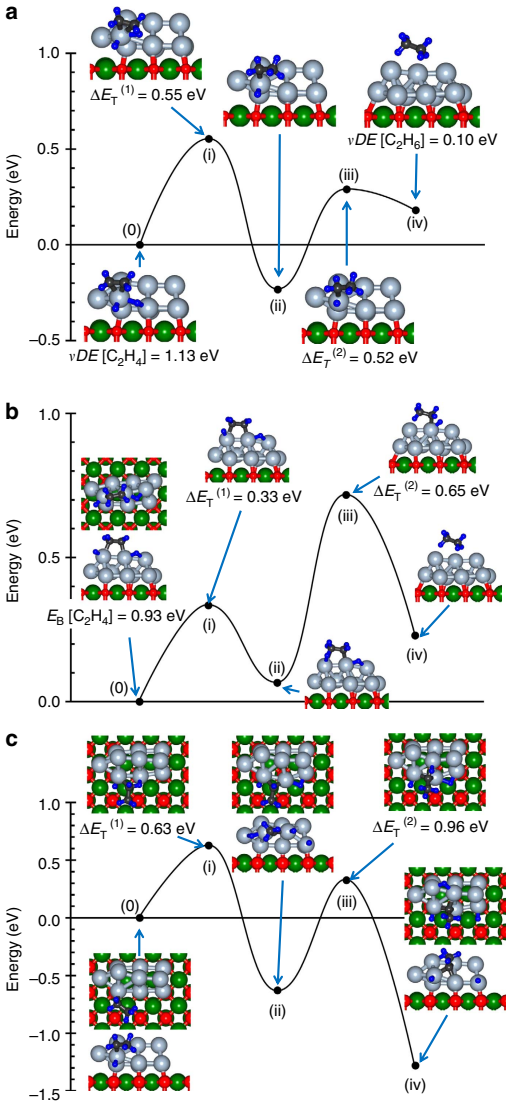

Figure 3 | Calculated first-principles steered reaction pathways catalysed by Pt_{10}/MgO. (**a**,**b**) Low-activation-barrier reaction pathways for the π (**a**) and di-σ (**b**) bonded ethylene (configuration on the left, marked 0), co-adsorbed with dissociated hydrogen. The activation energy barriers are denoted as $\Delta E_T^{(k)}$, k = 1,2. The reaction proceeds through the two successive hydrogenation steps described in the Horiuti-Polanyi mechanism. (**c**) SRP for the low-temperature generation of ethylidyne (≡CCH_3) on Pt_{10}/MgO, starting from the ethyl (-CH_2CH_3) intermediate (configuration (0), on the left) generated in the first step of the reaction for the π-bonded ethylene (depicted as configuration (ii) in **a**). The two activation barriers correspond to dehydrogenation processes, resulting in a strongly adsorbed ethylidyne molecule (≡CCH_3, configuration (iv)). Surmounting the barrier for the second dehydrogenation process is assisted by the highly exothermic (∼1.35 eV) formation of the -$CHCH_3$ intermediate (iii) resulting from the first dehydrogenation step.

Previous investigations (see review in ref. 7) identified two adsorption modes of ethylene on the (111) surface of platinum, the π and di-σ modes, where in the former the ethylene is thought to coordinate to a single Pt atom through a π bond, with the ethylene maintaining (at least to a large extent) sp^2 hybridization, and in the latter the adsorbed molecule is attached to two adjacent Pt atoms (in a η^2 manner) through two σ bonds showing a significant extent of sp^3 hybridization. On the extended Pt(111) surface, the π-bonded ethylene was found to be the preferred adsorption configuration only at very low temperatures, whereas for T = 100–240 K di-σ ethylene is preferred under ultra-high vacuum (UHV) conditions, with ethylidyne forming at higher temperatures. All the theoretical computational studies[25] corroborated the experimentally observed preference for di-σ over the π ethylene absorption mode, whereas the weakly adsorbed π-bonded species is experimentally believed to be the main reactant during hydrogenation of ethylene[9].

Contrary to extended surfaces, for the magnesia-supported Pt_n ($n \geq 9$) clusters, we find essentially the same propensity for adsorption in the π or di-σ mode, with the corresponding vertical desorption energies (VDEs) of the C_2H_4 molecules (co-adsorbed with a dissociated H_2 molecule in neighbouring sites) calculated to be VDE = 1.13 eV and 0.93 eV for the π and di-σ modes, respectively (see Figs 2g,h and 3a,b for details); note, in particular, the much higher value of the desorption energy for the π-bonded molecule compared with the corresponding calculated (0.87 eV (ref. 25) and measured (0.41 ± 0.10 eV (ref. 26) values on the Pt(111) surface. Furthermore, the π-bonded molecule (see Figs 2g and 3a for adsorption on Pt_{10}/MgO)) has a C–C bond length d(C–C) = 1.425 Å, which is close to the experimental value of 1.41 Å (ref. 27) this value is somewhat larger than d(C–C) = 1.334 Å value found in the isolated C_2H_4 molecule, indicating a certain degree of sp^3 rehybridization. In the di-σ adsorbed ethylene molecule, we find evidence for a larger degree of sp^3 hybridization, with d(C–C) = 1.469 Å, which is closer to the value found in the isolated C_2H_6 molecule (d(C–C) = 1.528 Å). Similar results were found by us for the two adsorption modes of ethylene on the supported Pt_{13} cluster (see the π-bonded adsorption configuration, marked 0, with VDE = 1.54 eV in Fig. 4a). The charge redistributions for both ethylene adsorption modes reflect the frontier orbital interactions leading to ethylene chemisorption, described by the Dewar–Chatt–Duncanson model[28,29] (see also Supplementary Note 2), involving electron donation from the highest occupied (π) ethylene orbital into an empty d orbital of the metal, and back-donation from the filled Pt d-orbitals into the ethylene lowest unoccupied (antibonding) π* orbital. The resulting electron charge isosurfaces (see right panels in Fig. 2g,h) portray the resulting redistribution of the electron density. Both the above bonding processes as well as the repulsive interactions

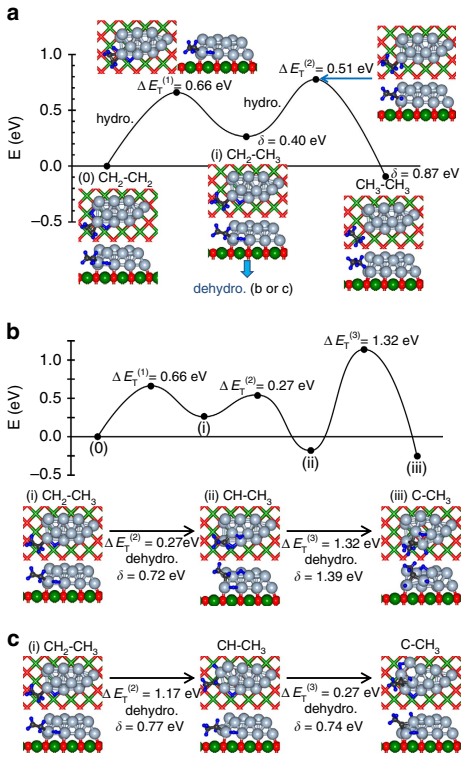

Figure 4 | Calculated first-principles steered reaction pathways catalysed by Pt_{13}/MgO. (**a**) Low-activation-barrier reaction pathway for hydrogenation of π-bonded ethylene configuration co-adsorbed with dissociated hydrogen on Pt_{13}/MgO. The reaction proceeds through the two successive hydrogenation steps described in the HP mechanism. The blue downward arrow near configuration (i) indicated the adsorbed ethyl intermediate (i) is the starting configuration for the **b** and **c** pathways. (**b**,**c**) Alternative reaction channels yielding ethylidyne (≡C-CH_3), starting from the π-bonded ethylene configuration co-adsorbed with dissociated hydrogen (marked (0) in **a**). The ethylene hydrogenation reaction producing ethane (see pathways in **a**) entails step (0)→(i), with $\Delta E_T{}^{(1)} = 0.66$ eV, followed by the activated second hydrogenation ($\Delta E_T{}^{(2)} = 0.51$ eV) that yields a weakly adsorbed C_2H_6 molecule. Two alternative dehydrogenation reaction channels that lead to formation of ethylidyne (starting from the ethyl, CH_2CH_3, intermediate, marked (i) in **a**, see blue downward arrow in **a**) are shown in **b** and **c**. The **b** and **c** pathways entail higher energy barriers (1.32 eV and 1.17 eV, in **b** and **c**, respectively) and thus their activation requires heating above room temperature, resulting in marked poisoning of the ethane-producing hydrogenation channel (see Fig. 5). The graph (profile) of the reaction path is shown only for channel **b**. The energy difference between the top of an activation barrier and the subsequent local minimum on the reaction pathway is given (in eV) by δ; this energy gives the height of the reverse reaction step, or it can assist (in part) passage over the subsequent energy barrier.

between the filled frontier orbitals of ethylene and occupied d-states of the metal catalyst particle (termed as Pauli[30,31] or four-electron repulsion[32]) depend on: (i) coordination of atoms making up the Pt particle, with reduced coordination, such as at edge and corner atoms, resulting in decreased repulsion, and (ii) occupation of metal d-states (with the Pauli repulsive interaction between filled orbitals of the metal cluster and the adsorbate increasing at cluster sites having larger excess electron charge); site-coordination and charging patterns can be ascertained from the calculated information given in Fig. 2a–f, and similar considerations apply also to the catalysed ethylene hydrogenation mechanism discussed below. In this context, it is pertinent to recall here our systematic study[33] of the effect of charging by cluster–substrate interactions on the adsorption and low-temperature combustion reaction of carbon monoxide and dioxygen, catalysed by MgO-supported gold clusters of sizes similar to those considered in the current investigation.

To gain insights into the microscopic ethylene hydrogenation mechanism, we carried out extensive first-principles steered reaction-pathway (SRP) simulations. For Pt_9, no low-activation-energy hydrogenation channel was found in the simulations (see Supplementary Figs 17–20 for details), in agreement with the TPR results (Fig. 1). On the other hand, multiple reaction pathways, characterized by relatively low activation barriers, were found in SRP simulations for the larger clusters, as illustrated in Figs 3 and 4 for Pt_{10} and Pt_{13}, respectively.

The simulated pathways starting from a π-bonded ethylene molecule co-adsorbed with a dissociated H_2 on the Pt_{10} and Pt_{13} clusters are shown in Figs 3a and 4a, respectively. For both cluster sizes, we observe two successive energy barriers (denoted as $\Delta E_T(i)$, $i = 1,2$) corresponding to the two hydrogenation steps of the HP mechanism, whose heights are sufficiently low to permit the experimentally observed low temperature reactivity, see Fig. 1 for details. In the first reaction step (marked (0)-(i) in Fig. 3a for Pt_{10}/MgO), one of the adsorbed hydrogen atoms approaches the nearest carbon atom (initially $d(C^{(1)}\text{–}H^{(1)}) = 2.432$ Å). The first activation barrier $\Delta E_T^{(1)} = 0.55$ eV, is characterized by $d(C^{(1)}\text{–}H^{(1)}) = 1.25$ Å and $d(C^{(1)}\text{–}C^{(2)}$; $\Delta E_T^{(1)}) = 1.487$ Å (compared with d(C–C) = 1.487 Å calculated for gaseous ethyl C_2H_5) portraying formation of an adsorbed ethyl-like top-of-the-barrier intermediate. In the local minimum (marked (ii)) that follows the first barrier $d(C^{(1)}\text{–}H^{(1)}) = 1.105$ Å, $d(C^{(1)}\text{–}C^{(2)}$; (ii)) = 1.529 Å, and the adsorbed ethyl intermediate is inclined with respect to the cluster ($d(C^{(1)}\text{–}Pt^{(1)})' = 3.065$ Å and $d(C^{(2)}\text{–}Pt^{(1)}) = 2.080$ Å). The closer value at the barrier-top of $d(C^{(1)}\text{–}C^{(2)}$; $\Delta E_T^{(1)})$ to $d(C^{(1)}\text{–}C^{(2)}$; (ii)) then to the initial state of the adsorbed ethylene, $d(C^{(1)}\text{–}C^{(2)}$;(0)) = 1.425 Å, qualifies $\Delta E_T^{(1)}$ as a 'late transition state barrier'. Full hydrogenation occurs in the second activation process—(ii) C_2H_5 → (iii) $\Delta E_T^{(2)} = 0.52$ eV → (iv) adsorbed C_2H_6 with VDE = 0.1 eV—resulting in the product ethane molecule. The pathways of the hydrogenation reaction of the di-σ-adsorbed ethylene molecule (shown for Pt_{10}/MgO in Fig. 3b) resemble the one described above, with the first activation barrier being lower (0.33 eV); for geometric details of the reaction pathways, see Supplementary Figs 21–27. Similar results were found in our SRP simulations for the Pt_{13}/MgO cluster (see Fig. 4a for the π-bonded ethylene molecule); for details, see Supplementary Figs 28–36).

The principal result of our analysis to this point is the discovery and explanation of the onset of low-temperature ethylene hydrogenation processes (peaking at temperatures of ~150 K) on magnesia-supported 3D Pt_n clusters for $n \geq 10$, with the calculated activation barriers for *both* the π and di-σ C_2H_4 adsorption modes on the Pt cluster catalysts being significantly smaller than those obtained for the Pt(111) surface; compared with values calculated for the lowest coverage (1/9) on Pt(111)[25]. This reflects significant enhancement of the hydrogenation reaction, achieved through the use of supported platinum clusters of <1 nm diameter (on the order of 10–15 Pt atoms); note, however, the absence of catalytic activity of 3D Pt_n clusters with $n \leq 9$. The measured larger hydrogenation reactivity of the Pt_{13} cluster correlates with the calculated larger number of active sites on this cluster for both H_2 dissociative adsorption (see Supplementary Fig. 1 and Methods for details), and low-barrier hydrogenation of co-adsorbed ethylene and hydrogen.

In addition to the low-activation-energy pathways found on the Pt_n/MgO ($n \geq 10$), we have found on these clusters (particularly on the larger cluster, Pt_{13}/MgO) several reaction sites characterized by higher ethylene-hydrogenation activation energy barriers; typically, $\Delta E_T > 0.8$–1.0 eV (see Supplementary Figs 21–36 for details). Most significantly, along with the low-temperature hydrogenation pathways (Fig. 3a,b) we found for the Pt_{10}/MgO catalyst a relativelyc low-barrier dehydrogenation reaction channel resulting in the formation of ethylidyne (Fig. 3c), whereas for the larger Pt_{13}/MgO cluster we found multiple high-energy ethylidyne formation pathways; see Fig. 4c,d manifesting energy-barriers of $\Delta E_T \sim 1.2$–1.3 eV. This finding implies for Pt_{13} an onset of significant ethylidyne formation upon heating to higher temperatures ($T \sim 350$–400 K), which acts as a blocking, or poisonous, agent for ethylene hydrogenation; for the Pt_{10} clusters such alternative reaction channels are open already at 300 K, see, for example, Fig. 3c.

Isothermal multi-catalytic-cycle experiments. The pulsed molecular beam technique was applied to determine TOFs under quasi-steady-state isothermal conditions (see Methods for experimental details). This method allows probing and verification, under actual catalytic conditions, of the trends deduced from the TPR experiments, as well as confirmation of the predictions obtained from first-principles calculations regarding ethylidyne formation (see above). At these elevated temperatures, processes such as cluster sintering become more probable, but our data did not show any indication that this was occurring during the time scale of our experiments and studies performed on size-selected clusters also cast strong doubt that sintering occurs already at 400 K, see Methods for further discussion.

The measured ethane TOFs at 300 K displayed in Fig. 5a (blue) show that at this temperature Pt_n clusters with $n < 10$ are active, as expected from the calculated activation energies on Pt_9. Furthermore, at this temperature, the distinct onset of reactivity for n>9 observed in the TPR, one-catalytic-cycle, experiments (see Fig. 1 for details) is not operative, and reactivity variations are observed only in a narrow size window for Pt_{11}–Pt_{14}, with a pronounced maximum activity for Pt_{13}. This demonstrates the emergence of a size window where the reaction is *size* (structure) sensitive, in contrast with the size (structure) insensitivity observed for other cluster sizes, nanoparticles and single-crystal surfaces[9,34–36]. This serves to illustrate that clusters (of the same chemical identity but different sizes) can exhibit both structure sensitivity and insensitivity and that a single atom can change this designation.

To investigate the influence on the hydrogenation of ethylene brought about by surface species generated by alternative reactions, for example, the aforementioned ethylidyne production channel, we have repeated the measurement of the TOF at 300 K, but this time after the clusters were exposed to 10 pulses of ethylene at 400 K in the presence of deuterium (Fig. 5a, red curve). The absolute change of the TOF for the sizes measured in Fig. 5a, depicted in Fig. 5b, clearly shows that Pt_{13}, as well as the other clusters within the enhanced reactivity size window shown in Fig. 5a, deactivate as a result of the 400 K heating step, whereas the other sizes show no significant change in activity. After the 400 K step, all cluster sizes show TOFs similar to the one measured on Pt(111), that is, the reaction has turned size insensitive. This observation is consistent with the results of the calculations (Figs 3c and 4c,d), where the activation barrier for the dehydrogenation pathway to the (hydrogenation blocking) ethylidyne species was found to be thermally accessible already at temperatures as low as $T < 300$ K for Pt_n ($n \leq 10$), whereas for Pt_{13} ethylidyne production was predicted to require heating to $T > 350$ K. Consequently, the size-insensitive clusters, as well as Pt(111), are all passivated already at 300 K, and only with a temperature increase do the more active sizes follow. To optimize reactivity for the hydrogenation of ethylene, it is thus not only essential to choose the right size window between Pt_{11} and Pt_{14}, but also the right temperature window $160\,K \leq T \leq 350$ K, where the hydrogenation of ethylene is thermally accessible but not the formation of poisoning species. This size-dependent behaviour of two competing reaction channels offers the potential for controlling and tuning more applied hydrogenation and dehydrogenation reactions on an atom-by-atom basis.

Further evidence for the formation of inhibiting carbon species has been obtained through the use of CO adsorption and infrared reflection absorption spectroscopy to probe the cluster catalysts before and after the reaction, as co-adsorption of carbonaceous species on platinum is known to induce a redshift in the CO stretch frequency because of electron donation to the metal[37–40]. The attribution of the redshifts reported here to carbon was strengthened by the fact that after the TPR experiment in Fig. 1a, no deuterium adsorption was observed on Pt_9, Pt_{10} and Pt_{13} indicating a blocking effect of an adsorbate on the clusters. The only plausible explanation would be a dehydrogenated product from ethylene. Although a change in cluster shape could also possibly induce such a small redshift, the inability of this hypothesis to reconcile the TPD and infrared data led to the assignment of co-adsorbed carbonaceous species as the origin of the redshift.

After running the reaction under conditions of highest activity (300 K), ten Langmuir of CO were adsorbed at 100 K and an infrared spectrum recorded (Fig. 5c, blue curves). The CO stretch is red-shifted by 13 cm^{-1} compared with spectra measured from pure metallic sites on all cluster sizes (see the shifted spectra in Fig. 5c and Fig. 5d for both the shifted and unshifted values, respectively). Importantly, the cluster of highest reactivity, Pt_{13}, also exhibits a shoulder (marked with an arrow in Fig. 5c) where the CO stretch on a clean cluster is found. In comparison, the Pt(111) crystal shows a much larger redshift (83 cm^{-1}, compare the frequencies given by the triangle and filled blue dot on the right in Fig. 5d), which is attributed to adsorbed ethylidyne[26,41,42]. Performing the same experiment after the 400 K heating steps brings about an even larger redshift of the CO stretch (34 cm^{-1}, compare the red and blue curves in the spectra displayed in Fig. 5c, and summarized in Fig. 5d), indicating a larger influence of inhibiting dehydrogenation products as well as complete site blocking on Pt_9. On Pt(111), the absorption peak decreases slightly in intensity but remains at the same position, which correlates to the expected stability of ethylidyne up to 400 K (ref. 43).

The finding that a CO stretch peak position comparable to that measured for CO on a clean (bare) cluster is found after reaction at 300 K only for the most active size, Pt_{13}, reflects the intrinsic resistance of ethylene on Pt_{13} to follow the dehydrogenation pathways leading to ethylidyne formation, as predicted by our theoretical results. The formation of more carbonaceous species on Pt_{13} (portrayed by a larger redshift after pulsing at 400 K) induces the subsequent structure insensitivity, previously established for other cluster sizes, nanoparticles and single crystals.

This combined pulsed molecular beam and infrared reflection absorption spectroscopy study demonstrates for the first time that the formation of carbon species is indeed the key factor underlying structure insensitivity of ethylene hydrogenation on larger particles and extended surfaces of platinum.

Discussion

The investigations discussed in this paper demonstrate that classification of a reaction as structure sensitive, or insensitive,

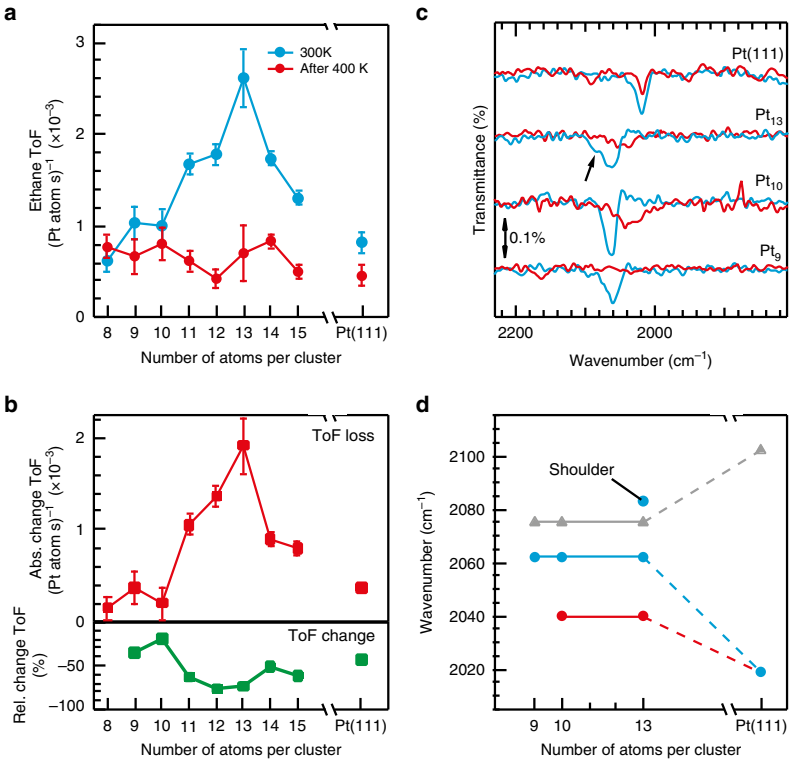

Figure 5 | Pulsed molecular beam of $C_2H_4 + H_2$ reacting on Pt_n/MgO along with infrared spectra. (**a**) Measured TOF at 300 K of the ethylene hydrogenation on Pt_{8-15} clusters and Pt(111) single-crystal surface, before (blue) and after (red) running the identical reaction at 400 K. The measured TOF has been normalized to the number of platinum atoms for Pt_{8-15} and the Pt(111) surface. A background deuterium pressure of 2×10^{-6} mbar was used for all experiments. (**b**) Decrease of the turnover frequency between the blue and red measurements as well as this value represented as a percent loss. (**c**) Infrared reflection absorption spectra of 10 L CO after the experiments in **a** measured at 100 K. Blue spectra were taken after pulsing at 300 K and red after the clusters had been exposed to the same reaction conditions at 400 K and again at 300 K. (**d**) Position of the CO stretch on clean cluster samples (grey data points) as well as after the blue and red data points were acquired. The error bars represent the standard deviation of multiple activity measurements on the same cluster size.

must be reassessed for materials with sizes in the non-scalable sub-nanometre size regime. This size range has been shown to exhibit surface chemical properties, which can be modulated by a single atom, and where each particle size displays its own mode of behaviour. The previously reported structure insensitivity of ethylene hydrogenation on Pt is shown here to be untenable in the cluster size range of Pt_7–Pt_{40}, where we find structure sensitivity of ethylene hydrogenation to emerge, with maximum reactivity for Pt_{13}. Structure-insensitive behaviour was observed to be inherent for specific cluster sizes at ambient temperatures and can be induced in the more active sizes (for example, Pt_{13}) by an increase in reaction temperature, which opens dehydrogenation reaction channels leading to the formation of carbonaceous species evidenced in the infrared spectra and predicted by first-principles calculations. Aside from addressing the applicability, at this size range, of common catalyst classification as structure sensitive or insensitive, our findings point to the possibility of controlling the activity and selectivity of hydrogenation and dehydrogenation reactions catalysed by clusters of these sizes. We remark that rather than treating an industrial hydrogenation catalyst under industrial conditions, we focus here, with the use of model catalysts of nanoscale dimensions, on a basic science question of great interest in the field of heterogeneous catalysis pertaining to the concept of structure sensitivity/insensitivity at the bottom of the catalyst size scale. For the catalyst cluster sizes considered here, the reaction is investigated in a temperature range lying mostly below, and up to, room temperature (with certain thermal treatment involving temporal heating to 400 K), which is lower than the temperatures used in typical industrial catalytic hydrogenation applications; the finding that nanocluster catalysts (particularly made of noble metals) catalyse reactions at temperatures significantly lower than larger clusters and extended surfaces made of these metals is rather common now (see, for example, refs 13,14,19,20,44,45). Correspondingly, the temperature-window selectivity and thermal-tuning that we discuss and demonstrate are operative, and are kinetically relevant, for these nanocatalysts under the above-specified temperature conditions. This also suggests that in conjunction with future employment of nanocatalysts in industrial-type processes, the concept of temperature selectivity/tuning windows, discussed in this work from a basic science perspective, may emerge also as one of practical relevance.

In the non-scalable size regime, the above findings make element-specific generalizations of catalytic properties, based on single crystals and nanoparticles, rather questionable. The first-principles simulations show that even similar atomic geometric arrangements can lead to widely differing physical and chemical properties. Consequently, each reaction must be individually

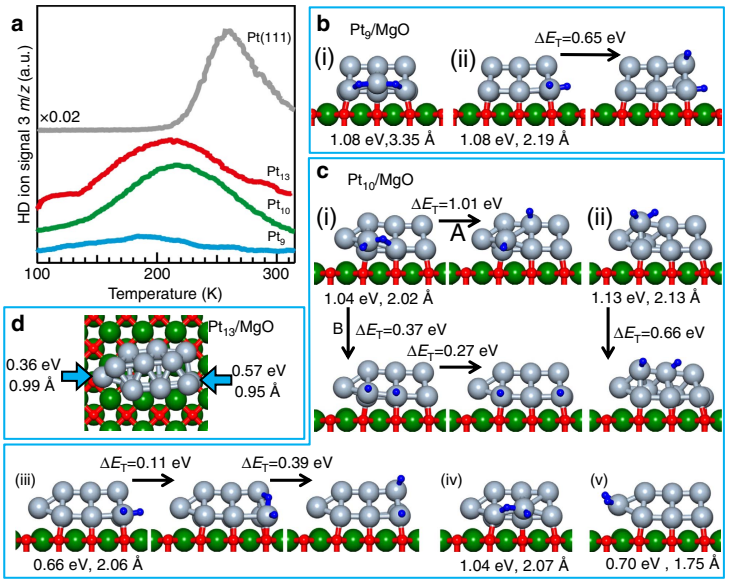

Figure 6 | Hydrogen adsorption on supported platinum clusters. (**a**) TPR measurements of the H/D exchange on Pt_n/MgO, $n = 9$, 10, 13 and on Pt(111). (**b**,**c**) Calculated hydrogen dissociative adsorption at various sites, and diffusion on Pt_9/MgO and Pt_{10}/MgO, respectively. The pair of values under an adsorption configuration give the H_2 adsorption energy and distance between the dissociated H atoms. ΔE_T denotes the activation barrier for diffusion between the corresponding H-atom configurations on the Pt cluster. (**d**) On Pt_{13}/MgO, H_2 dissociates at all sites except the ones marked by an arrow. Spheres colored green denote magnesium atoms, oxygen atoms are colored red, platinum atoms are coloured red, Pt atoms in grey, and hydrogen atoms are depicted by small blue spheres. The cluster configurations correspond to the lowest energy cluster-adsorption configuration on MgO(100).

tested in an atom-by-atom, size-selective, manner, in order to disentangle and reveal the catalytic properties of such systems. The use of structure (in)sensitivity has been a most useful concept for the description and systematization of catalytic processes on single crystals and particles possessing well-defined single-crystal facets. However, with decreasing particle sizes (that is, for higher dispersion), and in particular in the sub-nanometre size regime, extrapolations from systems of larger size are likely to become inadequate, requiring instead an atom-by-atom reassessment.

In closing, the results that we reported here demonstrate that hydrogenation and dehydrogenation reactions can be controlled and tuned by controlling the precise atomic size of the catalyst particle. This has implications for a broad range of chemical processes[46] ranging from chemical synthesis, to food chemistry, and energy applications, where the insight garnered here, as well as future investigations along these lines, could facilitate a deeper understanding of applied reaction systems, and may offer design strategies for catalysts with enhanced activity and/or selectivity.

Methods

Sample preparation and characterization. All experiments were perform in an ultra-high vacuum (UHV) chamber with a base pressure of 1×10^{-10} mbar[47]. The Mo(100) (MaTeck, Germany, 0.785 cm^2) single crystal was cleaned by heating to 2,000 K and subsequent oxidation at 900 K in a 5×10^{-7} mbar O_2 background (5.5 purity, Air Liquide Germany). The purity of the crystal was checked with Auger electron spectroscopy (AES) and ultraviolet photoelectron spectroscopy (UPS)[48]. The MgO(100) film was then grown at 600 K on the Mo(100) single crystal by evaporating a magnesium ($\geq$99.95%, Merck Germany) ribbon in front of the crystal in a 5×10^{-7} mbar background of O_2. After annealing the film at 800 K for $t > 10$ min, the film was characterized with AES and is estimated to have a thickness of ten atomic layers, the purity was further confirmed with AES, UPS and MIES.

The presence of surface defects has also been investigated and the films have been determined to be defect poor and exhibit a high degree of order. Oxygen vacancies (F-centres) have been shown to be detectable via MIES as a clear band beginning at a binding energy (BE) of 1 eV and peaking at 2 eV (refs 20,49). The MIES spectrum in Supplementary Fig. 2 shows this region from the MgO film prepared as described above. No characteristic emission peak below 4 eV is observed, clearly showing the absence of F-centre type defects or other under-coordinated electron-trapping sites.

Surface roughness can also play a factor in thin films and can also influence catalytic activity. Previous surface characterization of thin MgO films concluded that above 7 ML thin film thickness, global surface roughness decreases and (1×1) low energy electron diffraction (LEED) spots are visible[50]. As the films grown here are thicker than 7 ML and we have previously published this same LEED pattern from our film growth procedure[21], the films grown for this study possess low surface roughness.

This same property has also been characterized with the use of MIES, where a narrowing of the O2p band indicates surface ordering[51]. Their spectrum showed a full-width half-maximum O2p peak of 3.2 eV for a disordered film and 2.5 eV for an ordered film. The MIES spectrum in Supplementary Fig. 3 (complete spectrum of Supplementary Fig. 2) shows the full-width half-maximum of the O2p peak (BE = 5.5 eV) to be 2.13 eV for the films grown for this study. Again, this is further evidence that the MgO film is highly ordered.

Grain boundaries and islands can be directly detected using a CO TPD. The CO TPD from the thin film used in this study is displayed in Supplementary Fig. 4. The sample was dosed at 100K with 1 CO molecule per MgO surface atom, and a temperature ramp of 2 K/s was applied (see below for technical details regarding the TPD experiment). The spectrum shows only a single, narrow desorption peak at 105 K, which is concordant with a defect poor film. The absence of island formation and the absence of exposed Mo domains in our films was confirmed by the nonappearance of a characteristic desorption peak at about 290 K in our CO TPD measurement (see ref. 52).

In conclusion, the above data clearly show that our films are defect poor, in that they do not exhibit the established spectral and chemical properties expected from F-centres (or other under-coordinated electron trapping sites), rough/disordered films, island-like films and grain boundaries/corners/steps and so on.

The Pt(111) (MaTeck) single crystal was cleaned by cycles of argon ion sputtering at 900 K, followed by oxidation for 5 min at 650 K in a 5×10^{-7} O_2 background pressure and annealing at 1,300 K for 1 min. The purity was checked with AES, UPS and MIES.

The clusters were generated using a laser evaporation source; a detailed description can be found elsewhere[47]. In brief, the second harmonic of a Nd:YAG laser (InnoLas DPSS, 532 nm, 100 Hz) is focused onto a rotating platinum target (99.95% purity, Alfa-Aesar), with each pulse being thermalized and extracted into the vacuum with a delayed pulse of helium gas (6.0 purity, Westfalen). Electrostatic lenses guide the clusters to a bender where the positively charged species are guided into a quadrupole mass spectrometer (QMS; Extrel, 16,000 a.m.u.). The

cluster beam is then size selected and a single cluster size is deposited onto the MgO(100)/Mo(100) substrate. Retarding field analyses ensure that the clusters have a kinetic energy of no more than 1 eV per atom for soft-landing conditions. The clusters are neutralized by electron tunnelling through the MgO film and the resulting current is recorded and integrated in order to calculate a cluster coverage. It is assumed that each cluster has unit charge. All TPR curves shown were performed on 9×10^{12} clusters. The majority of the pulsed valve experiments were also performed with this coverage and extrapolating data measured on lower coverages to 9×10^{12} did not produce any significant variations in the TOF.

Cluster stability. Cluster stability at the relevant temperatures was ensured using a variety of techniques. For platinum clusters of various sizes, we have done repeated, consecutive, HD exchange or deuterium TPD experiments up to ~320–350 K and observe no change in the desorption peak temperature or area. From this observation, it was concluded that the TPD results (Fig. 1 in the manuscript) indeed reflect true size effects. In addition, the pulse-to-pulse variations, seen in Supplementary Fig. 6B at 300 and 400 K for Pt_9 and Pt_{10} (Supplementary Fig. 5), also reflect the stability of the clusters (against sintering, coalescence or fragmentation) under the reaction conditions of the isothermal (multi-cycle) experiments presented in this work. Any appreciable degree of sintering would be coupled with a very clear change in activity in both cases, which was not observed for the cluster sizes determined as being structure insensitive in a TPR run or at isothermal conditions.

Size-selected clusters have also been extracted from the experimental setup for stability studies on a silica support using nanoplasmonic sensing and transmission electron microscopy[53]. It was shown that after 21 h at 453 K, no sintering of size-selected samples (Pt_{22} and Pt_{68}) is observed. In addition, Pt_{68} resists sintering at 533 K during the hydrogen oxidation reaction. STM results from size-selected Pd clusters show that on relatively strongly, supported binding boronitride film surfaces, annealing to 500 K for 5 min does not change the cluster size distribution (height histogram)[54]. The underlying principle of this stability is on the one hand the suppression of the Ostwald ripening through the relatively weak interaction of the transporting species (Pt-atoms) with the oxide support[54] and the monodispersity of the cluster samples with the lack of the driving force for Ostwald ripening[53]. In fact, in these experiments, Ostwald ripening is only observed when reaching the Hüttig temperature of the cluster material, which for platinum is ~650 K. The observed absence of Smoluchowski ripening can be understood when considering the relative large binding energies of the clusters with the support material. A reliable estimate of the energy that anchors the cluster to the underlying MgO(100) supporting surface is given by the calculated vertical BE (vBE), given as

$$E_{\mathrm{vBE}}^{(n)} = E[\mathrm{Pt}_n]_{\mathrm{Pt}n/\mathrm{MgO}} + E[\mathrm{MgO}]_{\mathrm{Pt}n/\mathrm{MgO}} - E[\mathrm{Pt}_n/\mathrm{MgO}], \qquad (1)$$

where $E[\mathrm{Pt}_n/\mathrm{MgO}]$ is the total energy of the structurally relaxed (energy optimized) ground state (lowest energy isomer) of the Pt_n cluster adsorbed on the MgO surface, and $E[\mathrm{X}]_{\times/\mathrm{MgO}}$ is the total energy of the isolated component (X = Pt_n or MgO) of the combined adsorption system, each calculated in the geometry that it assumes in the relaxed (optimized) configuration. The calculated values for $E_{\mathrm{vBE}}^{(n)}$ for the three cluster sizes considered in this work, $n = 9$, 10 and 13, are: $E_{\mathrm{vBE}}{}^{(n)} = 6.96$, 7.65 and 9.09 eV, respectively. These values reflect strong bonding of the clusters to the MgO(100) surface, inhibiting Smoluchowski ripening processes.

TPR and H/D exchange experiments. The temperature programmed reaction (TPR) experiments were performed by dosing 0.4 H_2 (5.0 purity, Air Liquide) molecules per MgO surface atom ($1\,\mathrm{cm}^2 = 2.25 \times 10^{15}$ surface atoms) followed by 0.4 C_2H_4 (3.5 purity, Westfalen) ethylene molecules per MgO surface atom, using a calibrated molecular beam doser at a crystal temperature of 100 K. The crystal was then positioned ~5 mm away from a skimmer leading to a differentially pumped QMS (Balzers QMA 430, Liechtenstein) chamber. A temperature ramp was then applied (Eurotherm 2408) and the ion signal of 30 m/z (ethane parent peak) was recorded.

Before executing the TPR measurements displayed in Fig. 1, we performed measurements and theoretical calculations pertaining to a key step of the HP ethylene hydrogenation mechanism, namely the dissociative adsorption of H_2. To this end, we utilize isotopic H/D exchange (scrambling) TPR measurements. These HD-exchange experiments were performed in the same manner as described above for the other TPR measurements, except that a gas mixture of H_2 and D_2 (100.00%, Westfalen) was used where each partial pressure equaled 0.4 molecules per surface atom. A mass of 3 m/z was measured for these experiments. H/D exchange spectra have been recorded for a range of cluster sizes and the results for Pt_9, Pt_{10} and Pt_{13} are displayed in Fig. 6a showing a limited activity for the Pt_9 cluster compared with that of the larger clusters (peaking at $T \sim 200$ K), along with the measured record for the Pt(111) surface that shows onset of H/D exchange at a higher temperature and a peak centred at 260 K.

Hydrogen molecules are predicted from our DFT calculations to dissociatively adsorb on all Pt atoms of the bottom layer of Pt_9 (Fig. 6b), but do not bind to top layer atoms of the cluster; the only way that an H atom may adsorb on the top layer is by diffusing (with an activation energy of 0.65 eV) from a bottom atom after dissociation, see Fig. 6b(ii) for details). The limited adsorption and dissociation of hydrogen on the Pt_9 cluster correlate with the measured H/D exchange (Fig. 6a). On the other hand, dissociative H_2 adsorption occurs readily at all sites of the bottom layer of the supported Pt_{10} and Pt_{13} clusters, with diffusion of the dissociated adsorbed hydrogen atoms between bottom layer sites entailing small barriers of the order of 0.1–0.3 eV, and interlayer diffusion requiring barriers that are as low as 0.40 eV. Unlike the case of the smallest cluster (Pt_9), H_2 dissociatively adsorbs on one of the second layer atoms of the Pt_{10} clusters (see Fig. 6c(ii), diffusing to a neighbouring upper layer atom with an activation energy of 0.66 eV), and the Pt_{13} cluster dissociatively adsorbs H_2 at all sites (except one, see right arrow, Fig. 6d and Supplementary Fig. 1). The abundant sites for dissociative adsorption on both the bottom and top layers of the Pt_{10} and Pt_{13} clusters and the facile inter-site H-diffusion on these clusters correlate with the measured low-temperature H/D exchange signal (Fig. 6a).

The pulsed molecular beam technique. The pulsed molecular beams technique used in our laboratory has been previously described[55], and a brief overview will be given here. A piezo pulser, which allows for highly reproducible gas pulses, was filled with a 2-Torr background pressure of ethylene. From the time-resolved QMS response to a single ethylene pulse, it was determined that there are $\sim 10^{14}$ gas molecules per pulse giving a local pressure of $\sim 5 \times 10^{-7}$ mbar. A deuterium background pressure of 2×10^{-6} mbar was established with a leak valve and the temperature of the crystal was increased to 300 K. The crystal was again placed ~5 mm in front of the skimmer (same QMS as for the TPD experiments) and ethylene was pulsed onto the surface at a rate of 0.1 Hz. The ethane production was measured by monitoring the mass signal at 31 m/z with an oscilloscope (LeCroy Wave-runner 44Xi-A). Within the signal wave, we define a quasi-steady-state regime, where the ethane production maintains a constant value over the course of 80 ms. Approximately 20 pulses are then recorded and the quasi-steady-state signal is averaged and used to calculate the TOF. Supplementary Fig. 6A shows a representative average of pulses for Pt_{11}. A region displaying steady-state ethane production (in grey) is then defined and the TOF calculated from this signal. Supplementary Fig. 6B shows the pulse to pulse signal for the same experiment displayed in Supplementary Fig. 6A. The calibration of the mass spectrometer was performed by determining the QMS signal of a saturated monolayer of CO on Pt(111) using the TPD technique and then determining the sensitivity factor between ethane and CO. It should be noted that although we measure ethane at $m/z = 31$, the factor between the signal from equal amounts of pure ethane ($m/z = 30$) and deuterated ethane, measured on the peak $m/z = 31$, is roughly[56] 2. As this error is systematic, no influence on the trend observed, or even the order of magnitude of the signal, occurs.

Infrared reflection absorption spectroscopy. (Thermo Electron Corp. Nicolet FT-6700) was performed in single reflection mode with an external MCT-detector (Thermo Electron Corp., MCTA-TRS). At the experimental steps, a background spectrum was acquired by averaging 256 scans at a resolution of $4\,\mathrm{cm}^{-1}$ with the sample at ~100 K. Ten Langmuir of CO were dosed and a sample spectra recorded with the same parameters as the background.

First-principles computational methodology. To model the Pt_n/MgO systems, with $n = 8$, 9, 10, 13, we employed a four-layer MgO(100) slab with a calculational cell consisting of 7×6 unit cells; each layer consisted of 42 Mg and 42 oxygen atoms with the atoms in the bottom layer held stationary (at the experimental lattice constant of 4.21 Å) and the atoms in the other three layers allowed to relax to the optimal atomic arrangement. The experiments in this paper were performed for MgO films with thickness of ten layers or more. Under these conditions, there is no effect of the underlying Mo(100) substrate on the behaviour at the top of the film. Indeed, the effect of the Mo substrate has been predicted early on theoretically[57] to be limited to MgO films with a thickness of four to five layers; see also predicted thickness-dependent reactivities, where the catalytic activity of deposited metal clusters was predicted to depend on the thickness of the underlying metal-oxide film adsorbed on a metal substrate[58,59]. This has been verified experimentally in later reactivity studies of gold nanoclusters supported on MgO films of variable thicknesses[20] and most convincingly through work function measurements[60]. The above-mentioned prediction and experimental verifications justify the procedure used in our calculations, where no effect of the underlying Mo substrate on the charging behaviour at the MgO/Pt nanocluster interface is considered.

The optimal (minimum total energy) configurations were determined (through unconstrained relaxation of the atomic positions, using a conjugate gradient search) when the calculated energy converged within 0.001 eV. The bare clusters were positioned on the MgO(100) surface, and their configuration, together with the positions of the atoms of the underlying substrate, was optimized via unconstrained relaxations as described above. The calculational supercell, which included the MgO(100) slab and a 24-Å-thick vacuum region, was periodically replicated. Once the optimal cluster structures have been determined the binding (adsorption) energies and atomic positions of the reactants (that is, the individual H_2 and C_2H_4 molecules, as well as multiply adsorbed, and co-adsorbed, systems) were determined through total energy minimization. This relaxation procedure allows for adsorbate/reactant-induced structural relaxations of the underlying metal cluster and metal-oxide (MgO(100) substrate; this form of adsorbate-induced

cluster-catalyst relaxation (illustrated in Supplementary Fig. 16) is a manifestation of a more general class of cluster relaxation processes termed fluxionality[18], which includes also dynamical reaction-induced cluster fluxionality.

In the first-principles calculations of the reaction profiles (pathways), a reaction coordinate was judiciously chosen; typically, the reaction coordinate consists of the distance between two atoms of the reactant molecules (for example, an adsorbed H atom of a dissociated hydrogen molecule and the C atom of a reacting ethylene molecule); the reaction coordinate can in general be a combination of geometrical parameters (interatomic distances and/or angles). For each value of the reaction coordinate, the total energy of the system, calculated with density functional theory (DFT) was optimized through unconstrained relaxation of all of the other degrees of freedom of the system (reactants, other adsorbents, Pt cluster atoms and MgO slab atoms atoms). The reaction profiles (reaction paths) were obtained via repeating such calculations for a sequence of values of the chosen reaction coordinate. These calculations yield results that are the same as, or very close to, those obtained by other methods, for example, the nudged elastic band and variants thereof; see the ref. 13.

It is pertinent to note here that the structural relaxation following reactant adsorption and subsequent to each reaction step (using a conjugate gradient method) allows for distortions of the combined system (underlying support surface, adsorbed cluster and reactants) and leads to certain adsorption and reaction—induced structural rearrangements; for example, in some cases it can bring about transformation of the cluster geometry to a different structural isomeric form, as in the aforementioned example of dynamical reaction-induced cluster fluxionality (Supplementary Fig. 16). Global modifications of the structural motif of the adsorbed cluster/adsorbate system involve prohibitive activation energy barriers and are unlikely to occur as these transformations would be kinetically non-viable, particularly for the adsorption and reaction conditions considered in our studies that involve relatively low temperatures, ranging from below room temperature up to 400 K. Consequently, for kinetic reasons, it appears that relaxations involving local minima of the free-energy landscape of the combined catalytic system (rather than the global ones) are more effective here in steering the reaction pathway and determining the catalysed reaction barriers.

All the aforementioned first-principles electronic structure calculations employed the DFT method as implemented in the VASP-DFT package, using a plane-wave basis with a kinetic energy cutoff of 400 eV, projector augmented wave (PAW) pseudopotentials[61] and the Perdew, Burke & Ernzerhof (PBE) generalized gradient approximation for the exchange-correlation potential[62–66]. Γ- point sampling of the Brillouin zone was used.

References

1. Boudart, M. in *Advances in Catalysis* Vol. 20 (eds Herman, P., Weisz, P. B. & Eley, D. D.) 153–166 (Academic, 1969).
2. Boudart, M., Aldag, A., Benson, J. E., Dougharty, N. A. & Girvin Harkins, C. On the specific activity of platinum catalysts. *J. Catal.* **6,** 92–99 (1966).
3. Boudart, M., Aldag, A. W., Ptak, L. D. & Benson, J. E. On the selectivity of platinum catalysts. *J. Catal.* **11,** 35–45 (1968).
4. Bond, G. C. The origins of particle size effects in heterogeneous catalysis. *Surf. Sci* **156** Part 2 966–981 (1985).
5. Bond, G. C. Supported metal catalysts: some unsolved problems. *Chem. Soc. Rev.* **20,** 441–475 CS9912000441 (1991).
6. Che, M. & Bennett, C. O. in *Advances in Catalysis* Vol. 36 (eds Herman, P., Weisz, P. B. & Eley, D. D.) 55–172 (Academic, 1989).
7. Somorjai, G. A. & McCrea, K. Roadmap for catalysis science in the 21st century: a personal view of building the future on past and present accomplishments. *Appl. Catal. A* **222,** 3–18 (2001).
8. Boudart, M. & Djéga-Mariadassou, G. *Kinetics Of Heterogeneous Catalytic Reactions* (Princeton Univ., 1984).
9. Cremer, P. S., Su, X., Shen, Y. R. & Somorjai, G. A. Ethylene hydrogenation on Pt(111) monitored *in situ* at high pressures using sum frequency generation. *J. Am. Chem. Soc.* **118,** 2942–2949 (1996).
10. Horiuti, J. & Polanyi, M. Mechanism of the ethylene hydrogenation. *Trans. Faraday Soc* **30,** 1164–1172 (1934).
11. Boudart, M. Heterogeneous catalysis by metals. *J. Mol. Catal* **30,** 27–38 (1985).
12. Zaera, F. Key unanswered questions about the mechanism of olefin hydrogenation catalysis by transition-metal surfaces: a surface-science perspective. *Phys. Chem. Chem. Phys.* **15,** 11988–12003 (2013).
13. Heiz, U. & Landman, U. *Nanocatalysis* (Springer, 2007).
14. Landman, U., Yoon, B., Zhang, C., Heiz, U. & Arenz, M. Factors in gold nanocatalysis: oxidation of CO in the non-scalable size regime. *Top. Catal* **44,** 145–158 (2007).
15. Falsig, H. *et al.* Trends in the catalytic CO oxidation activity of nanoparticles. *Angew. Chem. Int. Ed.* **47,** 4835–4839 (2008).
16. Hvolbæk, B. *et al.* Catalytic activity of Au nanoparticles. *Nano Today* **2,** 14–18 (2007).
17. Janssens, T. V. W. *et al.* Insights into the reactivity of supported Au nanoparticles: combining theory and experiments. *Top. Catal.* **44,** 15–26 (2007).
18. Häkkinen, H., Abbet, S., Sanchez, A., Heiz, U. & Landman, U. Structural, electronic, and impurity-doping effects in nanoscale chemistry: supported gold nanoclusters. *Angew. Chem. Int. Ed.* **42,** 1297–1300 (2003).
19. Sanchez, A. *et al.* When gold is not noble: nanoscale gold catalysts. *J. Phys. Chem. A* **103,** 9573–9578 (1999).
20. Harding, C. *et al.* Control and manipulation of gold nanocatalysis: effects of metal oxide support thickness and composition. *J. Am. Chem. Soc.* **131,** 538–548 (2009).
21. Heiz, U. & Schneider, W.-D. Size-selected clusters on solid surfaces. *Crit. Rev. Solid State Mater. Sci* **26,** 251–290 (2001).
22. Barhen, J., Protopopescu, V. & Reister, D. TRUST: a deterministic algorithm for global optimization. *Science* **276,** 1094–1097 (1997).
23. Wales, D. J. & Scheraga, H. A. Global optimization of clusters, crystals, and biomolecules. *Science* **285,** 1368–1372 (1999).
24. Wolf, M. D. & Landman, U. Genetic algorithms for structural cluster optimization. *J. Phys. Chem. A* **102,** 6129–6137 (1998).
25. Zhao, Z.-J., Moskaleva, L. V., Aleksandrov, H. A., Basaran, D. & Rösch, N. Ethylidyne formation from ethylene over Pt(111): a mechanistic study from first-principle calculations. *J. Phys. Chem. C* **114,** 12190–12201 (2010).
26. Kubota, J., Ichihara, S., Kondo, J. N., Domen, K. & Hirose, C. π-Bonded ethene on Pt(111) surface studied by IRAS. *Surf. Sci.* **357–358,** 634–638 (1996).
27. Cassuto, A., Mane, M. & Jupille, J. Ethylene monolayer and multilayer on Pt(111) below 52 K: determination of bond lengths by near-edge X-ray fine structure. *Surf. Sci.* **249,** 8–14 (1991).
28. Chatt, J. & Duncanson, L. A. Olefin co-ordination compounds. Part III. Infra-red spectra and structure: attempted preparation of acetylene complexes. *J. Chem. Soc.* 2939–2947 (1953).
29. Dewar, M. A review of π Complex Theory. *Bull. Soc. Chim* **18,** C 71–C 79 (1951).
30. Neurock, M. & van Santen, R. A. A first principles analysis of C-H bond formation in ethylene hydrogenation. *J. Phys. Chem. B* **104,** 11127–11145 (2000).
31. van Santen, R. A. & Neurock, M. *Molecular Heterogeneous Catalysis: A Conceptual and Computational Approach* (Wiley-VCH, 2006).
32. Sautet, P. & Paul, J.-F. Low temperature adsorption of ethylene and butadiene on platinum and palladium surfaces: a theoretical study of the diσ/π competition. *Catal. Lett.* **9,** 245–260 (1991).
33. Yoon, B. *et al.* Probing of charging and reactivity of supported gold nanoclusters: Bonding of CO to gold octamers adsorbed on magnesia. *Science* **307,** 403–407 (2005).
34. Cortright, R. D., Goddard, S. A., Rekoske, J. E. & Dumesic, J. A. Kinetic study of ethylene hydrogenation. *J. Catal.* **127,** 342–353 (1991).
35. Rioux, R. M., Song, H., Hoefelmeyer, J. D., Yang, P. & Somorjai, G. A. High-surface-area catalyst design: synthesis, characterization, and reaction studies of platinum nanoparticles in mesoporous SBA-15 silica. *J. Phys. Chem. B* **109,** 2192–2202 (2005).
36. Song, H. *et al.* Hydrothermal growth of mesoporous SBA-15 silica in the presence of PVP-stabilized Pt nanoparticles: synthesis, characterization, and catalytic properties. *J. Am. Chem. Soc.* **128,** 3027–3037 (2006).
37. Beebe, Jr. T. P. & Yates, Jr. J. T. Spectroscopic detection of (111) facets on supported Pd crystallites: Site blocking by ethylidyne on Pd/Al2O3. *Surf. Sci* **173,** L606–L612 (1986).
38. Chen, P., Kung, K. Y., Shen, Y. R. & Somorjai, G. A. Sum frequency generation spectroscopic study of CO/ethylene coadsorption on the Pt(1 1 1) surface and CO poisoning of catalytic ethylene hydrogenation. *Surf. Sci* **494,** 289–297 (2001).
39. Lundwall, M. J., McClure, S. M. & Goodman, D. W. Probing Terrace and Step Sites on Pt Nanoparticles Using CO and Ethylene. *J. Phys. Chem. C* **114,** 7904–7912 (2010).
40. Rioux, R. M. *et al.* Adsorption and co-adsorption of ethylene and carbon monoxide on silica-supported monodisperse pt nanoparticles: volumetric adsorption and infrared spectroscopy studies. *Langmuir* **24,** 198–207 (2008).
41. Kesmodel, L. L., Dubois, L. H. & Somorjai, G. A. LEED analysis of acetylene and ethylene chemisorption on the Pt(111) surface: Evidence for ethylidyne formation. *J. Chem. Phys.* **70,** 2180–2188 (1979).
42. Mohsin, S. B., Trenary, M. & Robota, H. J. Infrared identification of the low-temperature forms of ethylene adsorbed on platinum/alumina. *J. Phys. Chem.* **92,** 5229–5233 (1988).
43. Land, T. A., Michely, T., Behm, R. J., Hemminger, J. C. & Comsa, G. Direct observation of surface reactions by scanning tunneling microscopy: Ethylene→ethylidyne→carbon particles→graphite on Pt(111). *J. Chem. Phys.* **97,** 6774–6783 (1992).
44. Lang, S. M., Bernhardt, T. B., R.N. Barnett, R. N. & Landman, U. Methane activation and catalytic ethylene formation on free Au_2^+. *Angew. Chem. Int. Ed.* **49,** 980–983 (2010).
45. Lang, S. M., Bernhardt, T. B., R.N. Barnett, R. N. & Landman, U. Temperature-tunable selective methane catalysis on Au_2^+: from cryogenicpartial oxidation yielding formaldehyde to cold ethylene production. *J. Phys. Chem. C* **115,** 6788–6795 (2011).

46. Ertl, G., Knözinger, H., Schüth, F. & Weitkamp, J. *Handbook of Heterogeneous Catalysis* 2 edn (Wiley-VCH, 2008).
47. Heiz, U., Vanolli, F., Trento, L. & Schneider, W.-D. Chemical Reactivity of size-selected supported clusters: an experimental setup. *Rev. Sci. Inst* **68,** 1986–1994 (1997).
48. Schweinberger, F. F. *et al.* Submonolayer sensitive adsorption study of trichloroethene on single crystal surfaces by means of MIES, UPS and TPD. *Surf. Sci.* **609,** 18–29 (2013).
49. Kolmakov, A., Stultz, J. & Goodman, D. W. Characterization of surface defects on MgO thin films by ultraviolet photoelectron and metastable impact electron spectroscopies. *J. Chem. Phys.* **113,** 7564–7570 (2000).
50. Benedetti, S., Benia, H. M., Nilius, N., Valeri, S. & Freund, H. J. Morphology and optical properties of MgO thin films on Mo(0 0 1). *Chem. Phys. Lett.* **430,** 330–335 (2006).
51. Kim, Y. D., Stultz, J. & Goodman, D. W. Characterization of MgO(1 0 0) thin film growth on Mo(1 0 0). *Surf. Sci* **506,** 228–234 (2002).
52. Zaera, F., Kollin, E. & Gland, J. L. Observation of an unusually low CO stretching frequency: CO chemisorption on a Mo(100) surface. *Chem. Phys. Lett.* **121,** 464–468 (1985).
53. Wettergren, K. *et al.* High sintering resistance of size-selected platinum cluster catalysts by suppressed Ostwald ripening. *Nano Lett.* **14,** 5803–5809 (2014).
54. Fukamori, Y. *et al.* Fundamental insight into the substrate-dependent ripening of monodisperse clusters. *ChemCatChem* **5,** 3330–3341 (2013).
55. Harding, C. J. *et al.* Dual pulsed-beam controlled mole fraction studies of the catalytic oxidation of CO on supported Pd nanocatalysts. *J. Catal.* **255,** 234–240 (2008).
56. Amenomiya, Y. & Pottie, R. F. Mass spectra of some deuterated ethanes. I. The effect of ionizing voltage. *Can. J. Chem.* **46,** 1735–1739 (1968).
57. Ricci, D., Bongiorno, A., Pacchioni, G. & Landman, U. Bonding trends and dimensionality crossover of gold nanoclusters on metal-supported MgO thin films. *Phys. Rev. Lett.* **97,** 036106 (2006).
58. Yoon, B. & Landman, U. Electric field control of structure, dimensionality, and reactivity of gold nanoclusters on metal-supported MgO films. *Phys. Rev. Lett.* **100,** 056102 (2008).
59. Zhang, C., Yoon, B. & Landman, U. Predicted oxidation of CO catalyzed by Au nanoclusters on a thin defect-free MgO film supported on a Mo(100) surface. *J. Am. Chem. Soc.* **129,** 2228–2229 (2007).
60. Vaida, M. E. *et al.* Ultrathin magnesia films as support for molecules and metal clusters: Tuning reactivity by thickness and composition. *Phys. Status Solidi B* **247,** 1001–1015 (2010).
61. Kresse, G. & Joubert, D. From ultrasoft pseudopotentials to the projector augmented-wave method. *Phys. Rev. B* **59,** 1758–1775 (1999).
62. Levy, M. & Perdew, J. P. Tightly bound and convexity constraint on the exchange-correlation-energy functional in the low-density limit, and other formal tests of generalized-gradient approximations. Phys. Rev. B **48**, 11638 (1993). *Erratum* **55,** 13321 (1997).
63. Levy, M. & Perdew, J. P. Tight bound and convexity constraint on the exchange-correlation-energy functional in the low-density limit, and other formal tests of generalized-gradient approximations. *Phys. Rev. B* **48,** 11638–11645 (1993).
64. Perdew, J. P. *Electronic Structure of Solids*. (eds Ziesche, P. & Eschrig, H.) 11–20 (Akademie, 1991).
65. Perdew, J. P., Burke, K. & Ernzerhof, M. Generalized gradient approximation made simple. *Phys. Rev. Lett.* **77,** 3865–3868 (1996).
66. Perdew, J. P. *et al.* Atoms, molecules, solids, and surfaces: Applications of the generalized gradient approximation for exchange and correlation. *Phys. Rev. B* **46,** 6671–6687 (1992).

Acknowledgements

The experimental work has been supported by the European Research Council (ERC) through the advanced research grant (246645-ASC3), and by the DFG through project HE3454/23-1. B.Y. was supported by the Air Force Office for Scientific Research (AFOSR) and U.L. by grant No. FG05–86ER45234 from the Office of Basic Energy Sciences of the US Department of energy (DOE). Computations were carried out at the Georgia Tech Center for Computational Materials science.

Author contributions

A.S.C., U.L. and U.H. conceived the project, A.S.C., M.D.R., C.J.R. and F.F.S. contributed to the experimental work, A.S.C., M.D.R, C.J.R., F.F.S. and U.H. analysed the experimental results, B.Y. executed the theoretical computations, B.Y. and U.L. analysed the computational results, A.S.C, U.L. and U.H. wrote the manuscript.

Additional information

Supplementary Information accompanies this paper at http://www.nature.com/naturecommunications

Competing financial interests: The authors declare no competing financial interests.

Reprints and permission information is available online at http://npg.nature.com/reprintsandpermissions/

How to cite this article: Crampton, A. S. *et al.* Structure sensitivity in the nonscalable regime explored via catalysed ethylene hydrogenation on supported platinum nanoclusters. *Nat. Commun.* 7:10389 doi: 10.1038/ncomms10389 (2016).

Supplementary Figures

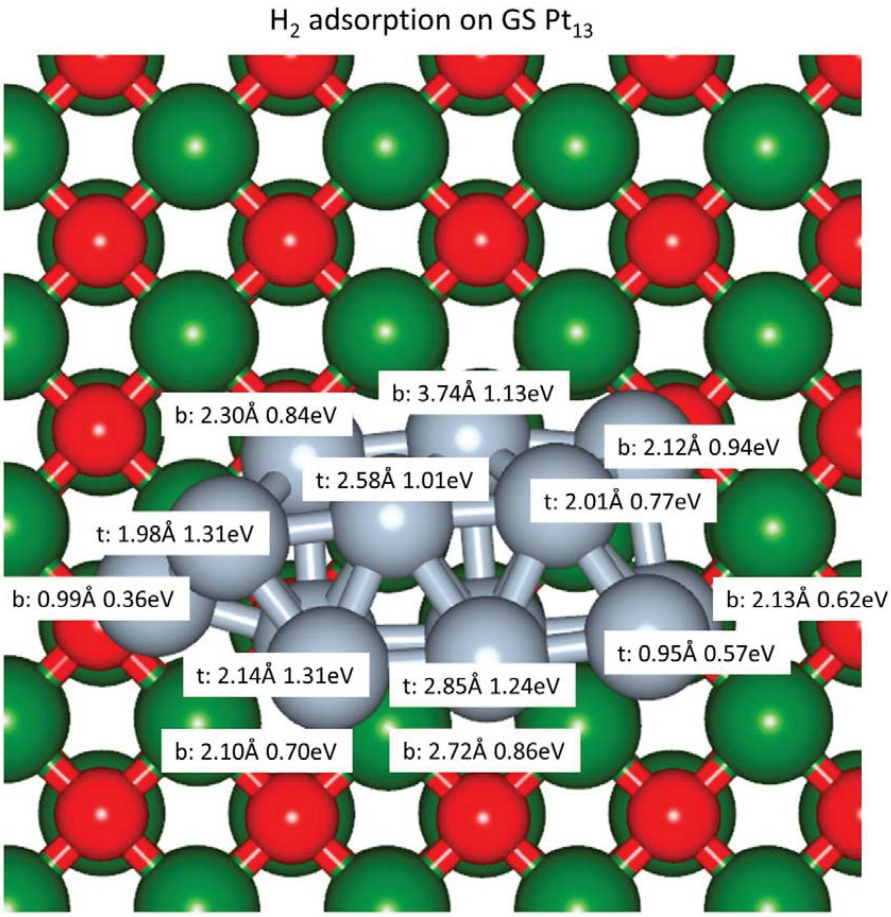

Supplementary Figure 1 | Hydrogen adsorption on a ground state supported Pt_{13} cluster. The platinuum atom are depicted by gray spheres adsorbed on MgO(100) (red speheres denote oxygen atoms, and green balls correspond to Mg atoms. The letters "b" and "t", for each of the cluster atoms designate "bottom" and "top" atoms of the cluster with respect to the cluster inteface with the MgO surface. Fot each of the sites we give the DFT-calculated distance between the two H atoms of the adsorbed H_2 molecules (with distances smaller than 1.0 Å corresponding to undissociated H_2 molecule, an dlarger values denoting a spontaneously dissociated molecule. The second value for each site gives the adsorption

energy of the molecule (in eV). It is evident that spontaneous dissociative adsorption occurs at all cluster sites except two – interestingly these two (H_2 molecular adsorption sites) are charcterized by a large excess electron density (see Figure. 2c of the main text and Supplementary figure 15).

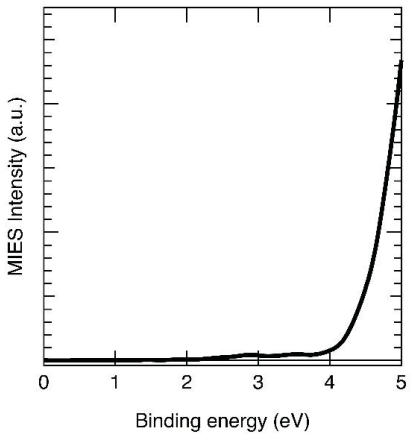

Supplementary Figure 2 | MIES spectrum of the MgO(100) thin film. The spectrum shows the valence band area of the MIES spectrum where no emission peak below 4 eV indicates the absence of F-center defects in the thin films.

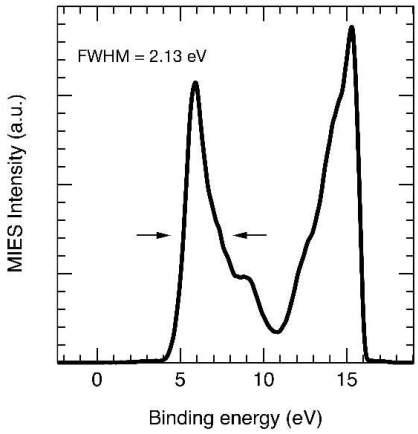

Supplementary Figure 3 | Complete MIES spectrum of MgO(100) thin film. The FWHM of the O2p peak is 2.13 eV, similar to that previously reported for a highly ordered film (see Ref. 51 of the main text).

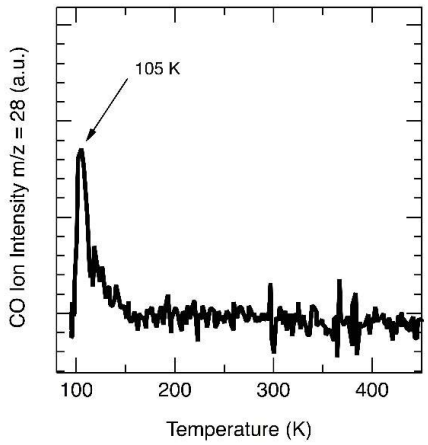

Supplementary Figure 4 | CO TPD from the MgO(100) thin film. One CO molecule per surface atom was dosed at 100 K and a temperature ramp of 2 K/s applied. The peak at 100 K is from a small amount of possible grain boundaries, corners and steps

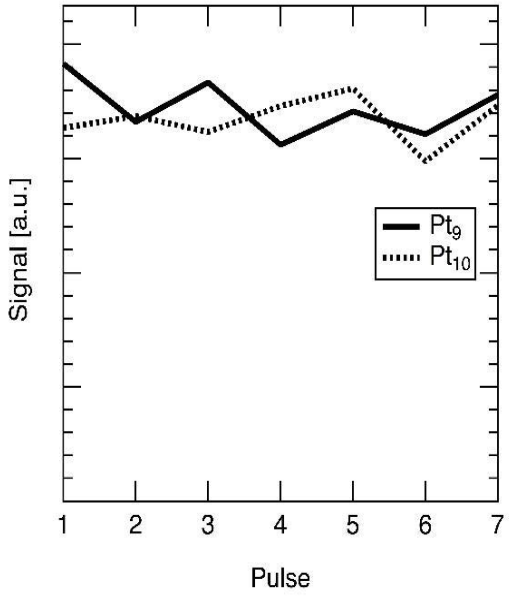

.

Supplementary Figure 5 | Pulse to pulse signal at 400 K from Pt_9 and Pt_{10}. The conditions were exactly the same as used for the catalytic experiments at 300 K (see Fig. 5a).

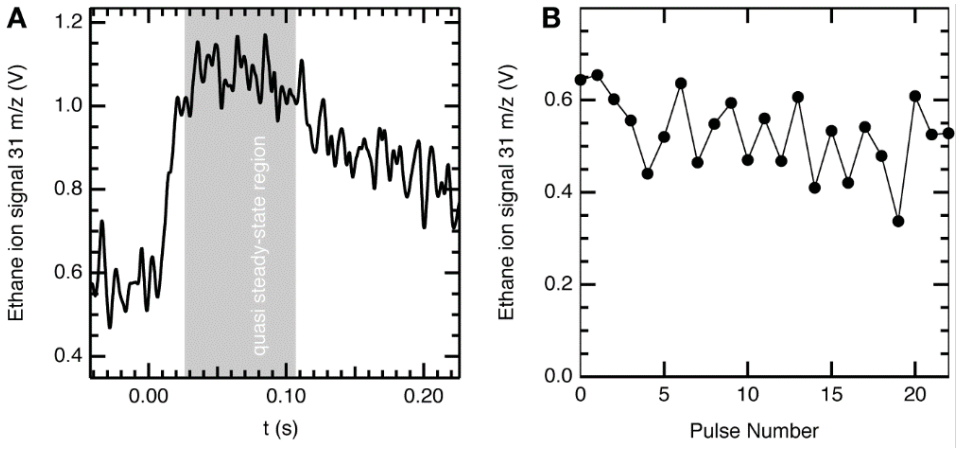

Supplementary Figure 6 | Representative pulsed molecular beam data for Pt_{11}. (A) Average ethane signal (31 m/z) of 20 pulses for Pt_{11} measured at 300 K. The gray, shaded area depicts the quasi steady state region (approx. 80 ms) where the turn over frequency was calculated. **(B)** Pulse to pulse ethane signal calculated for the same experiment as **A**.

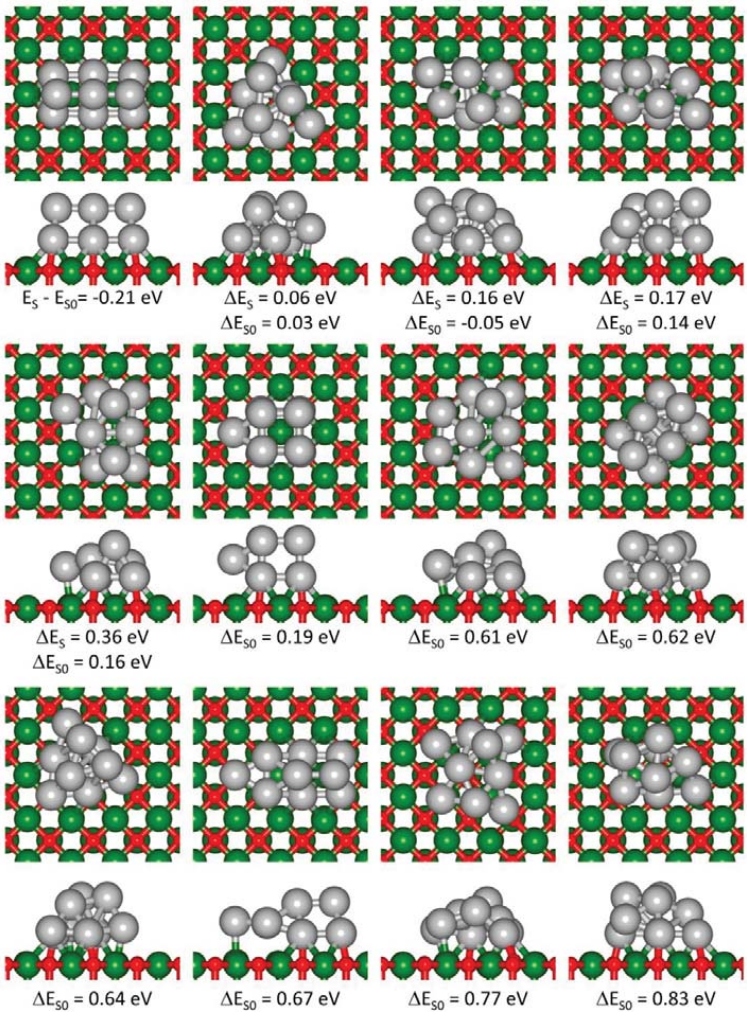

Supplementary Figure 7 | Ground state and higher –energy structural isomers for Pt_9/MgO(100). For the ground state (lowest energy) configuration (leftmost structure in the first row) E_s (E_{s0}) denote the energies calculated with (without, i.e. taking s=0)) spin optimization; in the calculations with spin optimization it has been found that the spin state of the bare adsorbed platinum clusters (Pt_n, n= 9,10, 13) is $N\uparrow$-$N\downarrow$=2 (where N_s is the number of electrons with spin s = ↑ or ↓). ΔE_s and ΔE_{s0} give the difference between the total energy of the isomer and the ground state, calclulated with (ΔE_s) and without (ΔE_{s0}) spin, repectively; ΔE_s is given for the first 5

isomers only. For each structure we give top (above) and side (below) views. Pt - gray spheres, Mg - green and O – red.

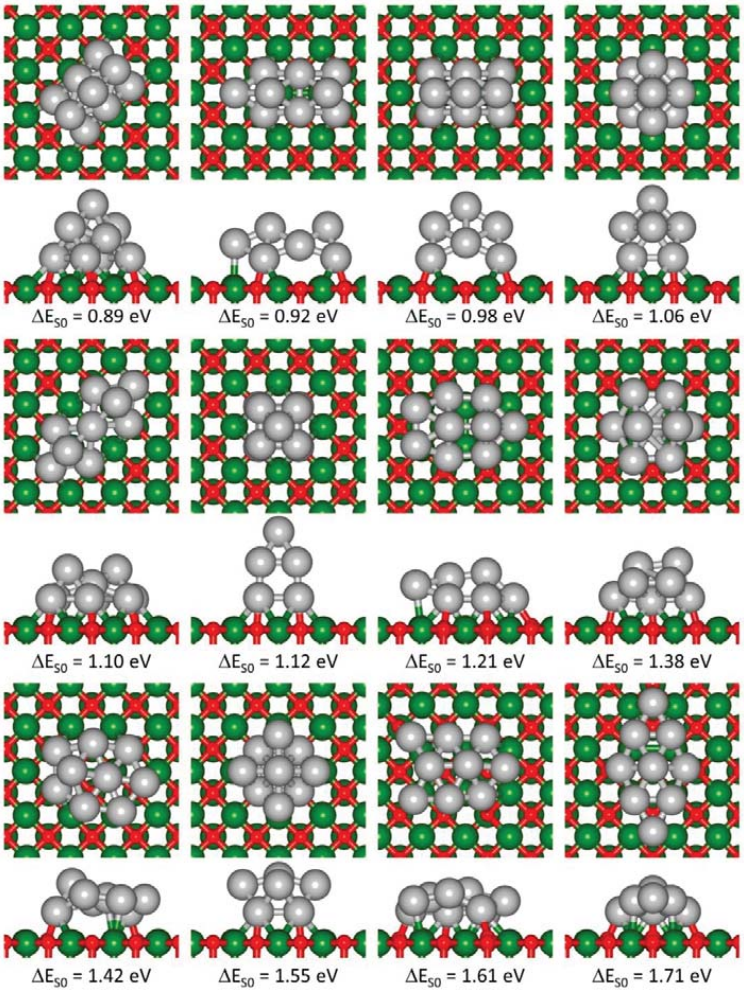

Supplementary Figure 8 | Ground state and higher –energy structural isomers for Pt_9/MgO(100). ΔE_{s0} gives the difference between the total energy of the isomer and the ground state (left-most structure in the first row of Supplementary Figure 7, calclulated without (ΔE_{s0}) spin, repectively. For each structure we give top (above) and side (below) views. Pt - gray spheres, Mg - green and O – red.

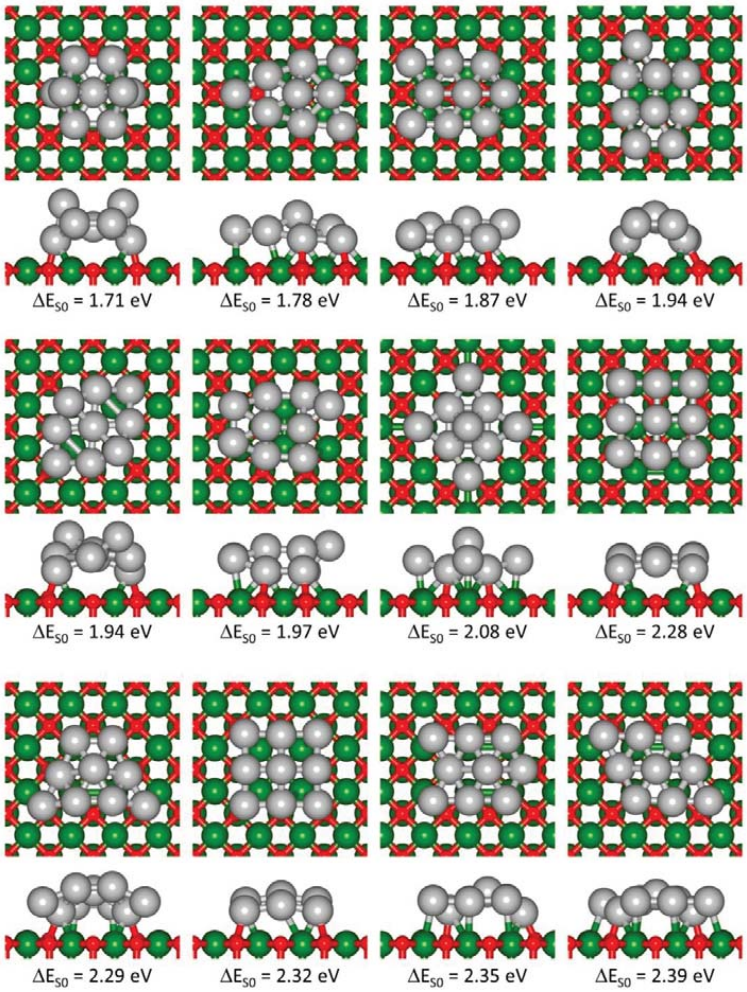

Supplementary Figure 9 | Ground state and higher –energy structural isomers for Pt_9/MgO(100). ΔE_{s0} gives the difference between the total energy of the isomer and the ground state (left-most structure in the first row of Supplementary Figure 7), calclulated without (ΔE_{s0}) spin, repectively, For each structure we give top (above) and side (below) views. Pt - gray spheres, Mg - green and O – red.

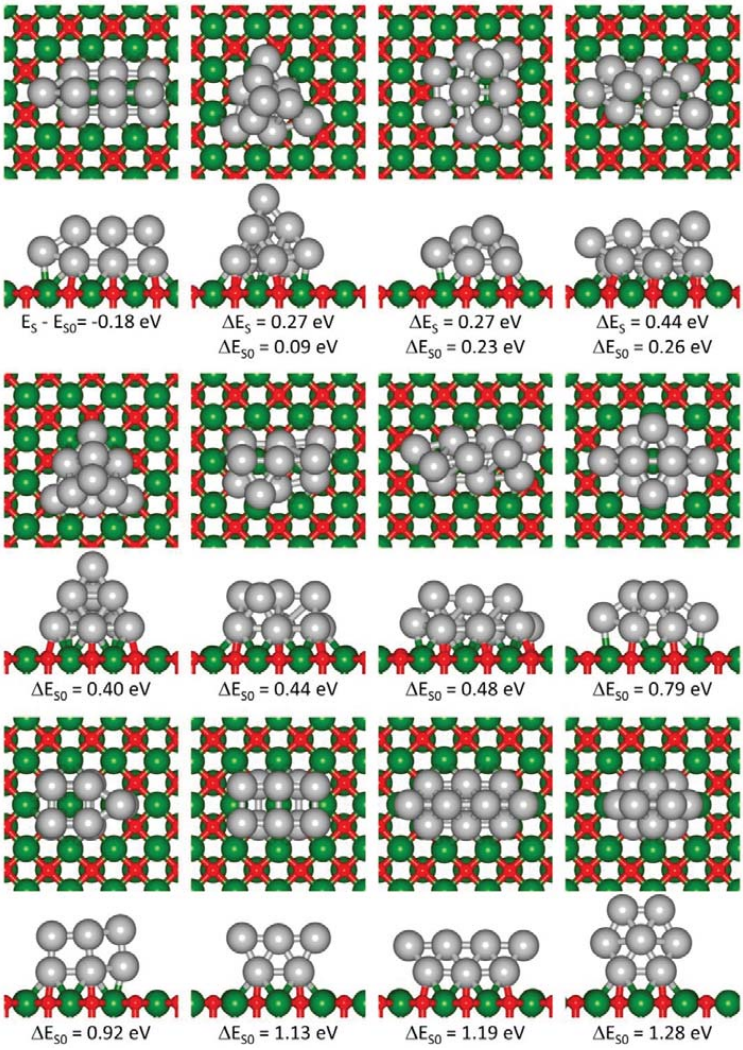

Supplementary Figure10 | Ground state and higher –energy structural isomers for Pt_{10}/MgO(100). For the ground state (lowest energy) configuration (leftmost structure in the first row) E_s (E_{s0}) denote the energies calculated with (without, i.e. taking s=0)) spin optimization. ΔE_s and ΔE_{s0} give the difference between the total energy of the isomer and the ground state, calclulated with (ΔE_s) and without (ΔE_{s0}) spin, repectively; ΔE_s is given for the first 4 isomers only. For each structure we give top (above) and side (below) views. Pt - gray spheres, Mg - green and O – red.

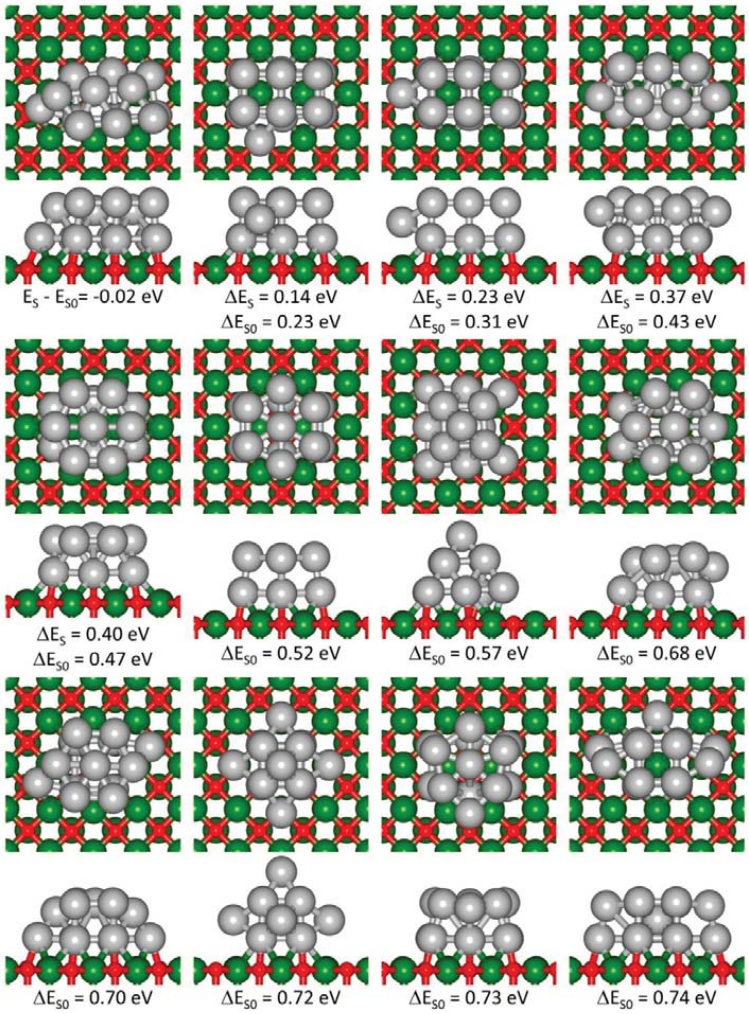

Supplementary Figure 11 | Ground state and higher –energy structural isomers for

Pt_{13}/MgO(100). For the ground state (lowest energy) configuration (leftmost structure in the first row) E_s (E_{s0}) denote the energies calculated with (without, i.e. taking s=0)) spin optimization. ΔE_s and ΔE_{s0} give the difference between the total energy of the isomer and the ground state, calclulated with (ΔE_s) and without (ΔE_{s0}) spin, repectively; ΔE_s is given for the first 4 isomers only. For each structure we give top (above) and side (below) views. Pt - Gray spheres, Mg - green and O – red.

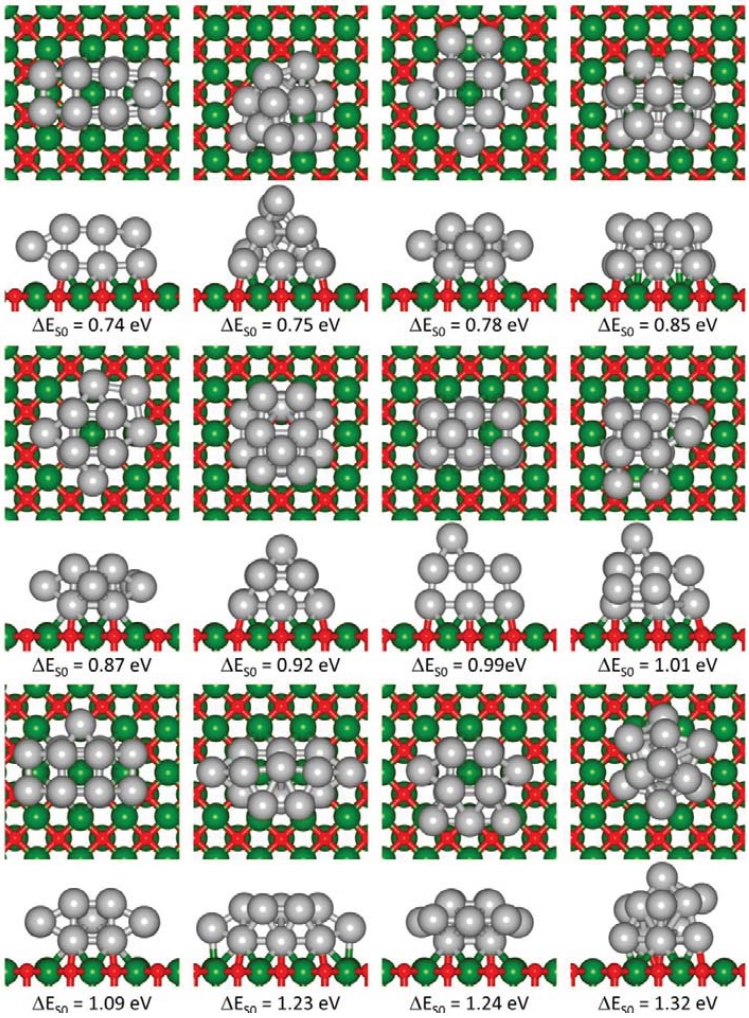

Supplementary Figure 12 | Ground state and higher –energy structural isomers for Pt_{13}/MgO(100). ΔE_{s0} gives the difference between the total energy of the isomer and the ground state (left-most structure in the first row of Figure S11, calclulated without (ΔE_{s0}) spin, repectively, For each structure we give top (above) and side (below) views. Pt - gray spheres, Mg - green and O – red.

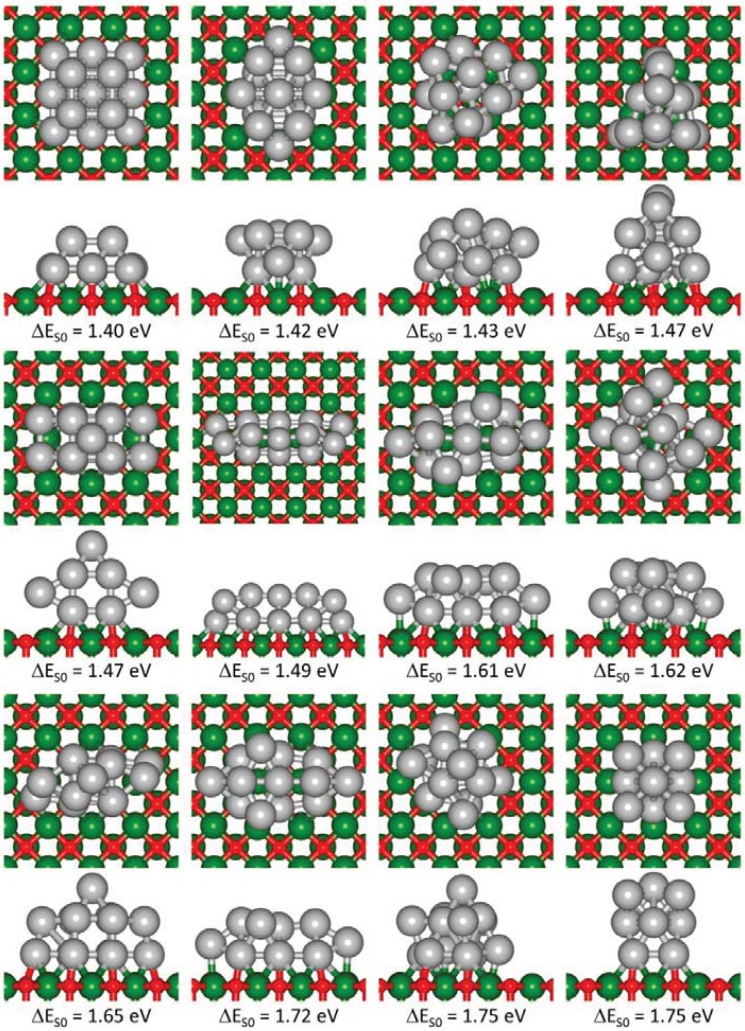

Supplementary Figure 13 | Ground state and higher –energy structural isomers for Pt_{13}/MgO(100). ΔE_{s0} gives the difference between the total energy of the isomer and the ground state (left-most structure in the first row of Supplementary Figure 11, calclulated without (ΔE_{s0}) spin, repectively, For each structure we give top (above) and side (below) views. Pt - gray spheres, Mg - green and O – red.

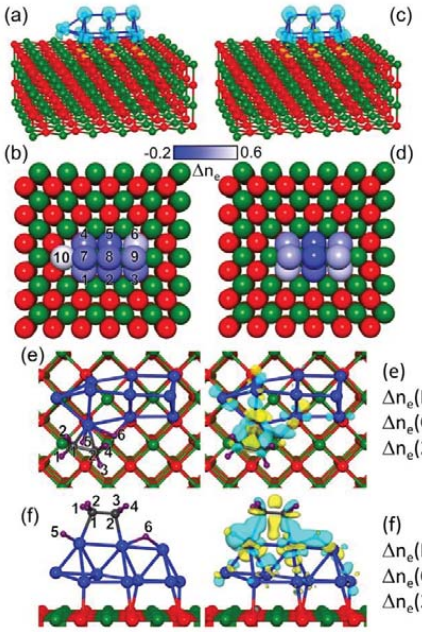

	Excess electrons for Pt_{10} on MgO	Excess electrons for Pt_9 on MgO
1	0.216	0.384
2	0.080	0.071
3	0.167	0.393
4	0.096	0.215
5	-0.023	-0.047
6	0.345	0.214
7	0.118	0.259
8	0.085	-0.080
9	0.188	0.275
10	0.512	

$\Delta n_e(Pt_{10}) = 1.78$ $\Delta n_e(Pt_9) = 1.68$

	e	f
Pt(1)	-0.341	0.144
Pt(2)	0.032	0.066
Pt(3)	0.204	0.212
Pt(4)	0.141	0.266
Pt(5)	0.097	0.080
Pt(6)	0.264	0.383
Pt(7)	0.209	-0.161
Pt(8)	0.022	-0.141
Pt(9)	0.236	0.078
Pt(10)	0.455	0.454
C(1)	0.196	0.105
C(2)	0.036	0.156
H(1)	-0.081	-0.037
H(2)	-0.106	-0.021
H(3)	-0.026	-0.068
H(4)	-0.027	-0.014
H(5)	0.167	0.097
H(6)	0.071	0.112

Supplementary Figure 14 | Optimal adsorption configurations and charge distribution on bare Pt_n / MgO (n= 9, 10) and co-adsorbed C_2H_4 +H_2 on Pt_{10}/MgO. In **a** and **c**, the blue and yellow contour hyper-surfaces correspond to excess (light blue) and deficient (yellow) charge distributions obtained as the difference between the total charges before and after adsorption of the clusters; these hypersurfaces are drawn such that the excess electronic (negative) charge inside the light blue hypersurface is 30% of the total electronic charge and the same for the positive charge inside the yellow hypersurfaces (for hypersurfaces corresponding to 50% of the excess negative (and positive) excess charges, see Fig. 2a and 2c, respectively, of the main manuscript text. Bader charge analysis is given in **b** and **d**, with lighter color corresponding to excess number of electrons (that is excess negative charge on the corresponding atom). For the values of the Bader charges are given in the table on the right. **(e,f)** Coadsorption of C_2H_4 and H_2 on Pt_{10}/MgO in the π (e) and di-σ (f) bonding modes. The adsorption geometries are shown on the left, and on the right we depict the bonding frontier orbitals of the adsorption system **(**the light blue and yellow denote different signs of the wave function); the σ-type Pt-C bonds are clearly seen in **f** (note the directed wave function contours on the right). In both **e** and **f**, atoms 5 and 6 are the proximal

dissociated coadsorbed H atoms. For the values of the Bader charges are given in the table on the right.

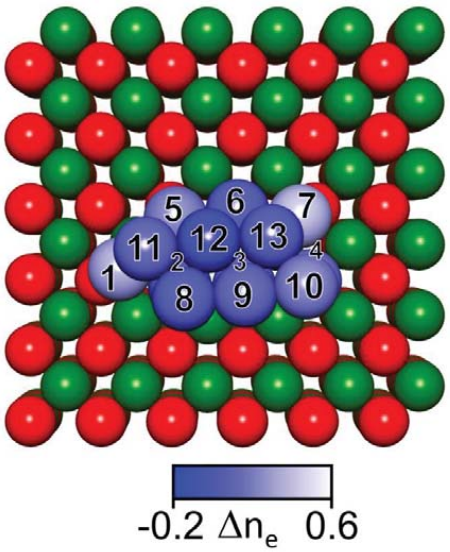

	Excess electrons for Pt_{13} on MgO
1	0.341
2	0.052
3	0.130
4	0.171
5	0.212
6	0.099
7	0.363
8	0.066
9	0.101
10	0.222
11	0.145
12	-0.038
13	0.058

$\Delta n_e\,(Pt_{13})_{Bader} = 1.922$

Supplementary Figure 15 | Optimal adsorption geometry of Pt_{13}/MgO and the Bader charge analysis. Lighter color corresponding to excess number of electrons (that is excess negative charge on the corresponding atom). For the values of the Bader charges are given in the table on the right. The excess electronic (negative) and positive charge hypersurfaces for the cluster are given in Fig. 2e of the main manuscript.

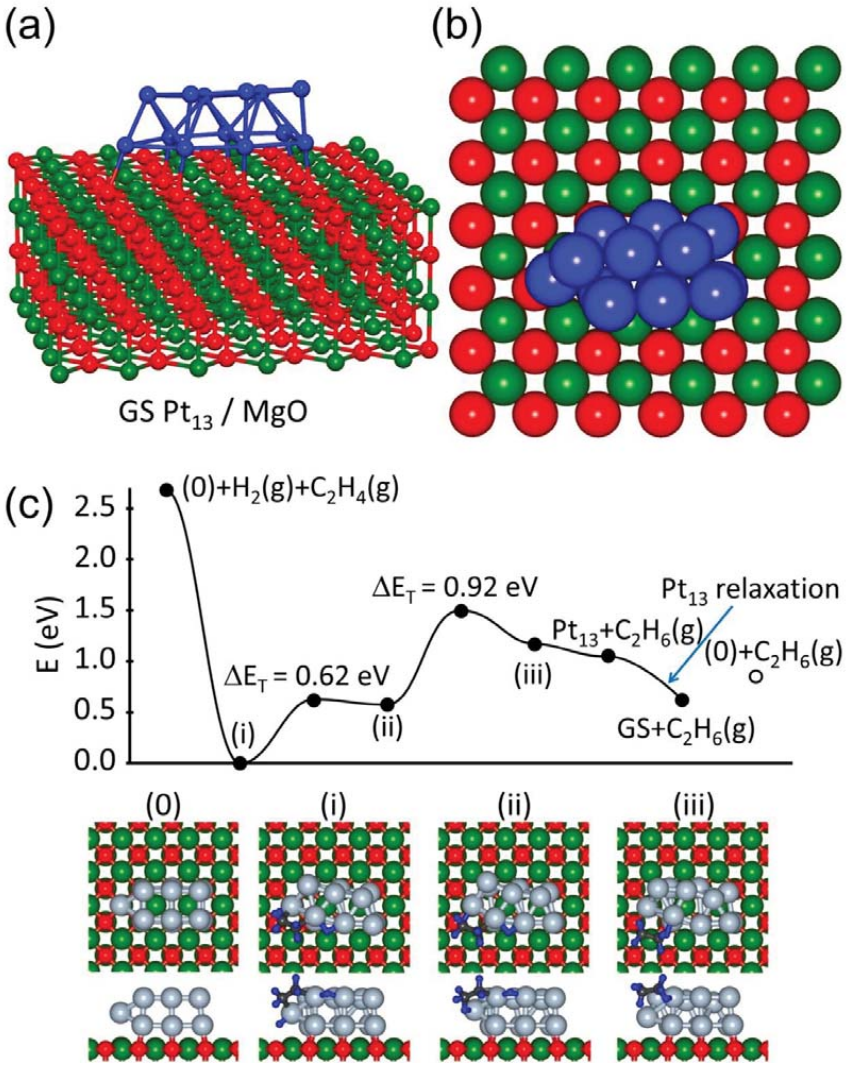

Supplementary Figure 16 | Adsorption and reaction induced structural fluxionality (**a,b**) side (**a**) and top (**b**) views of the ground state structure of Pt_{13}/MgO(100). (c) Fluxional transformation from an initial configuration (0) having a higher-in-energy isomer structure – see 2nd isomer in the top row of Supplementary Figure 11, with total energy (calculated without spin optimization) ΔE_{s0} = 0.31eV above the energy of the ground state, GS, isomer displayed in a&b of the current figure. This transformation is induced by the coadsorption of C_2H_4 and dissociated H_2, see configuration (i). Overcoming the two activation barriers

(0.66eV and 0.92 eV), the product at the end of the ethane (C_2H_6(g))-producing hydrogenation reaction contains a magnesia–supported Pt_{13} cluster with the GS structure (see a&b above) with a total energy lowering of the fully relaxed Pt_{13}/MgO system energy of 0.31 eV (compare the energy of the states GS + C_2H_6(g) denoted by the rightmost filled dot in the energy pathway in (**c**) with that of the state marked by the rightmost open dot, corresponding to (0) + C_2H_6(g), where (0) is the bare initial higher-in=energy isomer shown on the left of the bottom row of (**c**).

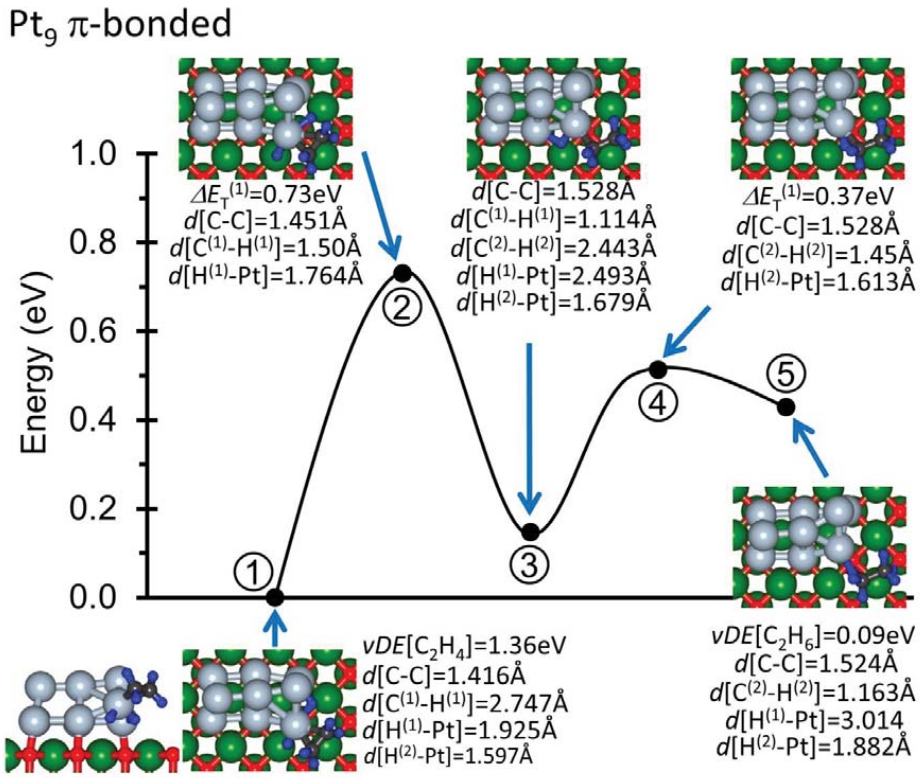

	d[C(1)-C(2)] (Å)	d[C(1)-H(1)] (Å)	d[C(1)-Pt] (Å)	d[H(1)-Pt] (Å)	d[C(2)-H(2)] (Å)	d[C(2)-Pt] (Å)	d[H(2)-Pt] (Å)
①	1.416	2.747	2.184	1.925	2.438	2.128	1.597
②	1.451	1.50	2.238	1.764	2.512	2.097	1.611
③	1.528	1.114	2.768	2.493	2.443	2.055	1.679
④	1.530	1.099	2.948	2.810	1.45	2.180	1.613
⑤	1.524	1.100	3.260	3.014	1.163	2.575	1.882

Supplementary Figure 17 | The lowest activation energy pathway for ethylene hydrogenation reaction on Pt_9/MgO. The reaction starts from a π-bonded C_2H_4 molecule coadsorbed with a dissociated H_2 molecule. The reaction follows the HP mechanism, with a first barrier of 0.73 eV. The geometric parameters along the reaction path are shown.

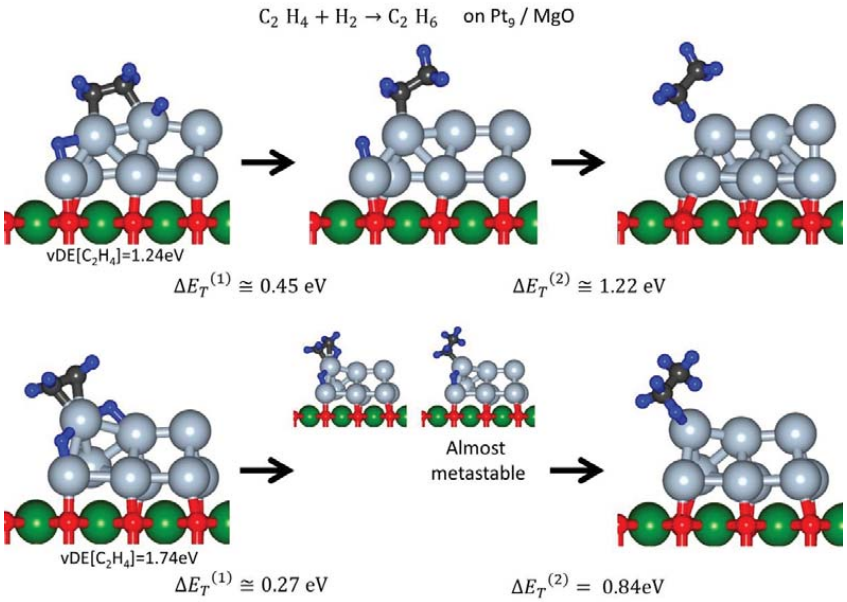

Supplementary Figure 18 | Higher-activation-barrier reactions on Pt_9/MgO(100). Upper row di-σ bonded, and bottom row π-bonded ethylene; H_2 does not spontaneously dissociate on top (second layer) of the adsorbed Pt_9 cluster, and H-diffusion from the interfacial layer entails an activation barrier.

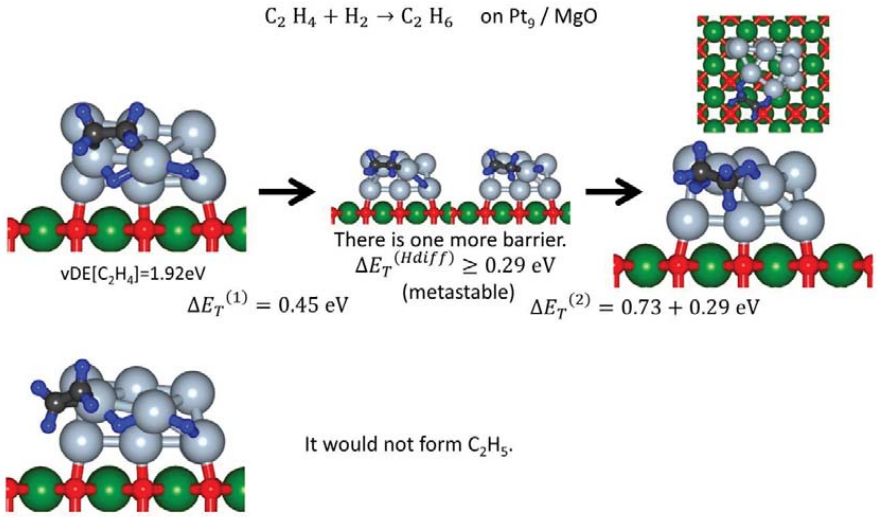

Supplementary Figure 19 | Higher-barrier ethylene hydrogenation reactions on Pt_9/MgO(100). In the bottom row the approach of the H atom to the adsorbed ethylene is accompanied by a repulsive interaction**.**

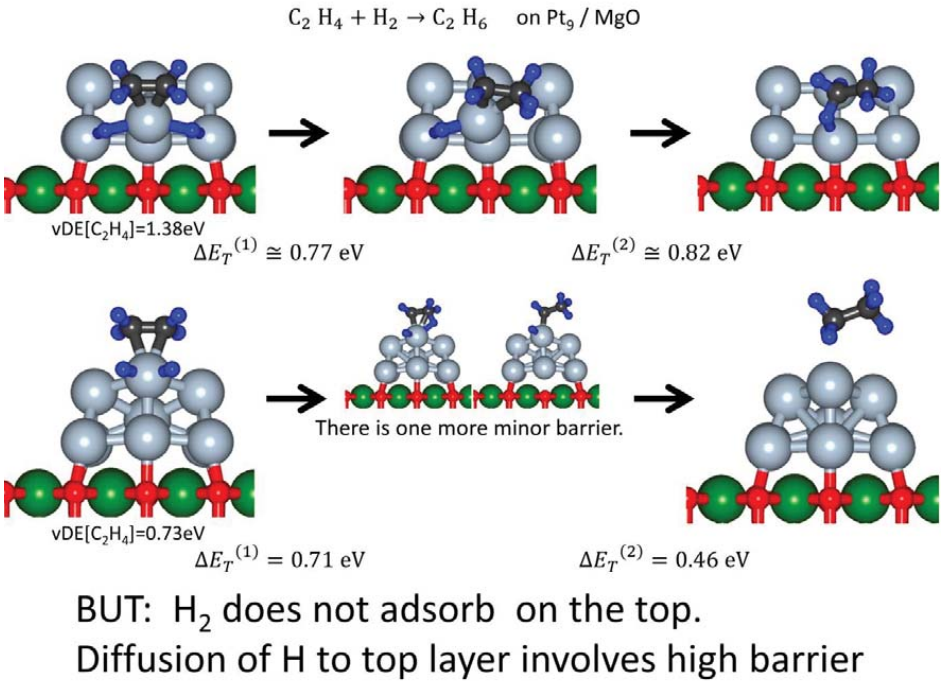

Supplementary Figure 20 | Higher-barrier ethylene hydrogenation reactions on Pt_9/MgO(100). Reactions starting from π –bonded ethylene to the central atom of the second-layer ridge.

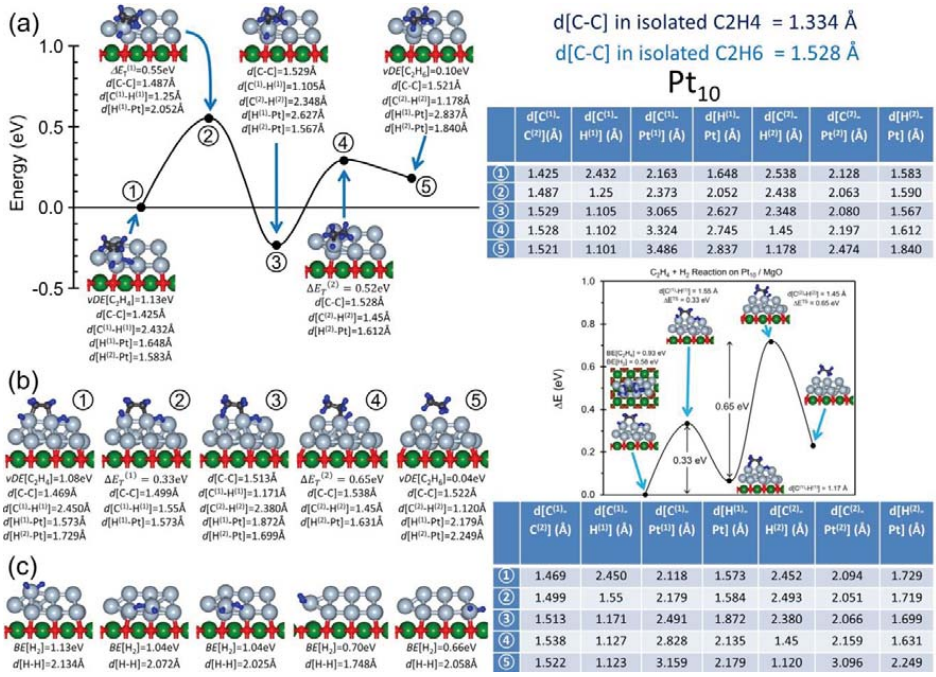

	d[C(1)-C(2)](Å)	d[C(1)-H(1)] (Å)	d[C(1)-Pt(1)] (Å)	d[H(1)-Pt] (Å)	d[C(2)-H(2)] (Å)	d[C(2)-Pt(2)] (Å)	d[H(2)-Pt] (Å)
①	1.425	2.432	2.163	1.648	2.538	2.128	1.583
②	1.487	1.25	2.373	2.052	2.438	2.063	1.590
③	1.529	1.105	3.065	2.627	2.348	2.080	1.567
④	1.528	1.102	3.324	2.745	1.45	2.197	1.612
⑤	1.521	1.101	3.486	2.837	1.178	2.474	1.840

	d[C(1)-C(2)] (Å)	d[C(1)-H(1)] (Å)	d[C(1)-Pt(1)] (Å)	d[H(1)-Pt] (Å)	d[C(2)-H(2)] (Å)	d[C(2)-Pt(2)] (Å)	d[H(2)-Pt] (Å)
①	1.469	2.450	2.118	1.573	2.452	2.094	1.729
②	1.499	1.55	2.179	1.584	2.493	2.051	1.719
③	1.513	1.171	2.491	1.872	2.380	2.066	1.699
④	1.538	1.127	2.828	2.135	1.45	2.159	1.631
⑤	1.522	1.123	3.159	2.179	1.120	3.096	2.249

Supplementary Figure 21 | Low-barrier Ethylene hydrogenation pathways on Pt_{10}/MgO. Geometric details of the reaction pathways of (a) π-bonded ethylene and (b) di-σ bonded ethylene, as well as dissociative adsorption of H_2 (in (c)).

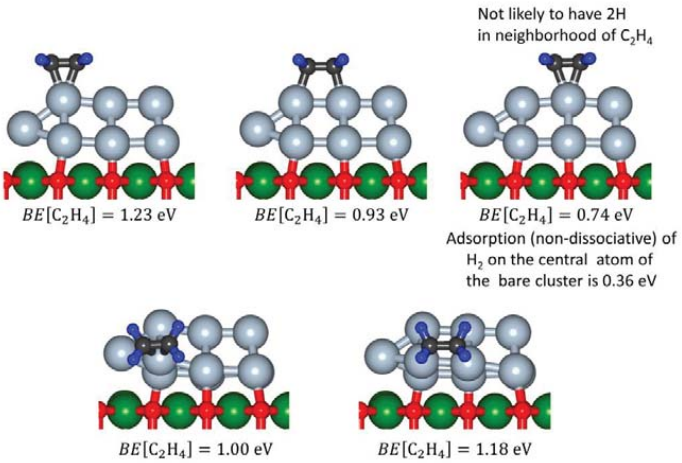

Supplementary Figure 22 | Selected Ethylene adsorption sites on Pt_{10}/MgO.

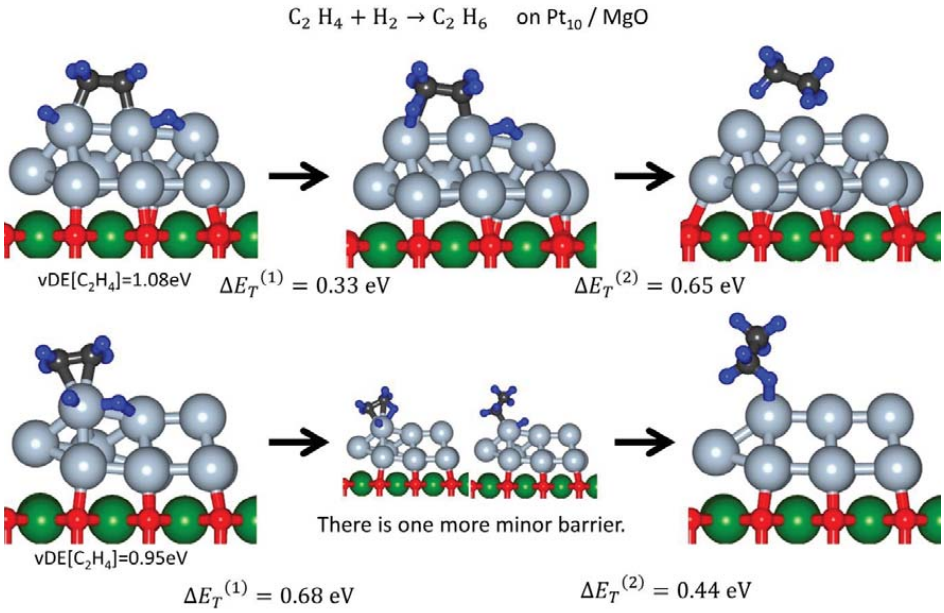

Supplementary Figure 23 | Relatively low-barrier ethylene hydrogenation pathways on Pt_{10}/MgO.

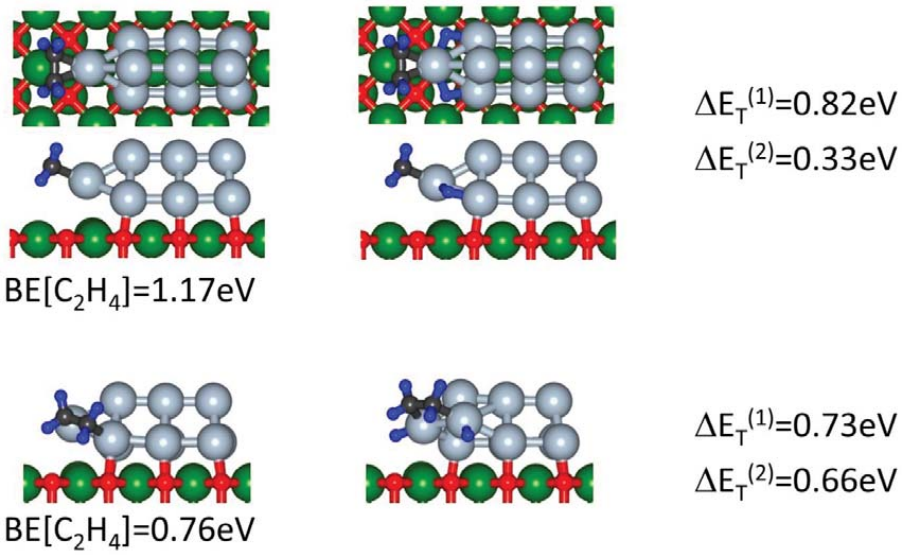

Supplementary Figure 24 | Higher energy ethylene hydrogenation sites.

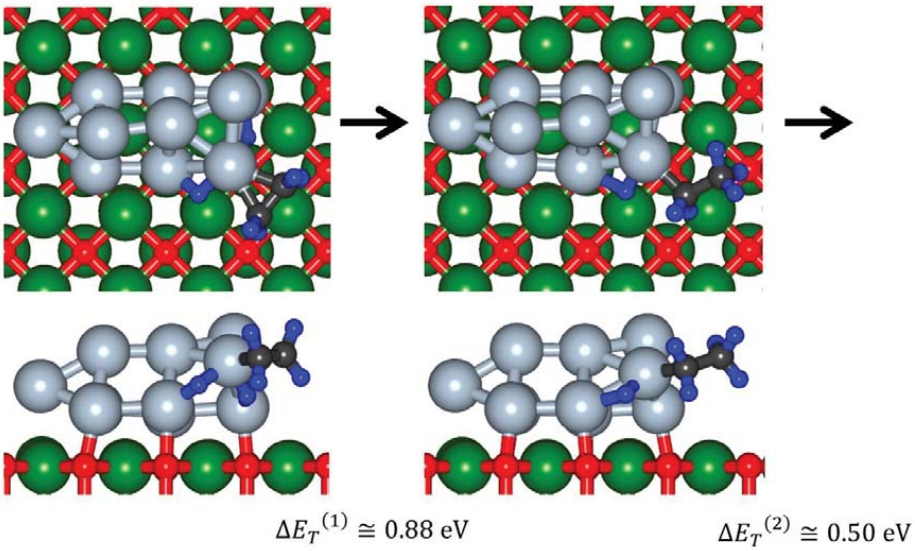

FIGURE S25: A higher energy ethylene hydrogenation site.

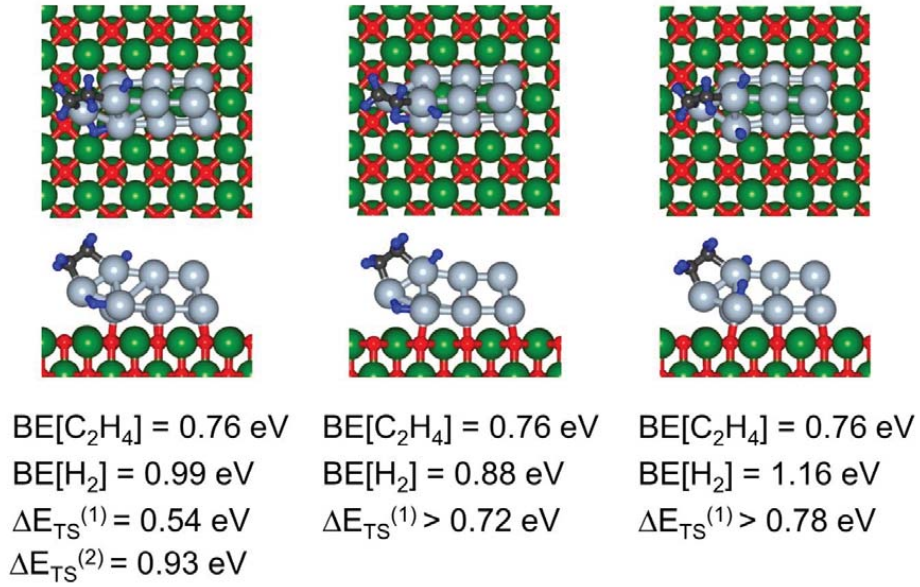

Supplementary Figure 26 | Additional higher energy ethylene hydrogenation sites.

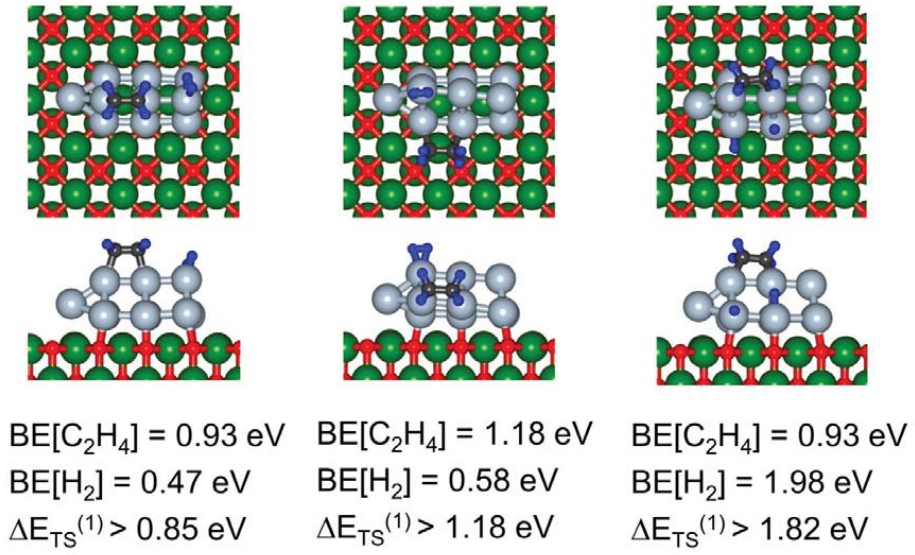

Supplementary Figure 27 | Even higher-barrier ethylene hydrogenation sites.

Supplementary Note 9: Ethylene Hydrogenation on Pt_{13}/MgO

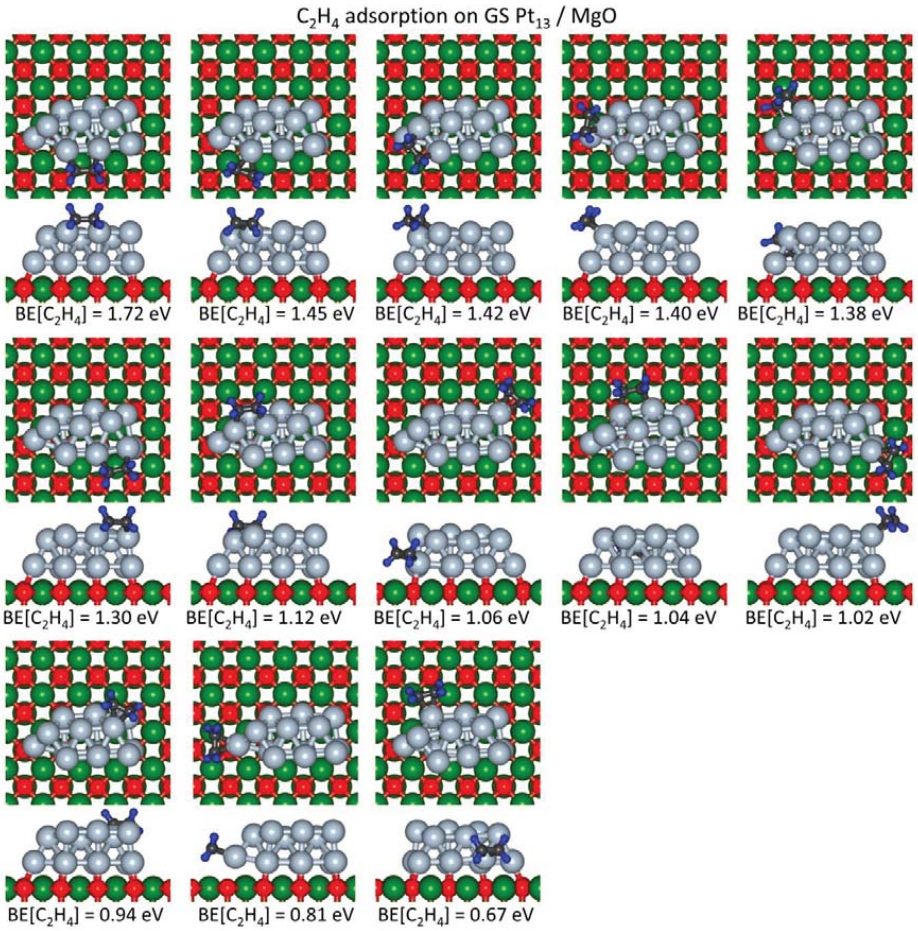

Supplementary Figure 28 | Binding sites of ethylene on the ground-state Pt_{13}/MgO system. The binding energies (BE) were obtained with the use of DFT calculations.

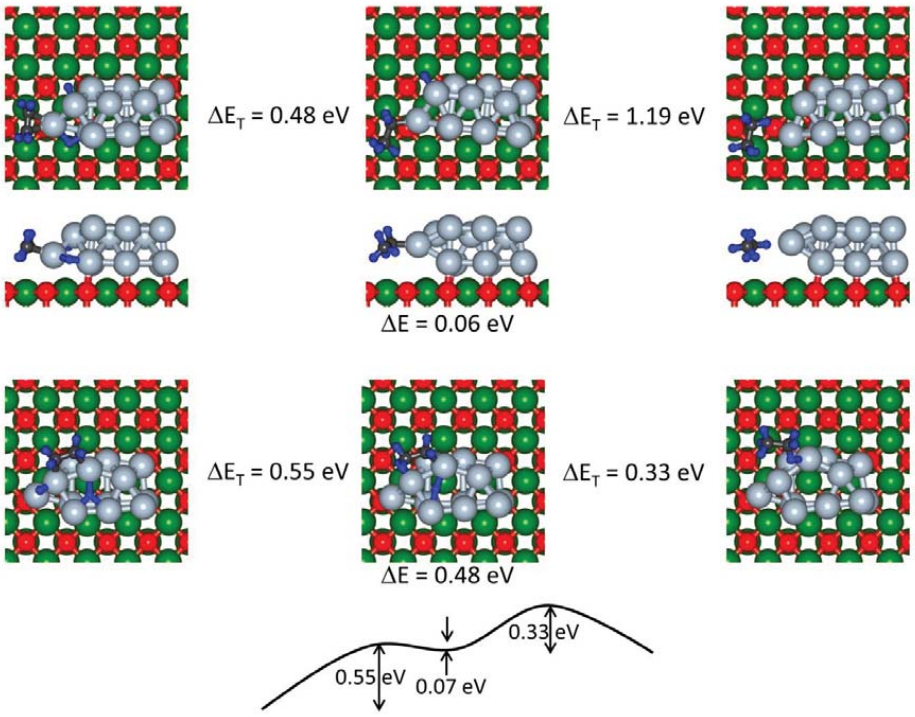

Supplementary Figure 29| Low and high barrier pathways of ethylene hydrogenation on Pt_{13}/MgO. Low-barrier (bottom row, starting from di-σ bonded C_2H_4 coadsorbed with dissociated H_2) and high-barrier (top-row, starting from π-bonded C_2H_4 coadsorbed with dissociated H_2) pathways of ethylene hydrogenation on Pt_{13}/MgO. ΔE_T = denotes the activation barrier, and ΔE gives the energy of the local minimum after the first activation barrier relative to the starting (initial) configuration (on the left).

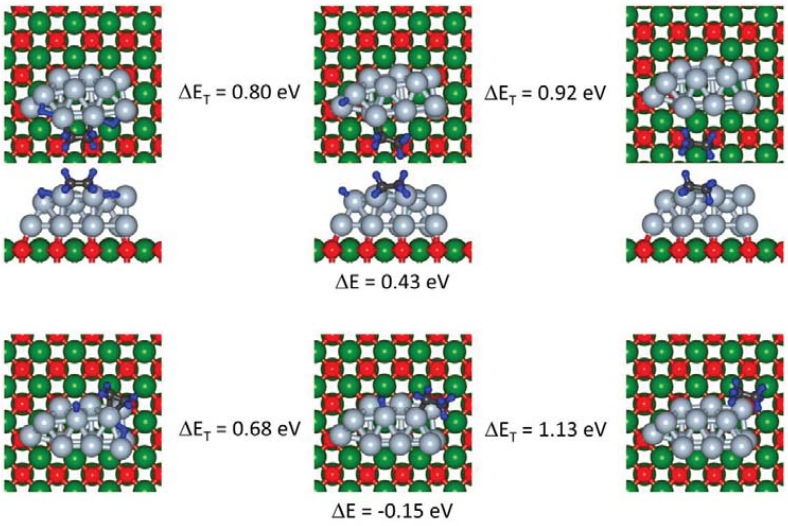

Supplementary Figure 30 | Higher-barrier pathways of ethylene hydrogenation on Pt_{13}/MgO. Higher-barrier (top-row, starting from di-σ bonded C_2H_4 coadsorbed with dissociated H_2) and high-barrier (bottom-row, starting from π-bonded C_2H_4 coadsorbed with dissociated H_2) pathways of ethylene hydrogenation on Pt_{13}/MgO.

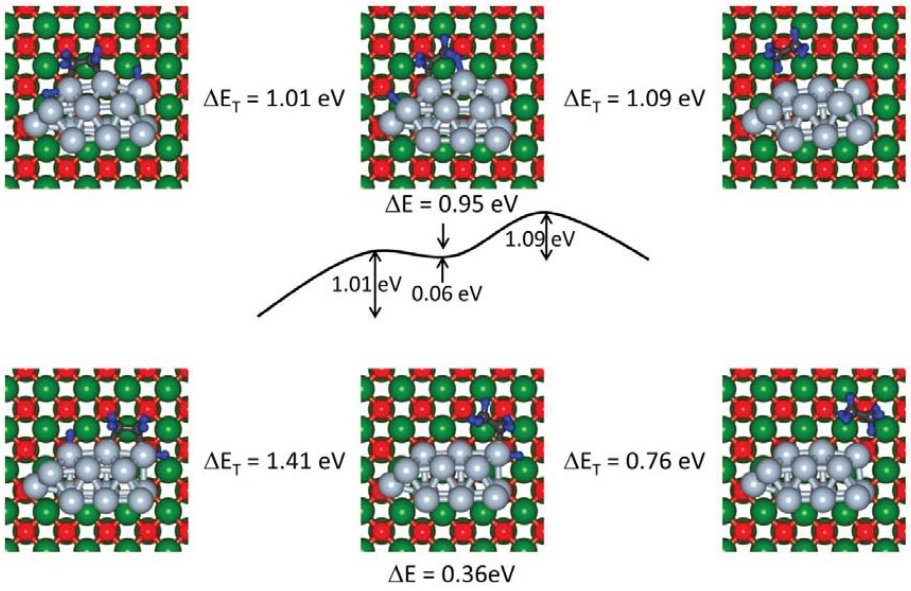

Supplementary Figure 31 | High-barrier pathways of ethylene hydrogenation on Pt_{13}/MgO.

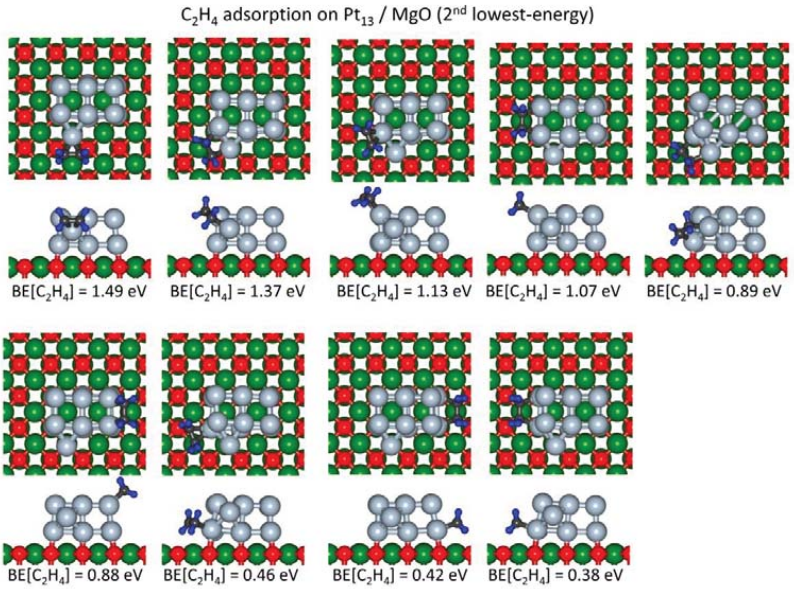

Supplementary Figure 32 | Binding sites of ethylene on the 2nd lowest isomer of the Pt_{13}/MgO system. see Supplementary Figure 11, isomer with ΔE = 0.14eV.

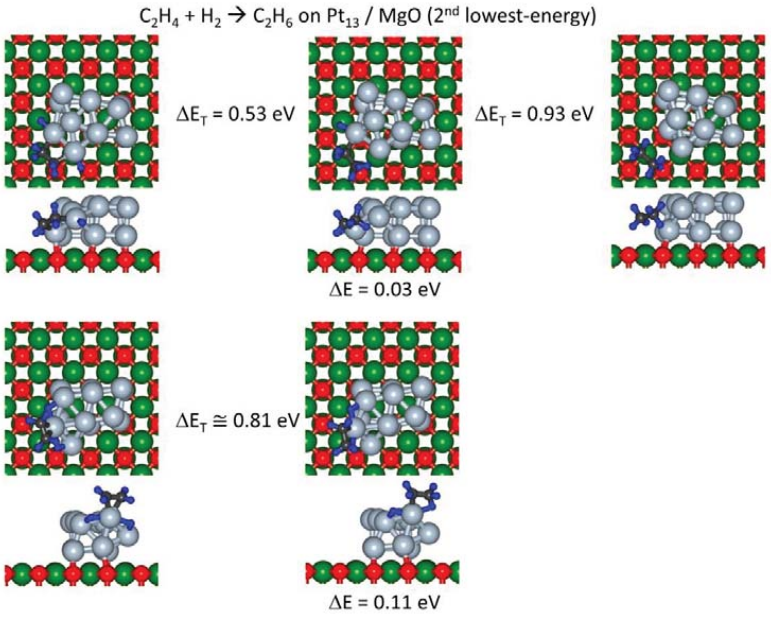

Supplementary Figure 33 | Higher-barrier pathways of ethylene hydrogenation on Pt_{13} (2^{nd} isomer)/MgO.

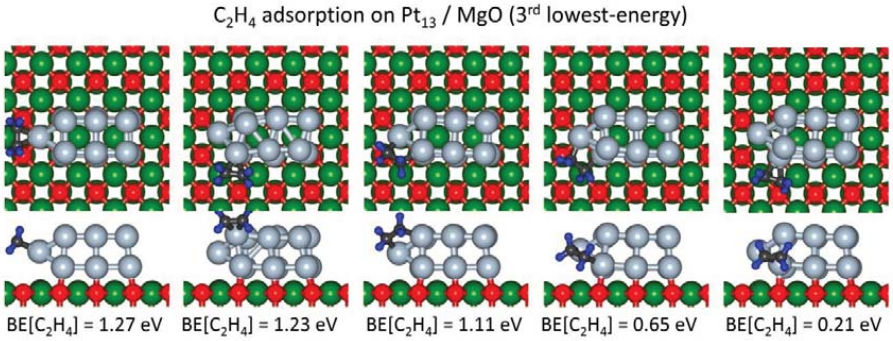

Supplementary Figure 34 | Binding sites of ethylene on the 3rd lowest isomer of the Pt_{13}/MgO system. See Supplementary Figure 11, isomer with ΔE = 0.23eV.

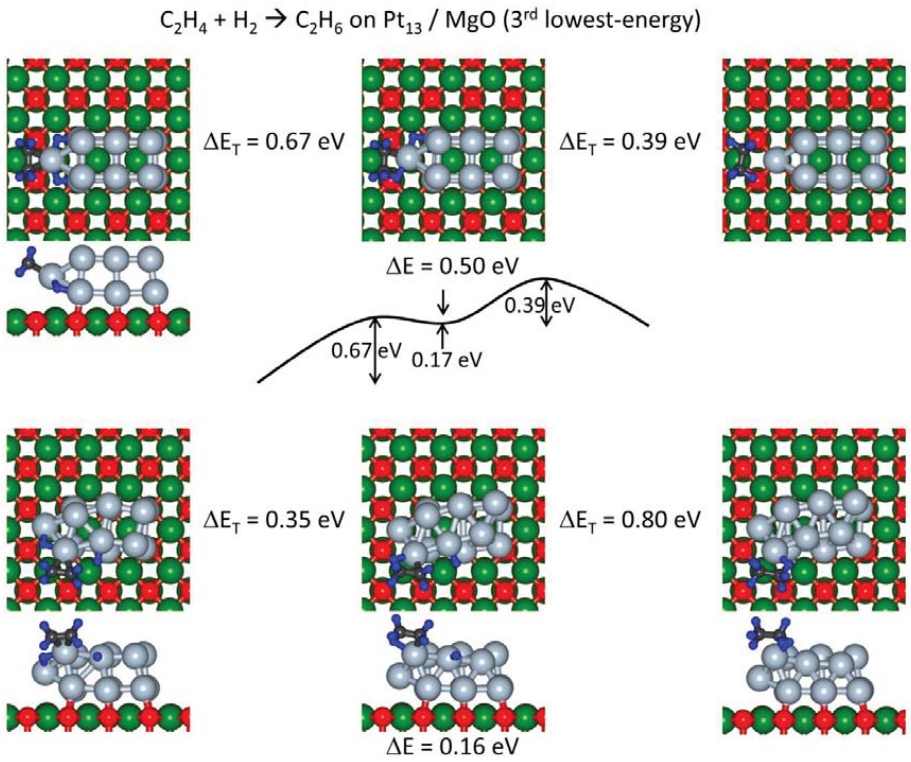

Supplementary Figure 35 | Low and hih energy barrier for ethelene hydrogenation on isomeric Pt_{13}/MgO. Low energy pathway (top row) and higher energy pathway (bottom row,) both starting from π-bonded C_2H_4 coadsorbed with dissociated H_2 on the 3rd-lowest isomer of the Pt_{13}/MgO system.

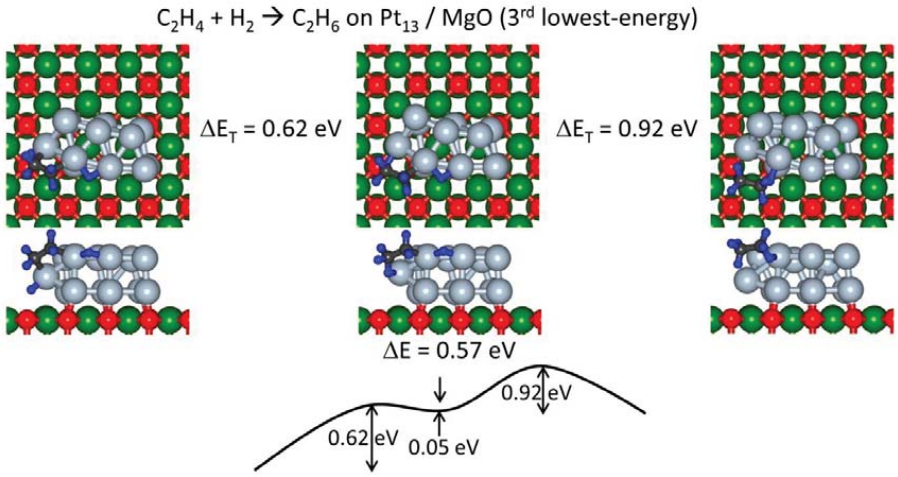

Supplementary Figure 36 | Higher energy pathway, starting from ethylene di-σ bonded with coadsorbed dissociated H_2. The path way is calculated for the 3rd-lowest isomer of the Pt_{13}/MgO system (compare to the high energy barrier patway calculated for the π-bonded C_2H_4 shown in Supplementary Figure 35).

Supplementary Note 1 | Structure insensitivity/sensitivity of ethylene hydrogenation

The Horiuti-Polanyi (HP) mechanism begins with hydrogen dissociation on the metal catalyst surface and following alkene (ethylene) adsorption, hydrogen additions occur in two subsequent steps: first, converting the alkene (C_2H_4) into an adsorbed alkyl intermediate (ethyl, -CH_2CH_3) followed by a second hydrogenation to form the alkane (ethane, C_2H_6) product which desorbs from the surface. Vibrational spectroscopy on single crystal surfaces revealed two strongly bound species present during the catalytic reaction on Pt(111) and Pt (100) surfaces (although with different relative concentrations)[1]: (i) di-σ ethylene where the carbon atoms of the adsorbed C_2H_4 molecule are each σ-bonded (in near sp^3 hybridization) to neighboring Pt surface atoms (see Fig. 2 in main article), and (ii) an ethylidyne (≡C-CH_3) molecule which may form through several pathways (for a recent discussion see [2]). Among these we note a favored reaction scheme that starts from adsorbed di-σ ethylene and proceeds through hydrogenation-dehydrogenation reactions with formation of the ethyl molecule (via hydrogenation) followed by two dehydrogenations: the first one converting CH_2CH_3 to ethylidene ($CHCH_3$) and the second yielding ethylidyne. Both the di-σ ethylene and ethylidyne molecules occupy three-fold hollow surface sites (involving reorganization of the neighboring metal atoms); on Pt(111) the ethylidyne is readily formed at around 280 K, and both, it and di-σ adsorbed ethylene are found on *all* platinum surfaces as stagnant spectators (that is they are strongly bound and do not participate in the reaction being measured). Instead the structure-insensitive hydrogenation of ethylene (occurring at higher hydrogen pressure and temperature) involves as reaction intermediates a weakly-bound π-bonded ethylene (in a near sp^2 hybridization) and the "half-hydrogenated" ethyl (C_2H_5) molecule; for a proposed reaction scheme see Fig. 13 in[3].

Real catalysis typically entails highly dispersed small particles supported on metal oxides or other high-surface-area substrates, whereas the results that were reviewed above were all obtained from investigations on extended single crystal metal surfaces. To bridge the so called "material - gap" attention has been shifted over the past decade to investigations involving finite particles on solid supports [4,5]. It is pertinent to remark here that the intrinsic size-effect of platinum particles supported on amorphous alumina in the hydrogenation of ethylene has been previously addressed [6]. In this investigation it was found that the reaction on Pt particles larger than 1.7 nm was structure insensitive and a turn over frequency (TOF) maximum was found for a particle size of ~ 0.6 nm (containing 10-20 atoms), with a similar

result found for a Pt/SiO_2 system. From these results, it was suggested that underlying the apparent structure sensitivity at small sizes was "increased atom accessibility"; this interpretation was reached, in the absence of realistic quantitative estimates, based on analysis that considered rather idealized simple polyhedral models and heuristic arguments. Additionally, the above experiment has been carried out on polydispersed particle samples, and a deconvolution of the effect of the particle-size distribution could not be made unambiguously. Several studies on the catalytic properties of Pt particles have been reported in the past few years, [see refs. 11-18 in Ref [7]] finding structure insensitivity for ethylene hydrogenation on particles in the range of 1-11 nm, albeit using polydispersed particle samples.

To summarize: current opinion is that while the adsorption of ethylene is structure sensitive, the overall hydrogenation reaction is structure insensitive.

Supplementary Note 2 | The Dewar-Chatt-Duncanson model

In all cases (including hydrogenation of C_2H_4 on Pt(111)) the microscopic reaction mechanism has been found to follow a frontier orbital description that find its origins in an adaptation of the Dewar-Chatt-Duncanson (DCD) model; here the addition of a hydrogen atom to the adsorbed molecule is described as an agnostic process (a term used to refer specifically to situations in which a hydrogen atom is covalently bonded to both a carbon and a transition metal atom[8], with the change in the C-H distance affecting (increasing) the energy gap between the bonding (σ_{CH}) and antibonding (σ_{CH}^*) states that shift away from the Fermi level as the C-H distance reduces (or equivalently the Pt-H distance increases). At the top of the activation barrier, the interaction between the σ_{CH} and σ_{CH}^* orbitals with the s-, p- and d-electrons of the Pt clusters brings about orbital mixing that may be described in term of the DCD donation and back-donation terms, culminating in attachment of the transferred H atoms (initially bonded to the Pt cluster) to the adsorbed molecule.

Supplementary references

1 Cremer, P. S., Su, X., Shen, Y. R. & Somorjai, G. A. Ethylene Hydrogenation on Pt(111) Monitored in Situ at High Pressures Using Sum Frequency Generation. *J. Am. Chem. Soc.* **118**, 2942-2949 (1996).

2 Zhao, Z.-J., Moskaleva, L. V., Aleksandrov, H. A., Basaran, D. & Rösch, N. Ethylidyne Formation from Ethylene over Pt(111): A Mechanistic Study from First-Principle Calculations. *J. Phys. Chem. C* **114**, 12190-12201 (2010).

3 Somorjai, G. A. & McCrea, K. Roadmap for catalysis science in the 21st century: a personal view of building the future on past and present accomplishments. *Appl. Catal. A* **222**, 3-18 (2001).

4 Gao, F. & Goodman, D. W. M\odel Catalysts: Simulating the Complexities of Heterogeneous Catalysts. *Annual Review of Physical Chemistry* **63**, 265-286 (2012).

5 St.Clair, T. P. & Goodman, D. W. Metal nanoclusters supported on metal oxide thin films: bridging the materials gap. *Topics in Catalysis* **13**, 5-19 (2000).

6 Masson, A. *et al.* Intrinsic size effect of platinum particles supported on plasma-grown amorphous alumina in the hydrogenation of ethylene. *Surf. Sci.* **173**, 479-497 (1986).

7 Sapi, A. *et al.* Recovery of Pt Surfaces for Ethylene Hydrogenation-Based Active Site Determination. *Catal. Lett.* **144**, 1151--1158 (2014).

8 Brookhart, M. & Green, M. L. H. Carbon-hydrogen-transition metal bonds. *J. Organometall. Chem.* **250**, 395-408 (1983)

3.1.1 Larger Cluster Sizes on MgO

In addition to the cluster sizes shown in the previous section, ethylene hydrogenation was also performed on larger platinum clusters supported on MgO. Figure 3.1 shows the TOF of all the sizes shown previously, as well as Pt_{20}, Pt_{25} and Pt_{30}.

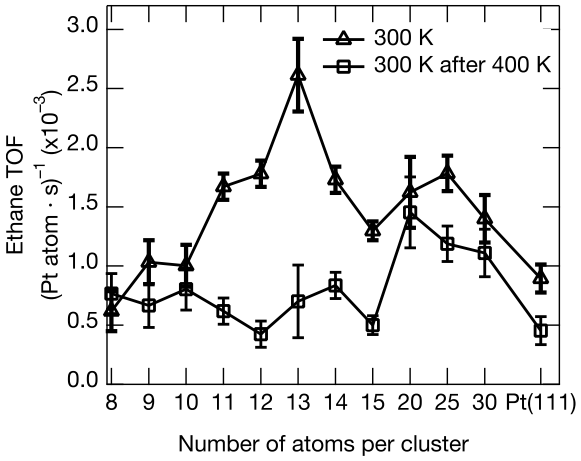

Figure 3.1: Ethylene hydrogenation TOF at 300 K for MgO supported clusters ranging from Pt_7 to Pt_{30}, and the TOF at 300 K after exposing the clusters to 10-15 pulses of ethylene at 400 K.

The trend in reactivity at 300 K again shows a size-dependent behavior, manifested in an increase in TOF for Pt_{20} and Pt_{25}, followed by a decrease for Pt_{30}. Pt_{30}, according to TEM data [135], approaches a particle diameter of 1 nm and therefore the activity for cluster sizes larger than 30 are expected to converge with that of Pt(111). This represents the border of the structure insensitive size regime, where no differences in activity are observed for different particle sizes [56].

The activity at 300 K after a temperature increase to 400 K is also shown in figure 3.1. Interestingly, the larger cluster sizes show an attenuated deactivation compared to Pt_{11-15}. Using the rationale developed for the smaller cluster sizes, it is probable that these larger sizes between 20-30 atoms, possess higher activation barriers for ethylene dehydrogenation pathways, but do not have the higher hydrogenation reactivity associated with Pt_{13}.

IRRAS coupled with CO adsorption was applied to investigate Pt_{20} and Pt_{30} before and after reaction. The spectra from these two sizes can be seen in figure 3.2. The position of the CO stretch for these larger sizes can be seen in figure 3.3. The results show the well known redshift as the particle size decreases. This is from under coordinated platinum atoms exhibiting more overlap with the $2\pi^*$ orbital of CO, thereby weakening the $C-O$ bond [64]. After performing the reaction at 300 K, an 18 cm^{-1} redshift is observed for Pt_{20} and a 40 cm^{-1} redshift for Pt_{30}. This larger redshift compared to the other cluster sizes shows the tendency of these larger particles, especially Pt_{30}, to possess bulk like properties, as Pt(111) exhibits an 83 cm^{-1} redshift after the 300 K reaction step. A strange observation for the

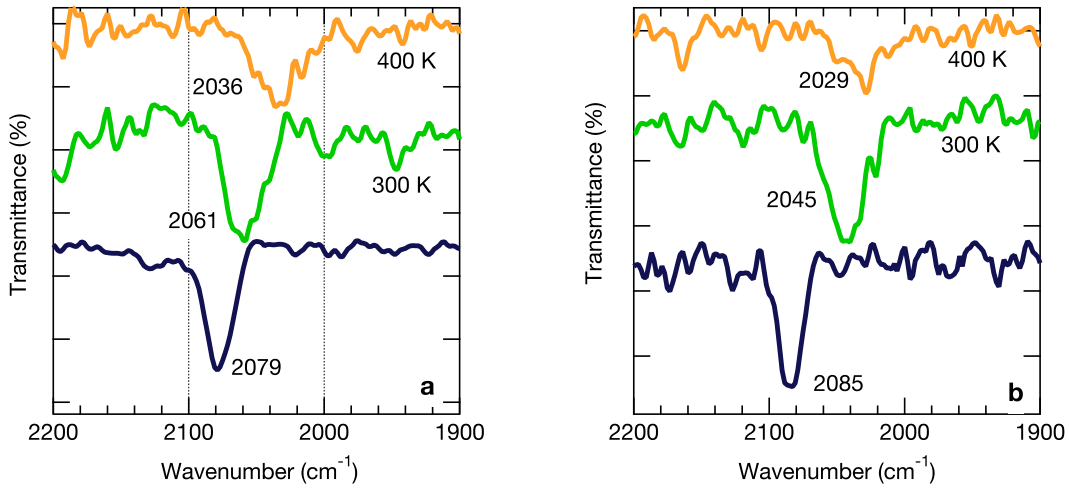

Figure 3.2: CO IRRAS from Pt_{20} (a) and Pt_{30} (b) before and after the reaction steps shown in figure 3.1.

larger cluster sizes is that an increased redshift after performing the 300 → 400 → 300 K reaction sequence is observed, but the activity change in figure 3.1 is minimal and does not lead to structure insensitivity. The additional redshift in the CO stretch observed on all cluster sizes after the 400 K temperature increase indicates that dehydrogenation of the carbon fragments present on the clusters has occurred, but on larger sizes, i.e. $Pt_{n>15}$, this has not poisoned, or adversely perturbed, active sites for ethylene hydrogenation.

In chapter 1.1.2 it was shown that ethylene has a diverse chemistry on platinum, with different adsorbed intermediates possible. It has also been pointed out that the dehydrogenated species on small particles has yet to be identified and is probably not ethylidyne [61]. The results here support this conclusion and show furthermore that whatever species is formed at 300 K can be further chemically changed with a temperature increase to 400 K, in contrast to Pt(111) where ethylidyne is stable from 300 to approximately 450 K. A probable dehydrogenation reaction product, that is not ethylidyne, would be a vinyl or ethylidene moiety. The temperature increase to 400 K then induces a further dehydrogenation step, possibly leading to ethylidyne. This seems like a plausible scenario, but still does not explain why on the larger cluster sizes the activity remains enhanced. As the data show that a second dehydrogenation occurs at 400 K, the same as with the smaller sizes ($Pt_{n<15}$), it seems that without learning more about the nature of these carbon species on each cluster size, any definitive statements on this point will remain elusive.

The results from larger cluster sizes has introduced a new size window where, again, the reaction characteristics display unique properties. The larger sizes display a surprising ability to maintain higher hydrogenation reactivity than the Pt(111) single crystal, even after the 400 K temperature increase, which was shown previously to induce passivation in the more active sizes Pt_{11-14}. Pt_{30} begins to show a disposition towards bulk like behavior,

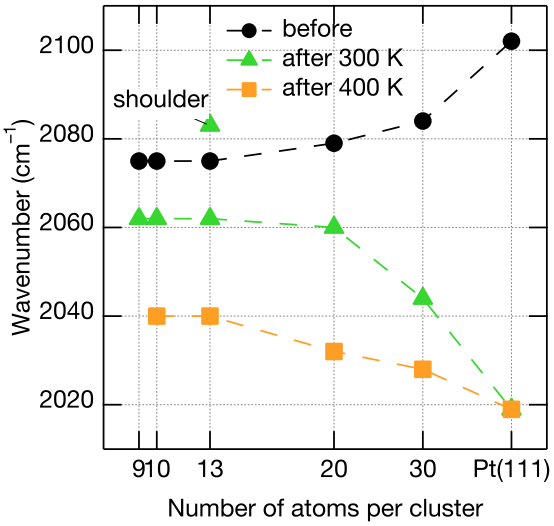

Figure 3.3: CO stretch position for MgO supported Pt_9, Pt_{10}, Pt_{13}, Pt_{20}, Pt_{30} and Pt(111) before and after reaction steps.

both in ethylene hydrogenation activity, and the CO frequency redshift after the reaction has been performed.

3.1.2 Comparison of Pt(111) Data to Ambient Pressure

The data from the Pt(111) single crystal yields the opportunity for a comparison of kinetic data to high pressure results. One of the major difficulties of such a comparison is the aforementioned dependency of reaction order on the pressure conditions (chapter 1.1.3), as well as the difficulty in determining the local pressure of ethylene during which the activity is measured. For sake of argument, a reaction order of unity can be assumed for hydrogen, and this generally is the approximate measured value on most systems. Equation 3.1 then shows the kinetic expressions used for this analysis:

$$r_{UHV} = k \cdot (p_{C_2H_4})^n \cdot p_{D_2} \tag{3.1}$$

$$r_{Amb} = k \cdot (p_{C_2H_4})^n \cdot p_{D_2} \tag{3.2}$$

where r_{UHV} is the rate under UHV conditions, r_{Amb} is the ambient pressure rate, k is the rate constant, p_x is the partial pressure of molecule (x), and n is the reaction order with respect to ethylene. The data for the ambient pressure experiment on Pt(111) (at 300 K) are 10 Torr ethylene and 100 Torr deuterium and are taken from ref. [23]. The TOF under these conditions was 7.95. For the UHV results, the deuterium pressure is known to be

$2{\cdot}10^{-6}$ mbar and the ethylene pressure was determined to be $5.93 \cdot 10^{-7}$ mbar (see chapter 2.2.6).

Plugging these values into the kinetic expression, assuming that k is constant and dividing, yields:

$$\frac{8.9 \cdot 10^{-4}}{7.95} = \left(\frac{5.93 \cdot 10^{-7}}{13.3322}\right)^{\mathrm{n}} \cdot \left(\frac{2 \cdot 10^{-6}}{133.322}\right)$$

which gives a value of n = -0.53. From ref. [23], the order with respect to ethylene was found to be -0.6 ± 0.05 which compares well with our value. This shows, in a first approximation, that UHV studies of ethylene hydrogenation can compare with ambient pressure experiments.

3.2 Ethylene Hydrogenation on SiO_2 Supported Platinum Clusters

With an established procedure for the reproducible synthesis of amorphous, 3-dimensional silicon dioxide films (see chapter 2.4), the effect of the metal-oxide support on ethylene hydrogenation was investigated on size-selected platinum clusters. It was shown in chapter 3.1 that sub-nanometer size clusters (7-15 atoms/particle) supported on MgO(100)/Mo(100), exhibit size-dependent behavior for ethylene hydrogenation, which was attributed to the formation of carbonaceous species co-adsorbed on the clusters. The influence of the metal-oxide support material on the same size clusters under the same reaction conditions is a topic that has not been studied. Changing thin film thickness has been shown to influence reactivity [103] and morphology [127] of gold clusters on MgO, and palladium cluster's reactivity on Al_2O_3 [105], but no study has been carried out on size-selected clusters under the same reaction conditions on two chemically different metal-oxide films. As smaller particles should exhibit a greater interaction with the thin film (see chapter 3.1), there is a large probability of being able to tune a variety of reactions on the same clusters size on two different supports.

In general, the chemical nature of the support material can be an important factor in understanding the potential effects on adsorbed metal particles. For example, the acidity of a metal-oxide can be an indicator of the type of charging to expect from the thin film which has been shown to influence adsorbate bonding [169] and also reactivity [170]. This section presents a combined TPR, PMB and IRRAS study on size-selected platinum clusters in the 8-20 atom/cluster range supported on a three-dimensional SiO_2 thin film grown on Pt(111). The experimental parameters were kept identical to those from the MgO data (see chapter 3.1), i.e. the same analysis chamber, instrumentation, gas dosing, cluster source, ambient background etc., which provides the most auspicious conditions, and prerequisites for comparison.

Results

TPR spectra for ethylene hydrogenation are displayed in figure 3.4a along with their respective integrals normalized to the number of platinum atoms in figure 3.4b. The TPR integration shows a size dependent reactivity, with Pt_8, Pt_{12}, Pt_{13} and Pt_{15} displaying lower reactivity compared to the other cluster sizes, but similar to Pt(111). Pt_9, Pt_{10} and Pt_{14} are all significantly more reactive. The temperature maximum is observed to be $\approx$ 175 K, which is 70 K lower than that observed for Pt(111).

Figure 3.5 shows the ethylene hydrogenation TOF at 300 K on size-selected platinum clusters supported on silica. Pt_{8-10} show an increase in activity with cluster size until a decrease for Pt_{12} and Pt_{13}. Pt_{14} then recovers the activity and another decrease is observed going to Pt_{20}. All cluster sizes, except for Pt_{13} show an increased activity compared to the Pt(111) single crystal. This observation is similar to that on Pt clusters supported by MgO, where in the sub-nanometer particle size regime the reaction exhibits structure sensitivity.

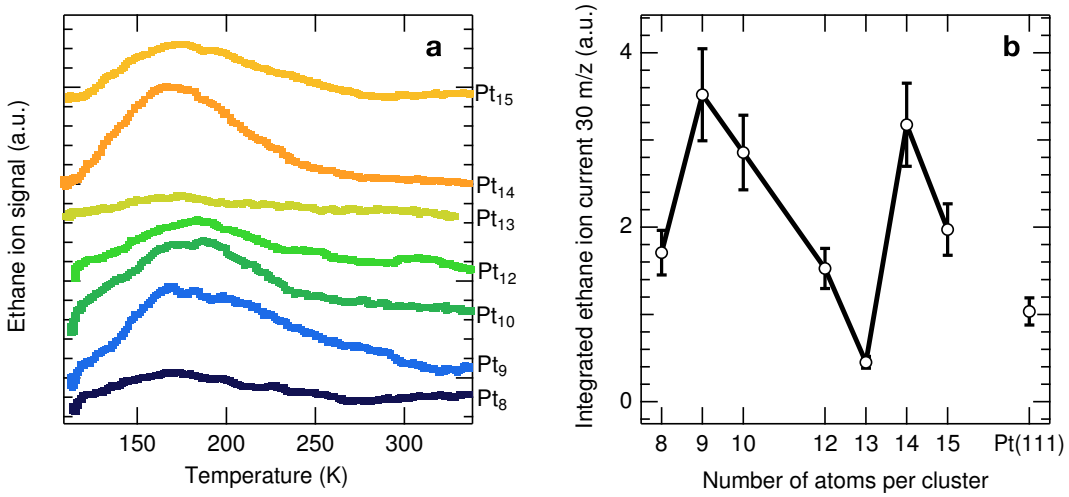

Figure 3.4: TPR (a) and corresponding integration per Pt atom (b) from size-selected platinum clusters supported on SiO_2. 0.4 H_2 molecules per surface atom were dosed followed by 0.4 C_2H_4 per surface atom.

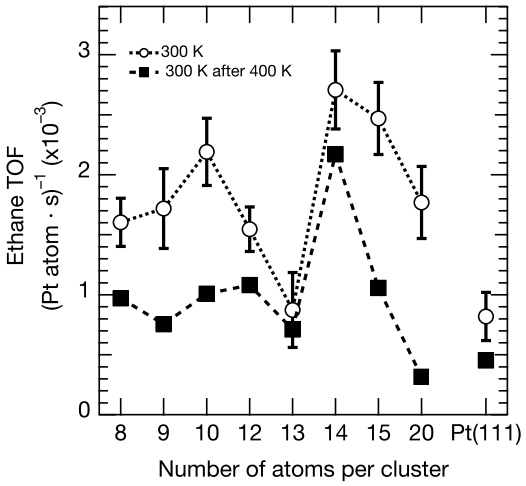

Figure 3.5: TOFs at 300 K for ethylene hydrogenation on SiO_2 supported Pt clusters within the size range of 8-20 atoms. The TOF at 300 K after 10-15 ethylene pulses at 400 K is also shown.

The TOF at 300 K after running the reaction at 400 K is also displayed in figure 3.5. All cluster sizes exhibit a deactivation down to the activity of Pt(111) and Pt_{13}, except for Pt_{14} which still remains more active.

After performing the reaction with the temperature step to 400 K, IRRAS was performed

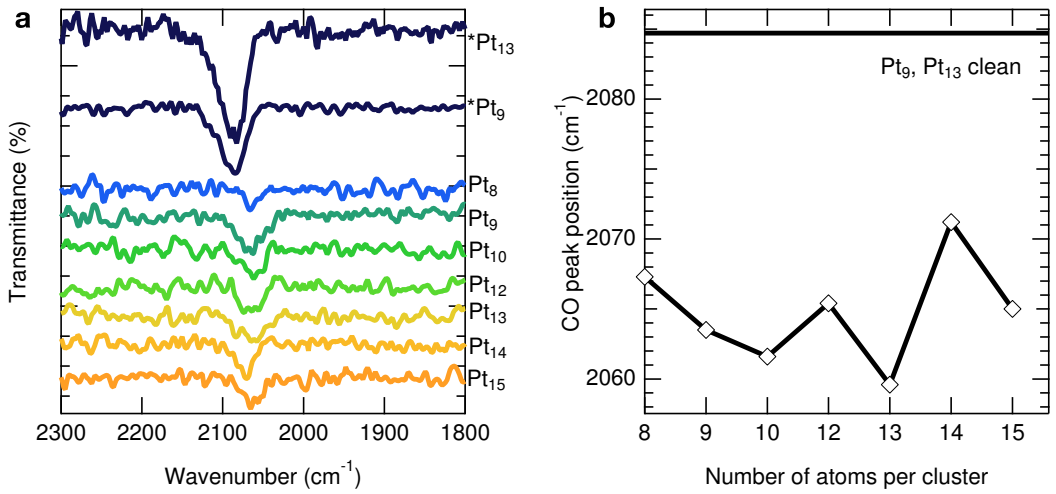

Figure 3.6: (a) IRRAS spectra of CO after running the complete reaction sequence in figure 3.5 (300 → 400 → 300 K). (b) peak position of the CO stretch from the spectra.

using CO as a probe molecule. The resulting spectra can be seen in figure 3.6a along with the peak position of the linear CO stretch in figure 3.6b. Included is the result from a clean sample of Pt_9 and Pt_{13}. The CO peak position from these two cluster sizes is taken as representative of this size regime, as results from MgO have also shown a constant peak position for these sizes (see figure 3.3). From the peak positions in figure 3.6b a clear redshift is observed for all cluster sizes after the reaction has been performed.

Discussion

The TPR and PMB data show a similar trend in terms of reactivity and activity. Pt_8, Pt_{12}, Pt_{13} and Pt_{15} from the TPR data show similar behavior to Pt(111), indicating that these cluster sizes are structure insensitive. However, the temperature shift compared to the Pt(111) indicates that the intrinsic activation barriers on these small clusters is lower. The higher reactivity of the other cluster sizes combined with this temperature shift is symbolic of a structure sensitive reaction. The PMB data supports this classification, except Pt_8, Pt_{12} and Pt_{15} are now within the more active size regime, and only Pt_{13} displays an activity similar to that of Pt(111). These results stand in stark contrast to the results from Pt/MgO, where Pt_{13} was observed, in both TPR and PMB, to have the highest activity. As the experiments were all performed under the exact same conditions in a UHV environment, the perplexing change in behavior between the two data sets must be directly attributed to the thin film support. This will be further discussed in chapter 3.3 but initial DFT results point to unique interaction between the clusters and the support, similar to that observed for palladium atoms on silica thin films grown on Mo(112) [129, 130].

Increasing the reaction temperature has been shown to open up dehydrogenation

reaction channels for ethylene, which cause the formation of carbon deposits on the cluster catalysts with a subsequent decrease in activity to structure insensitive values. For Pt/SiO_2, the same effect is observed for all clusters sizes except for Pt_{14}, which remains in the more active region. The lack of deactivation is a strong indication that the dehydrogenation pathways on this cluster size are not yet energetically accessible at 400 K. This size-dependency for dehydrogenation reaction pathways was shown in chapter 3.1, where the calculated difference in dehydrogenation activation barriers of Pt_{10} and Pt_{13} was over 0.5 eV.

On Pt/MgO, a similar redshift of the CO stretching frequency for Pt_{10} and Pt_{13} was observed after running the 300 $\rightarrow$ 400 $\rightarrow$ 300 K reaction sequence, but on SiO_2 a clear cluster size dependency is present. In particular, Pt_{13} is redshifted by 25 cm^{-1} and Pt_{14} by only 13.5 cm^{-1}, a difference of 12 cm^{-1} between the two cluster sizes. In general, Pt_{14} exhibits a smaller redshift than all the other cluster sizes on SiO_2 and MgO. As the redshift from the clean CO stretch frequency has been attributed to the presence of carbon species on the clusters, the IR results indicate a greater degree of carbon interaction with all cluster sizes compared to Pt_{14}, and most pronounced is the case of Pt_{13}. This carbon formation again causes a deactivation of the cluster catalysts, essentially masking any underlying activity differences and inducing size-insensitivity (as observed after 400 K for the sizes with a larger redshift). The data in figure 3.6 corroborates both the measured activity at 300 K and the subsequent deactivation after the temperature increase to 400 K, as the smaller redshift of Pt_{14} implies an intrinsic resistance to dehydrogenation reaction pathways which lead to carbon species on the cluster and a lowered activity. The dependency in cluster size observed in the IR data is another indication of a fundamental difference between the effect of the SiO_2 and MgO thin films on platinum clusters, indicating in particular that dehydrogenation activation barriers are changed on the same cluster size as one changes the support material.

Conclusion

The size-dependent ethylene hydrogenation activity of platinum clusters on SiO_2 using both temperature programmed and isothermal experiments showed a pronounced change in activity between Pt_{13} and Pt_{14}, with the latter showing not only an enhanced activity, but also a strong resistance to poisoning from ethylene dehydrogenation. This was corroborated by infrared spectroscopy, where the carbon induced redshift in the CO stretch was observed to be smallest for Pt_{14}.

The pronounced difference in the data from size-selected platinum clusters supported on MgO and SiO_2 indicate that cluster size effects can vary greatly by changing the support material. The next section will deal with comparing the results from these two different supports and an initial attempt at explaining the origins of the observed behavior.

3.3 Comparison of Ethylene Hydrogenation on Platinum Clusters Supported by MgO and SiO_2

The preceding two sections have shown that there is a unique size-dependency of ethylene hydrogenation activity on small platinum clusters supported on two different supports. It is apparent, however, that the two different supports impart very different behavior on individual cluster sizes, and this is most evident for Pt_{13}. In this section a comparison between the two supports is presented and discussed.

Comparing Activity

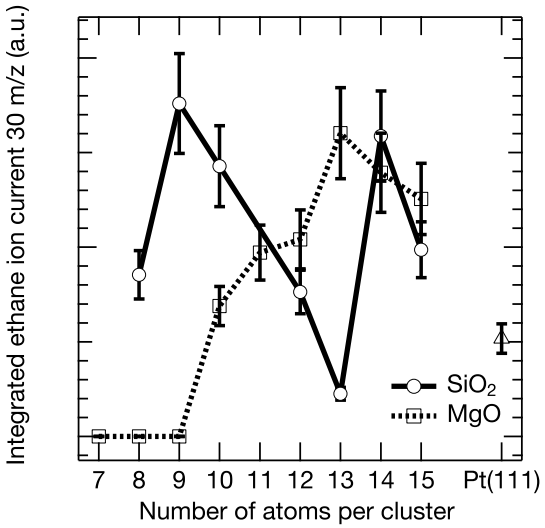

Figure 3.7: TPR integrals from size-selected platinum clusters supported on MgO (squares) and SiO_2 (circles).

Figure 3.7 shows the integrated TPR intensities normalized to the number of atoms for size-selected platinum clusters on MgO and SiO_2. The data clearly exhibit that the two different supports impart drastically different characteristics on the clusters as Pt_8 and Pt_9 show clear reactivity on SiO_2 compared to no reactivity on MgO. Most surprising is that the most reactive cluster size on MgO, Pt_{13}, is the most inactive on SiO_2. This exemplifies once again the unique nature of size-selected clusters. Beyond the fact that on the same support every size must be investigated to extract any meaningful trends, when changing between two unreactive supports, SiO_2 and MgO, each size can again show disparate behavior.

Figure 3.8 shows a combined graph of the ethylene hydrogenation TOFs for cluster sizes ranging from 8-20 atoms on SiO_2 and MgO, as well as the value measured on Pt(111). The first datapoint to stand out is the clear discrepancy between Pt_{13} on the two different supports. Pt_{13} is more than twice as active on MgO than on SiO_2. Aside from Pt_{13}, Pt_{8-10},

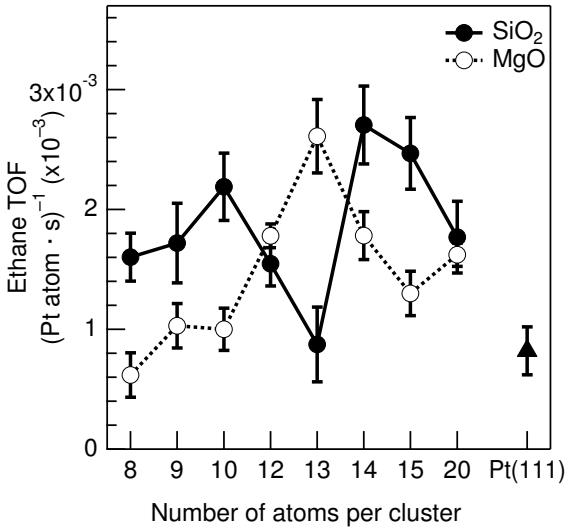

Figure 3.8: Ethylene hydrogenation TOF at 300 K for size-selected platinum clusters in the range of 8-20 atoms and the Pt(111) single crystal.

Pt_{14} and Pt_{15} all show an increased hydrogenation activity on silica, with Pt_{12} and Pt_{20} exhibiting almost identical TOFs.

The well known physical differences between an MgO and SiO_2 support include an increased acidity for SiO_2 [168]. This means that, compared to MgO, metal particles adsorbed on SiO_2 should be more electron deficient. An additional effect that must be taken into consideration is the underlying metal single crystal, i.e. Mo(100) and Pt(111), for MgO and SiO_2, respectively, as they possess work functions differing by almost 1.5 eV. Since the SiO_2 film is expected to be only 4-5 atomic layers thick and MgO about ten, this can lead to a polarization effect of the adsorbed cluster (see ref. [171]) or possible electron tunneling from the underlying metal [103, 126, 172], which all possibly influence reactivity or particle morphology (see chapter 1.3.2).

A general trend for the platinum clusters, Pt_{8-10}, Pt_{14} and Pt_{15}, on SiO_2 compared to MgO can be found based on the acid/base properties of the support. MgO is known to be a basic support and therefore it has a propensity to donate electron density, whereas the acidic SiO_2 tends to withdraw electron density. It has been shown on extended surfaces that a shift in the d-band center away from the Fermi level has been correlated to a lowering of the activation barrier for the ethylene hydrogenation but also an increase in the activation barrier for ethylene dehydrogenation [173]. The converse of this situation was also shown, in that a shift of the d-band center towards the Fermi level is associated with a lowered activation barrier for ethylene dehydrogenation and an increased barrier for hydrogenation. With this theoretical model, the activity differences between the two supports can be understood to a first approximation.

If other possible effects are neglected, the increase in activity on SiO_2 can be attributed

to a decrease in the cluster's electron density near the Fermi level and hence a lowering of the activation barrier for ethylene hydrogenation while concomitantly increasing the barrier for dehydrogenation. Similar behavior has also been observed on a nickel catalyst, where the electron rich MgO support was observed to influence the bonding of hydrogen which led to a decreased activity for the hydrogenation of pyridine to piperidine [170].

Experimental evidence for the effect of electron donation between the two supports can be observed in figure 3.9. The CO stretch frequency is seen to be redshifted on the MgO support by 10 cm^{-1}, indicating a greater degree of overlap between the metal and the CO $2\pi^*$ orbital, induced by electron donation from the more basic MgO support [64].

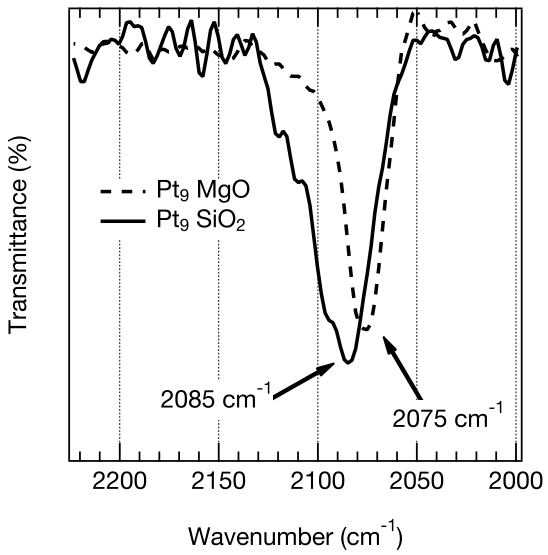

Figure 3.9: CO stretch on $Pt_9/MgO(100)$ and Pt_9/SiO_2. The redshift on the MgO surface can be attributed to electron donation into the cluster, enhancing the overlap between the metal and $2\pi^*$ CO orbital.

Pt_{13} presents an interesting case, as it exhibits a drastically different behavior compared to the other sizes and the effect is too substantial to explain through a simple charging argument. A change of particle morphology, such as a 2-D to 3-D transition observed for gold clusters on MgO, is a more probable explanation, but it is puzzling that Pt_{14} exhibits such a higher activity. Preliminary calculations currently being performed indicate that the lowest energy Pt_{13} and Pt_{14} structures have a much stronger interaction with the silica support, similar to that observed for adsorbed palladium atoms on silica thin films grown on Mo(112), where atoms can penetrate into the silica thin film [129, 130]. This leads to a fundamentally different adsorbed cluster structure as well as the orientation of the exposed atoms. The origins of this effect could be a combination of factors, such as the acidic SiO_2 support, the interaction of the local silicon-oxygen surface structures with the cluster and possibly the large work function of the underlying Pt(111) single crystal. The latter parameter can be investigated by growing the amorphous silica film on a Mo(112) single crystal in order to investigate the effects (if any) that the underlying metal support

has, and this experiment is currently in its preliminary stages. Determining which factor(s) leads to the structure insensitive activity of Pt_{13} is an ongoing research topic which will hopefully be addressed in the future.

The same activity of Pt_{20} on both surfaces is an indication that the Pt particles in this size range are beginning to show the known structure insensitivity, irrespective of the support. However, after the 400 K step, (see figures 3.1 and 3.5) Pt_{20} deactivates to the structure insensitive regime on SiO_2 but maintains the improved activity on MgO. This is again an example of each cluster size requiring in-depth investigations on each support but also demonstrates that even at 20 atoms per cluster one is still within the non-scalable size regime.

In the future it would be interesting to see if the activities on the two supports continue to be similar –and converge toward Pt(111) as the cluster size increases–, as well as further elucidating the differences between clusters supported on SiO_2 and MgO.

3.4 Influence of SiO_2 Support Stoichiometry on the Pt_{13} Catalyzed Ethylene Hydrogenation

In the previous section the metal-oxide thin film has been shown to effect unexpected changes in the reaction properties of size-selected clusters. Going one step further, the stoichiometry of the metal-oxide support can also be modified, as has been described in chapter 1.3.2. The Goodman Group readily identified that silica films grown on Mo(112) could be synthesized in a way which controlled the film stoichiometry. In particular, three types of silica films were produced: silicon rich, stoichiometric and oxygen rich [131]. Adsorption of silver atoms onto these films produced no observed influence of the defect sites, but catalytic reactivity has yet to be investigated [132]. In this section, the ethylene hydrogenation TOF on Pt_{13} clusters supported on the three aforementioned supports is presented. This set of experiments shows the real potential that model catalysis can have, as the UHV methodology allows for the ultimate control of all parameters (even the particle size down to a single atom) except for the one to be studied: support stoichiometry. This allows for the identification of individual characteristics which can underlie diverse reaction outcomes.

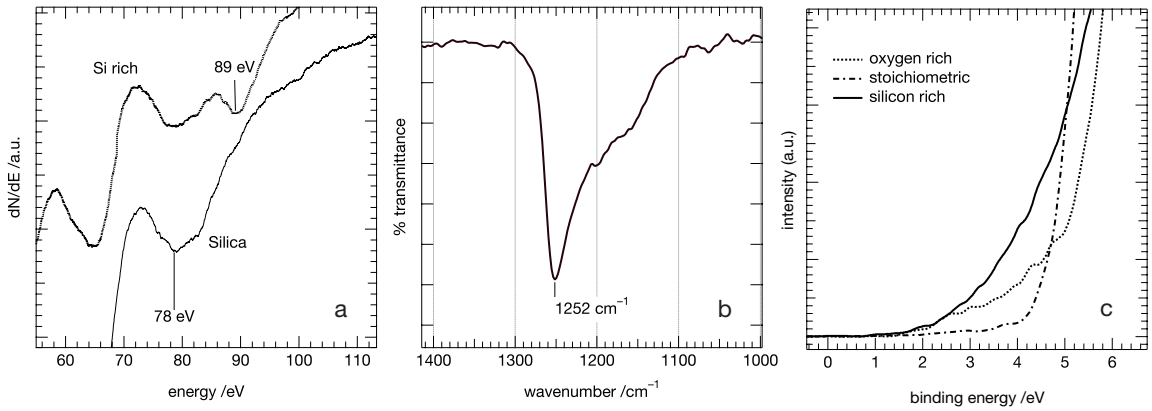

Figure 3.10: (a) AES showing the characteristic features of a stoichiometric and silicon rich film. (b) IRRAS showing the unequivocal identification of the stoichiometric film as three-dimensional. (c) MIES of the three film types with the oxygen rich and silicon rich film showing defect states within the band gap.

Three different vitreous silica supports were synthesized on a Pt(111) single crystal using the procedure described in chapter 2.4, wherein the stoichiometric film was thoroughly characterized with IRRAS, MIES, AES and TPD [174]. The supports can be identified by the silicon and oxygen stoichiometry and representative spectra revealing these differences can be seen in figure 3.10. The silicon rich film (figure 3.10a) was produced by growing the film for just over 10 minutes, at which point a characteristic Si-O transition at 89 eV is observed in the Auger spectrum. This feature remains intact as long as the film is not annealed at temperatures above 800 K. The stoichiometric silica film (figure 3.10a,b), SiO_2, can be generated by simply annealing the silicon rich film at 1200 K for 10 minutes in an oxygen background pressure of $2 \cdot 10^{-6}$ mbar at which point the well known bulk silica vibrational band can be observed with IRRAS at 1252 cm^{-1} [175, 176]. The oxygen rich

film is synthesized by growing the silica film for 10 minutes and then simply annealing at 800 K. This avoids the appearance of the Si-O feature seen in the Auger spectra but ensures that the film has bulk-like silica properties and completely covers the underlying Pt(111) surface. Oxygen defects, and those from silicon in the silicon rich film, can be observed in the MIES spectrum in 3.10c, where electron density is observed within the silica band gap [131].

These three films provide a unique opportunity to investigate a catalytic reaction on a single cluster size under ideal UHV conditions while changing the chemical and electronic properties of the support material. The silicon rich film is expected to exhibit electron donating properties, which, coupled with the high electronegativity of platinum, leads to electron rich clusters. The oxygen-rich surface will have more electron withdrawing properties, thereby pulling charge from a deposited cluster. The stoichiometric film represents the neutral case between the two extremes. These trends regarding the impact of oxygen and silicon rich films have been recently analyzed with theory in the literature for Pt_{13} supported on amorphous silica [133].

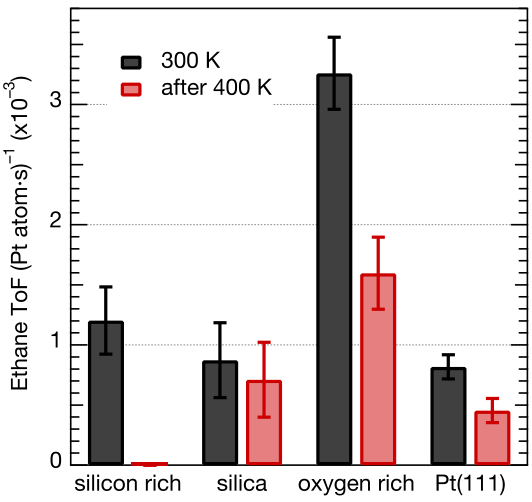

Figure 3.11: Pt_{13} TOF at 300 K as a function of silica support stoichiometry before (black) and after (red) pulsing at 400 K.

The TOF of Pt_{13} as a function of the type of silica support at 300 K along with the TOF measured after pulsing at 400 K are shown in figure 3.11. There is a clear reactivity trend which follows the support stoichiometry. The Pt_{13} clusters supported on the silicon rich film, and the stoichiometric support show similar activity at 300 K with the Pt(111) single crystal. The oxygen-rich film, however, displays a marked increase in activity at 300 K. After pulsing at 400 K the clusters supported by the silicon rich film are completely deactivated, while on the oxygen rich film approximately half the activity is lost. The clusters supported on the stoichiometric film show almost no deactivation, while the Pt(111) single crystal shows a noticeable decrease.

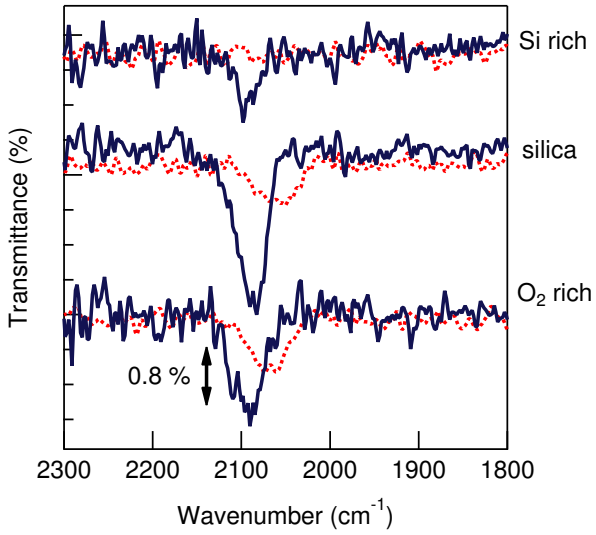

Figure 3.12: CO stretch on different Pt_{13} cluster samples before and after the 300 → 400 → 300 K reaction sequence. The top spectrum shows the signal from the silicon rich film, the middle from the stoichiometric film and the bottom from the oxygen rich film.

IRRAS spectra of CO adsorbed on Pt_{13} before and after the 300 → 400 → 300 K reaction sequence are shown in figure 3.12. The results from the clean cluster samples show a CO stretch peak centered at 2098, 2085 and 2090 cm^{-1} for the silicon rich, stoichiometric and oxygen rich films, respectively. The CO peak from the oxygen rich film is blueshifted compared to the stoichiometric film and shows a shoulder at even higher wavenumbers. This shift can be directly interpreted using the charge transfer mechanism, whereby decreased electron density in the cluster attenuates the interaction with the $2\pi^*$ orbital of CO, thus strengthening the CO bond [64]. The silicon rich film is a puzzling result, as based on the charging argumentation, a redshift should be observed when compared to the stoichiometric film. It is plausible that the silicon rich film has such a strong influence on the cluster, that a comparison of CO adsorption between the three films cannot be fully understood using just a simple charging argument. If, for example, the cluster morphology has significantly changed, then CO adsorption sites could be different than those from the same cluster on the other films. As has been previously discussed in chapter 1.3.2, electron donation into a particle can lead to a wetting of the surface, which was observed for gold. The high electronegativity of platinum indicates that this mechanism could also be operative here. If the Pt_{13} cluster is indeed wetting the surface, then a probable atomic arrangement would be a (111) like structure. The CO stretch measured on Pt(111) was 2102 cm^{-1} (see chapter 3.1), which is almost exactly the same as that measured on the silicon rich film. Another possibility is that the silicon rich film induces an enhanced dipole-dipole coupling on the cluster, which has been shown to blueshift the CO stretch frequency on Ni_{11} clusters [177].

Using the theoretical model described earlier (see chapter 3.3 and ref. [173]), the trends observed on the three different films can be rationalized. The silicon rich film

is characterized by under coordinated silicon, i.e. excess electrons, which means that an electronegative substance such as platinum should be able to acquire this excess charge and therefore increase its electron density near the Fermi level. This lowers the activation barrier for dehydrogenation compared to the stoichiometric film and this is the reason for the complete deactivation at 400 K (a complete covering of the cluster in dehydrogenated ethylene species). As this effect is not present on the stoichiometric film, in this case Pt_{13} possesses an activation barrier for this complete deactivation step that cannot be overcome and therefore no activity is lost.

The fact that at 300 K Pt_{13} displays a similar activity to Pt(111) on the silicon rich and stoichiometric support indicates that these systems exhibit structure insensitive behavior, i.e. activity invariance to particle size. This property has been postulated as stemming from carbon species present on the surface, which implies that at 300 K, ethylene adsorbed on Pt_{13} on both the silicon rich and stoichiometric support dehydrogenates to an as yet unknown species and induces structure insensitivity. Ethylidyne is the most attractive candidate, but, as shown in chapter 3.1, no experimental evidence for ethylidyne has been observed, and the small redshift observed (compared to Pt(111)), followed by a second redshift after heating to 400 K, implies that a species other than ethylidyne is forming on the clusters. One possibility, which has been previously mentioned, is ethylidene, which has been proposed as the reaction intermediate in the formation of ethylidyne on Pt(111) [178].

Converse to the silicon rich film, the oxygen rich film has the opposite effect on Pt_{13}, and pulls electron density from the clusters. This increases the activation barrier for dehydrogenation as well as lowering the barrier for hydrogenation. Clearly, the dehydrogenation process at 300 K leading to structure insensitivity is attenuated for Pt_{13} on the oxygen rich film, and therefore the activity for hydrogenation is higher. On the oxygen rich film, the temperature increase to 400 K, begins to initiate the dehydrogenation process leading to the structure insensitive behavior and therefore some activity is lost at 300 K.

After the full reaction sequence from figure 3.11, both the oxygen-rich and silica film show a similar CO stretch frequency, which is slightly redshifted from that of the as deposited clusters. This redshift is again attributed to CO co-adsorbed on platinum with carbon species [61, 62]. The silicon rich film shows no CO stretch indicating that the clusters are completely covered in a carbonaceous species. This exemplifies the effect of electron donation into the cluster, namely, increased electron density facilitates the formation of carbon deposits (through dehydrogenation pathways) and quenches ethylene hydrogenation activity. However, the failure of this charging argument to explain the CO stretch position on clean Pt_{13} means that another mechanism could be operative. The most straightforward explanation is that the single atom CO adsorption sites being probed on the clean clusters are not a predictor of ethylene dehydrogenation propensity. This is also to be expected as ethylene dehydrogenation products almost always require multiple atomic adsorption sites [79].

The poisoning and carbon contamination is displayed graphically in figure 3.13. The silicon rich and stoichiometric film both cause an initial dehydrogenation, similar to Pt(111), and this induces structure insensitivity in the Pt_{13} clusters on these supports. After the step to 400 K, the silicon rich film causes a poisoning of the clusters due to electron donation from

the support lowering dehydrogenation barriers. This does not occur on the stoichiometric film and therefore the clusters maintain the same activity. The oxygen rich film is able to resist the initial dehydrogenation found on the other supports due to electron withdrawing effects and therefore has a larger activity at 300 K. Ethylene on Pt_{13} on this support begins to dehydrogenate at 400 K and therefore activity is lost.

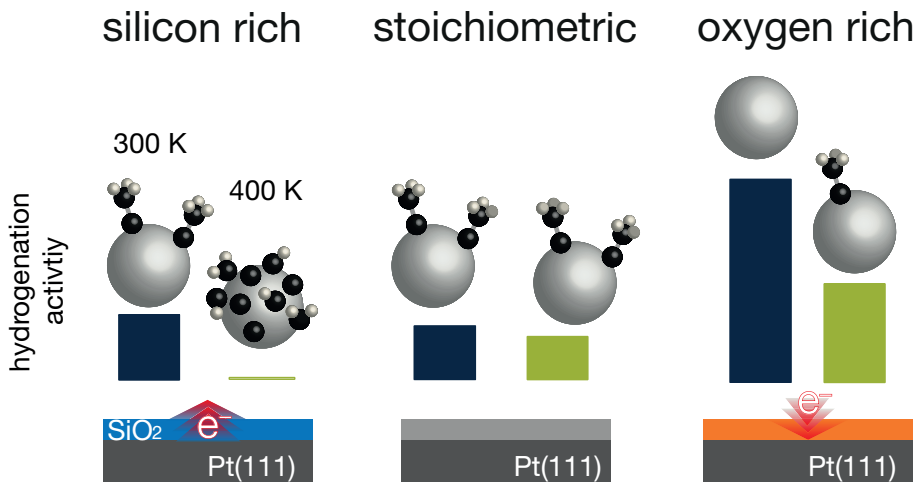

Figure 3.13: Carbon contamination on Pt_{13} supported on various silica thin films after reaction steps in figure 3.11

These data show that the support stoichiometry can be used to influence the selectivity of a hydrocarbon catalytic reaction. The tendency to hydrogenate or dehydrogenate ethylene was shown to follow charging arguments based on a model from extended surfaces. The charging arguments which explain the data, has also been recently predicted theoretically for exactly a Pt_{13} cluster adsorbed on these types of silica films. This shows a novel approach for influencing the selectivity of a hydrocarbon catalytic system.

3.5 Influence of Catalyst Metal on the Ethylene Hydrogenation

A last aspect to be investigated is the choice of metal catalyst for ethylene hydrogenation with the goal of these experiments to see if there was any trend between how polydisperse nickel, palladium and platinum clusters behaved under identical experimental conditions. The application of the cluster source as a nanoparticle synthesis tool allows for highly pure catalysts, where no influence from precursors, etc. can play a role. Additionally, they are deposited on a well-defined MgO(100) single crystal thin film, which provides a highly reproducible support and facilitates direct comparison between the metals. Reprinted from: Ethylene hydrogenation on supported Ni, Pd and Pt nanoparticles: Catalyst activity, deactivation and the d-band model, Vol. 333 , Andrew S. Crampton, Marian D. Rötzer, Florian F. Schweinberger, Bokwon Yoon, Uzi Landman, Ueli Heiz, pp. 51-58, Copyright (2016), with permission from Elsevier. Link to publication: http://www.sciencedirect.com/science/article/pii/S0021951715003516 and doi:10.1016/j.jcat.2015.10.023

Journal of Catalysis 333 (2016) 51–58

Contents lists available at ScienceDirect

Journal of Catalysis

journal homepage: www.elsevier.com/locate/jcat

Priority Communication

Ethylene hydrogenation on supported Ni, Pd and Pt nanoparticles: Catalyst activity, deactivation and the d-band model

Andrew S. Crampton [a], Marian D. Rötzer [a], Florian F. Schweinberger [a], Bokwon Yoon [b], Uzi Landman [b], Ueli Heiz [a,*]

[a] Technische Universität München, Lehrstuhl für Physikalische Chemie, Zentralinstitut für Katalyseforschung und Fakultät für Chemie, Lichtenbergstr. 4, 85748 Garching, Germany
[b] School of Physics, Georgia Institute of Technology, Atlanta, GA 30332-0430, USA

ARTICLE INFO

Article history:
Received 20 July 2015
Revised 29 September 2015
Accepted 13 October 2015

Keywords:
Model catalysis
Nickel
Palladium
Platinum
d-band
Ethylene de-/hydrogenation

ABSTRACT

Ethylene hydrogenation catalyzed at 300 K by 1–1.5 nm nanoparticles of Ni, Pd and Pt supported on MgO (100) with a narrow size-distribution, as well as the deactivation under reaction conditions at 400 K, was investigated with pulsed molecular beam experiments. Ni nanoparticles deactivate readily at 300 K, whereas Pd particles deactivate only after pulsing at 400 K, and Pt particles were found to retain hydrogenation activity even after the 400 K heating step. The hydrogenation turnover frequency normalized to the number of particles exhibited the trend, Pt > Pd > Ni. The activity/deactivation was found to scale with the location of the particles' d-band centroid, ε_c, with respect to the Fermi energy of the respective metals calculated with density-functional theory. An ε_c closer to the Fermi level is indicative of a facile deactivation/low activity and an ε_c farther from the Fermi level is characteristic of higher activity/impeded deactivation. CO adsorption, probed with infrared reflection absorption spectroscopy was used to investigate the clusters before and after the reaction, and the spectral features correlated with the observed catalytic behavior.

1. Introduction

The correlation between the electronic structure and the catalytic activity of materials is one of the fundamental principles underlying the understanding, and systematization of investigations in heterogeneous catalysis. It is also a powerful aid in the selection and design of catalysts, and the interpretation of trends measured across the periodic table. For transition metal catalysts, the d-band model has been particularly useful in investigating and systematizing the above correlation [1–3]. For model heterogeneous catalysis, ethylene hydrogenation represents the most basic hydrogenation reaction catalyzed by noble metals and as such it has been thoroughly investigated on Ni, Pd, and Pt single crystals [4–11], small particles [12–17], as well as a variety of supported metal catalysts [18]. A theoretical study of the ethylene hydrogenation on pseudomorphic Pd films grown on different metal single crystals, employing the d-band model, concluded that the activation barriers for hydrogenation and dehydrogenation depend on the location of the d-band center of the metal catalyst with respect to the Fermi level [19]. Specifically, a d-band center closer to the Fermi level facilitated a lower activation barrier for the dehydrogenation of ethylene to vinyl, and a higher activation barrier for the hydrogenation to ethane.

In this letter we report on an investigation of ethylene hydrogenation on MgO-supported Ni, Pd and Pt nanoparticles with a narrow size distribution of 1–1.5 nm. These investigations were carried out under ultra-high vacuum (UHV) conditions with the use of pulsed molecular beams to study the catalytic behavior of these clusters under isothermal conditions. Infrared reflection absorption spectroscopy (IRRAS), with CO as a probe molecule, was used to probe the catalysts before and after the hydrogenation reaction. Trends in the measured ethylene hydrogenation activity and in the deactivation of the cluster catalysts were found to correlate with the electronic structure of the supported metal particles, in particular the aforementioned d-band centroid model, calculated with first-principles density functional theory (DFT).

2. Methods

All experiments were performed in an UHV chamber with a base pressure of $2 \cdot 10^{-10}$ mbar shown in Fig. 1. The details of the chamber and cluster preparation are described elsewhere [20].

The MgO(100) thin film as support material was grown on a Mo (100) single crystal, and characterized, using techniques that have

* Corresponding author.

http://dx.doi.org/10.1016/j.jcat.2015.10.023
0021-9517/

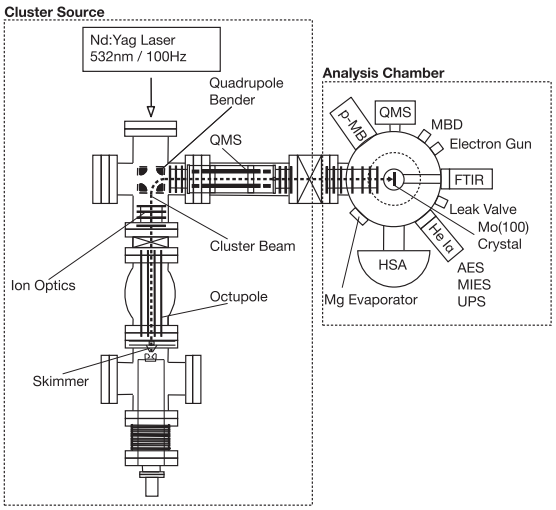

Fig. 1. Schematic of the experimental setup used for this study. On the left, the cluster source is depicted. The 2nd harmonic of a Nd:YAG laser impinges on a rotating metal target and the metal vapor is extracted though the skimmer into the vacuum. It is guided by electrostatic lenses to a bender, and then sent through a QMS which was operated as an ion guide. The particles are then deposited on a MgO (100)/Mo(100) thin film. The right side depicts the analysis chamber with a variety of surface science techniques including pulsed molecular beams, a quadrupole mass analyzer, infrared reflection absorption spectroscopy, Auger electron spectroscopy, Mg evaporator. See [20] for technical details.

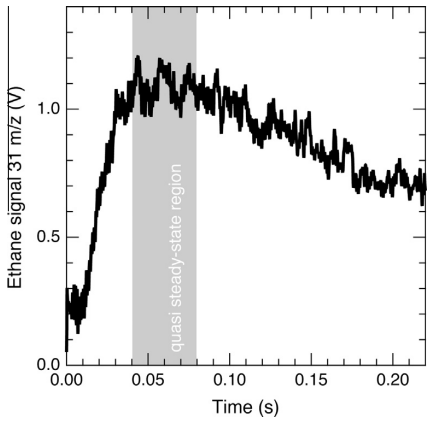

Fig. 2. Representative average of 20 pulses of the ethane (31m/z) signal from Pd nanoparticles at 300 K. The area marked in gray defines a region of quasi steady-state conditions, from which the catalytic data were extracted.

been previously described [21]. The Ni (99.98% purity, Goodfellow, England), Pd (99.95%, ESG Edelmetalle, Germany) and Pt (99.95%, Alfa-Aesar, Germany) nanoparticles are generated by a laser vaporization source, coupled with a mass spectrometer. For this work, the quadrupole mass spectrometer (QMS) (Extrel, USA) was operated with only the AC voltage component, which leads to the spectrometer functioning as an ion guide and a high pass mass filter. The size distribution is then determined by the settings of the cluster source [22]. Recent TEM studies on Pt have shown that the particle area distribution of a sample deposited with these settings can be fitted by a log-normal distribution [23–25] and approximately correspond to the size distribution from the source. In these studies a particle size distribution of 1–1.5 nm was determined and this is the expected size range studied in this paper. The coverage is measured by integrating the deposition current and assuming unit charge for all impinging particles. For all measurements, $9 \cdot 10^{12}$ particles were deposited onto the 0.785 cm^2 single crystal.

Catalytic measurements were performed at 300 K using a piezo driven valve, of in house design, to pulse (pulse width = 600 μs, 0.1 Hz) well defined amounts of ethylene (3.5 purity, Westfalen, Germany) onto the sample. The local pressure of ethylene was determined to be $5 \cdot 10^{-7}$ mbar, from the time profile and QMS response from a single ethylene pulse. A background deuterium (100% purity, Westfalen, Germany) pressure of $2 \cdot 10^{-6}$ mbar was applied and the crystal was held approximately 0.5 cm from the piezo valve nozzle and the skimmer leading to the QMS (Balzers QMA 430, Liechtenstein) for reactivity studies.

Fig. 2 shows an average of 20 pulses for the Pd samples. Between a time of 40 ms and 80 ms we define a 'quasi steady state' regime and use this value for the calculation of turnover frequencies (TOF) [26]. The TOF was determined by calibrating the QMS with a monolayer CO TPD from Pt(111) in the same chamber, and determining the sensitivity factor with respect to ethane (m/z = 30). The measured mass was 31 = m/z as deuterium was used to minimize any possible background signals. Since the QMS calibration was performed with non-deuterated ethane, a systematic error is present in the absolute TOF values calculated. However, it has been shown experimentally that the sensitivity factor of the m/z = 31 fragment of $C_2H_4D_2$ with respect to non-deuterated ethane, at an ionizing voltage of 70 V, is approximately a factor of $\frac{1}{2}$ and therefore the values reported here are of the correct order of magnitude [27].

IRRAS (Thermo Electron Corp. Nicolet FT-6700) measurements were performed in single reflection mode, with an external MCT-detector (Thermo Electron Corp., MCTA-TRS), at 100 K after dosing 10 L of CO (256 scans, 4 cm^{-1} resolution). One spectrum was taken with a freshly deposited sample of clusters and the other spectrum after performing the aforementioned catalytic experiment with a freshly deposited sample. This technique of probing metal particles with CO before and after performing ethylene adsorption and/or hydrogenation, has often been used to investigate particle morphology and the presence of carbon deposits [28–32].

For modeling the experimentally obtained size-distribution a representative cluster of 30 atoms for each metal was chosen. To model M_{30}/MgO (M = Ni, Pd, and Pt) systems, we employed a four-layer MgO(100) slab with a calculational cell consisting of 7×6 unit cells; each layer consisted of 42 Mg and 42 oxygen atoms with the atoms in the bottom layer held stationary (at the experimental lattice constant of 4.21 Å) and the atoms in the other three layers allowed to relax to the optimal atomic arrangement; optimal configurations (using a conjugate gradient search) were determined when the calculated energy converged within 0.001 eV. The bare M_{30} cluster was positioned on the MgO(100) surface, and its configuration was optimized, see [33] for details regarding the particle geometry. The calculational supercell, which included the MgO(100) slab and a 24 Å thick vacuum region, was periodically replicated.

The first-principles electronic structure calculations used the density-functional theory (DFT) method employing the VASP-DFT package, using a plane-wave basis with a kinetic energy cutoff of 400 eV, PAW pseudopotentials [34] and the PBE generalized gradient approximation (GGA) for the exchange–correlation potential [35]. Γ-point sampling of the Brillouin zone was used. The angular-momentum projected local density of states (PLDOS) was calculated by using the spherical harmonics, Y_{lm}, projectors (in particular l = 2 for the d-band PLDOS). The PLDOS of the entire cluster

is the sum of the projected contributions calculated for each of the atoms of the adsorbed metal cluster, with the position of the atom taken as the center for the angular-momentum projection and the integration carried out over a sphere of radius 1.22 Å (Ni), 1.37 Å (Pd, Pt) about each of the atoms; this radius is taken as half of the average bond-length to minimize overlap.

3. Results

Fig. 3a displays the pulse-to-pulse ethane signal from deposited Ni, Pd and Pt clusters at 300 K. The pulse-to-pulse signal from the same samples measured at 100 K is also included as a background and can be seen to be approximately zero. The plotted Pd and Pt results also show, in addition, the ethane signal measured at 300 K after exposing the samples to 15 ethylene pulses at 400 K. Since the Ni data show a fast deactivation of the particles after only 15 pulses at 300 K, the effect of heating to 400 K was not probed. For Pd nanoparticles the product (ethane) signal at 300 K slowly decreases as the number of pulses increases, but catalytic activity maintains even after 20 pulses. However, after pulsing the nanoparticles with ethylene at 400 K the sample is observed to have lost all hydrogenation activity. The Pt nanoparticles exhibit a similar behavior at 300 K to that of Pd, but hydrogenation activity persists even after ethylene pulsing at 400 K.

The IR spectra of CO adsorbed on the Ni, Pd and Pt nanoparticles before and after the experiments in Fig. 3a are displayed in Fig. 3b. The Ni spectrum before the reaction shows a single peak at 2088 cm^{-1}, with a broad feature at 1900–1950 cm^{-1} corresponding to linear and bridge bonded CO, respectively. After the reaction has been run, the bridge bonded peak disappears and the linear

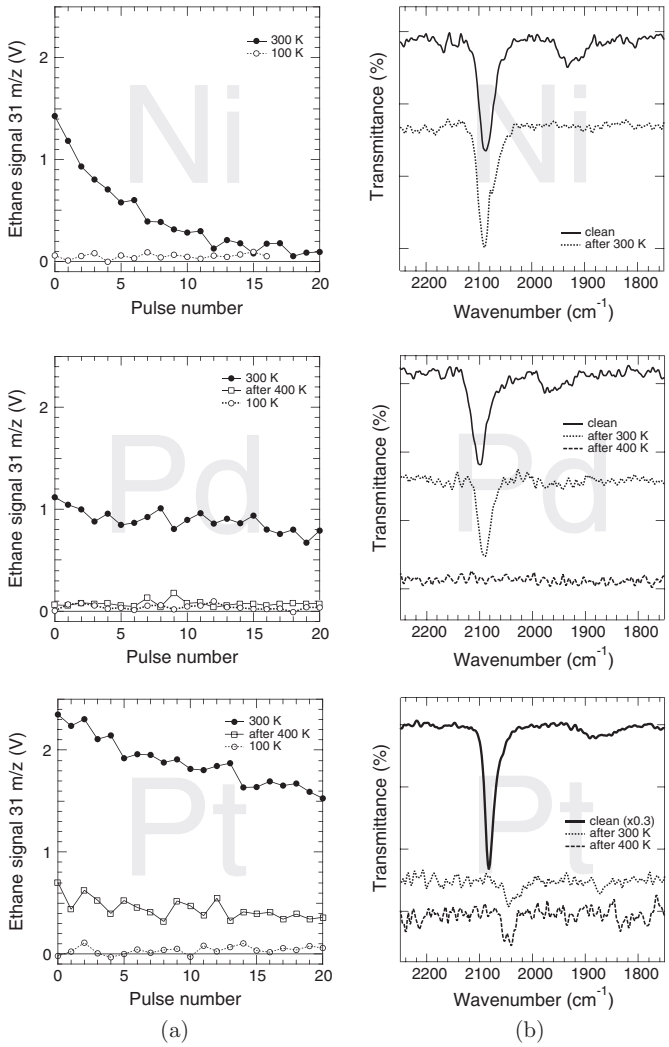

Fig. 3. Pulsed molecular beam (a) and IRRAS (b) data from Ni, Pd and Pt nanoparticles of the size range 1–1.5 nm. In all cases the data in (a) show the ethane signal progression of single ethylene pulses, and the data shown in (b) were recorded before and after the completion of the experiments shown in (a). The Ni data (top panels) in (a) show the pulse-to-pulse ethane signal taken at 300 K and at 100 K, and in (b) measurement of the linear- and bridge-bonded CO stretch on clean Ni nanoparticles and after pulsing at 300 K. The Pd data (middle panels) in (a) depict the pulse-to-pulse data at 100 K, at 300 K, and at 300 K but subsequent to pulsing ethylene at 400 K. The Pd IR spectra in (b) show the linear- and bridge-bonded CO stretch on a clean sample, and after the corresponding experiments displayed in (a), except the one at 100 K. The Pt measurements (bottom panels) in (a) and (b) were performed under the same conditions described for the Pd data.

bonded peak shifts slightly to higher wavenumbers and now has a shoulder at 2075 cm^{-1}. The Pd IR spectrum before the reaction shows the linear and bridge bonded CO species at 2098 cm^{-1} and 1960 cm^{-1}, respectively, as with Ni. Following ethylene pulsing at 300 K the bridge bonded disappears and the linear peak is slightly redshifted to 2088 cm^{-1}. After running the reaction subsequent to ethylene pulsing at 400 K, no CO peak is observed.

The Pt IR spectrum before the reaction shows a linear bonded species on the clean particles at 2082 cm^{-1} and bridge bonded centered at 1870 cm^{-1}. After pulsing at 300 K there is a redshift in the CO stretch and after ethylene pulsing at 400 K, a double peak at 2054 and 2040 cm^{-1} is measured. Both Pt spectra after the two reaction cycles ('300 K' and 'after 400 K', Fig. 3a) display a very strong decrease in signal intensity compared to the Ni (top) and Pd (middle) cases.

A cluster consisting of 30 atoms was chosen as a model for the studied nanoparticle systems, as this size has dimensions similar to the size distribution investigated. To determine optimal structures of the adsorbed 30-atom clusters on the Mg(100) surface we have focused on the Pd_{30} cluster; once alternative structural motifs have been constructed and tested, the optimal ones have been relaxed subject to the characteristic pseudopotentials of the three metals (Ni, Pd, and Pt). On the clean surface of MgO(100) (prior to adsorption of the Pd_{30} cluster), the oxygen atoms of the topmost layer are located 0.053 Å higher (i.e., toward the vacuum) than the Mg atoms. After adsorption of the pyramidal Pd_{30} cluster on the surface, the 16 O atoms in the area covered by the base of the cluster (see Fig. 4) are found to be located 0.009 Å higher than the corresponding 16 Mg atoms. The ground-state structure of the supported Pd_{30} cluster is found to be a square pyramid (Fig. 4a and b), with the energy of the optimal Pd_{30}(pyramid)/MgO system found to be lower by 1.84 eV compared to an alternative (fully relaxed) two-layer structure (Fig. 4c and d). On the other hand, the (vertical) adsorption energy of the two layer Pd_{30} cluster isomer to the MgO(100) surface is slightly higher (E_{ads}(2-layer) = 10.45 eV) than that of the pyramidal cluster (E_{ads}(pyramid) = 10.08 eV); E_{ads} [vertical binding energy, vBE, in Table 1] is calculated as the difference between the total energies of the individual components (free cluster and clean surface, both in the configurations of the optimally adsorbed system) and that of the combined adsorption system Pd_{30}/MgO. As found in earlier first principles investigations, free [36] and supported [37] Pd clusters exhibit spontaneous magnetization. The optimal minimum energy configuration of the Pd_{30} (pyramidal) cluster has a spin state with $N\uparrow - N\downarrow = 4$ (where $N\uparrow$ is the number of spin-up electrons and $N\downarrow$ is the number of spin-down electrons); the energy of this magnetic state is lower by 0.05 eV than that with no magnetic moment, i.e., $N\uparrow = N\downarrow$. In the current investigation we give results for the non-magnetic states of the clusters, because of the very small influence that they have on the geometrical and electronic properties of the adsorbed clusters. Details of the structural parameters for the ground-state pyramidal and 2-layer structural isomers of the 30-atom Ni, Pd and Pt clusters are given in Tables 2 and 3.

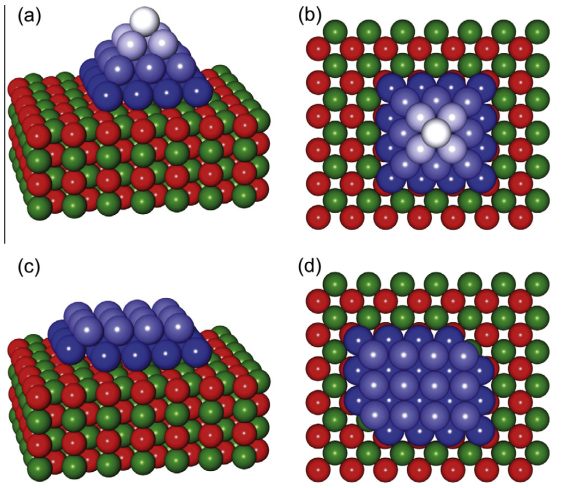

Fig. 4. Optimal structures of pyramidal (a, b) and two-layer (c, d) Pd_{30} clusters adsorbed on a MgO(100) surface. The atoms of the Pd_{30} clusters are colored by a blue color gradient for clarity. The color depends on the distance of the Pd atoms from the MgO surface, with those closer to the MgO surface depicted in a deeper blue color. The Mg atoms are green spheres and the oxygen atoms are red. The adsorbed pyramidal Pd_{30} cluster is 1.84 eV lower in energy than the two-layer cluster. (a) and (b): Pyramidal Pd_{30}. The numbers of Pd atoms from the bottom Pd layer to the top layer are 16, 9, 4, and 1. The spacing between the bottom Pd layer and the topmost O (Mg) atoms under the Pd_{30} cluster is 2.267 Å (2.258 Å). The spacing between the bottom (first) layer and the Pd cluster and the layer above it (second layer) is d_{12} = 1.987 Å. The spacing between the consecutive layers is d_{23} = 1.795 Å and d_{34} = 1.790 Å. The average Pd–Pd bond length on the bottom edge of the Pd_{30} pyramid is 2.66 Å. (c) and (d): Two-layer Pd_{30}. The numbers of Pd atoms of lower and upper Pd layers are 18 and 12. The spacing between the lower Pd layer and the topmost O (Mg) atoms under Pd_{30} is 2.284 Å (2.283 Å). The spacing between two Pd layers is d_{12} = 1.999 Å.

Table 1
Total energy differences and vertical binding energy of the X_{30} cluster to the Mg(100) surface. $\Delta E = E_{tot}[X_{30}(2\text{-layer})/MgO] - E_{tot}[X_{30}(pyramid)/MgO]$ and $vBE = E[\text{frozen } X_{30}] + E[\text{frozen MgO}] - E_{tot}[X_{30}(2\text{-layer})/MgO]$ where X = Ni, Pd, and Pt. E[frozen X_{30}] and E[frozen MgO] denote the total energies of the isolated 30 atom cluster and the bare underlying MgO surface in the geometries they have when the cluster is adsorbed on the surface (for which the total energy is given as $E_{tot}[X_{30}$(pyramid or 2-layer)/MgO]). Energies in units of eV.

	Ni_{30}/MgO	Pd_{30}/MgO	Pt_{30}/MgO
ΔE (eV)	2.47	1.84	3.93
$vBE_{pyramid}$ (eV)	11.09	10.08	10.99
$vBE_{2\text{-layer}}$ (eV)	12.19	10.45	11.87

Table 2
Interlayer and interatomic distances for the pyramidal adsorbed clusters. d_{1-O} is the spacing between the bottom layer of the cluster and the top 16 O (oxygen) atoms under the cluster, d_{1-Mg} is the spacing between the bottom layer of the cluster and the top 9 Mg atoms under the cluster, d_{1-2} is the spacing between the bottom and the 2nd cluster layer, d_{2-3} is the spacing between the 2nd cluster layer and the 3rd cluster layer, d_{3-4} is the spacing between the 3rd cluster layer and the 4th cluster layer. ⟨bl⟩ is the average bond length of the bottom edge atoms of the cluster.

	Ni_{30}(pyramid)/MgO	Pd_{30}(pyramid)/MgO	Pt_{30}(pyramid)/MgO
d_{1-O} (Å)	2.035	2.267	2.272
d_{1-Mg} (Å)	2.107	2.258	2.262
d_{1-2} (Å)	1.557	1.987	1.970
d_{2-3} (Å)	1.622	1.795	1.762
d_{3-4} (Å)	1.659	1.790	1.838
⟨bl⟩ (Å)	2.482	2.664	2.645

Table 3
Interlayer and interatomic distances for the two-layer adsorbed clusters d_{1-O} is the spacing between the bottom layer of the cluster and the top 18 O atoms under the cluster, d_{1-Mg} is the spacing between the bottom layer of the cluster and the top 10 Mg atoms under the cluster, d_{1-2} is the spacing between the bottom and the 2nd cluster layer, and ⟨bl⟩ is the average bond length of the bottom edge atoms of the cluster.

	Ni_{30}(2-layer)/MgO	Pd_{30}(2-layer)/MgO	Pt_{30}(2-layer)/MgO
d_{1-O} (Å)	2.055	2.284	2.271
d_{1-Mg} (Å)	2.123	2.283	2.268
d_{1-2} (Å)	1.583	1.999	1.981
⟨bl⟩ (Å)	2.541	2.691	2.668

4. Discussion

From comparison of the catalytic reactivities of the three metal nanoparticles (Fig. 3a) a clear trend can be established as a function of an elements period within the same group of the periodic table. In particular, the tendency for a group 10 metal to deactivate in the course of ethylene hydrogenation increases as the period decreases – namely, Ni (period 4) exhibits the highest deactivation tendency (see sharp falloff of the activity with increasing number of pulses in Fig. 3a), whereas Pt (period 6) displays a much reduced deactivation (maintains reactivity after ethylene pulsing at 400 K), and Pd (period 5) shows an intermediate behavior (deactivation only after ethylene pulsing at 400 K).

In the case of extended surfaces it has been found (based on the d-electron model [1,2]) that the activation barrier for ethylene hydrogenation increases as the d-band center shifts closer to the Fermi level, while the activation barrier for dehydrogenation, resulting in formation of carbonaceous species (that poison the hydrogenation reaction) decreases [19]. To assess the validity of these results for the case of the nanoparticles investigated here, we show in Fig. 5 the DFT calculated DOS for M_{30}/MgO(100), [M = Ni, Pd and Pt], evaluated for the structure of the representative 30-atom adsorbed cluster shown as inset in the middle panel of Fig. 5, which has been found previously to be the lowest – energy optimal configuration for Pd_{30}/MgO [33]. The cluster d-band centers, $\varepsilon_c^M = E_c^M - E_F$, for M = Ni, Pd, and Pt, where E_F is the Fermi energy of the cluster, obtained from the d-level projected DOS (PLDOS, see red-filled areas in Fig. 5), were calculated to be $\varepsilon_c^{Ni} = -1.33$ eV, $\varepsilon_c^{Pd} = -1.86$ eV, $\varepsilon_c^{Pt} = -2.40$ eV. These values are rather similar to those calculated for the d-band centers in extended (bulk) Ni, Pd, and Pt surfaces −1.29 eV, −1.89 eV and −2.25 eV, respectively [38], and thus the general conclusions drawn about the hydrogenation reaction catalyzed by the extended (bulk) surfaces of these metals [19] are expected to extend to the supported nanoparticles in the size-range of 1–1.5 nm. This expectation is apparent from Fig. 3a for deactivation and quantified in Fig. 6 where the scaling of ε_c^M with the hydrogenation activities of the three nanoparticle systems is depicted. Here, the hydrogenation activity is expressed in terms of the hydrogenation (ethane production) TOF, which has been calculated per particle from the average of pulses showing a constant activity. Fig. 6 illustrates that for the clusters of M = Ni, Pd and Pt studied here the predicted scaling of the hydrogenation reaction TOF with ε_c^M is maintained.

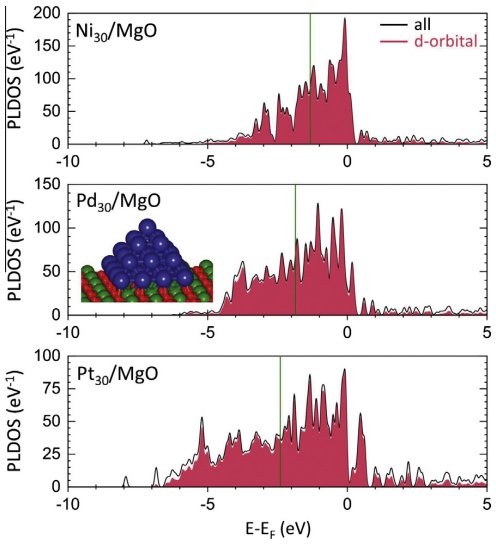

Fig. 5. Density of states (DOS, black line) and d-band projected DOS (PLDOS, red filled) for the optimized pyramidal structures of Ni_{30} (top), Pd_{30} (middle) and Pt_{30} (bottom) clusters adsorbed on Mg(100). The structure of the Pd_{30}/Mg(100) system is shown as an inset in the middle panel (Pd atoms in blue, Mg in green and oxygen in red); the numbers of Pd atoms from the bottom Pd layer to the top layer are 16, 9, 4, and 1 (for geometrical details see Table 2). The calculated d-electron centers, ε_c^M, are marked by green vertical lines.

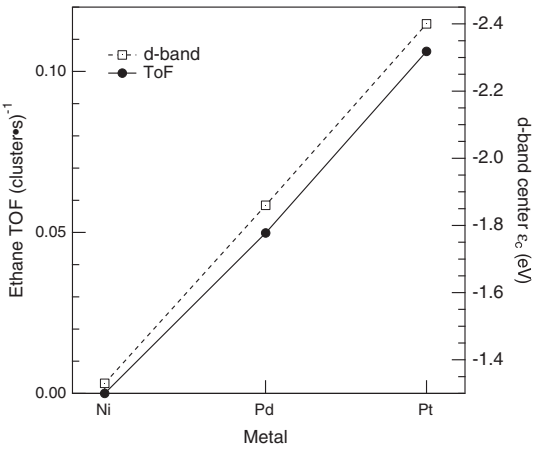

Fig. 6. Ethane TOF for Ni, Pd and Pt nanoparticles plotted against the calculated d-band center, ε_c (see Fig. 5). The closer the d-band center is to the Fermi level, the lower the activity and the more facile the deactivation (see Fig. 3a). The TOF has been calculated from pulse 17 to 20 for all three metals.

While the general behavior of the catalysts can be well rationalized with the d-band model, the microscopic picture is still uncertain. In particular, Ref. [19] only investigated an initial dehydrogenation step to a vinyl intermediate, which may or may not be the final product/intermediate at a given temperature on a given metal.

In order to investigate features of the nanoparticle surface subsequent to reaction, IRRAS of CO (see Fig. 3b) provides a powerful tool, where a decrease in the CO absorption intensity can indicate a loss of adsorption sites and a redshift indicates co-adsorbed carbonaceous species [28–32].

After pulsing at 300 K the signal corresponding to bridge-bonded CO on Pd disappears, but the linearly-adsorbed CO adsorption peak is still visible and 10 cm^{-1} redshifted, see Fig. 3b. The loss of CO adsorption sites from ethylene decomposition on Pd has been previously reported [28,29] and our results support this finding. Following pulsing at 400 K, however, resulting in completely deactivating the catalyst (Fig. 3a), there is no detectable CO adsorption, implying blocking of all CO adsorption sites on the particles by carbon species. Such a complete loss of all CO adsorption sites (down to the detection limit) has, to our knowledge, not been observed previously; Refs. [28,29] only investigated the effect of ethylene decomposition at 300 K, with ethylidyne identified as the resulting surface species [29]. The effect of higher temperatures on further dehydrogenation and subsequent CO adsorption has not been studied, but a temperature-dependent model of ethylene adsorption on Pd nanoparticles has been proposed based on temperature programmed desorption, IRRAS and X-ray photoelectron spectroscopy studies [13]. The authors identified three distinct temperature regions: (i) $T < 300$ K, here ethylene can be π- or di-σ-bonded to Pd particles, with the di-σ species being able

to convert to ethylidyne between 250 and 300 K. (ii) 300 K < T < 400 K, ethylidyne can dehydrogenate further to form C–H surface species. (iii) T > 400 K, in this region a complete dehydrogenation occurs and the particles are covered with carbon deposits. This proposed model explains the results of the CO IRRAS experiments here. At temperatures up to 300 K a limited amount of dehydrogenation occurs, possibly to form ethylidyne, which is evidenced by the loss of bridge bonded CO and slight redshift. At temperatures up to 400 K further dehydrogenation reactions occur, resulting in the blocking of CO adsorption sites (no CO IR peak), and poisoning of the ethylene hydrogenation reaction.

The similarity between the IR spectra taken after the two reaction cycles on Pt indicates that the temperature increase to 400 K has not caused any reduction in CO adsorption capability, but from Fig. 3a has caused a decrease in activity. The activity decrease is likely an effect of accelerated ethylene dehydrogenation at elevated temperatures leading to increased site blocking, as particles in this size range have been previously proposed to suppress ethylene dehydrogenation at 298 K [17]. The presence of a small CO peak after the 400 K step is not unexpected, as CO is able to penetrate an ethylidyne surface layer [31] and dehydrogenated fragments tend to have low saturation coverages due to repulsive interactions [39]. The identification of ethylidyne as the dehydrogenation product on Pt nanoparticles is, however, tenuous at particle sizes smaller than 2 nm, but the redshift and loss of intensity compared to the clean spectrum clearly indicate the presence of carbon. It has been proposed that ethylidyne requires 3-fold symmetric sites to form and that smaller particles present less of these sites, thereby suppressing ethylidyne formation [40,29]. Experimental identification of the carbon species chemical nature after reaction at 300 K was not possible, due to the very low concentration of catalyst used. One possibility is the formation of ethylidene, which was shown to be the likely precursor of ethylidyne on Pt(1 1 1) [41]. If this species is produced at 300 K as a precursor to ethylidyne, then it would in effect have a similar site blocking effect as ethylidyne, as both species would have similar coverages. Ethylidene would have, however, a different chemical interaction with Pt, as it would only be coordinated with two Pt atoms, therefore attenuating its effect on ethylene hydrogenation. Ethylidyne would then be the next species formed at temperatures up to 400 K, and its coordination with three Pt atoms leads to a distinct deactivation of the catalyst, but its relative coverage is the same as ethylidene and therefore CO adsorption properties remain the same.

The measured intensity decrease on the Pt nanoparticles has also been shown on Pt(1 1 1), where the linear CO stretch intensity decreased by a factor of seven when the surface was pretreated with ethylene at 330 K, which led to a saturated coverage of the dehydrogenated product, ethylidyne (upon which ethylene hydrogenation activity is still present) [10,30]. Our results show a factor of 15, but we have only dosed 10 L of CO, whereas the experiment on Pt(1 1 1) was performed in a background CO pressure of 10^{-7} Torr. Additionally, our result showing CO adsorption after the 400 K step is consistent with findings that ethylidyne further dehydrogenates on Pt(1 1 1) only at temperatures above 400 K, which would then lead to a more complete sight blocking [42,43].

Ni presents unexpected behavior as the supported nanoparticles appear to have lost all activity after a few pulses at 300 K as well as all bridge bonded CO (Fig. 3a), but still display a linear CO feature of similar intensity to that of the clean sample (Fig. 3b). It is plausible that the dehydrogenation product at 300 K on Ni is displaced by CO, in contrast to Pt where a signal of small intensity was observed. This behavior has been observed previously on a Ni catalyst supported by silica, where at room temperature the largest IR absorption peak attributed to ethylene disappeared upon CO adsorption [44]. Another possibility is the selective ethylene dehydrogenation on active Ni sites for hydrogenation, in contrast to Pd or Pt where dehydrogenation occurs primarily elsewhere. This also follows our interpretation from the d-band model. Taking into consideration a single active site for hydrogenation on Ni, Pd and Pt, then from our interpretation, ethylene dehydrogenates on Ni exactly at this site with a high probability due to a low activation barrier. On Pt and Pd, the probability to dehydrogenate at an equivalent site is much lower due to a higher activation barrier. In both cases, the activation barrier is a direct result of the d-band center, ε_c^M. This interpretation, however, only requires ethylene dehydrogenation on the active sites on each particle, leaving open the possibility that ethylene dehydrogenation does not occur (as observed on Ni), or does occur (as observed on Pt), on other sites where CO can adsorb. This leads, in the case of Ni, to a very similar CO IR spectrum compared to the clean sample, but the presence of carbon is still observable (loss of bridge bonded and redshifted shoulder in Fig. 3b). For Pt however, the before and after spectra show strong deviations as ethylene dehydrogenates not on an active site (as with Ni) but rather where it competes with CO for adsorption sites. Supporting this point are data from single crystal studies, where the dehydrogenation pathway on Ni proceeds through a vinyl species to acetylene [45], in contrast to Pt where ethylene is known to form ethylidyne from possibly an ethylidene intermediate [41]. These two different reaction pathways indicate a fundamental difference in ethylene dehydrogenation chemistry, which can also be occurring on nanoparticles. Another important aspect to consider is that even though dehydrogenation fragments such as vinyl and ethylidyne form very strong bonds to the surface, their coverages remain relatively low due to repulsive interactions [39]. The large signal intensity of CO on Ni, could also be due to strong repulsive interactions between carbon fragments leaving a large amount of free CO adsorption sites. This puzzling result from Ni indicates that there is still much unknown about the molecular nature of dehydrogenation intermediates and products on small nanoparticles.

5. Conclusion

In conclusion, from pulsed molecular beam experiments of the hydrogenation reaction of ethylene catalyzed by Ni, Pd, and Pt nanoparticles, of 1–1.5 nm size-distribution, we found that the reaction efficiency (TOF) scales with the metal's calculated d-band center, using a 30 atom particle as a model system for the calculations. In this size range of nanoparticles the behavior observed was shown to be that which would be expected from extrapolating bulk properties to this size range, i.e. the calculated d-band center and predicted reactivity of bulk structures are, in this case, scalable down to 1–1.5 nm particles. Specifically, the proclivity for nanoparticle deactivation was observed to decrease in the order Ni > Pd > Pt, following the reverse trend exhibited by the calculated d-band centroid of the clusters, that is $\varepsilon_c^{Ni} < \varepsilon_c^{Pd} < \varepsilon_c^{Pt}$. Clearly, understanding of the molecular details and elucidation of the mechanisms of the involved reactions, require microscopic treatment, beyond the d-electron model used here. Certain aspects that remain unresolved are evidenced by the IRRAS results recorded after running the reaction at 300 K, where a complete deactivation of Ni did not preclude the adsorption of CO. This is indicative of a different interaction and composition of the inhibiting species compared to e.g. Pd, where a complete deactivation was coupled with no CO adsorption. Additionally, Pt showed a very limited CO adsorption after reaction at 300 K even though the activity was measured to be higher per cluster than Pd.

The application of a cluster source for the production of nanoparticles is a powerful tool for explorations of heterogeneous catalytic reaction. Comparative experimental investigations with

respect to the identity of the metal catalysts, in combination with DFT calculations of model systems, can offer insight into subtle differences between the surface chemical behavior within the scalable size range. These basic studies can serve as a foundation for the investigation of size-selected clusters in the sub-nanometer size range (i.e. particles containing up to 20 atoms) where the scalability of these properties breaks down [46,47].

Acknowledgments

B.Y. was supported by the Air Force Office for Scientific Research (AFOSR) and U.L. by Grant No. FG05-86ER45234 from the Office of Basic Energy Sciences of the US Department of energy (DOE). Computations were made at the Gatech Center for Computational Materials Science. The experimental work was supported by an ERC Advanced Grant and the DFG (Project HE 3454/23-1).

References

[1] B. Hammer, J.K. Nørskov, Electronic factors determining the reactivity of metals, Surf. Sci. 343 (1995) 211–220.
[2] B. Hammer, J.K. Nørskov, Theoretical surface science and catalysis, Adv. Catal. 45 (2000) 71.
[3] I. Chorkendorff, J.W. Niemantsverdriet, Concepts of Modern Catalysis and Kinetics, second ed., Wiley-VCH, Weinheim, 2007.
[4] F. Zaera, Hydrogenation and H-D exchange of chemisorbed ethylene on Ni (100) under vacuum, J. Catal. 121 (2) (1990) 318–326, http://dx.doi.org/10.1016/0021-9517(90)90240-K.
[5] C. Egawa, S. Oki, M. Kaneko, N. Minami, I. Suzuki, Ethylene hydrogenation on a Ni(100) surface, Surf. Sci. 427–428 (1999) 268–271, http://dx.doi.org/10.1016/S0039-6028(99)00277-0.
[6] D. Stacchiola, S. Azad, L. Burkholder, W.T. Tysoe, An investigation of the reaction pathway for ethylene hydrogenation on Pd(111), J. Phys. Chem. B 105 (45) (2001) 11233–11239, http://dx.doi.org/10.1021/jp012553h.
[7] H. Molero, D. Stacchiola, W.T. Tysoe, The kinetics of ethylene hydrogenation catalyzed by metallic palladium, Catal. Lett. 101 (3–4) (2005) 145–149, http://dx.doi.org/10.1007/s10562-005-4881-7.
[8] F. Zaera, G.A. Somorjai, Hydrogenation of ethylene over platinum (111) single-crystal surfaces, J. Am. Chem. Soc. 106 (8) (1984) 2288, http://dx.doi.org/10.1021/ja00320a013.
[9] F. Zaera, On the mechanism for the hydrogenation of olefins on transition-metal surfaces: the chemistry of ethylene on Pt(111), Langmuir 12 (1) (1996) 88, http://dx.doi.org/10.1021/la9407020.
[10] P.S. Cremer, X. Su, Y.R. Shen, G.A. Somorjai, Ethylene hydrogenation on Pt(111) monitored in situ at high pressures using sum frequency generation, J. Am. Chem. Soc. 118 (12) (1996) 2942, http://dx.doi.org/10.1021/ja952800t.
[11] A. Tilekaratne, J.P. Simonovis, M.F. López Fagúndez, M. Ebrahimi, F. Zaera, Operando studies of the catalytic hydrogenation of ethylene on Pt(111) single crystal surfaces, ACS Catal. 2 (11) (2012) 2259–2268, http://dx.doi.org/10.1021/cs300411p.
[12] Y. Hadj Romdhane, B. Bellamy, V. De Gouveia, A. Masson, M. Che, Structure sensitivity: hydrogenolysis of n-butane and hydrogenation of ethylene on nickel clusters condensed onto amorphous silica, Appl. Surf. Sci. 31 (3) (1988) 383–401, http://dx.doi.org/10.1016/0169-4332(88)90101-8.
[13] S. Shaikhutdinov, M. Heemeier, M. Bäumer, T. Lear, D. Lennon, R. Oldman, S. Jackson, H.-J. Freund, Structure–reactivity relationships on supported metal model catalysts: adsorption and reaction of ethene and hydrogen on Pd/Al_2O_3/NiAl(110), J. Catal. 200 (2) (2001) 330–339, http://dx.doi.org/10.1006/jcat.2001.3212.
[14] A. Binder, M. Seipenbusch, M. Muhler, G. Kasper, Kinetics and particle size effects in ethene hydrogenation over supported palladium catalysts at atmospheric pressure, J. Catal. 268 (1) (2009) 150–155, http://dx.doi.org/10.1016/j.jcat.2009.09.013.
[15] R.D. Cortright, S.A. Goddard, J.E. Rekoske, J.A. Dumesic, Kinetic study of ethylene hydrogenation, J. Catal. 127 (1) (1991) 342–353, http://dx.doi.org/10.1016/0021-9517(91)90230-2.
[16] R.M. Rioux, H. Song, J.D. Hoefelmeyer, P. Yang, G.A. Somorjai, High-surface-area catalyst design: synthesis, characterization, and reaction studies of platinum nanoparticles in mesoporous SBA-15 silica, J. Phys. Chem. B 109 (6) (2005) 2192, http://dx.doi.org/10.1021/jp048867x.
[17] H. Song, R.M. Rioux, J.D. Hoefelmeyer, R. Komor, K. Niesz, M. Grass, P. Yang, G. A. Somorjai, Hydrothermal growth of mesoporous SBA-15 silica in the presence of PVP-stabilized pt nanoparticles: synthesis, characterization, and catalytic properties, J. Am. Chem. Soc. 128 (9) (2006) 3027–3037, http://dx.doi.org/10.1021/ja057383r.
[18] J. Horiuti, K. Miyahara, Hydrogenation of Ethylene on Metallic Catalysts, NSRDS-NBS (13), 1968.
[19] V. Pallassana, M. Neurock, Electronic factors governing ethylene hydrogenation and dehydrogenation activity of pseudomorphic PdML/Re (0001), PdML/Ru(0001), Pd(111), and PdML/Au(111) surfaces, J. Catal. 191 (2) (2000) 301–317, http://dx.doi.org/10.1006/jcat.1999.2724.
[20] U. Heiz, F. Vanolli, L. Trento, W.-D. Schneider, Chemical reactivity of size-selected supported clusters: an experimental setup, Rev. Sci. Inst. 68 (1997) 1986–1994.
[21] F.F. Schweinberger, A.S. Crampton, T. Zimmermann, G. Kwon, C.J. Ridge, S. Günther, U. Heiz, Submonolayer sensitive adsorption study of trichloroethene on single crystal surfaces by means of MIES, UPS and TPD, Surf. Sci. 609 (2013) 18–29, http://dx.doi.org/10.1016/j.susc.2012.09.005.
[22] S. Kunz, K. Hartl, M. Nesselberger, F.F. Schweinberger, G. Kwon, M. Hanzlik, K.J. J. Mayrhofer, U. Heiz, M. Arenz, Size-selected clusters as heterogeneous model catalysts under applied reaction conditions, Phys. Chem. Chem. Phys. 12 (35) (2010) 10288–10291, http://dx.doi.org/10.1039/C0CP00288G.
[23] M.J. Berr, F.F. Schweinberger, M. Döblinger, K.E. Sanwald, C. Wolff, J. Breimeier, A.S. Crampton, C.J. Ridge, M. Tschurl, U. Heiz, F. Jäckel, J. Feldmann, Size-selected subnanometer cluster catalysts on semiconductor nanocrystal films for atomic scale insight into photocatalysis, Nano Letters 12 (11) (2012) 5903–5906, http://dx.doi.org/10.1021/nl3033069.
[24] K. Wettergren, F.F. Schweinberger, D. Deiana, C.J. Ridge, A.S. Crampton, M.D. Rötzer, T.W. Hansen, V.P. Zhdanov, U. Heiz, C. Langhammer, High sintering resistance of size-selected platinum cluster catalysts by suppressed ostwald ripening, Nano Letters 14 (10) (2014) 5803–5809, http://dx.doi.org/10.1021/nl502686u.
[25] F.F. Schweinberger, Catalysis with Supported Size-selected Pt Clusters, Springer Theses, Springer International Publishing, Switzerland, Cham, 2014.
[26] C. Harding, S. Kunz, V. Habibpour, V. Teslenko, M. Arenz, U. Heiz, Dual pulsed-beam controlled mole fraction studies of the catalytic oxidation of CO on supported pd nanocatalysts, J. Catal. 255 (2) (2008) 234–240, http://dx.doi.org/10.1016/j.jcat.2008.02.008.
[27] Y. Amenomiya, R.F. Pottie, Mass spectra of some deuterated ethanes. I. The effect of ionizing voltage, Can. J. Chem. 46 (10) (1968) 1735–1739, http://dx.doi.org/10.1139/v68-288.
[28] W.G. Durrer, H. Poppa, J.T. Dickinson, C. Park, Decomposition of ethylene on small Pd particles, J. Vac. Sci. Technol. A 3 (3) (1985) 1545–1548, http://dx.doi.org/10.1116/1.573159.
[29] T.P. Beebe Jr., J.T. Yates Jr., Spectroscopic detection of (111) facets on supported pd crystallites: site blocking by ethylidyne on Pd/Al_2O_3, Surf. Sci. 173 (2–3) (1986) L606–L612, http://dx.doi.org/10.1016/0039-6028(86)90186-X.
[30] P. Chen, K.Y. Kung, Y.R. Shen, G.A. Somorjai, Sum frequency generation spectroscopic study of CO/ethylene coadsorption on the Pt(111) surface and CO poisoning of catalytic ethylene hydrogenation, Surf. Sci. 494 (3) (2001) 289–297, http://dx.doi.org/10.1016/S0039-6028(01)01512-6.
[31] R.M. Rioux, J.D. Hoefelmeyer, M. Grass, H. Song, K. Niesz, P. Yang, G.A. Somorjai, Adsorption and co-adsorption of ethylene and carbon monoxide on silica-supported monodisperse pt nanoparticles: volumetric adsorption and infrared spectroscopy studies, Langmuir 24 (1) (2008) 198–207, http://dx.doi.org/10.1021/la702685a.
[32] M.J. Lundwall, S.M. McClure, D.W. Goodman, Probing terrace and step sites on pt nanoparticles using CO and ethylene, J. Phys. Chem. C 114 (17) (2010) 7904, http://dx.doi.org/10.1021/jp9119292.
[33] B. Yoon, U. Landman, V. Habibpour, C. Harding, S. Kunz, U. Heiz, M. Moseler, M. Walter, Oxidation of magnesia-supported Pd30 nanoclusters and catalyzed CO combustion: size-selected experiments and first-principles theory, J. Phys. Chem. C 116 (17) (2012) 9594–9607, http://dx.doi.org/10.1021/jp301314s.
[34] G. Kresse, D. Joubert, From ultrasoft pseudopotentials to the projector augmented-wave method, Phys. Rev. B 59 (3) (1999) 1758–1775, http://dx.doi.org/10.1103/PhysRevB.59.1758.
[35] J.P. Perdew, K. Burke, M. Ernzerhof, Generalized gradient approximation made simple, Phys. Rev. Lett. 77 (18) (1996) 3865–3868, http://dx.doi.org/10.1103/PhysRevLett.77.3865.
[36] M. Moseler, H. Häkkinen, R.N. Barnett, U. Landman, Structure and magnetism of neutral and anionic palladium clusters, Phys. Rev. Lett. 86 (12) (2001) 2545–2548, http://dx.doi.org/10.1103/PhysRevLett.86.2545.
[37] M. Moseler, H. Häkkinen, U. Landman, Supported magnetic nanoclusters: soft landing of Pd clusters on a MgO surface, Phys. Rev. Lett. 89 (17) (2002) 176103, http://dx.doi.org/10.1103/PhysRevLett.89.176103.
[38] A. Ruban, B. Hammer, P. Stoltze, H.L. Skriver, J.K. Nørskov, Surface electronic structure and reactivity of transition and noble metals, J. Mol. Catal. A 115 (3) (1997) 421–429, http://dx.doi.org/10.1016/S1381-1169(96)00348-2.
[39] U. Starke, A. Barbieri, N. Materer, M.A. Van Hove, G.A. Somorjai, Ethylidyne on Pt(111): determination of adsorption site, substrate relaxation and coverage by automated tensor LEED, Surf. Sci. 286 (1–2) (1993) 1–14, http://dx.doi.org/10.1016/0039-6028(93)90551-T.
[40] T.P. Beebe, J.T. Yates, An in situ infrared spectroscopic investigation of the role of ethylidyne in the ethylene hydrogenation reaction on palladium/alumina, J. Am. Chem. Soc. 108 (4) (1986) 663–671, http://dx.doi.org/10.1021/ja00264a016.
[41] F. Zaera, T.V. Janssens, H. Öfner, Reflection absorption infrared spectroscopy and kinetic studies of the reactivity of ethylene on Pt(111) surfaces, Surf. Sci. 368 (1–3) (1996) 371, http://dx.doi.org/10.1016/S0039-6028 96 01078-3.
[42] J. Creighton, J. White, A SIMS study of the dehydrogenation of ethylene on Pt (111), Surf. Sci. 129 (2–3) (1983) 327, http://dx.doi.org/10.1016/0039-6028(83)90183-8.
[43] T.A. Land, T. Michely, R.J. Behm, J.C. Hemminger, G. Comsa, Direct observation of surface reactions by scanning tunneling microscopy:

ethylene>ethylidyne>carbon particles>graphite on Pt(111), J. Chem. Phys. 97 (9) (1992) 6774–6783, http://dx.doi.org/10.1063/1.463655.
[44] M. Primet, N. Sheppard, Modifications of the infrared spectra from chemisorbed CO as a measure of hydrogen coverage of a nickel surface: dependence of the spectra of chemisorbed ethylene on hydrogen coverage, J. Catal. 41 (2) (1976) 258–270, http://dx.doi.org/10.1016/0021-9517(76)90341-9.
[45] F. Zaera, R.B. Hall, High-resolution electron energy loss spectroscopy and thermal programmed desorption studies of the chemisorption and thermal decomposition of ethylene and acetylene on nickel(100) single-crystal surfaces, J. Phys. Chem. 91 (16) (1987) 4318–4323, http://dx.doi.org/10.1021/j100300a023.
[46] U. Heiz, U. Landman, P. Avouris, B. Bhushan, D. Bimberg, K. von Klitzing, H. Sakaki, R. Wiesendanger (Eds.), Nanocatalysis, Nanoscience and Technology, Springer Berlin Heidelberg, Berlin, Heidelberg, 2007.
[47] U. Landman, B. Yoon, C. Zhang, U. Heiz, M. Arenz, Factors in gold nanocatalysis: oxidation of CO in the non-scalable size regime, Top. Catal. 44 (1–2) (2007) 145–158, http://dx.doi.org/10.1007/s11244-007-0288-6.

4 Conclusion and Outlook

In the preceding chapter the results of a thorough, fundamental study of ethylene hydrogenation on size-selected clusters in UHV have been presented, addressing a number of important aspects in catalysis. These include: (i) cluster size in the sub-nanometer size range, (ii) effect of co-adsorbates on catalytic activity, (iii) influence of the metal-oxide thin film used as a catalyst support, (iv) effect of the metal-oxide thin film stoichiometry and (v) influence of the catalytic metal used for the reaction. The utilization of surface science techniques enabled targeted investigations pertaining to each of these points and revealed unexpected behavior from a classical model catalytic system.

The influence of **cluster size** was shown to answer long-standing questions regarding the use of structure sensitivity or insensitivity to classify catalytic reactions, specifically with respect to ethylene hydrogenation. It was shown that cluster catalysts in the non-scalable size regime exhibit size-dependent activity, both in single shot TPR experiments and isothermal PMB experiments. It was observed that Pt_{7-9} supported on MgO, exhibited no reactivity for the ethylene hydrogenation in a TPR experiment, and only beginning with Pt_{10} was ethane production observed. *Ab initio* calculations carried out by the Landman group showed that this 'on/off' effect was due to a higher activation barrier for Pt_9 compared to Pt_{10}, which could be rationalized by the distribution of charge over the cluster's atoms upon adsorption on the MgO surface. Pt_{13} displayed highest reactivity in the TPR experiments with larger sizes converging to the single crystal reactivity. Isothermal PMB catalysis at 300 K also showed the same trend, with Pt_{13} exhibiting the highest reactivity. The size-dependent TOF showed that ethylene hydrogenation is indeed a structure sensitive reaction in the sub-nanometer particle size-range, finally applying the criterion of Geoffrey Bond with examining particle sizes of *all* dispersions, including unity (see chapter 1.2 and ref. [67]). Pt_{7-9} were also observed to have a similar activity to Pt(111), which was to be expected from the theoretical calculations, where at 300 K the hydrogenation activation barrier is surmountable. Along with Pt_{10}, these cluster sizes displayed structure insensitive behavior at 300 K, that is they all have the same TOF as the Pt(111) single crystal.

It was also observed that applying a few ethylene pulses at 400 K effected a loss of this size dependent activity at 300 K for Pt_{11-15}, which could be directly attributed to the formation of dehydrogenated ethylene species on the clusters. These species were detected indirectly using CO coupled with IRRAS as a chemical probe. This answered a long standing question regarding observed structure sensitivity, where it was posited, but never experimentally demonstrated, that carbon species mask the underlying properties of platinum causing the observed structure insensitivity from single crystals to nanoparticles as small as 1.6 nm. Some cluster sizes, however, were observed to be resistant to the deactivation at 400 K, an observation which should be investigated further.

Support effects were also studied by performing the ethylene hydrogenation on size-selected platinum clusters supported on SiO_2. The SiO_2 thin films used in this work also represented an advancement, as a three dimensional, closed, amorphous film was successfully grown on a Pt(111) single crystal for the first time [174]. Previous attempts had only achieved a bilayer, open structure, which was unsuitable for experiments on model catalysts. The cluster TPR experiments from this support exhibited a completely different spectrum of reactivity, where Pt_{13} now showed the lowest reactivity (comparable to Pt(111)), no on/off was observed between Pt_9 and Pt_{10}, and Pt_{14} was observed to be the most reactive cluster. Again, this same trend was observed with PMB experiments, where the TOF from Pt_{13} was similar to Pt(111) and Pt_{14} exhibited the highest activity. After pulsing at 400 K, Pt_{14} remained surprisingly more active than other cluster sizes, which all lost their size-dependence as observed on MgO. Using CO as a chemical probe, the activity, and deactivation, of the clusters mirrored the magnitude of the redshift observed after the 400 K reaction step. The fact that the most active size, Pt_{14}, was also the most resistant to deactivation, and displayed the smallest redshift, demonstrates that this cluster size has an inherent resistance to ethylene dehydrogenation reactions.

Comparing the results from **MgO and SiO_2**, Pt_{13} presents a most interesting case due to the high activity on MgO and low activity on SiO_2. Theoretical calculations by the Landman Group are underway to investigate the interaction of Pt_{13} with the silica support. Initial results indicate that there is a much stronger cluster-support interaction leading to a pronounced difference in cluster morphology compared to the MgO film. Additionally, it was observed that other cluster sizes tended to be more active on the silica films. As silica is a more acidic support (electron withdrawing), the Pallassana-Neurock Model [173], was used to explain the difference in activity. The activity of Pt_{20} was observed to be identical on the two supports, which is to be expected as larger particle sizes begin to converge to the bulk, structure insensitive properties.

The effect of **changing the support stoichiometry** was investigated through the activity of Pt_{13} on different silica supports. The silicon rich film displayed the greatest propensity to poisoning by completely deactivating after the temperature step to 400 K, but had a similar activity at 300 K as the stoichiometric film and Pt(111) due to the formation of carbon species on all these systems already at this temperature which induce structure insensitivity. The oxygen rich film effected a much higher activity on Pt_{13} (more active than Pt(111)) indicating that the ethylene hydrogenation rate can be controlled by changing the stoichiometry of the support material. The presence of CO adsorption sites on the stoichiometric and oxygen rich film after the reaction was performed indicated a lesser degree of catalyst poisoning compared to the silicon rich film, where no CO adsorption was observed. The differences and similarities when comparing CO adsorption before and after the reaction indicated that the nature of single atomic sites, where CO is bonded, is a poor predictor of ethylene hydrogenation chemistry. This was especially true for the silicon rich film, and this could possibly be from a drastic change in particle morphology to a (111) type of structure, introduced by electron donation from silicon. This implies that geometric arrangements of multiple atoms are decisive, a property predicted for structure sensitive reactions. The results observed in the reactivity and CO adsorption experiments were partially explained by considering the nature of the more abundant species in each

film. Silicon acts as an electron donating species and therefore it was postulated that Pt_{13} clusters acquire a more negative charge than on the stoichiometric silica. The converse is then expected for the oxygen rich film, where electron withdrawal produces a more positive charge on the clusters. By utilizing the Pallassana-Neurock model [173], these trends were rationalized.

The **effect of the metal** on the ethylene hydrogenation activity was investigated on samples of nickel, palladium and platinum with a particle size of 1-1.5 nm. The PMB technique was applied and a significant change in behavior for each of the metals was observed. Nickel clusters showed an immediate deactivation at 300 K, but oddly CO adsorption was only slightly reduced, with no bridge-bonded species visible and a redshifted shoulder on the main CO peak. Palladium showed a complete deactivation at 300 K only after pulsing at 400 K, and no CO adsorption was observed, indicating a poisoning of the surface through dehydrogenation products. Platinum also showed a deactivation, after the 400 K step, but still retained activity. The presence of CO adsorption after the temperature step also corroborated this result. The experimental observations confirmed the trend predicted theoretically by Pallassana and Neurock [173]. The d-band centers of nickel, palladium and platinum M_{30} clusters were calculated and the trend in deactivation was directly comparable to this value. Nickel's d-band center is located closest to the Fermi level and exhibited the most facile deactivation, whereas platinum's d-band is farthest away, and therefore showed the highest resistance to deactivation.

In terms of purely ethylene hydrogenation, it was shown that this reaction is actually structure sensitive on platinum and that dehydrogenation of ethylene on the catalyst induces the structure insensitive behavior observed for nanoparticles and single crystals. The data showed that the influence and identity of these carbon species is expected to be strongly dependent on the cluster size, and this is an aspect that should be investigated in the future.

The work presented in this dissertation is only the tip of the iceberg with regards to future measurements of more complex molecules. Figure 4.1 depicts preliminary results from the hydrogenation of 3-hexyne with deuterium on MgO supported, size-selected platinum clusters. These results are the integrals of TPR curves as a function of cluster size. 3-hexyne represents a distinct increase in complexity due to the multiple reaction pathways now available, which include the observed hydrogenation to the alkene, self-hydrogenation and cyclo-dehydrogenation to form benzene. From the data it can be observed that there are pronounced differences in reactivity for different platinum cluster sizes as well as differing proclivities for the aforementioned reaction paths. The cyclo-dehydrogenation pathway, figure 4.1a, is first observed for clusters consisting of 4 atoms which is a strong indication of the bonding geometry of the relevant intermediate needed for this reaction. The self-hydrogenation reaction, figure 4.1b, requires 7 atoms and is also observed to exhibit differing reactivities as a function of cluster size. The true hydrogenation reaction (differentiated by the fact that deuterium was used), requires 8 atoms and also shows a size-dependent reactivity. These results show that the chemistry of 3-hexyne strongly differs to that of ethylene and also shows promise for controlling reaction selectivity. Aside from 3-hexyne, hydrocarbons exhibiting more than one functional group, such as crotonaldehyde, will be studied to examine the effect of cluster size on chemoselectivity. This reaction is already

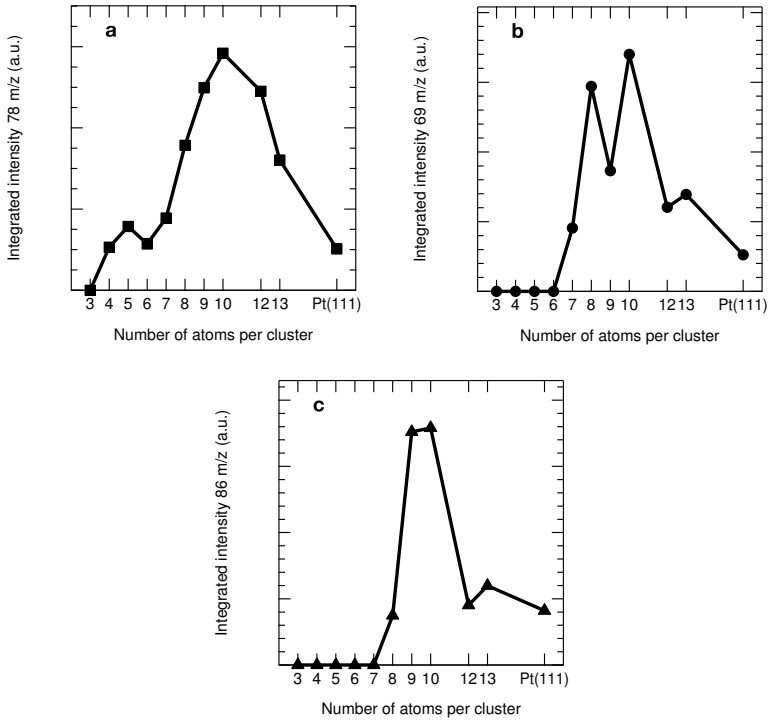

Figure 4.1: Integrated intensity of TPR data from 3-hexyne hydrogenation with deuterium on MgO(100) supported platinum clusters and Pt(111). (a) depicts the results for the formation of benzene (78 m/z), (b) non-deuterated 3-hexene (69 m/z) from the the self-hydrogenation of 3-hexyne, and (c) hexane-d_2 (86 m/z) from the hydrogenation of 3-hexyne with deuterium.

known to exhibit size-dependent activity and selectivity on platinum nanoparticles [179], which indicates that the behavior in the sub-nanometer regime should show unexpected behavior.

This dissertation has shown that hydrocarbon chemistry and catalytic transformations can be controlled by a number of different parameters including cluster size, support material, support stoichiometry and metal. The systematic investigation of these factors revealed many unique and unprecedented properties which can be further investigated for more applied systems. These studies will hopefully reveal how singular variables can influence a catalytic reaction which leads to determining foundational catalyst design principles. By applying these design principles, extracted from studies like the one performed for this dissertation, important advancements can be made in making more active, selective and cheaper catalyst materials, but also understanding the underlying molecular mechanisms at work.

Bibliography

[1] Sabatier, P.; Senderens, J.-B. *Compt. rend. Acad. Sci* **1897**, *124*, 1358.

[2] Horiuti, I.; Polanyi, M. *Trans. Farad. Soc.* **1934**, *30*, 1164–1172.

[3] Horiuti, J.; Miyahara, K. *NSRDS-NBS* **1968**,

[4] Lyon, H. B.; Somorjai, G. A. *J. Chem. Phys.* **1967**, *46*, 2539–2550.

[5] Morgan, A. E.; Somorjai, G. A. *J. Chem. Phys.* **1969**, *51*, 3309–3320.

[6] Stair, P. C.; Somorjai, G. A. *J. Chem. Phys.* **1977**, *66*, 2036–2044.

[7] Smith, D. L.; Merrill, R. P. *J. Chem. Phys.* **1970**, *52*, 5861–5872.

[8] Ibach, H.; Hopster, H.; Sexton, B. *Appl. Surf. Sci.* **1977**, *1*, 1–24.

[9] Kesmodel, L. L.; Dubois, L. H.; Somorjai, G. A. *Chem. Phys. Lett.* **1978**, *56*, 267–271.

[10] Baró, A. M.; Ibach, H. *J. Chem. Phys.* **1981**, *74*, 4194–4199.

[11] Demuth, J. E. *Surf. Sci.* **1980**, *93*, L82–L88.

[12] Demuth, J. E. *Surf. Sci.* **1979**, *80*, 367–387.

[13] Skinner, P.; Howard, M. W.; Oxton, I. A.; Kettle, S. F. A.; Powell, D. B.; Sheppard, N. *J. Chem. Soc., Farad. Trans. 2* **1981**, *77*, 1203–1215.

[14] Albert, M. R.; Sneddon, L. G.; Eberhardt, W.; Greuter, F.; Gustafsson, T.; Plummer, E. W. *Surf. Sci.* **1982**, *120*, 19–37.

[15] Steininger, H.; Ibach, H.; Lehwald, S. *Surf. Sci.* **1982**, *117*, 685–698.

[16] Salmeron, M.; Somorjai, G. A. *J. Phys. Chem.* **1982**, *86*, 341.

[17] Creighton, J.; White, J. *Surf. Sci.* **1983**, *129*, 327.

[18] Ibach, H.; Lehwald, S. *J. Vac. Sci. Tech.* **1978**, *15*, 407–415.

[19] Koestner, R. J.; Van Hove, M. A.; Somorjai, G. A. *J. Phys. Chem.* **1983**, *87*, 203–213.

[20] Hugenschmidt, M. B.; Dolle, P.; Jupille, J.; Cassuto, A. *J. Vac. Sci. Tech. A.* **1989**, *7*, 3312–3316.

[21] Cassuto, A.; Touffaire, M.; Hugenschmidt, M.; Dolle, P.; Jupille, J. *Vacuum* **1990**, *41*, 161.

[22] Cassuto, A.; Kiss, J.; White, J. *Surf. Sci.* **1991**, *255*, 289.

[23] Zaera, F.; Somorjai, G. A. *J. Am. Chem. Soc.* **1984**, *106*, 2288.

[24] Engel, T.; Ertl, G. *Chem. Phys. Lett.* **1978**, *54*, 95–98.

[25] Engel, T.; Ertl, G. *J. Chem. Phys.* **1978**, *69*, 1267–1281.

[26] Bozso, F.; Ertl, G.; Grunze, M.; Weiss, M. *J. Catal.* **1977**, *49*, 18–41.

[27] Ertl, G.; Lee, S. B.; Weiss, M. *Surf. Sci.* **1982**, *114*, 515–526.

[28] Imbihl, R.; Behm, R. J.; Ertl, G.; Moritz, W. *Surf. Sci.* **1982**, *123*, 129–140.

[29] Ertl, G. *J. Vac. Sci. Tech. A.* **1983**, *1*, 1247–1253.

[30] Berlowitz, P.; Megiris, C.; Butt, J. B.; Kung, H. H. *Langmuir* **1985**, *1*, 206.

[31] Yagasaki, E.; Backman, A. L.; Chen, B.; Masel, R. I. *J. Vac. Sci. Tech. A.* **1990**, *8*, 2616–2621.

[32] Yagasaki, E.; Masel, R. *Surf. Sci.* **1990**, *226*, 51–60.

[33] Godbey, D.; Zaera, F.; Yeates, R.; Somorjai, G. A. *Surf. Sci.* **1986**, *167*, 150–166.

[34] Zaera, F. *J. Phys. Chem.* **1990**, *94*, 5090–5095.

[35] Beebe, T. P.; Yates, J. T. *J. Am. Chem. Soc.* **1986**, *108*, 663–671.

[36] Zaera, F. *J. Phys. Chem.* **1990**, *94*, 8350–8355.

[37] Mohsin, S. B.; Trenary, M.; Robota, H. J. *J. Phys. Chem.* **1988**, *92*, 5229.

[38] Cremer, P. S.; Su, X.; Shen, Y. R.; Somorjai, G. A. *J. Am. Chem. Soc.* **1996**, *118*, 2942.

[39] Zaera, F. *Langmuir* **1996**, *12*, 88.

[40] Öfner, H.; Zaera, F. *J. Phys. Chem. B* **1997**, *101*, 396.

[41] McCrea, K. R.; Somorjai, G. A. *J. Mol. Catal. A* **2000**, *163*, 43–53.

[42] Masson, A.; Bellamy, B.; Romdhane, Y.; Che, M.; Roulet, H.; Dufour, G. *Surf. Sci.* **1986**, *173*, 479–497.

[43] Wood, D. M. *Phys. Rev. Lett.* **1981**, *46*, 749–749.

[44] Cortright, R. D.; Goddard, S. A.; Rekoske, J. E.; Dumesic, J. A. *J. Catal.* **1991**, *127*, 342–353.

[45] Boudart, M.; Djéga-Mariadassou, G. *Kinetics Of Heterogeneous Catalytic Reactions*; Princeton University Press, Princeton, N.J., 1984.

[46] Goddard, S. A.; Cortright, R. D.; Dumesic, J. A. *J. Catal.* **1992**, *137*, 186–198.

[47] Ko, M. K.; Frei, H. *J. Phys. Chem. B* **2004**, *108*, 1805.

[48] Wasylenko, W.; Frei, H. *J. Phys. Chem. B* **2005**, *109*, 16873–16878.

[49] Grunes, J.; Zhu, J.; Yang, M.; Somorjai, G. A. *Catal. Lett.* **2003**, *86*, 157.

[50] Tang, D. C.; Hwang, K. S.; Salmeron, M.; Somorjai, G. A. *J. Phys. Chem. B* **2004**, *108*, 13300.

[51] Contreras, A. M.; Grunes, J.; Yan, X. M.; Liddle, A.; Somorjai, G. A. *Catal. Lett.* **2005**, *100*, 115.

[52] Rioux, R. M.; Song, H.; Hoefelmeyer, J. D.; Yang, P.; Somorjai, G. A. *J. Phys. Chem. B* **2005**, *109*, 2192.

[53] Song, H.; Rioux, R. M.; Hoefelmeyer, J. D.; Komor, R.; Niesz, K.; Grass, M.; Yang, P.; Somorjai, G. A. *J. Am. Chem. Soc.* **2006**, *128*, 3027–3037.

[54] Tilekaratne, A.; Simonovis, J. P.; López Fagúndez, M. F.; Ebrahimi, M.; Zaera, F. *ACS Catalysis* **2012**, *2*, 2259–2268.

[55] Ebrahimi, M.; Simonovis, J. P.; Zaera, F. *J. Phys. Chem. Lett.* **2014**, *5*, 2121–2125.

[56] Sapi, A.; Thompson, C.; Wang, H.; Michalak, W. D.; Ralston, W. T.; Alayoglu, S.; Somorjai, G. A. *Catal. Lett.* **2014**, *144*, 1151–1158.

[57] Jung, U.; Elsen, A.; Li, Y.; Smith, J. G.; Small, M. W.; Stach, E. A.; Frenkel, A. I.; Nuzzo, R. G. *ACS Catalysis* **2015**, 1539–1551.

[58] Chen, P.; Kung, K. Y.; Shen, Y. R.; Somorjai, G. A. *Surf. Sci.* **2001**, *494*, 289–297.

[59] Ainsworth, M. K.; McCoustra, M. R. S.; Chesters, M. A.; Sheppard, N.; De La Cruz, C. *Surf. Sci.* **1999**, *437*, 9–17.

[60] Stoop, F.; Toolenaar, F. J. C. M.; Ponec, V. *J. Catal.* **1982**, *73*, 50–56.

[61] Rioux, R. M.; Hoefelmeyer, J. D.; Grass, M.; Song, H.; Niesz, K.; Yang, P.; Somorjai, G. A. *Langmuir* **2008**, *24*, 198–207.

[62] Lundwall, M. J.; McClure, S. M.; Goodman, D. W. *J. Phys. Chem. C* **2010**, *114*, 7904.

[63] Brandt, R. K.; Hughes, M. R.; Bourget, L. P.; Truszkowska, K.; Greenler, R. G. *Surf. Sci.* **1993**, *286*, 15–25.

[64] Kappers, M. J.; Maas, J. H. v. d. *Catal. Lett.* **1991**, *10*, 365–373.

[65] Boudart, M. In *Advances in Catalysis*; D.D. Eley, H. P. a. P. B. W., Ed.; Academic Press, 1969; Vol. 20; pp 153–166.

[66] Taylor, H. S. *Proc. R. Soc. London, Ser. A* **1925**, *108*, 105–111.

[67] Bond, G. C. *Chem. Soc. Rev.* **1991**, *20*, 441–475.

[68] Bond, G. C. *Surf. Sci.* **1985**, *156, Part 2*, 966–981.

[69] Klasovsky, F.; Claus, P. In *Metal Nanoclusters in Catalysis: Effects of Nanoparticle Size, Shape and Structure*; Corain, B., Schmid, G., Toshima, N., Eds.; Elsevier, 2008; Chapter 8, pp 167–181.

[70] Boudart, M. *J. Mol. Catal.* **1985**, *30*, 27–38.

[71] Thomson, S. J.; Webb, G. *J. Chem. Soc., Chem. Comm.* **1976**, 526–527.

[72] Zaera, F. *Phys. Chem. Chem. Phys.* **2013**, *15*, 11988–12003.

[73] Spencer, N.; Schoonmaker, R.; Somorjai, G. *J. Catal.* **1982**, *74*, 129.

[74] Carter, J. L.; Cusumano, J. A.; Sinfelt, J. H. *J. Phys. Chem.* **1966**, *70*, 2257–2263.

[75] Martin, G. *J. Catal.* **1979**, *60*, 452.

[76] Guczi, L.; Gudkov, B. S. *Reaction Kinetics and Catalysis Letters* **1978**, *9*, 343–347.

[77] Nazimek, D.; Ryczkowski, J. *Reaction Kinetics and Catalysis Letters* **1989**, *40*, 145–150.

[78] Goodman, D. W. *Surface Science* **1982**, *123*, L679–L685.

[79] Watwe, R. M.; Cortright, R. D.; Nørskov, J. K.; Dumesic, J. A. *J. Phys. Chem. B* **2000**, *104*, 2299.

[80] Rioux, R.; Song, H.; Yang, P.; Somorjai, G. In *Metal Nanoclusters in Catalysis: Effects of Nanoparticle Size, Shape and Structure*; Corain, B., Schmid, G., Toshima, N., Eds.; Elsevier, 2008; Chapter 7, pp 149–166.

[81] Ertl, G. *Surf. Sci.* **1994**, *299–300*, 742–754.

[82] Goodman, D. W. *J. Phys. Chem.* **1996**, *100*, 13090–13102.

[83] Boudart, M. *Top. Catal.* **2000**, *13*, 147–149.

[84] Somorjai, G. A.; Li, Y. *Proc. Nat. Acad. Sci.* **2011**, *108*, 917–924.

[85] de Heer, W. A. *Rev. Mod. Phys.* **1993**, *65*, 611.

[86] Heiz, U., Landman, U., Eds. *Nanocatalysis*; Nanoscience and Technology; Springer Berlin Heidelberg: Berlin, Heidelberg, 2007.

[87] Watanabe, Y. *Science and Technology of Advanced Materials* **2014**, *15*, 063501.

[88] Heiz, U., Landman, U., Eds. *Nanocatalysis*; Springer, 2008.

[89] Meiwes-Broer, K.-H., Ed. *Metal Clusters at Surfaces*; Springer Verlag, 2000.

[90] Heiz, U.; Sanchez, A.; Abbet, S.; Schneider, W.-D. *J. Am. Chem. Soc.* **1999**, *121*, 3214–3217.

[91] Watanabe, Y.; Wu, X.; Hirata, H.; Isomura, N. *Catal. Sci. Tech.* **2011**, *1*, 1490.

[92] Haruta, M. *Catalysis Today* **1997**, *36*, 153–166.

[93] Sanchez, A.; Abbet, S.; Heiz, U.; Schneider, W.-D.; Häkkinen, H.; Barnett, R. N.; Landman, U. *J. Phys. Chem. A* **1999**, *103*, 9573–9578.

[94] Herzing, A. A.; Kiely, C. J.; Carley, A. F.; Landon, P.; Hutchings, G. J. *Science* **2008**, *321*, 1331–1335.

[95] Röttgen, M. A.; Abbet, S.; Judai, K.; Antonietti, J.-M.; Wörz, A. S.; Arenz, M.; Henry, C. R.; Heiz, U. *J. Am. Chem. Soc.* **2007**, *129*, 9635–9639.

[96] Harding, C.; Kunz, S.; Habibpour, V.; Teslenko, V.; Arenz, M.; Heiz, U. *J. Catal.* **2008**, *255*, 234.

[97] Yoon, B.; Landman, U.; Habibpour, V.; Harding, C.; Kunz, S.; Heiz, U.; Moseler, M.; Walter, M. *J. Phys. Chem. C* **2012**, *116*, 9594–9607.

[98] Moseler, M.; Walter, M.; Yoon, B.; Landman, U.; Habibpour, V.; Harding, C.; Kunz, S.; Heiz, U. *J. Am. Chem. Soc.* **2012**, *134*, 7690–7699.

[99] Kaden, W. E.; Wu, T.; Kunkel, W. A.; Anderson, S. L. *Science* **2009**, *326*, 826.

[100] Kaden, W. E.; Kunkel, W. A.; Roberts, F. S.; Kane, M.; Anderson, S. L. *Surf. Sci.* **2014**, *621*, 40–50.

[101] Kunz, S.; Schweinberger, F. F.; Habibpour, V.; Röttgen, M.; Harding, C.; Arenz, M.; Heiz, U. *J. Phys. Chem. C* **2010**, *114*, 1651–1654.

[102] Bonanni, S.; Aït-Mansour, K.; Harbich, W.; Brune, H. *J. Am. Chem. Soc.* **2012**, *134*, 3445–3450.

[103] Harding, C.; Habibpour, V.; Kunz, S.; Farnbacher, A. N.-S.; Heiz, U.; Yoon, B.; Landman, U. *J. Am. Chem. Soc.* **2009**, *131*, 538–548.

[104] Yoon, B.; Landman, U.; Woerz, A. S.; Antonietti, J.-M.; Abbet, S.; Judai, K.; Heiz, U. *Science* **2005**, *307*, 403.

[105] Kane, M. D.; Roberts, F. S.; Anderson, S. L. *J. Phys. Chem. C* **2015**, *119*, 1359–1375.

[106] Abbet, S.; Sanchez, A.; Heiz, U.; Schneider, W.-D.; Ferrari, A. M.; Pacchioni, G.; Rösch, N. *J. Am. Chem. Soc.* **2000**, *122*, 3453–3457.

[107] Abbet, S.; Sanchez, A.; Heiz, U.; Schneider, W. D.; Ferrari, A. M.; Pacchioni, G.; Rösch, N. *Surf. Sci.* **2000**, *454–456*, 984–989.

[108] Wörz, A. S.; Judai, K.; Abbet, S.; Heiz, U. *J. Am. Chem. Soc.* **2003**, *125*, 7964–7970.

[109] Vajda, S.; Pellin, M. J.; Greeley, J. P.; Marshall, C. L.; Curtiss, L. A.; Ballentine, G. A.; Elam, J. W.; Catillon-Mucherie, S.; Redfern, P. C.; Mehmood, F.; Zapol, P. *Nature Materials* **2009**, *8*, 213–216.

[110] Lee, S.; Vece, M. D.; Lee, B.; Seifert, S.; Winans, R. E.; Vajda, S. *Phys. Chem. Chem. Phys.* **2012**, *14*, 9336–9342.

[111] Häkkinen, H.; Abbet, S.; Sanchez, A.; Heiz, U.; Landman, U. *Angew. Chem. Int. Ed.* **2003**, *42*, 1297–1300.

[112] Wang, B.; Yoon, B.; König, M.; Fukamori, Y.; Esch, F.; Heiz, U.; Landman, U. *Nano Letters* **2012**, *12*, 5907–5912.

[113] Roettgen, M. A.; Abbet, S.; K.Judai,; Antonietti, J.-M.; Woerz, A. S.; Arenz, M.; Henry, C. R.; Heiz, U. *J. Am. Chem. Soc.* **2007**, *129*, 9635.

[114] Kunz, S.; Hartl, K.; Nesselberger, M.; Schweinberger, F. F.; Kwon, G.; Hanzlik, M.; Mayrhofer, K. J. J.; Heiz, U.; Arenz, M. *Phys. Chem. Chem. Phys.* **2010**, *12*, 10288–10291.

[115] Schweinberger, F. F.; Berr, M. J.; Döblinger, M.; Wolff, C.; Sanwald, K. E.; Crampton, A. S.; Ridge, C. J.; Jäckel, F.; Feldmann, J.; Tschurl, M.; Heiz, U. *J. Am. Chem. Soc.* **2013**, *135*, 13262–13265.

[116] Berr, M. J.; Schweinberger, F. F.; Döblinger, M.; Sanwald, K. E.; Wolff, C.; Breimeier, J.; Crampton, A. S.; Ridge, C. J.; Tschurl, M.; Heiz, U.; Jäckel, F.; Feldmann, J. *Nano Letters* **2012**, *12*, 5903–5906.

[117] Fukamori, Y.; König, M.; Yoon, B.; Wang, B.; Esch, F.; Heiz, U.; Landman, U. *ChemCatChem* **2013**, *5*, 3330–3341.

[118] Bonanni, S.; Aït-Mansour, K.; Harbich, W.; Brune, H. *J. Am. Chem. Soc.* **2014**, *136*, 8702–8707.

[119] Wettergren, K.; Schweinberger, F. F.; Deiana, D.; Ridge, C. J.; Crampton, A. S.; Rötzer, M. D.; Hansen, T. W.; Zhdanov, V. P.; Heiz, U.; Langhammer, C. *Nano Letters* **2014**, *14*, 5803–5809.

[120] Proch, S.; Wirth, M.; White, H. S.; Anderson, S. L. *J. Am. Chem. Soc.* **2013**, *135*, 3073–3086.

[121] von Weber, A.; Baxter, E. T.; White, H. S.; Anderson, S. L. *J. Phys. Chem. C* **2015**, *119*, 11160–11170.

[122] Jin, R. *Nanoscale* **2010**, *2*, 343–362.

[123] Kurashige, W.; Niihori, Y.; Sharma, S.; Negishi, Y. *J. Phys. Chem. Lett.* **2014**, *5*, 4134–4142.

[124] Chorkendorff, I.; Niemantsverdriet, J. W. *Concepts of Modern Catalysis and Kinetics*, 2nd ed.; Wiley-VCH, 2007.

[125] Pacchioni, G.; Giordano, L.; Baistrocchi, M. *Phys. Rev. Lett.* **2005**, *94*, 226104.

[126] Ricci, D.; Bongiorno, A.; Pacchioni, G.; Landman, U. *Phys. Rev. Lett.* **2006**, *97*, 036106.

[127] Sterrer, M.; Risse, T.; Heyde, M.; Rust, H.-P.; Freund, H.-J. *Phys. Rev. Lett.* **2007**, *98*, 206103.

[128] Risse, T.; Shaikhutdinov, S.; Nilius, N.; Sterrer, M.; Freund, H.-J. *Acc. Chem. Res.* **2008**, *41*, 949–956.

[129] Giordano, L.; Vitto, A. D.; Pacchioni, G. *J. Chem. Phys.* **2006**, *124*, 034701.

[130] Baron, M.; Stacchiola, D.; Ulrich, S.; Nilius, N.; Shaikhutdinov, S.; Freund, H.-J.; Martinez, U.; Giordano, L.; Pacchioni, G. *J. Phys. Chem. C* **2008**, *112*, 3405–3409.

[131] Kim, Y. D.; Wei, T.; Goodman, D. W. *Langmuir* **2003**, *19*, 354–357.

[132] Kim, Y. D.; Wei, T.; Wendt, S.; Goodman, D. W. *Langmuir* **2003**, *19*, 7929–7932.

[133] Ewing, C. S.; Hartmann, M. J.; Martin, K. R.; Musto, A. M.; Padinjarekutt, S. J.; Weiss, E. M.; Veser, G.; McCarthy, J. J.; Johnson, J. K.; Lambrecht, D. S. *J. Phys. Chem. C* **2015**, *119*, 2503–2512.

[134] Heiz, U.; Vanolli, F.; Trento, L.; Schneider, W.-D. *Rev. Sci. Inst.* **1997**, *68*, 1986–1994.

[135] Schweinberger, F. F. *Catalysis with Supported Size-selected Pt Clusters*; Springer Theses; Springer International Publishing, Switzerland, 2014.

[136] Briggs, D.; Seah, M. P. *Practical Surface Analysis by Auger and X-ray Photoelectron Spectroscopy*; John Wiley and Sons, 1983.

[137] Ertl, G.; Küppers, J. *Low Energy Electrons and Surface Chemistry*; Wiley-VCH, 1985.

[138] Henzler, M.; Göpel, W. *Oberflächenphysik des Festkörpers*; Teubner, 1994.

[139] Harada, Y.; Masuda, S.; Ozaki, H. *Chem. Rev.* **1997**, *97*, 1897.

[140] Hüfner, S. *Photoelectron Spectroscopy: Principles and Applications*, 3rd ed.; Springer Verlag, 2003.

[141] Niemantsverdriet, J. W. *Spectroscopy in Catalysis: An Introduction*, 3rd ed.; Wiley-VCH, 2007.

[142] Kunz, S. Cluster Catalysis Under UHV and Ambient Conditions. Ph.D. thesis, Technische Universität München, 2010.

[143] Crampton, A. S. Electron Spectroscopy With Metastable Atoms - New Insights Into Classical Systems And Promise for Size-Selected Clusters. Master Thesis, Technische Universität München, 2011.

[144] Einstein, A. *Annalen der Physik* **1905**, *322*, 132.

[145] Günster, J.; Liu, G.; Kempter, V.; Goodman, D. *Surface Science* **1998**, *415*, 303–311.

[146] Spirkl, F. M.; Kunz, S.; Schweinberger, F. F.; Farnbacher, A. N.; Schröter, R.; Heiz, U. *Rev. Sci. Inst.* **2012**, *83*, 013114.

[147] Demuth, J. E.; Eastman, D. E. *Phys. Rev. Lett.* **1974**, *32*, 1123–1127.

[148] Kelemen, S. R.; Fischer, T. E. *Surf. Sci.* **1981**, *102*, 45–55.

[149] Freund, H.-J.; Neumann, M. *Appl. Phys. A* **1988**, *47*, 3.

[150] Ertl, G. *Surf. Sci.* **1979**, *89*, 525–539.

[151] Sesselmann, W.; Woratschek, B.; Ertl, G.; Küppers, J.; Haberland, H. *Surf. Sci.* **1984**, *146*, 17–42.

[152] Hoffmann, F. M. *Surf. Sci. Rep.* **1983**, *3*, 107–192.

[153] Yates, J. T. *Vibrational Spectroscopy of Molecules on Surfaces*; Plenum Press, New York, 1987.

[154] Chabal, Y. J. *Surf. Sci. Rep.* **1988**, *8*, 211–357.

[155] Malik, I. J.; Brubaker, M. E.; Mohsin, S. B.; Trenary, M. *J. Chem. Phys.* **1987**, *87*, 5554–5561.

[156] Bozack, M. J.; Muehlhoff, L.; J. N. Russel, J.; Choyke, W. J.; Yates, J. *J. Vac. Sci. Tech. A.* **1987**, *5*, 1–8.

[157] Winkler, A.; Yates, J. T. *J. Vac. Sci. Tech. A.* **1988**, *6*, 2929.

[158] Roettgen, M. Untersuchung von katalytischen Eigenschaften größenselektierter Cluster mittels gepulster Molekularstrahlen. Ph.D. thesis, Technische Universität München, 2007.

[159] Christmann, K.; Ertl, G.; Pignet, T. *Surface Science* **1976**, *54*, 365–392.

[160] Schwarz, J. A.; Madix, R. J. *J. Catal.* **1968**, *12*, 140–144.

[161] Olander, D. R. In *Proc. Fourth Intern. Materials Symp*; Somorjai, G. A., Ed.; Wiley, New York, 1969; pp 45–1.

[162] Jones, R. H.; Olander, D. R.; Siekhaus, W. J.; Schwarz, J. A. *J. Vac. Sci. Tech.* **1972**, *9*, 1429–1441.

[163] Schwarz, J. A.; Madix, R. J. *Surf. Sci.* **1974**, *46*, 317–341.

[164] Sawin, H. H.; Merrill, R. P. *J. Vac. Sci. Tech.* **1981**, *19*, 40–46.

[165] Günther, S. Moderne Methoden der Spektroskopie und Mikroskopie II. TUM Lecture, 2010.

[166] Ertl, G.; Neumann, M.; Streit, K. M. *Surf. Sci.* **1977**, *64*, 393–410.

[167] Davis, L. E.; MacDonald, N. C.; Palmberg, P. W.; Riach, G. E.; Weber, R. E. *Handbook of Auger Electron Spectroscopy*; Physical Electronics Industries, Inc., 1976.

[168] Yazawa, Y.; Yoshida, H.; Takagi, N.; Komai, S.-i.; Satsuma, A.; Hattori, T. *J. Catal.* **1999**, *187*, 15–23.

[169] Koningsberger, D. C.; Ramaker, D. E.; Miller, J. T.; Graaf, J. d.; Mojet, B. L. *Top. Catal.* **2001**, *15*, 35–42.

[170] Zhao, J.; Chen, H.; Xu, J.; Shen, J. *J. Phys. Chem. C* **2013**, *117*, 10573–10580.

[171] Zangwill, A. *Physics At Surfaces*; Cambridge University Press, 1988.

[172] Vaida, M. E.; Bernhardt, T. M.; Barth, C.; Esch, F.; Heiz, U.; Landman, U. *Phys. Status Solidi B* **2010**, *247*, 1001–1015.

[173] Pallassana, V.; Neurock, M. *J. Catal.* **2000**, *191*, 301–317.

[174] Crampton, A. S.; Ridge, C. J.; Rötzer, M. D.; Zwaschka, G.; Braun, T.; D'Elia, V.; Basset, J.-M.; Schweinberger, F. F.; Günther, S.; Heiz, U. *J. Phys. Chem. C* **2015**, *119*, 13665–13669.

[175] Wendt, S.; Ozensoy, E.; Wei, T.; Frerichs, M.; Cai, Y.; Chen, M. S.; Goodman, D. W. *Phys. Rev. B* **2005**, *72*, 115409.

[176] Yang, B.; Kaden, W. E.; Yu, X.; Boscoboinik, J. A.; Martynova, Y.; Lichtenstein, L.; Heyde, M.; Sterrer, M.; Włodarczyk, R.; Sierka, M.; Sauer, J.; Shaikhutdinov, S.; Freund, H.-J. *Phys. Chem. Chem. Phys.* **2012**, *14*, 11344–11351.

[177] Heiz, U. *Appl. Phys. A* **1998**, *67*, 621–626.

[178] Zaera, F.; Janssens, T. V.; Öfner, H. *Surf. Sci.* **1996**, *368*, 371–376.

[179] Grass, M. E.; Rioux, R. M.; Somorjai, G. A. *Catal. Lett.* **2008**, *128*, 1–8.

List of Figures

List of Tables

Acknowledgments

I would first like to thank Ueli Heiz for giving me the opportunity to work in his group and providing a most auspicious working environment. The freedom which is given to PhD students allows for a much more creative and instructional atmosphere than in more patriarchal systems, and these past years have truly been the most educational of my life.

A thank you must be given to Gustav Wiberg, Karl Mayrhofer and Matthias Arenz, who were my first colleagues here in the summer of 2007 and it was through my work with them that I was introduced to the Heiz Group.

Along this same line, Sebastian Kunz, Florian Spirkl, Martin Thämer, Aras Kartouzian, Josef Kiermaier belong to my first acquaintances here in Munich, and to them I owe a debt of gratitude for making both in and out of the work place an enjoyable experience. A special thanks also goes out to Sebastian Kunz who recruited me to the Nanocat Lab and was an important mentor as I began my Master Studies here in 2009.

My first lab partners and, Tobi Zimmermann, Wiebke Friedrich, Gihan Kwon are the people who I learned how to do experiments with on the machine. I am grateful to Florian Schweinberger, who has been in the lab for all of my time here, for always being helpful with learning the ins and outs of vacuum techniques and providing critical readings of my work. What we have accomplished together from all facets in the Nanocat Lab over the past few years has been quite impressive.

The new crowd of PhD students also deserves mention for providing a great work environment and also for the afternoons spent on our private balcony, The GaN Brothers: Constantin Walenta and Sebastian Kollmannsberger, Gas Phase: Jan Eckhardt, Daniel Neuwirt, STM: Fabian Knoller, Yves Fukamori and Michael König, SS-SHG-CRD: Tobias Lünskens and Alex von-Weber. To my current lab partner Marian Rötzer I am also very grateful for the time we worked together (or played chess), and I know that the lab, although it may not always seem like it, will keep on producing important results in the future.

Some of the PhD/PostDocs who have already left the group deserve mention here: Katrin Lange, Brad Visser, Bo Wang, Andreas Winbauer and Phillip Heister. I must thank my longtime partner in the lab, with whom the entire ethylene hydrogenation story first began to take shape, Claron Ridge.

The "elders" of the group are also due a great deal of thanks, Friedrich Esch for always showing me how to be enthusiastic about science and also for having such an admirable curiosity about nature. Sebastian Günther as both a teacher and colleague has taught me more about vacuum techniques than probably any other person and whose knowledge is second to none in the realm of surface science and greatly improved the work done in the Nanocat Lab. Lastly, to Martin Tschurl, who has not only been a great friend since 2007,

but also a wonderful chess teacher and a great person for discussing everything from science to life in general.

Lastly, I am forever grateful to my parents Andy and Barbara, my sister Nicole and her husband Jeff, along with their children, Kyndelin, Kyla, Kloe, Kelsey and Jeffrey, my sister Jill and her husband John along with their children Kali and Kylie. I could not ask for a more supporting, loving and caring family.

To my now official German family I am also very thankful, to Kurt and Gabi for our memorable city trips and the many Christmases we celebrated together. To Petra and Asma, thank you for being like family to me here in Munich over the years. The birthday parties, beer garden evenings and Ausflüge were always a great time.

I can honestly say that a singular event over 12 years ago is without a doubt in my mind the only reason why I am here today obtaining a graduate degree in chemistry. That was when I picked up my future wife, Kristina, and took her to a party in Pepperell, MA. Little did I know that 12 years later we would be married and that looking back on my academic career, if she was not there to motivate me to push my limits and be the best that I could be, I would never have thought about taking this career path. I am truly grateful to have someone who challenges me in a way that no one else can and with whom I want to spend the rest of my life with.

I think it's the only method [the scientific method] we have to try to get some approximate understanding of the world. I don't have faith that it will reach the truth or even that it is leading us in the true direction. In fact, as someone committed to the scientific method I'm also committed to its consequences and among them are that you and I and the rest of the species are organic creatures who have our specific capacities and limitations and we simply don't know and have no reason to believe that these capacities are such that we can gain the truth about the world. We do our best but that's the most we can do.

Noam Chomsky

See here how everything
lead up to this day
and it's just like
any other day
that's ever been

- The Grateful Dead